

**Top-down Emissions Verification (TDEV) of
Industrial Emissions in Houston
Based on TexAQS II Data**

FINAL REPORT
TCEQ/Lamar Project 582-7-83975-03
and
TERC Project H85 (582-4-65587)
Project period: 1 September 2007 – 31 August 2008

Submitted by

Noor V. Gillani, PI
Kevin Doty, Co-I

Earth System Science Center
University of Alabama in Huntsville
Huntsville, AL 35899

Submitted to

Dr. Thomas Ho, Project Officer
Lamar University
Beaumont, TX

Dr. Richard Karp, Project Rep.
Texas Commission on Env. Quality
Austin, TX

Dr. Eduardo Olaguer, Project officer
Houston Advanced Research Center
The Woodlands, TX

September 2008

(intentionally left blank)

EXECUTIVE SUMMARY

A major finding of TexAQS I was that emissions of the ozone precursor HRVOC (particularly ethene and propene) were grossly under-estimated in the emission inventories (EIs) of industrial (petrochemical) point sources in the Houston-Galveston-Brazoria area (HGB), and that this was a major cause of error in photochemical modeling used in the SIP process. The EIs pointed to small emissions of HRVOC compared to NO_x, leading to relatively slow initial chemistry of such emissions. It was found, however, that these sources emit comparable and substantial amounts of both NO_x and HRVOC, causing very rapid ozone production in the point-source plumes. The finding was a result of top-down emissions verification (TDEV) using field data. TDEV attempts to reconcile the emissions inventories of ozone precursors NO_x and VOC (particularly the HRVOC) with ambient observations were focused either on measured concentrations of the precursors themselves (direct TDEV) or of their secondary products, e.g., ozone, formaldehyde (indirect TDEV). In TexAQS I, the ambient measurement of speciated HRVOC was very sparse and generally a fair distance downwind of the emissions. Hence direct TDEV was very suggestive, but of large uncertainty. Indirect TDEV involves use of secondary formations from the emissions over mesoscale distances, and such formations from the emissions were inferred using Lagrangian Reactive Plume Modeling (LRPM) and then compared with the corresponding observations. Iterative adjustments of the emissions to bring reconciliation between measured and modeled secondary formations showed under-estimations of the HRVOC EI of one or two orders of magnitude. A decision was made to devote much more resources to TDEV studies in TexAQS II, with close-in and continuous measurements of HRVOC, and high-resolution diagnostic modeling also, since the depletion of the ozone precursors and peak ozone production are very rapid and in relatively narrow plumes, and not accurately modeled by the usual operational urban-regional photochemical grid models.

This is the Final Report of two related contracts to the University of Alabama in Huntsville (UAH), one from Texas Commission on Environmental Quality (TCEQ) through Lamar University and another from Texas Environmental Research Consortium (TERC) through Houston Advance Research Center (HARC). Both contracts were aimed at TDEV of emissions from industrial (petrochemical) point sources using high-resolution diagnostic modeling and TexAQS II field data of 13 September 2006. The Lamar contract called for very high-resolution Eulerian modeling using the UAH-LESchem (Large Eddy Simulation with detailed chemistry) model, which explicitly resolves large energy-containing turbulent eddies at a horizontal spatial resolution of 150m, and has variable vertical resolution of about 20m near ground and 1 km in the upper troposphere. The HARC contract (H-85) called for high-resolution Lagrangian Reactive Plume Modeling (LRPM) using the UAH-LRPM, with lateral plume resolution ranging from about 20m near the source and gradually relaxing with downwind distance, and vertical resolution ranging from 10m near ground to about 100m outside the daytime mixing layer. LRPM uses parameterized atmospheric turbulence. LESchem has a temporal resolution of 2.5s, while LRPM has an advection step of about 5 min, with much finer time steps for chemistry, and hourly resolution of input variables.

Since LESchem resolves the turbulent eddies, it is capable of performing the chemistry not only between mean concentrations of the reactants, as is done in operational air quality models (OAQMs) such as LRPM and CMAQ, but also the chemistry between the turbulent

fluctuating components of the reactants (this chemistry is ignored in OAQMs). The ratio of the rate of turbulent chemistry (after time-averaging to an hour so) and the rate of mean chemistry in the reaction $A + B \rightarrow C$ is called the segregation coefficient ($s \equiv \overline{C_A' C_B'} / \overline{C_A} \overline{C_B}$). The application of LESchem to a relatively simple case of industrial plume transport and chemistry in TexAQS I data analyses (that of the isolated rural emissions from the Sweeny industrial plant in Brazoria Co.) had shown that for the co-emission of HRVOC and NO_x, as from Sweeny, s is far from zero (as assumed by OAQMs) during near-source transport (when the chemistry is vigorous), is usually negative in the near-field (hence tending to slow down the chemistry), and does so by as much as 70% for some of the key photochemical reactions. The importance of s gradually decreases, becoming negligible in an hour or so. An objective of LESchem application was to explore the role of such turbulent chemistry, and explore its significance in emissions estimation.

Specifically for TDEV studies, a Solar Occultation Flux (SOF) monitor in a mobile ground vehicle was commissioned from Sweden. It makes on-line FTIR spectral analysis of the absorption of IR light from the sun to provide continuous measurement of the vertically integrated concentrations of some key HRVOC including as ethene and propene. The vehicle drives upwind and downwind of the target sources in crosswind paths on existing highways. The crosswind integral of the signal, weighted by the wind direction, provides the mass flow rate of the target species across the vertical plane of measurement, and the difference of upwind and downwind mass flow rates provides an estimate of the emissions. The SOF process cannot resolve in the vertical, so the Baylor Aztec aircraft made crosswind measurements at different heights in these planes to provide some vertical information about mass distribution. The Aztec then made measurements farther downwind to obtain data of the secondary formations so that indirect TDEV could also be performed. The NOAA P-3 aircraft was also in the field on this day, making an elaborate range of chemical measurements, including continuous ethene. The purpose of this Project was to use all these and other available data (e.g., meteorological) to perform diagnostic modeling to infer NO_x and HRVOC emissions by direct and indirect TDEV, and also to assess the impact of the emissions on downwind ozone formation.

September 13 was a day with suitable meteorology for TDEV study. The winds were fairly steady and uniform in approximately the north-to-south direction during much of the daytime when the measurements were made. The measurements of the SOF, Aztec and the P-3 were focused on the emissions from the Houston Ship Channel (HSC), the largest concentration of industrial point sources in Houston. The SOF had some problems on this day and ended up making only limited measurements around a path enclosing much of the HSC sources (once around only). The Aztec made substantial measurements of the vertical distribution of the emissions just downwind of the HSC, and then made a number of crosswind traverses of the HSC plume farther downwind to about 70km. The P-3 made an upwind traverse and three traverses at increasing downwind distances, one of them less than 10km downwind, and the last of them about 100km downwind. Unfortunately, the ethene data are missing at critical times during the flight.

We collected and processed a vast array of chemical and meteorological data sets of the study, including the SOF, Aztec, P-3 data, an array meteorological data, and the full array of EI data of point sources and area sources with CB05 chemical speciation. We upgraded the

LESchem and LRPM models to process the chemistry with the CB05 chemical mechanism. We have presented substantial data volumes of most of these datasets in the report. For the SOF, Aztec and the P-3, we performed detailed mission reconstructions, and the data have been presented in graphical form by key mission events, e.g., individual traverses and spirals etc.

Our Sweeny simulations with LESchem following TexAQS I were simplified by assuming flat surface for the transport domain, and using periodic boundary conditions (BC), i.e., we used the downwind outflow model results without the Sweeny emissions as upwind inflow. This is reasonable when the target source is small, isolated and rural, as Sweeny is. But the HSC source complex is large (our LES domain is ~45km wide and ~25km alongwind --- perhaps the largest domain ever used in an LES simulation, certainly with detailed chemistry), and in an urban area. For such a source domain, cyclic BC cannot be used, but rather, realistic initial and boundary conditions (IC/BC) must be first constructed. To do so, we had to run the LES in a nested domain inside outer domains generating and supplying appropriate meteorological IC/BC. Our LES is implemented as the RAMS-LES. We had to add an on-line chemical module with CB05 chemistry, and like the rest of RAMS-LES, the chemistry module had to be made into a parallelized code. The outer domains had to be run with chemistry also. To do so, we also inserted the chemical module in RAMS, to run it as RAMSchem. We ended up running RAMS in an outer 12.15 km horizontal mesh domain of nearly 800km x 500km, with four sequentially nested domains of 4.05km, 1.350km, 450m and 150m meshes, the last one being the LES domain. In spite of much effort, we did not receive the results of the 12 km CMAQ run (the basis for the first attempt to generate the chemical IC/BC for the outermost domain of RAMSchem) from University of Houston until 27 August 2008. Partly for this reason and partly because our meteorological runs without the chemistry themselves took much effort, much of our work was focused on the dynamic simulations before the contract ran out on us.

Plume chemistry is highly sensitive to plume dynamics. Hence, we had to be sure to obtain realistic dynamics, particularly because TDEV requires comparison of instantaneous measurements with instantaneous model outputs. Much of our effort ended up being devoted to attempts to simulate realistic meteorological and dynamical simulations, with assimilation of observations as much as possible, and otherwise testing the results against observations. For a number of reasons discussed in the report, we were unable to obtain realistic dynamical conditions, particularly of the wind field. The wind field is affected by the thermal and moisture fields, and we made many attempts to nudge these fields to improve the dynamical simulations. We found, in some cases, that we did not have adequate observational information for such purpose. For example, there is a range of forests north of Houston, which is an important upwind region impacting the dynamics in Houston on a day with flow from the north. There is no observational information there. In other cases, so much time was devoted to such efforts to obtain realistic dynamics that we ran out of contract time and could not make optimum use of all available meteorological data. We also used high-resolution satellite data of landuse to generate land classifications as required by RAMS. Much effort went into this task. More work is also needed to optimize this application. In the end, we ran out of time and had to stop the work.

Our conclusion is that perhaps it was premature to try to do this complex and pioneering LES project. Certainly, we greatly underestimated the scope of the needed work. Perhaps it will take some years of research before LES can be applied to a complex region, dynamically and

kinetically, as HGB, especially the HSC area, before realistic dynamical fields can be simulated. So what is to be done about the incorporation of turbulent chemistry effects in TDEV work? It is our feeling that we must work up starting from attainable results. One approach is to focus an LES study on the Sweeny source, with cyclic BC, with incorporation of satellite data of land use in an optimum way, and using as input for the outer meteorology the *observed* information. Without the proper land use and other sophistications, we still had greater success with the Sweeny simulations in TexAQS I than in the current effort focused on the HSC (see, for example, the results in Fig. 2.8). I believe it is possible to simulate the Sweeny LES dynamics reasonably well by performing some targeted nudging. Then we can run the LESchem and use the LES information to develop a parameterization of s in terms of *mean* quantities that are relevant to it, such as the mean reactant concentrations and some parameter representing the mean intensity of turbulence --- quantities that LRPM generates or uses. Such a parameterization can be developed for use in LRPM. Then, we can apply the LRPM (*a la* Fig. 2.3) with the parameterized effect of turbulent chemistry in it, to the HSC sources. This, for the near future, and without elaborate new research, appears to be the most realistic interim solution.

TABLE OF CONTENTS

1	INTRODUCTION.....	1
2	PREVIOUS WORK.....	4
2.1	Diagnostic Lagrangian Reactive Plume Modeling for TDEV	4
2.2	Diagnostic LESchem Plume Modeling.....	9
3	THE MODELING TOOLS.....	15
3.1	The UAH-LRPM	15
3.1.1	Single-plume Version	15
3.1.2	Multi-plume Version.....	16
3.2	The UAH-LESchem.....	18
4	THE PLAN OF DIAGNOSTIC DATA ANALYSIS FOR 13 SEPTEMBER 2006	21
5	THE HSC SOURCE CONFIGURATION AND THE EI DATA.....	27
6	THE AVAILABLE DATABASE FOR 13 SEPTEMBER 2006	42
6.1	The SOF Data	43
6.2	The Aztec Data	49
6.3	The NOAA-WP3 Data.....	50
7	DIAGNOSTIC DATA ANALYSIS	105
7.1	Introduction.....	105
7.2	Description of RAMS Model Application.....	105
7.2.1	Overview of model application.....	105
7.2.2	Nested grid setup and model options chosen.....	106
7.3	Required input data	107
7.4	Synoptic Situation on 13 September 2006.....	111
7.4.1	Large-scale and preliminary aspects.....	111
7.4.2	Discussion of the observed analyses on the 12.15-km grid	111
7.5	Landuse Characteristics	115
7.6	Overview of profiler data.....	121
7.6.1	Data sources	121
7.6.2	Overview of sounding characteristics	124
7.7	Control and Soil Moisture Simulations for the 12.15-km Grid	138
7.7.1	Soil moisture adjustment procedures	138
7.7.2	Comparison of 12.15-km grid control and soil moisture adjustment simulations 141	
7.8	Comparison of Model and Observed Wind Profiles.....	151
7.8.1	Wind data processing techniques.....	151
7.8.2	Statistical summary of model/observed wind profile comparisons	153
7.8.3	Spatial plots of the wind error summary statistics	154
7.8.4	Time-height wind speed and direction bias errors	157
7.8.5	Model and observed profiles at the Laporte location.....	160

7.8.6	Discussion of model wind errors	164
7.9	Comparison of Model and Observed Mixing Heights	166
7.9.1	Statistical summary	166
7.9.2	Analysis of time series of model and observed mixing heights.....	166
7.9.3	Spatial distribution of mixing heights on the 150-m grid.....	169
7.10	Summary	169
7.11	Conclusions.....	171
7.12	Suggestions	173
8	CONCLUSION	174
9	REFERENCES.....	175

1 INTRODUCTION

A number of metropolitan areas in East Texas continue to remain in violation of the NAAQS for ozone, despite significant improvement in recent decades. In some cases, as in the Dallas-Ft. Worth area (DFW), the upwind inflow itself brings high levels of ozone into the metropolitan area on high ozone days and is a significant contributor to the exceedances, while in other cases, as in the Houston-Galveston-Brazoria area (HGB), a major contributor to the exceedances is local emissions, particularly co-emissions of HRVOC (highly reactive volatile organic compounds) and NO_x, from the local petrochemical industry, which result in rapid chemistry on summer days, producing ozone and ozone violations in the corresponding plumes. At the turn of the century, models failed to simulate the observations of such violations, making it difficult to manage the air quality effectively. A program of intensive field measurements was started in summer 2000, beginning with the Texas Air Quality Study I (TexAQS I), to try to improve the understanding of the underlying physical-chemical processes and to improve their simulation. Top-down emissions verification (TDEV), i.e., verification of the emissions through their reconciliation with ambient concentration and meteorological measurements, was not a major explicit target in the planning of TexAQS I. Yet, a major finding of the study turned out to be that perhaps the main reason for the failure of models to explain the reasons for the observed ozone violations in HGB was that the emission inventories of ozone precursors, particularly of HRVOC, were grossly under-estimating the actual emissions of this very important ingredient of the ozone photochemistry, perhaps by as much as two orders of magnitude. While there was sufficient confidence in this finding, at least qualitatively, it was also known that the measurements on which the conclusion was based were far from optimum (closest-in downwind measurements were not close enough to the sources, and the speciated measurements of the HRVOC were extremely sparse). In a follow-up intensive measurement program in summer 2006 (TexAQS II), TDEV measurements were explicitly planned, and these measurements were also a significant improvement compared to those of 2000, and indeed were considered to be state-of-the-art (for example, closest-in downwind measurements were quite close to the target sources, and at least some of the speciated measurements of the HRVOC were continuous). Data analyses of the TexAQS II data for TDEV also included state-of-the-art approaches involving diagnostic analyses of the data in conjunction with appropriate modeling, including very high resolution modeling, to account for the rapid near-source chemistry of the co-emissions of HRVOC and NO_x from the petrochemical source complexes.

This is the Final Report of two separate but related projects focused on such TDEV: one involving funding from the Texas Commission on Environmental Quality (TCEQ) via a Lamar University Contract to UAH, entitled: “Top-down Emissions Verification (TDEV) of Petrochemical Sources in Houston”, and another involving funding from the Texas Environmental Research Consortium (TERC) managed by the Houston Advanced Research Center (HARC), of a project entitled: “Diagnostic Lagrangian Modeling for Top-down Emissions Verification and Secondary Products Impact of Houston Ship Channel (HSC) Petrochemical Emissions” (identified as HARC Project H85). The two contracts involved analyses including different kinds of high-resolution diagnostic modeling of HRVOC and NO_x emissions from HSC (the largest industrial source complex emitting HRVOC and NO_x in HGB), and their transport and chemistry based on the field data of one particular day of field measurements from TexAQS II, viz. 13 September 2006. The TCEQ/Lamar contract was to be focused on very high-resolution

LES (Large Eddy Simulation) modeling with chemistry of near-field transport and chemistry of the emissions using the UAH-LESchem model, and the TERC/HARC contract was to be focused on transport and chemistry farther downwind, based on diagnostic modeling using the UAH-LRPM (Lagrangian Reactive Plume Model).

In the past, UAH had performed diagnostic modeling using the LESchem model only for the isolated rural emissions from the relatively small source complex of the Sweeny petrochemical facility southwest of Houston (Gillani and Wu, 2003a). In that case, because of the relatively small size of the source complex (~ 300m x 300m), the modeling domain was also relatively small (30km downwind x 10 km crosswind), and because of the isolated rural setting of the emissions and the relatively flat terrain of the transport domain, the LES application had been simplified using cyclic boundary conditions (BC), i.e., the turbulent outflow at the downwind end of the domain was used as the inflow at the upwind end. The model-data comparison was made at a downwind distance of about 23 km from Sweeny, where the closest-in aircraft field measurements had been performed by the NCAR (National Center for Atmospheric Research) Electra aircraft operated by the team from NOAA's Aeronomy Lab (NOAA-AL). The simulation was first performed without the Sweeny emissions, in order to generate the cyclic BC at the upwind end. The Sweeny emissions were then added continuously into this flow field, and the subsequent simulation was performed for a shorter time than the time taken for these Sweeny emissions to reach the downwind end of the domain (hence there was no inflow of these emissions at the upwind-end cyclic BC), but for long enough time that the emissions had passed the first downwind measurement cross-section about 23 km from the source, so that model-data comparison could be made there. The conditions were quite different and far more complex on 13 September 2006, for which the current projects were performed. First of all the sampling on that day was done in the plumes of the emissions from a large segment of the HSC under north to south flow conditions, in which the HSC source complex considered is about 40 km wide and is composed of a large number of sources from a number of petroleum refineries and other sources. Also, the HSC is located in an urban setting close to complex terrain (land-water interface) so that cyclic boundary conditions could not be employed. The LES source domain in this case had to be about 45 km wide (crosswind) and about 25 km alongwind. This is the largest domain over which the LES had ever been applied, especially with detailed chemistry. Also, since cyclic BC could not be used, the initial conditions (IC) and the upwind BC for the LES domain had to be derived from a nested simulation of a meteorology-chemistry model involving five sequentially smaller domains, of which the LES domain was the smallest, with a horizontal spatial resolution of 150m (the largest outermost domain had a horizontal spatial resolution of 12.15 km). The LES component of this study was of a pioneering nature. The measurements to be used in this project had been performed by two aircraft as well as a mobile ground vehicle, the nearest downwind ones being over a plane from less than 1 km to nearly 10 km downwind of the target HSC sources, and included continuous measurement of speciated VOC. The LES domain extended a little farther downwind of this measurement plane. Our plan was to use the diagnostic LES simulation results at this downwind location as input to the LRPM run, which would then continue much farther downwind, almost a further 100 km, exploring the result of the transport and chemistry of the emissions over such a domain, over which aircraft measurements had been made. Diagnostic LRPM simulation upwind of the LES domain was also to be performed and used to refine the input IC/BC for the LES domain. Thus, the LES and the LRPM tasks were intimately intertwined to optimize the application of each other. UAH had performed diagnostic

LRPM simulations of the Texas industrial emissions before in TDEV studies based on the data of TexAQS I, with good success (e.g., Gillani and Wu, 2003b).

Section 2 of this report provides a summary of the previous diagnostic applications of LESchem and LRPM to the Houston setting, to clarify the capability and relevance of each type of modeling to the problem at hand. Section 3 describes the basics of the LESchem and LRPM models. Section 4 provides the problem definition for the 13 September 2006 scenario, and an overview of the analysis plan. Section 5 outlines the source picture and the available EI data. Section 6 summarizes the database of the main field measurements available for 13 September 2006. Section 7 describes the LESchem application as far as it went. Because of a variety of unexpected problems encountered in this pioneering LES study, and because of time limitations imposed by the contracts, the originally planned work of the projects could not be completed and had to be terminated at that point. A somewhat modified plan for LRPM application for 13 September 2006 has now been added to the work of another project aimed at LRPM diagnostic application to another four days of data of TexAQS 2006, so that at least that work related to 13 September can be completed. Section 8 provides a conclusion and recommendations of this study.

2 PREVIOUS WORK

2.1 Diagnostic Lagrangian Reactive Plume Modeling for TDEV

Figure 2.1 shows a map of the HGB area centered over downtown Houston, highlighting the locations of the five main industrial (petrochemical) VOC and NO_x source complexes in the area, viz. the Houston Ship Channel (HSC, the largest complex) just to the east of downtown, and smaller ones at Texas City (TC), Chocolate Bayou (CB), Freeport (FP) and Sweeny (Sw) in the southern part of the map.

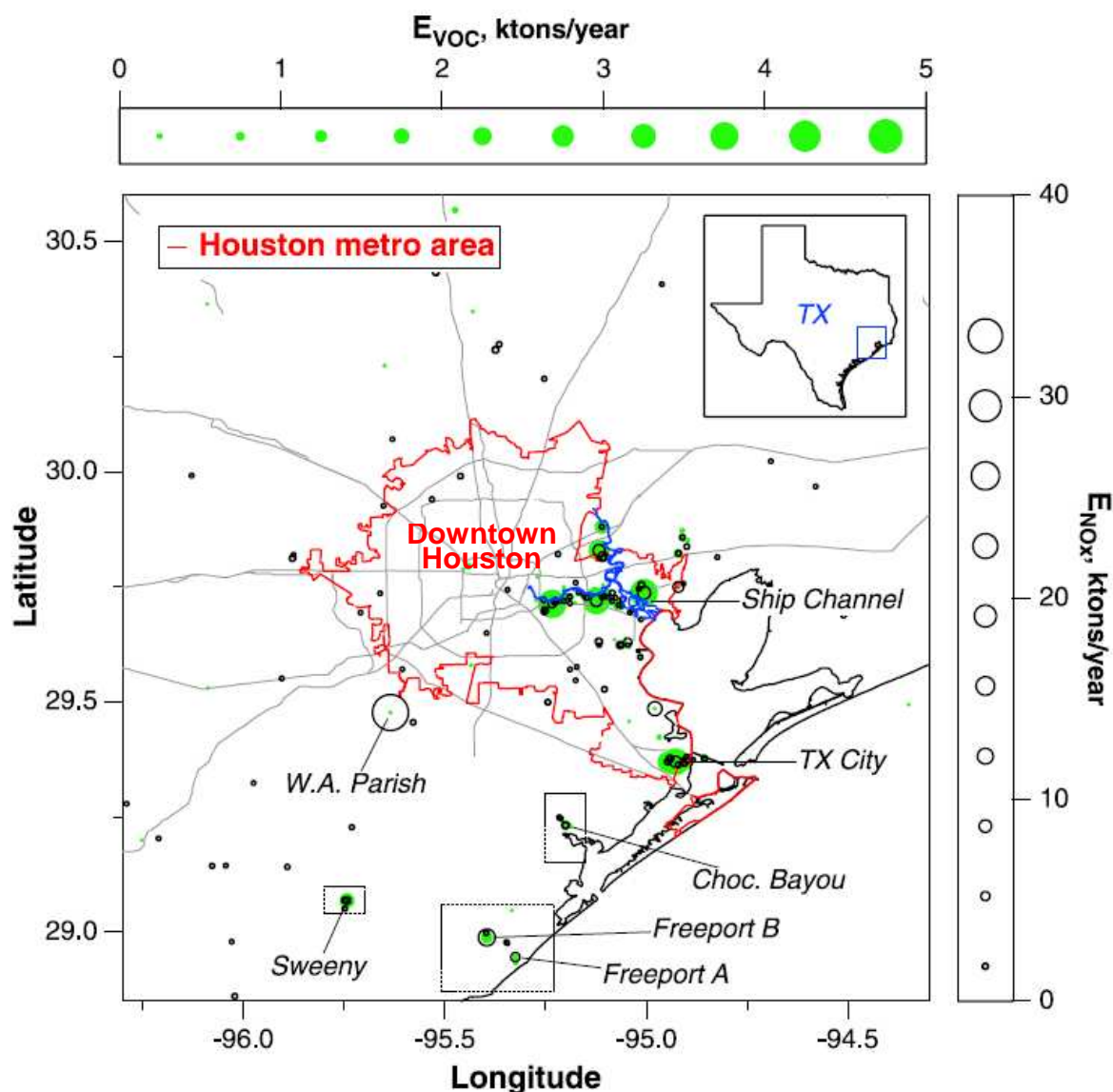


Figure 2.1 Map of HGB showing the locations of the major industrial source complexes of both NO_x and VOC in the Houston Ship Channel, and at Texas City, Chocolate Bayou, Freeport and Sweeny, along with locations and EI values (c. 2000) of the major individual point sources ($E > 100$ t/y) of VOC (shaded green circles) and NO_x (open black circles). The largest EGU is the Parish power plant. (Map taken from Ryerson et al., 2003)

In TexAQS I, the only aircraft data of speciated VOC available were based on very sparse batch-mode (canister) samples of whole air, later analyzed in the lab for VOC speciation. Two kinds of TDEV studies were performed for the HGB petrochemical emissions based on the TexAQS I data, one involving direct reconciliation of the emissions of HRVOC (specifically ethene and propene) and NO_x with their measured ambient concentrations (sparse point measurements for VOC and continuous data for NO_x species) in the NCAR Electra aircraft operated by NOAA-AL, and another involving indirect TDEV based on reconciliation of HRVOC and NO_x emissions with observed secondary formations of ozone (continuous aircraft data) and formaldehyde (semi-continuous aircraft data), based on agreement between observed ambient concentrations and modeled concentrations of these species based on LRPM. The indirect TDEV was performed because of the availability of continuous (O₃) or semi-continuous (HCHO) data of the secondary species which are sensitive to the HRVOC of interest. The first direct reconciliation was performed by two research organizations: NOAA-AL and UAH, based on the data of two particular missions of the Electra --- those of August 27 and 28, 2000. Meteorologically, the two days were very similar, with rather uniform winds from the south through much of the daytime. The flight patterns of the two missions were also quite similar. The flight pattern for 28 August is shown in

Figure 2.2. During the measurement period and the transport period of the sampled plumes from the five petrochemical source complexes, the flow was rather steady and uniform approximately from south to north. The figure shows arrows to indicate the transport trajectories of the relevant sampled plumes. The aircraft made nine long crosswind traverses, as shown, four of them (identified as T1, T2, T3 and T4) being south of HSC and the other five (T5 – T9) being north of HSC. The five southern traverses captured the plumes of the smaller isolated industrial sources (TC, CB, FP and Sw), and the five northern traverses captured the HSC plume at increasing downwind distances. The increasing concentrations of ozone in the aging plumes are apparent.

The NOAA TDEV study (Ryerson et al., 2003) was focused on emissions from three isolated source complexes, those of Sweeny, Freeport and Chocolate Bayou. The continuous measured data of NO_x and NO_y were used in a flux calculation to check the EI values of NO_x, and it was shown that these were generally within about a factor of two of those suggested by the ambient measurements. The downwind batch-mode canister data of speciated VOC (very sparse measurements) were used to compare the measured values of ethene/NO_y and propene/NO_y concentration ratios with the corresponding EI values of ethene/NO_x and propene/NO_x emission ratios. Such a TDEV assumes ethene, propene and NO_y to have been co-emitted and then similarly dispersed by the prevailing meteorology, and to have been similarly depleted by kinetic processes (chemistry and removal). Such assumptions are questionable, partly because VOC and NO_x are not exactly co-emitted, and particularly because some of the measurements were more than 20 km downwind of the target source(s), so that depletion by chemistry and removal could have been substantial and unequal for VOC and NO_x. However, the EI values of ethene/NO_x and propene/NO_x were found to be about 1-2 *orders of magnitude* lower than the corresponding measured concentration ratios, indicating that the EIs of ethene and propene *were* gross underestimates by more than an order of magnitude, at least qualitatively, despite the assumption errors.

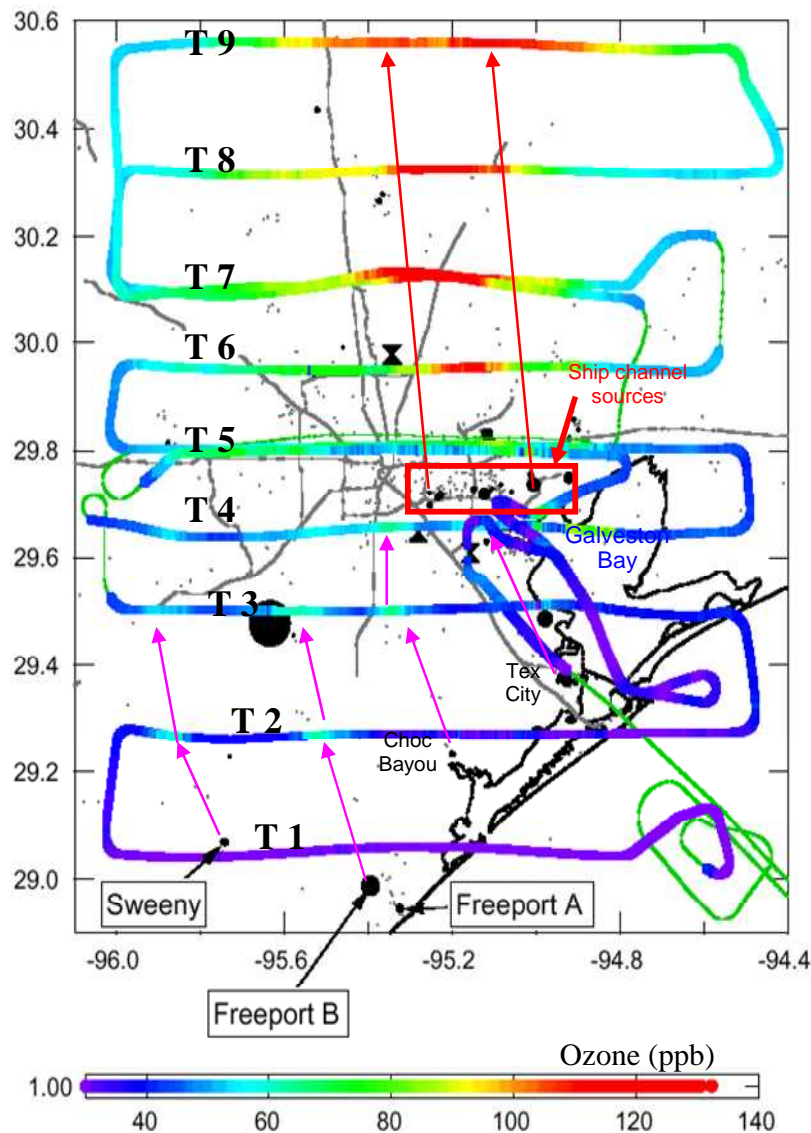


Figure 2.2 Map of the H-G area showing the flight path of the NCAR Electra aircraft mission of 28 Aug 2000. The color coding along the flight path shows measured ozone concentration distribution along the path. Approximate plume trajectories for emissions from the main industrial point source clusters (HSC, TC, CB, FP, Sw) are also shown by arrows downwind of the clusters. (Base plot taken from Trainer et al., 2001; some additional information also included)

Gillani and Wu (2003 b) also performed the above type of data-EI comparisons with their potentially large uncertainties, with similar findings. They also performed LRPM simulations of the plumes from all five source complexes, explicitly taking account of effects of dispersion and kinetics (chemistry and removal) on the emissions before comparing the resulting model concentrations with measured concentrations of not only the primary emission species (continuous NO_x and sparse VOC), but also of secondary products of the photochemistry, such as ozone and formaldehyde, for which the measurements were substantive (continuous ozone and semi-continuous formaldehyde). Such comparisons were performed iteratively, adjusting the NO_x and VOC emissions in two steps, to achieve emissions reconciliation with downwind measurements. First,

NO_x emissions were iteratively adjusted such that the measured NO_y data close to the sources matched the model values, to arrive at estimates of the corrected NO_x emissions. Second, with the “correct” NO_x emissions, VOC emissions were iteratively adjusted such that the model values of downwind ethene and propene concentrations matched their sparsely-measured values, and also such that the more detailed measured and model values of the secondary products ozone and formaldehyde matched. A sampling of the results is shown in Figure 2.3 for the HSC plumes in T7 at ~50 km downwind.

For purposes of modeling, the many sources in HSC were represented by a composite of 23 point sources, and an additional 6 sources represented upwind emissions from Texas City and sources between Texas City and HSC (e.g., those at Bayport). The emissions from each of these sources were iteratively adjusted and then processed in the model for transport, chemistry and removal in order to perform the reconciliation. Most of the NO_x emissions in the EI were found to be more or less in agreement with the measurements on the east side of the HSC, but some on the west side had to be adjusted upward by a factor of 2 or more. For adjustment of emissions of ethene (ETH in CB4, the chemical mechanism used in the model) and propene (OLE in CB4), the single canister measurement midway through the traverse served a useful purpose, but was inadequate to provide adequate confidence in the reconciliation. Ozone served better, but the most useful measurements were those of formaldehyde (FORM in CB4), which has higher sensitivity to HRVOC than ozone. The plots in the left panels of Figure 2.3, based on EI inputs of emissions, show considerable discrepancy between observed (red traces) and model (black) traces for ETH, OLE, ozone and FORM. The plots in the right panels based on adjusted emissions inputs show very good reconciliation between observed and model traces. While the ethene/NO_x and propene/NO_x values in the EI were typically between 0.01 and 0.1 for most sources, they were of the order of 1 in the adjusted emissions, indicating two conclusions: (1) that the ethene and propene emissions were underestimated by 1 – 2 orders of magnitude in the EI, and (2) that their emissions, in reality, were comparable to those of NO_x, leading to substantial co-emission of HRVOC and NO_x, which then leads to rapid photochemistry close to the sources on summer days. For Texas City, the emissions were lumped into two point sources, for both of which the NO_x emissions in the EI were found to be in agreement with the measurements, while for ethene and propene, the emissions had to be adjusted upward from their EI values by a factor of about 10 for ethene and about 5 for propene, for both sources.

Of course, the modeling and source reconciliation was more complex for the many sources of HSC than for the other four smaller complexes --- TC (two composite sources), CB (two composite sources), FP (three composite sources) and Sw (one composite source). The results for these other sources were qualitatively similar to those of HSC. The above LRPM TDEV study was documented in Gillani and Wu (2003a,b). Gillani and Wu also did a pioneering study based on LESchem for just the Sweeny emissions (Gillani and Wu, 2003a). A brief discussion of that follows below.

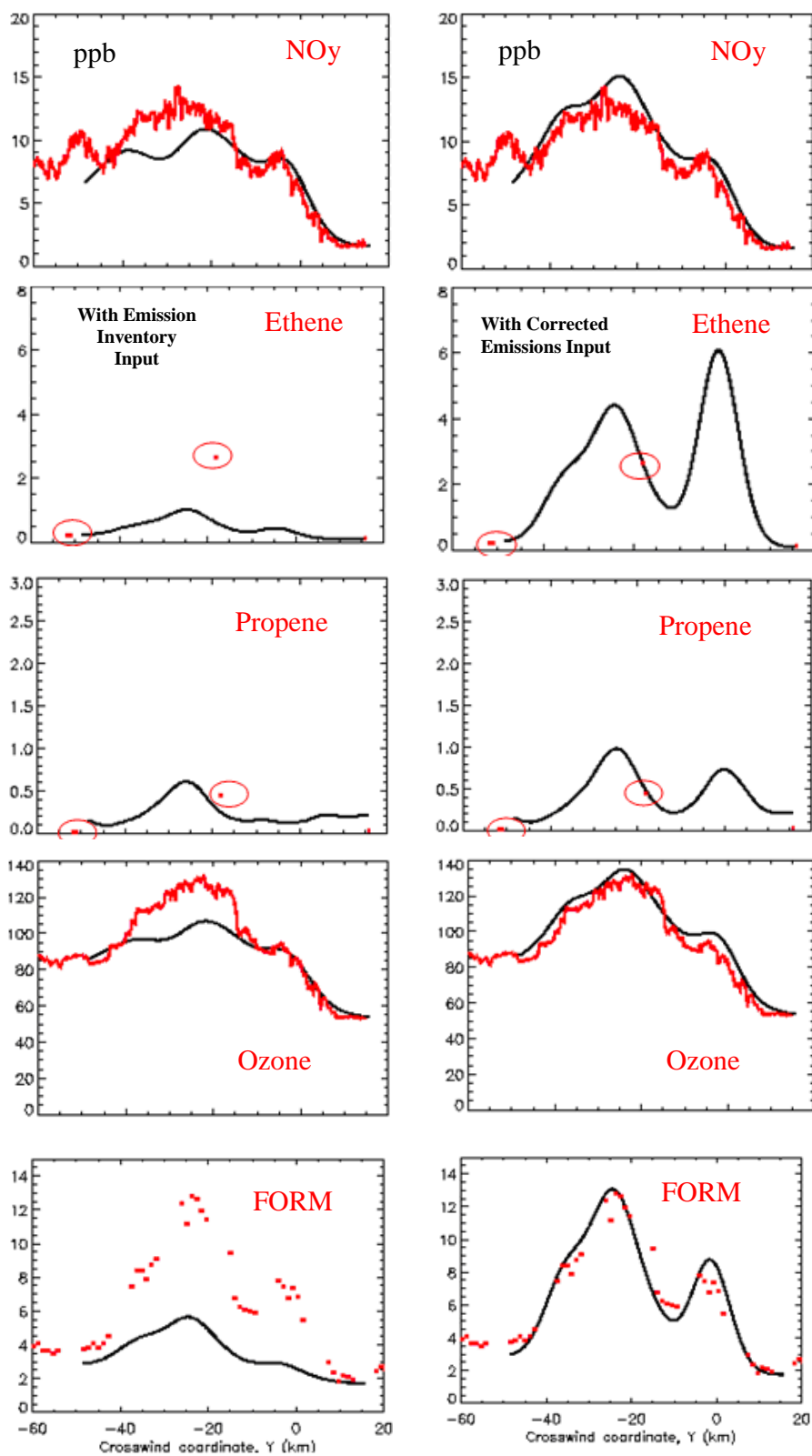


Figure 2.3 LRP outputs of the crosswind profiles of concentrations of chemical species in the simulation of the Houston Ship Channel plume of 28 Aug 2000, at ~50 km downwind section in traverse T7 for two cases of emissions inputs :

(left panels) EI inputs

(right panels) 'Corrected' emissions inputs to reconcile model outputs (black) with measured concentrations (red). Taken from Gillani & Wu (2003b)

2.2 Diagnostic LESchem Plume Modeling

Why the need for LES modeling? With almost co-emissions of HRVOC and NO_x, the plume photochemistry is rapid close to the source, where the spatial-temporal scales of the processes are small. Hence, errors in that regime tend to be large in operational air quality models (OAQMs) such as the LRPM and the urban-regional grid models. While the LRPM can have fairly fine spatial resolution in most respects, it cannot have spatial resolution of the wind field over any vertical plane perpendicular to the transport direction. The operational grid models, e.g., CMAQ, even at 4 km horizontal resolution, distort the emission field substantially right from the beginning, by homogenizing all emissions within a grid cell. Furthermore, all OAQMs do not allow for chemistry related to turbulent fluctuations of the reactant concentrations, which is quite important in the near-source regime, as will be shown below. The reactant chemistry in the OAQMs only permits chemistry between mean concentrations. Below, we provide a sense of the significance of these errors in OAQMs.

First of all, the emissions of VOC and NO_x are not exactly co-emissions even at a single facility. Figure 2.4 shows a depiction (based on the EI) of the physical distribution of the sources of NO_x, ethene and propene for the relatively small Sweeny source complex, which has a petroleum refinery and a chemical plant. All the sources of NO_x and VOC at this facility are within a 300m x 300m horizontal box. Also, the VOC sources are largely (not all) below 25m, while the NO_x sources are more distributed vertically up to 75m. Figure 2.5 shows the near-source dynamic behavior of a plume emitted from a point source. Observe that the fresh plume from such a source under convective conditions undergoes substantial looping (vertically) and meandering (horizontally) due to the turbulence of the flow field. The instantaneous dimensions of the plume are quite different from the time-mean (hourly or so in the OAQMs) Gaussian plume envelopes, and this makes a large difference in the reactant concentrations on which the chemistry is based. The instantaneous plume fluctuates greatly at the spatial-temporal scale of the largest turbulent eddies. Effectively, thus, the reactant concentrations vary with the scale of turbulence, and may be represented more accurately as $C = \bar{C} + C'$, with the components on the right denoting the mean concentration and the turbulent fluctuating concentration. For a reaction $A + B \rightarrow C$ with reaction constant k , the reaction rate R is then

$$R = k(\bar{C}_A + C'_A)(\bar{C}_B + C'_B) \sim k(\bar{C}_A \bar{C}_B + \overline{C'_A C'_B}) \sim k\bar{C}_A \bar{C}_B [1 + s],$$

where $s \equiv \overline{C'_A C'_B} / \bar{C}_A \bar{C}_B$. s is called the segregation coefficient. OAQMs assume that it is negligible and equal to zero. However, when the reaction between the turbulent components of the reactants (i.e., the covariance term in the numerator of s) is not negligible, as in the case of a petrochemical plume in its early stages, the OAQMs can lead to significant error. LESchem explicitly resolves the dynamics of the large eddies and includes the effect of s .

Figure 2.6 shows an LESchem simulation of ozone in the Sweeny plume of 28 August 2000 in a mean wind speed of about 3.5 m/s (lowest panels) over the first 30 km of downwind transport. For comparison, it also shows the same simulation at hypothetical wind speeds of ~ 1 and 2 m/s in the upper panels. The figure also shows the results in both the x-y and x-z planes. The key information in all three cases is that the ozone formation in the plume peaks in a little over 1 h of transport, which is quite rapid (in one hour, the transport distance is 3.6 km, 7.2 km and 12.6 km at wind speed s of 1, 2 and 3.5 m/s, respectively). This is precisely the early phase

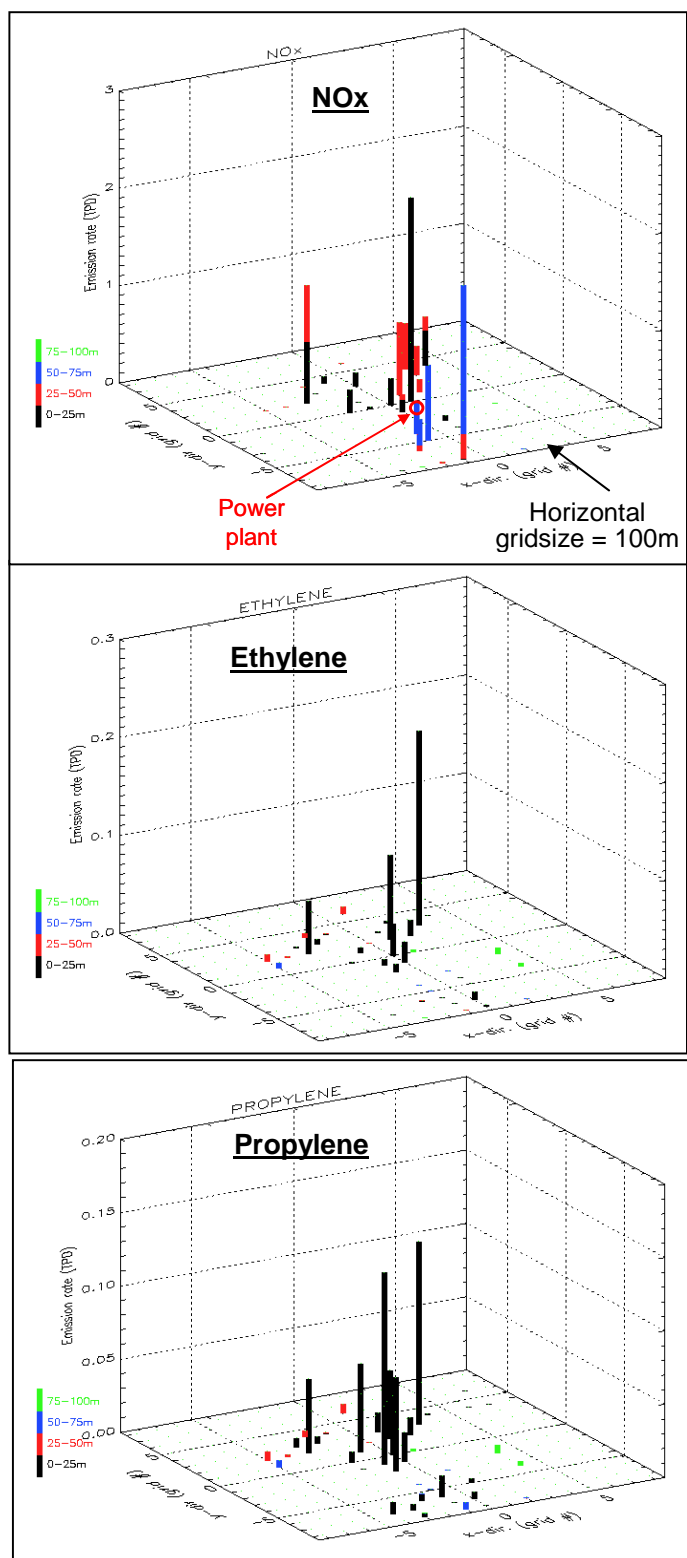


Figure 2.4 A depiction of the physical source configuration at Sweeny, which has a petroleum refinery and a chemical plant. The entire facility has dimensions less than 300m x 300m. There are a large number of individual sources of NOx and VOC. The figure shows such sources of NOx, ethene and propene in the three panels shown. For each, not only is the horizontal location of individual sources shown, but also the height of the emission (color coded in 25m segments up to 100 m). It may be observed that:

- a) the sources of the three emissions are not exactly co-located horizontally or vertically; and,
- b) while most of the VOC are emitted below 25m, the vertical distribution of NOx emissions is more spread out.

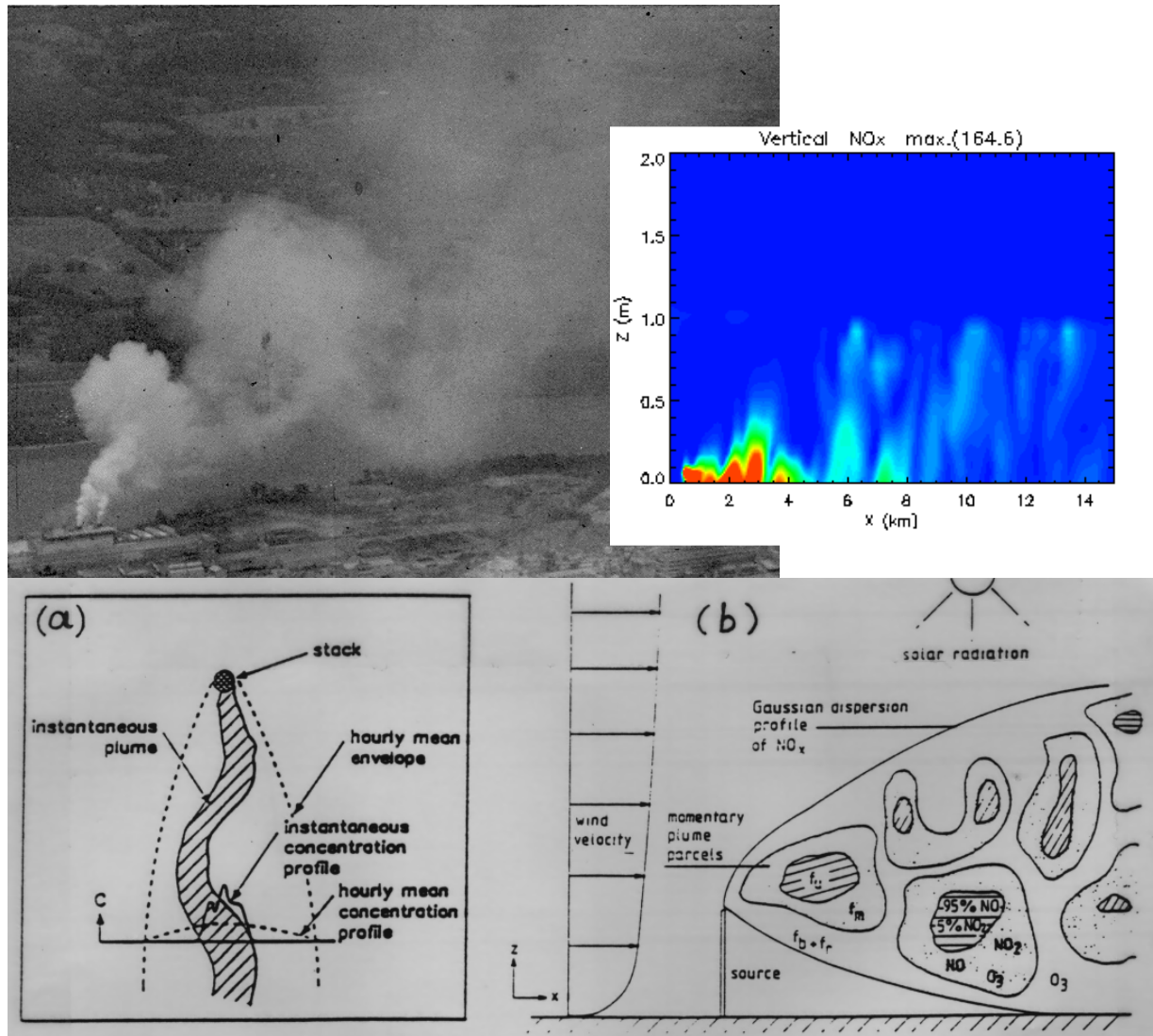


Figure 2.5 The physical behavior of a fresh point-source plume in convective conditions. The top-left panel shows a photograph of a power plant plume. Observe, in particular, the looping of the plume during early transport. The lower right panel (b) shows such looping behavior schematically, with chunks of plume material shown enclosed within a Gaussian envelop of an averaged (hourly or so) plume; the lower left panel (a) shows the meandering behavior of a fresh plume in the horizontal plane, enclosed within a Gaussian envelop of an averaged (hourly or so) plume. The chemistry between the reactants in such a fresh plume occurs for concentrations within the instantaneous plume, which changes due to turbulence at the spatial-temporal scale of the largest energy-containing eddies. The upper-right panel (color plot) shows an instantaneous view from the LES simulation of the x-z plane of the Sweeny plume emission near the ground for the first 15 km under convective conditions. Observe the looping of the plume in this simulation.

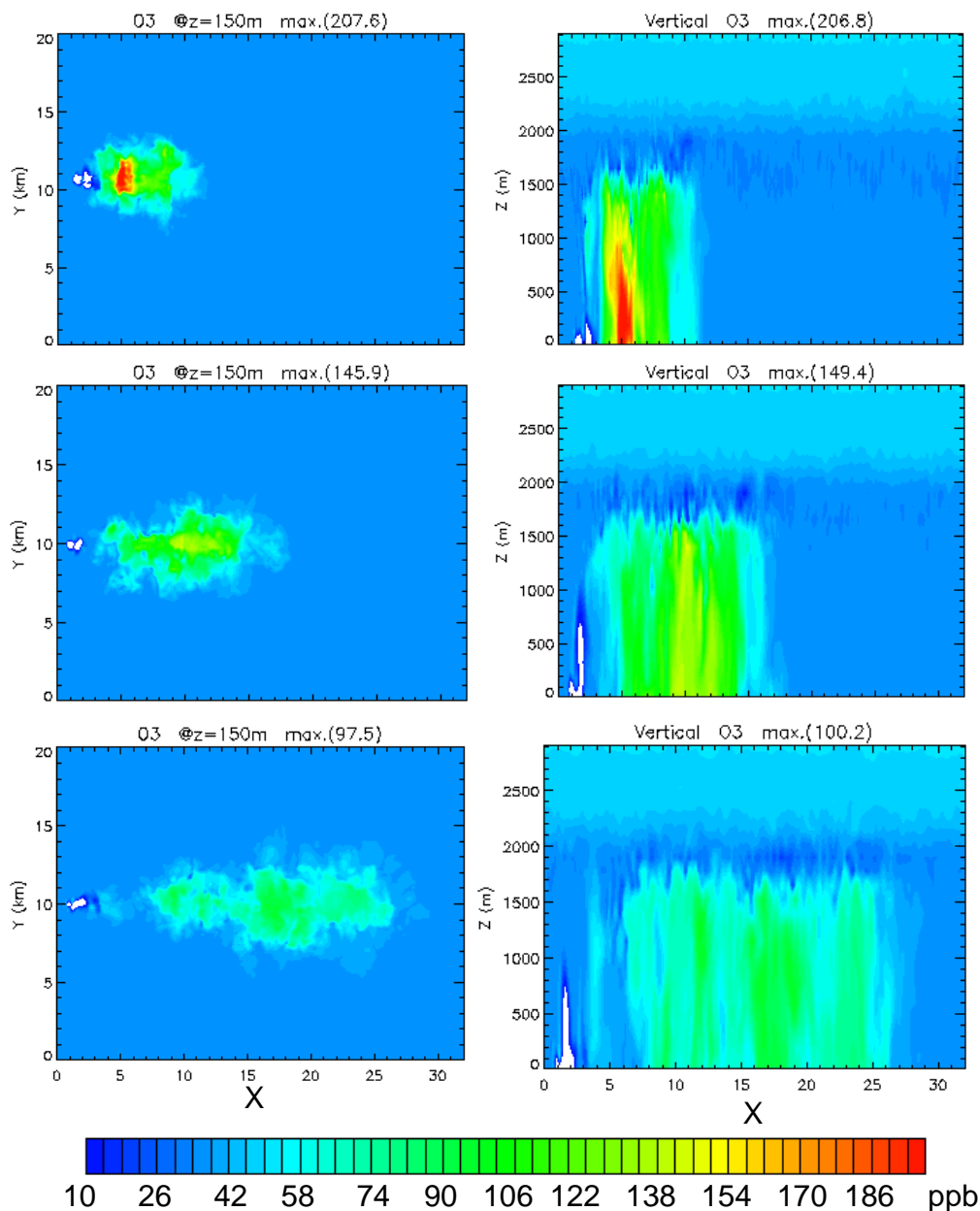


Figure 2.6 Ozone concentration in the LESchem simulation of the Sweeny plume of 28 August 2000 with the TDEV-corrected emissions. The left panels show the view in the horizontal x-y plane at 150m height, and the right panels show the view in the vertical x-z plane through plume centerline. The emission is at $x = 1$ km, and the white area near the source represents ozone concentration of 0 ppb due to complete titration of ozone by the NO_x in the fresh plume. The top, middle and bottom panels are for simulations, respectively, at mean wind speeds of 1, 2 and ~3.5 m/s. In each case, plume ozone peaks where the plume age is a little over 1h. The actual wind speed on 28 August 2000 was ~3.5 m/s (the simulation shown in the lowest panels). (Taken from Gillani and Wu, 2004)

of plume chemical evolution in which the role of turbulent chemistry is most pronounced. Figure 2.7 shows a plot of $1+s$ for six key photochemical reactions as a function of downwind distance for the LESchem simulation of the Sweeny plume of 28 August 2000. Here s is the result of averaging the covariance term over both time and plume crosswind direction. The

departure of $1+s$ from 1 indicates the departure of the reaction rate from that used in OAQMs. It may be seen, first, that $1+s$ is generally less than 1 for x less than about 12.6 km (\sim the transport distance in 1 h at the prevailing mean wind speed of about 3.5 m/s). This means that s is generally negative during this time. Its effect is to reduce the reaction rate compared to that used in OAQMs, by as much as $\sim 75\%$ for the reaction $\text{NO}_2 + \text{C}_2\text{O}_3$ which results in the production of PAN, and as much as 40% or more for the other reactions shown. The OAQMs cause much more rapid mixing of the reactants than is the case in reality, and hence result in faster chemistry. The error of neglecting the turbulent chemistry varies for different reactions, but is generally large in early plume transport, and decreases with plume age. This early period of plume transport is precisely the period most important in TDEV studies. It is for this reason that this project aimed to include such role of turbulent chemistry in LESchem.

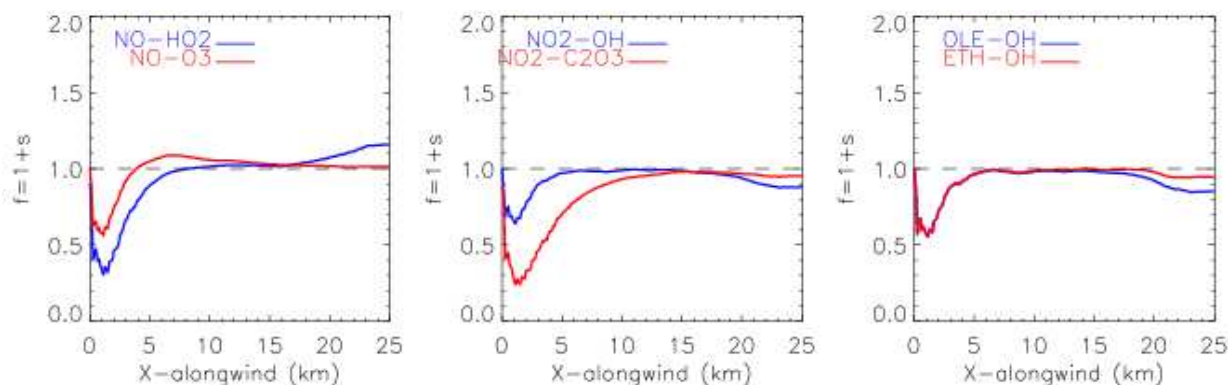


Figure 2.7 Variation of crosswind-averaged “reaction enhancement factor” ($f = 1 + s$) at plume release height with downwind distance for six key photochemical smog reactions based on the LESchem simulation of the Sweeny plume of 28 August 2000 for “TDEV-corrected” emission rates as follows: $Q_{\text{NO}_x} = 1.8 Q_{\text{NO}_x(\text{EI})}$, $Q_{\text{ETH}} = 3.6 Q_{\text{NO}_x}$, $Q_{\text{OLE}} = 2.0 Q_{\text{NO}_x}$. The departure of f from 1 denotes the effect of including the turbulent chemistry. (Taken from Gillani and Wu, 2003a)

Figure 2.8 shows comparison of the measured concentrations of NO_y , O_3 , OLE (single point measurement of a canister sample) and FORM with the corresponding LRPM and LESchem simulations of the crosswind profile during traverse T2 ($x \sim 23$ km) of the Electra in the Sweeny plume of 28 August 2000. The LRPM comparison with the observation appears to be “better” than the LESchem comparison. The difference is mainly due to the fact that in LRPM, the plume dynamics (e.g., plume spread rate) are external inputs derived from the measurements (and therefore quite accurate), while in LESchem, plume dynamics are as simulated by LES. In the results presented, a number of simplifications were made in the LESchem simulation which resulted in less plume spread than that observed. For example, surface roughness was assumed to be uniform and that for a flat terrain. Also the input mean flow field was assumed to be fairly uniform. In the current project, much effort was given to try to make such inputs as close to realistic as possible by the use of high-resolution satellite observations of the land surface and derivation of the mean meteorological boundary conditions based on urban-regional modeling. It may also be pointed out that the LRPM emissions with TDEV-corrections were selected to give a good match of the measured and modeled concentrations. In reality, since LRPM neglects the turbulent chemistry, it tends to accelerate the close-in chemistry artificially, hence causing somewhat excessive depletion of VOC and NO_x , thereby over-estimating the TDEV-corrected emissions of these ozone precursors somewhat. If the LES model had not failed to simulate the plume dynamics correctly, it would have led to a better TDEV correction of the VOC and NO_x .

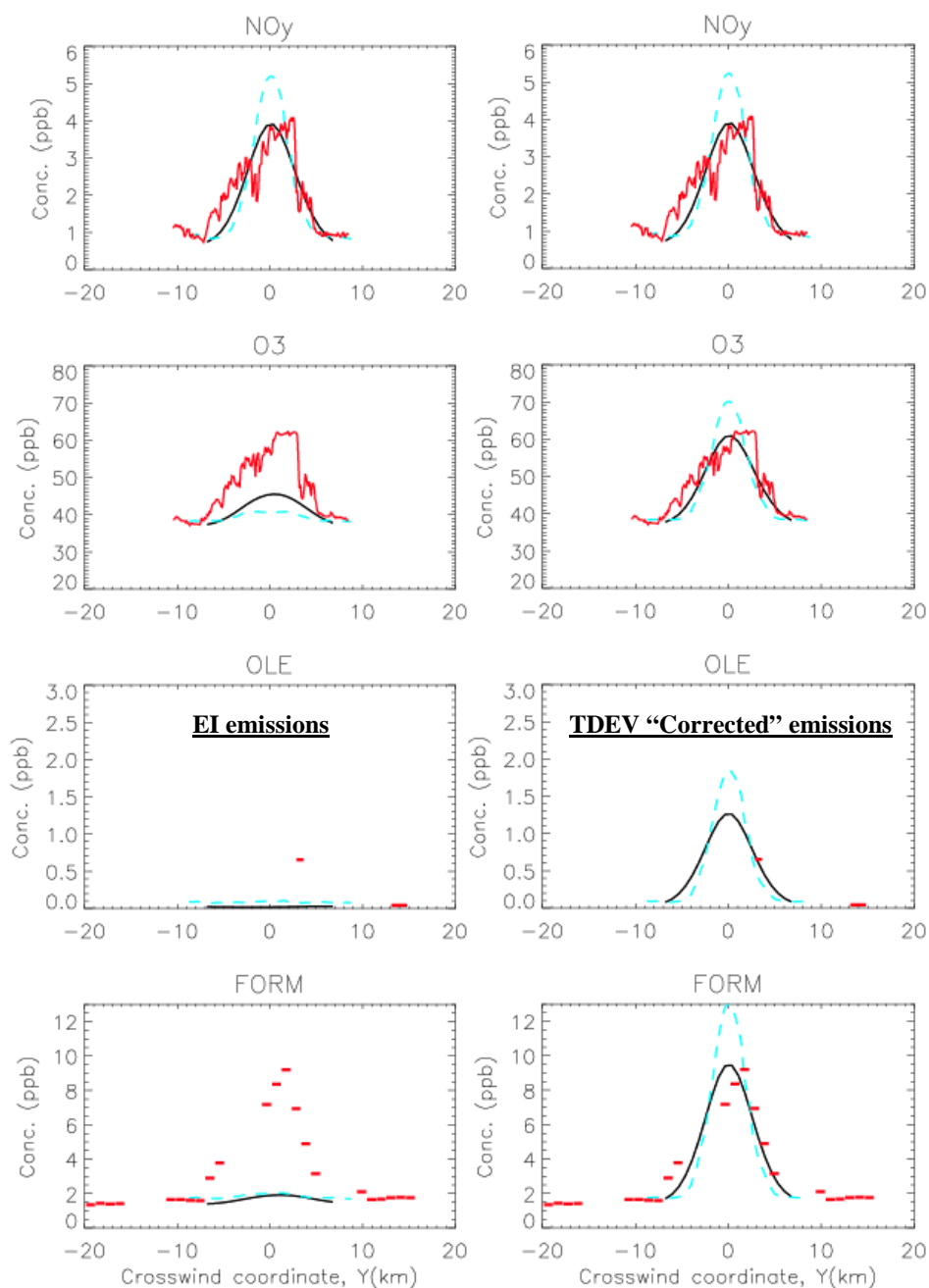


Figure 2.8 Comparison of LRPM (black trace) and LESchem (broken blue trace) simulations of the mean crosswind concentration profile of selected species with Electra measurements (red trace) in the Sweeny plume during traverse T2 ($x \sim 23$ km) on 28 August 2000, with EI-emissions (left panels) and TDEV-corrected emissions (right panels) of VOC and NO_x as given in the caption of Figure 2.7. For OLE, there was a single canister measurement within the plume at $y \sim 3$ km. (Taken from Gillani and Wu, 2003a)

emissions. The LES, in principle, would also have simulated the dynamics based on 3D variability of the meteorological variables.

3 THE MODELING TOOLS

3.1 The UAH-LRPM

3.1.1 *Single-plume Version*

The UAH-LRPM originated as the Gillani-LRPM (Gillani 1986), and further evolved as UAH-LRPM, first during its upgrade for use as the building block of the Plume-in-Grid (PinG) module (Gillani et al., 1998; Gillani and Godowitch, 1999) of EPA's urban-regional modeling system, Models-3/CMAQ (EPA 1999), and more later. Conceptually, the model simulates the time-dependent, two-dimensional concentration evolution within a lagrangian vertical rectangular slab moving with the average transport wind, which may vary with time (in speed and direction) along the slab trajectory. However, it does not allow for wind shear/veer effects; hence, its application is best suited in the convective summer boundary layer during the daytime, and particularly when wind shear effects are not very significant. Such was indeed the condition in its application to the simulations of the case studies considered for TexAQS I (27, 28 August 2000). The slab framework of our LRPM permits arbitrary spatial resolution (externally specified) in both the crosswind (y) and the vertical (z) directions --- all variables may vary with this resolution over a cross-section, except the wind speed/direction (which may vary with time and x). The model is designed to simulate the change in concentration of all modeled chemical species in each slab cell, in response to emissions, their subsequent lateral and vertical dilution and diffusion, gas-phase chemistry and dry deposition at the surface (for selected species). The model is quite suitable for plume(s) with inhomogeneous (including asymmetric) spatial concentration distributions in the plume(s). Emissions may be from an elevated point source at a given time, as well as continuously from the surface in a spatially-temporally variable gridded areal distribution. The chemistry can be based on any externally specified chemical mechanism; the CB-IV mechanism, with the condensed Carter isoprene scheme (Carter, 1996), was used in the TexAQS I analyses. For the current project, modifications were made to use the CB-V mechanism.

Horizontal diffusion is based on horizontally homogeneous eddy diffusion (K_y), but different options are available for vertical diffusion (details in Gillani and Wu, 2003c), including height-dependent eddy diffusion (K_z), asymmetric convective mixing (ACM, Pleim and Chang 1992) in the convective boundary layer (CBL), and a combination of eddy diffusion (in the lowest 15% of the CBL) and ACM (higher up in the CBL). This last combination best simulates the observed profiles of species emitted at the surface, which have significant gradients in the lowest part of the CBL, but a more well-mixed profile higher up. This hybrid option was exercised in all simulations included in this report. The vertical domain of the model must extend to at least the peak mixing height of the day, in order to allow for realistic fumigation or entrainment of mass from above the mixing layer into the mixing layer as this layer grows during the morning hours. A constant small value of K_z is used for vertical diffusion in the aloft layers outside the CBL.

Every model run of a point source plume actually involves two parallel slab simulations, one with the point-source emission into a dynamic and kinetic background (the "plume" run), and another without such emission (the "background" run). Both runs include crosswind and vertical spatial resolution, the same distribution of surface emissions, and the same physical-chemical

processes. From the difference between the two parallel simulations, we can determine plume excess concentrations above the background in a very local sense. The spatial resolution of the background is fixed in time: the background slab has a constant crosswind width (chosen to be significantly wider than the widest simulated plume width) and a constant horizontal spatial resolution (typically, 1.5 km); the vertical domain is chosen to significantly exceed the peak mixing height during the full simulation period, and is resolved into 32 layers of varying thicknesses, the lowest five typically chosen to be 10m thick each, and the coarsest ones above the mixing layer to be 100 m. The spatial resolution of the plume slab is variable in time. Horizontally, the expanding plume width, $W_p(t)$, can be divided into an arbitrary number of plume pillars of arbitrary widths. Our common practice in the simulation of isolated single plumes is to divide $W_p(t)$ into 20 side-by-side pillars of equal width. Thus, plume horizontal resolution is very fine in the very fresh plume (typically, $\sim 20\text{m}$), and gradually relaxes to approach the background pillar resolution (1.5 km) in the aged plume (plume width $\sim 30\text{ km}$). Vertically, plume core (= initial plume thickness at the end of the plume rise stage) is divided into a selected fixed number of thin layers (typically about 20m in thickness each), and as the plume expands, it does so sequentially into the adjacent layers of the plume slab.

In a typical simulation, the background (in the mixing layer and aloft) is initialized at 0600, and is subsequently evolved dynamically (physics) and kinetically (emissions, chemistry and removal). The background slab simulation is arranged to pass the point-source plume release location at the desired plume release time. The plume slab is then initialized 15 minutes after plume release time at the appropriate downwind location. At such initialization, the plume cross-section is centered at the effective stack height of the emission, and has finite width and height (externally specified, based on the Plume Rise Module of our Plume Dynamics Model, PDM, which is described in Gillani and Godowitch, 1999). The plume emission mass of each species is injected into this finite plume area (on top of the underlying background concentration field) in an assumed initial 2-D Gaussian distribution, calculated using the specified input values of the species emission rate and the current local wind speed. The NO_x emission is assumed to be as NO. The distributions then evolve as the plume is advected along its pre-calculated trajectory (from the PDM run), under the influence of the various physical-chemical processes identified above. The model requires several inputs related to these processes: e.g., point-source and surface emissions; the dynamic mixing height [$z_i(t)$] and plume width and height [$W_p(t)$, $H_p(t)$]; diffusion parameters (scaled to match the observed plume spread rate); the j -values of the photolytic species; the deposition velocities (v_d) of the depositing species; meteorological variables, p , T , RH (used in the chemical mechanism); etc. These inputs may be empirical or semi-empirical (calculated based on parameterizations available in PDM), or some of them may be derived from larger-scale grid model results (e.g., p , T , RH , Z_i , J , etc.).

3.1.2 Multi-plume Version

Large coal-fired power plants operated by large utilities in the US typically emit between 10K and 100K tons of NO_x (as NO_2) per year, or about 25 to 250 kmol(NO)/h. By comparison, the largest sources of NO_x in the HSC emit about 25-50 kmol(NO)/h. Some of them are power plants (negligible VOC emissions), but most co-emit both NO_x and VOC. There are a large number of major industrial point sources (IPSs) in the HSC. Within a fairly short distance downwind of the HSC, the plumes of these sources begin to merge; some of these

plumes are totally embedded in larger plumes emitted upwind. The treatment of such multiple interacting plumes is a complex challenge, particularly in the context of a *plume* model such as UAH-LRPM, with a rather fine spatial resolution (say, 200 m or finer horizontally) in the near-source downwind stretch where the plume merging is occurring. As shown in Figure 2.1, most of the IPSs are concentrated in five clusters or local complexes --- three relatively small and more or less isolated ones, viz., Sweeney, Freeport and Chocolate Bayou in the south of the HGB area, and two (Texas City and the HSC), which are larger and tend to interact with each other. HSC is by far the largest complex with quite a large number of individual IPSs of significant size. We have modified the single plume version of UAH-LRPM specifically for the TDEV studies in the HGB area, to create a new multi-plume version (M-LRPM).

Conceptually, our approach in multiplume modeling is to initialize the plume slab just downwind of the most upwind source in the complex, then simulate its processes during downwind transport past the next source downwind until the new source has reached a certain minimum width (we have chosen that as 2 km). At that point, if there is physical interaction between the two plumes (based on overlap of their widths), then the plume slab is reinitialized, with the two plumes merged into a new single inhomogeneous plume with two (or more) concentration modes of the primary emission species. The merged plume has a new geometry, pillar configuration, spatial resolution, and rate of growth, as well as a new merged concentration distribution of the transported species (free radical species adjust rapidly to a new equilibrium with the new distribution of the transported species). The new plume is then transported and evolved downwind until it interacts with the next downwind plume which is at least 2 km wide. If so, then these interacting plumes are again merged and the simulation is re-initialized and resumed. This process is continued (i.e., re-initialization of the master plume at each new interaction) until all plumes in the complex have been accommodated in the master plume simulation. Thereafter, the simulation of the combined (master) plume is continued to the end of the prescribed simulation time and location.

In practice, a new plume physics preprocessor to M-LRPM was developed and implemented, which uses PDM to perform the dynamics of each individual plume in the complex independently, determines when plume interactions occur and the criteria for merging are met. It sets up flags to indicate when particular identified plumes are ready to be merged. M-LRPM thus receives its multi-plume dynamics and merging information from the preprocessor outputs. When a plumes-merge is flagged, M-LRPM picks up the plume dynamics and merge information, rechecks the merge criteria, and if satisfied, performs the actual merge (re-initialization of the merged plume), and then proceeds forward with the LRPM simulation of the merged plume.

One important practical issue to contend with in such multi-plume simulation is that when two plumes of different ages and stages of development interact and are flagged as ready for merge, they will have different spatial resolutions. Our approach is to limit maximum plume cell size (horizontally) to 200 m during the merge phase; at merge time, the new resolution of the merged plume is set at the coarser of the two individual plume resolutions, or 200m, whichever is smaller (remember that the newer of the two plumes will have a resolution of at least 100m before merge, because of the merge criterion that each member plume to be merged must be at least 2 km wide, and because each isolated plume has 20 pillars before it is merged). One

problem in this process is that fairly fresh plumes (of width comparable to, or less than, the turbulent eddy scale) have a lateral diffusion rate which is different from that of a more aged plume in which turbulent eddies are significantly smaller than plume dimension, and merely perform internal plume diffusion. When two such diverse plumes are merged, the model limitation of a single lateral diffusivity for the whole plume (that of the larger member) leads to somewhat excessive post-merging diffusion of the younger member plume. This is one of the limitations of our approach. This is the reason that we require each merging plume member to be at least 2 km wide, so that it has already spread to a width which is larger than the turbulent eddy scale. Thus, if the smaller plume is embedded within the larger plume at its emission, then it will be simulated as an isolated plume until it is 2 km wide. While this will introduce some error, we do not think that such error will be too large in the total scheme of things. Two better approaches for simulation of plume-plume interactions, both requiring much more computation, are the LES approach (Eulerian) and the *puff* modeling approach (Lagrangian) with fine spatial resolution (e.g., with the requirement that puffs are split up when they reach some critical size, e.g., 200 m). Both of these approaches also have the advantage that they can naturally and explicitly simulate wind shear effects. However, using either of those approaches is much more computation-intensive.

3.2 The UAH-LESchem

LES involves Eulerian grid modeling at very high spatial-temporal resolution capable of resolving individual large energy-containing turbulent flow eddies. Subgrid-scale information is parameterized. Most applications of LES have been for the convective boundary layer (CBL), and without chemistry, and even then, mainly to small domains (<10 km to a side horizontally and <4 km vertically). In the past (pre-2000), LES application with chemistry to a point-source plume appears to have been limited to just one study by Sykes et al. (1992), in which they included just the three-reaction photostationary chemistry of NO, NO₂ and ozone. Subsequently, a limited number of studies, such as that of Herwehe (2000), explored the inclusion of detailed organic photochemistry (Trainer chemistry, in their case) into existing LES models (henceforth, LESchem), for application to small CBL domains. Herwehe et al. (2002) applied their LESchem (modified to implement the CB-IV chemistry) to idealized plumes from industrial point sources co-emitting VOC and NO_x. Gillani and Wu (2003c) performed a fairly detailed study of UAH-LESchem application to power plant plumes. Thus, any application of LES, with detailed gas-phase chemistry, to point-source plumes, with or without co-emissions of NO_x and VOC, is still of a pioneering nature at this time.

When we started looking into a candidate LESchem for our use a few years ago, we had two potential options, the RAMS-LESchem of Herwehe and the NCAR-LESchem. RAMS (Regional Atmospheric Modeling System) is a well-established, well-evaluated, and widely-used, mesoscale-regional meteorological model (Pielke et al., 1992) which, for some years now, has included an LES option (Hadfield, 1989; Hadfield et al. 1991a,b; Walko et al., 1992; Avissar et al. 1998). For LES, RAMS is run in the non-hydrostatic configuration, solving the prognostic equations for the three velocity components (u , v , w), potential temperature (θ), perturbation Exner function (π), and subgrid-scale turbulent kinetic energy (ϵ). Subgrid (smaller turbulent eddies than the resolved scale of large eddies) diffusion is parameterized in terms of ϵ , as in Deardorff (1980). Hadfield (1991) reported that RAMS-LES simulates a field of updrafts and

downdrafts with the right dimensions, characteristic velocities, and the crucial property that ϵ is transported upwards. Herwehe (2000) added (hard-wired) the Trainer chemistry with simplified isoprene mechanism (Trainer et al., 1987; 1991) into the then current version of RAMS (v. 3.2b, limited to single-processor implementation only, in the LES option), and applied the model to the CBL. At first, it was our plan to use that version of LES, but the single-processor limitation seemed too confining. We, therefore, also explored the possible use of the NCAR-LESchem, which was developed for, and implemented on, the CRAY, and included the massively parallel computing option. We were also granted the use of up to 250 hours of CRAY time on the NCAR CRAY for such application for our project, at no cost. We, therefore, decided to try out that option.

The NCAR-LES was developed by Moeng (1984; 1986), and has been applied by Moeng and Wyngaard (1988; 1989), Moeng and Rotunno (1990), Moeng et al. (1996) and Bretherton et al. (1999). In essence, it is similar to RAMS-LES, except for one important difference in the numerical integration technique for the spatial coordinates: whereas RAMS-LES applies finite differencing in all three spatial directions, NCAR-LES utilizes a pseudospectral representation in the horizontal directions (x and y), and finite differencing in the vertical. Also, NCAR-LES is more hard-coded in terms of input specifications. Later, Moeng added detailed chemistry to the NCAR-LES (hard-wired). All testing and applications of the NCAR-LES were for the CBL. We devoted considerable effort to become familiar with this NCAR LESchem. We started with CBL applications, and it performed very well. Unfortunately, when we began exploring its application to point-source plumes (without chemistry), we ran into a ringing problem (systematic spurious periodic ringing effect of mass along both horizontal axes through the point source of emissions). We suspect the source of this problem is related to the pseudospectral treatment in the model. We tried to smear the source over multiple grid cells, without success. It was a serious enough problem that needed substantial code modifications to correct, which we were not in a position to perform. Finally, we abandoned use of the NCAR-LESchem, and returned our attention to RAMS-LES. By then, however, there was a new version of RAMS (v 4.2), which did include the parallel processing facility in the LES option. Our tests with point-source emission of a tracer in this RAMS-LES showed no ringing effect. We, therefore, undertook the task of adding generalized (not hard-wired) detailed chemistry into that latest version of RAMS, and developed it into a state-of-the-art RAMS-LESchem (UAH-LESchem). All applications of LESchem to the Sweeny plume of 28 August 2000 used the full CB-IV chemistry with the one-product isoprene mechanism of Carter (1996).

Our original chemistry module was coded in FORTRAN 90 and was platform-independent, but was not parallelized. That version of LESchem was applied to the Sweeny plume simulations of 28 August 2000, with spatial resolution (grid size) of 125m horizontally, and staggered vertically from 40m near the surface, in 15% incremental steps, to 125m (reached at the 10th cell), and held constant above, to a domain height of 4000m. The temporal resolution was 2.5 s. Each hour of real-time run in such a Sweeny application took about 72 h of CPU time on a 2.4 GHz Pentium-4 processor in a dual-processor node with available memory of about 2 GB. The simulation was started at 0900, and the first 8500s were devoted to model spin-up --- 7000s of spin up with just CBL physics and a further 1500s with CBL chemistry also (based on initial conditions and spatially-averaged surface emissions of chemical species derived from the appropriate operational model inputs or simulations, such as CAMx and UAH-LRPM).

Thereafter, the Sweeny emission was initiated (at about 1120), with the elevated emissions being injected into a single grid cell at an effective stack height of about 150m. Such full run with CBL physics, steady point-source emission, and chemistry, was maintained for about 4h (~1120 – 1530), during which time, the mixing height was simulated in its dynamic mode, through input of spatially-uniform, but temporally variable, surface heat flux. The Electra sampling of the Sweeny plume during T2 on 8/28 was around 1315, and estimated to be of the release at about 1150. In order to have enough runtime for meaningful averaging of information in each grid cell (16000s after local plume impact), we run two realizations (on separate processors) with the Sweeny emissions offset slightly in space. It took nearly 20 days of CPU time on each of two separate single processors for each 4h application of the Sweeny plume simulation (total run from ~0900 to 1530). And in each case, we used most of the available memory. We have since upgraded our chemistry code for multi-processing in the form of an MPI code, so that we can run ship channel applications to a much larger domain requiring much more CPU time and memory. Also, we now have a cluster of 60 much faster Linux CPUs with considerably more memory. We have also integrated the MPI code in the most current version of RAMS (v. 6.0). The application of the parallelized LESchem within a nested RAMS application was the task of the current project. The chemistry module was updated to use the CB-V chemical mechanism.

4 THE PLAN OF DIAGNOSTIC DATA ANALYSIS FOR 13 SEPTEMBER 2006

Figure 4.1 shows an illustration of the data measurement *plan* for the SOF vehicle and the Baylor Aztec aircraft on 13 September 2006 as part of a TDEV study of the emissions from both the core HSC sources and the TC sources, under predicted steady north-to-south winds during the daytime. The main objective of the measurements was a TDEV study of the emissions from the HSC and TC, and also a downwind mesoscale transport and chemistry study of these

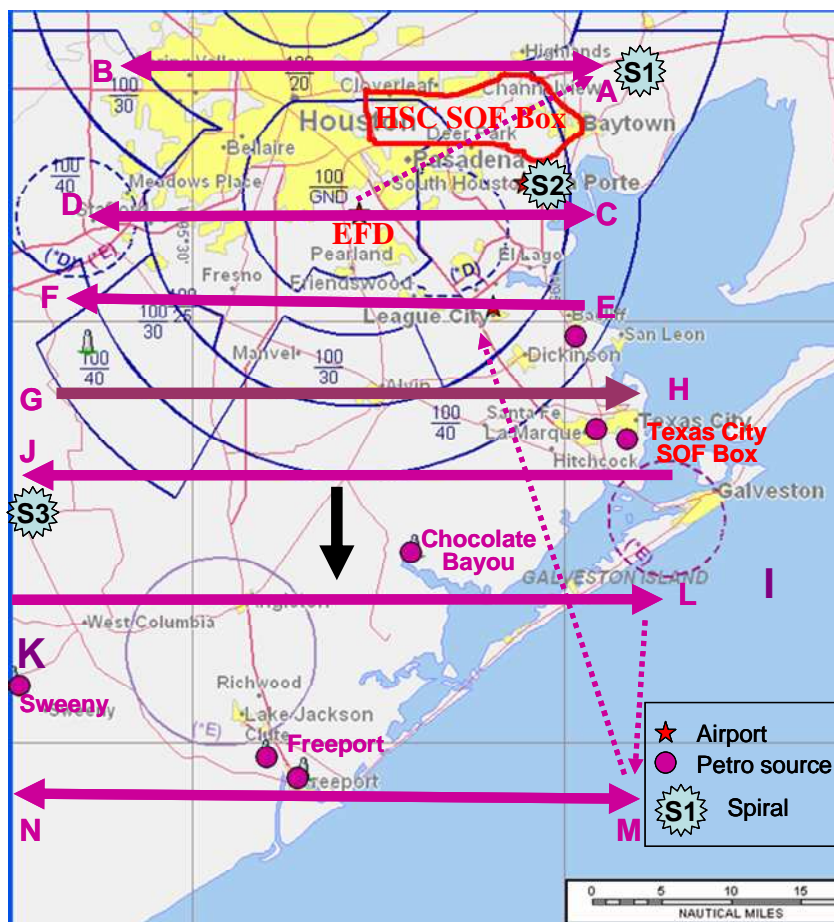


Figure 4.1 A map of the HGB area showing the TDEV mission plan of the SOF vehicle and the Baylor Aztec aircraft for 13 September 2006 under north-to-south flow conditions (black arrow). The SOF vehicle was to make measurements around the HSC SOF Box in the morning and then make measurements in the afternoon around the two main Texas City sources along a smaller Texas City SOF Box. The Baylor Aztec was to make morning measurements between AB and CD, with detailed measurements over the HSC SOF Box, as well as two spirals (vertical soundings) at S1 (beginning of flight) and S2 (end of flight). In the afternoon, the Aztec was to make traverses along EF, GH, IJ, KL and MN, with a spiral at S3 and detailed measurements at multiple heights over the TC SOF Box.. NOAA was to release a smart balloon from the LaPorte airport (near the site of S2) late in the morning and track it along a Lagrangian path, marking the HSC plume. The NOAA P3 aircraft was to take off around noon, make an upwind traverse (~AB), then four long traverses roughly between CD and MN.

emissions. The core HSC area is shown enclosed in the red HSC SOF Box which has borders along existing highways. A similar TC SOF Box was also defined along highways around the two main petrochemical sources in Texas City. More detailed Google-maps showing the HSC and TC SOF Boxes and the bordering highways are shown in Figure 4.2. The SOF was to make measurements in the morning along the HSC SOF Box and in the afternoon along the TC SOF Box. The Baylor Aztec aircraft was to make detailed measurements close to the HSC in the morning in support of the SOF, and in the afternoon make measurements near TC in support of the SOF, as well as mesoscale measurements downwind of both HSC and TC. More

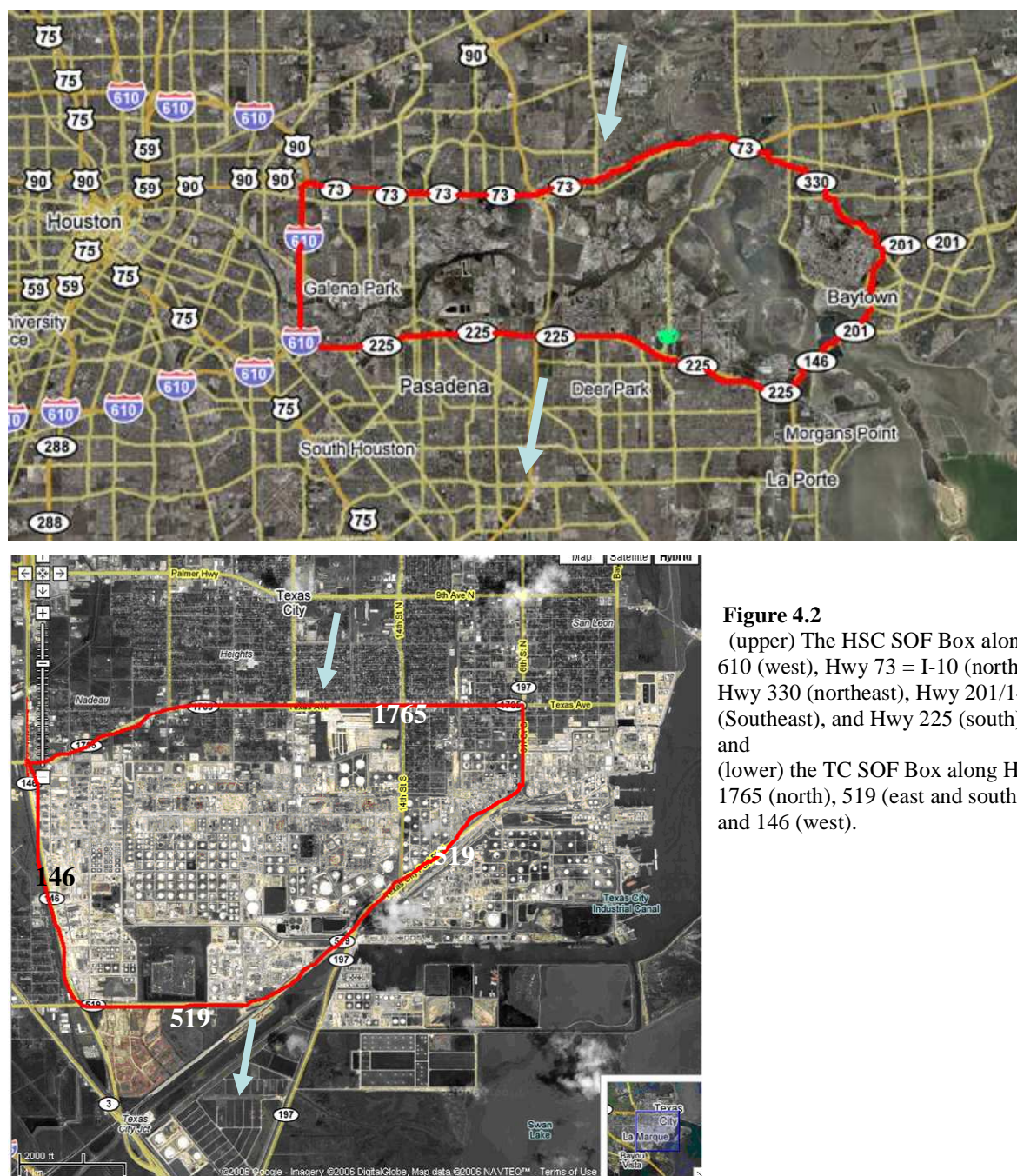


Figure 4.2

(upper) The HSC SOF Box along I-610 (west), Hwy 73 = I-10 (north), Hwy 330 (northeast), Hwy 201/146 (Southeast), and Hwy 225 (south), and
(lower) the TC SOF Box along Hwys 1765 (north), 519 (east and south), and 146 (west).

specifically, the Aztec was to take off from EFD (Ellington Field airport) at 0730, make a spiral at S1 near A, then back and forth upwind traverses between A and B, then detailed measurements over the SOF Box, including multiple traverses at different heights over the downwind leg of the SOF Box, then continue with back and forth downwind traverses between C and D, and finally close out the morning flight with a spiral at S2 before noon. In the afternoon, the Aztec was to fly traverses over the legs shown as EF, GH, IJ, KL and MN, make a spiral at S3 near J, and also make detailed flights at multiple heights over the TC SOF Box. The NOAA smart balloon was to be launched in the late morning near LaPorte airport (near the location of spiral S2) and tracked along its Lagrangian path for as long as possible. The NOAA P3 aircraft was to take off around noon and fly a long traverse upwind of the HSC and downtown Houston, and then multiple long traverses downwind of these and other emissions, much like the afternoon traverses of the Aztec. The weather turned out much as predicted and the measurement plan was carried out more or less as planned by all the platforms discussed above except the SOF, which could not make measurements in the morning, and therefore made measurements around the HSC SOF Box in the afternoon. No SOF measurements were made in Texas City on this day.

Our plan of diagnostic data analysis is briefly described in the context of the maps presented in Figure 4.3. Each panel of the figure covers the outermost Eulerian modeling domain of our runs of the RAMS mesoscale model at the horizontal spatial resolution of 12.15 km. The upper right and the bottom panels of the figure show the spatial distribution of the area-source emissions of isoprene, NO_x and OLE according to the TCEQ 12 km area-source EI. The upper left panel illustrates our Eulerian modeling grid configuration. The outermost box represents our 12.15 km resolution domain. Sequentially nested within this domain were four sub-domains of 4.05 km, 1350m, 450m and 150m resolutions. The smallest of these domains (150m) is our LES domain, shown in the figure (upper left panel) as the red shaded area. It includes the HSC area. The blue shaded area is the TCEQ domain of the Houston 2km x 2km area-source EI. It is approximately equal to our 4.05km domain. Thus, we have used this 2km area-source EI for all of our nested grids other than the 12.15 km grid, which uses the 12 km gridded EI.

Our prime interest was in performing the TDEV for the HSC emissions in the LES domain, and then perform Lagrangian modeling over a mesoscale distance downwind to study the transport and chemistry of the HSC and downwind emissions. The SOF team analyzed their data to make estimates of the HSC emissions of ethene, propene and total alkanes. Given the nature of the SOF data (to be discussed in the next section), this was generally expected to be the best direct TDEV estimate of the industrial emissions. However, there are some uncertainties in these SOF estimates, and our objective was to try to improve their TDEV estimates based on diagnostic modeling. First, SOF assumes that its downwind measurements of vertically integrated concentrations of the target species a short distance downwind of the sources include the full emissions. In fact, as we have seen in Section 2, the near-source chemistry in the industrial source plumes is vigorous, and there is likely to be significant chemical depletion of the HRVOC and NO_x emissions before its sampling by SOF (and perhaps also some ground removal of the emitted species as they are emitted quite close to the ground), depending on its downwind distance at sampling. Thus, the SOF emission estimates are likely to be under-estimates. To limit the size of this error, the SOF attempts to make measurements as close to the sources as possible. But there is a limit to how closely it must make such measurements. If it

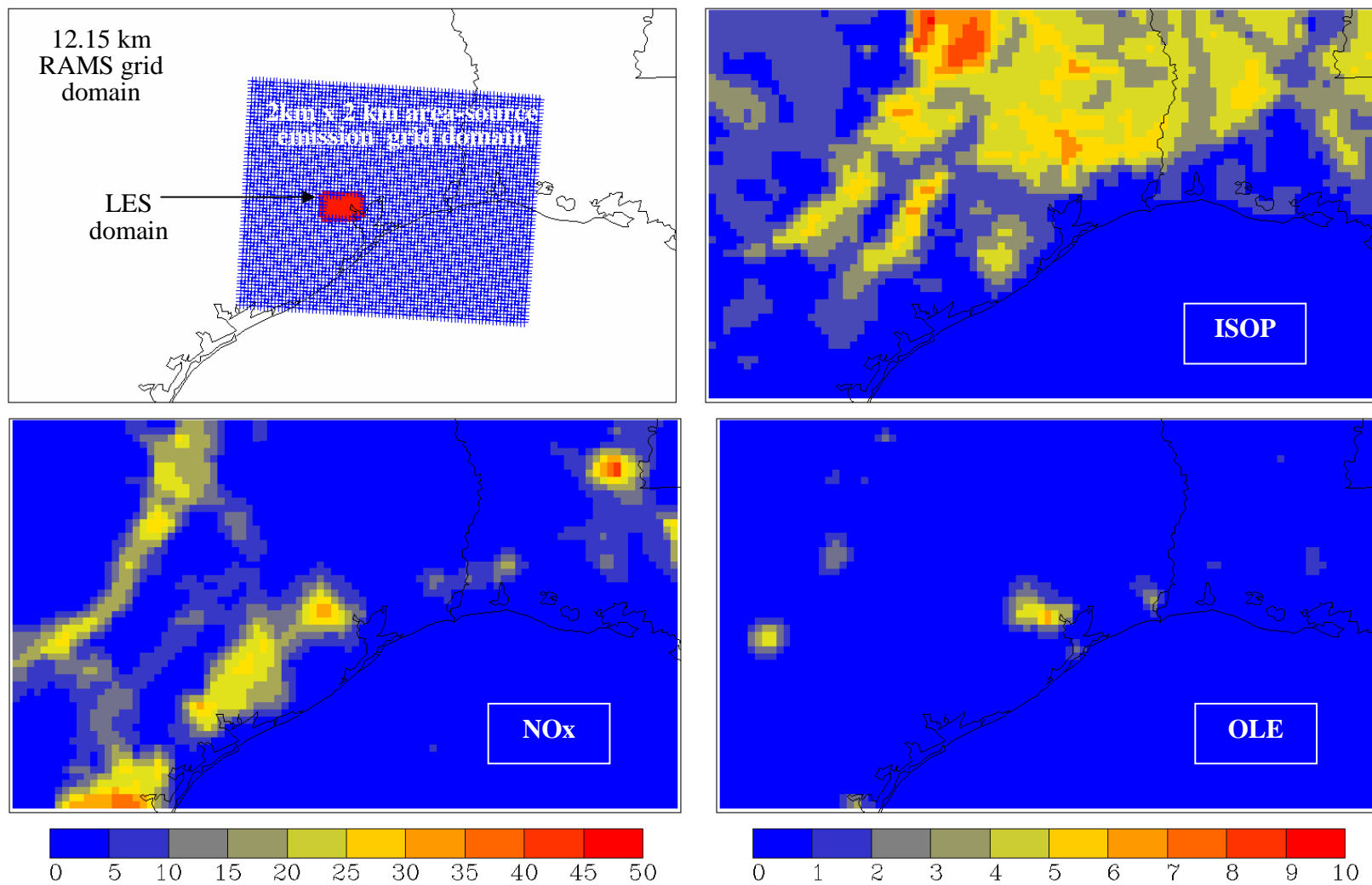


Figure 4.3 Modeling grid configuration (upper left), and 12-km area-source emission distributions of isoprene (upper right), NOx (lower left) and OLE (lower right). The grid configuration map (upper left) shows the RAMS 12.15 outermost grid domain, the 2km x 2 km grid domain of the highest-resolution Houston area-source emissions inventory (blue shaded area), and the 150m x 150m LES grid domain (red shaded area). The emissions maps are based on EI data at a spatial resolution of 12 km.

gets too close, then the plumes are likely to be still experiencing significant looping and meandering, which increases the chances of multiple-counting emissions to some extent, which would make the estimates of the emissions an over-estimate. Secondly, SOF measures vertically integrated concentrations with no vertical resolution of the measurements. Its data analysis to convert these measurements to emissions requires weighting their chemical data by wind speed. Consequently, it applies a single wind speed over the full vertical extent of the plume. This procedure, in fact, is believed to be the cause of the largest uncertainty in SOF estimates of emissions.

Our approach is to use LESchem modeling with detailed characterization of the 4D concentration and wind fields, and including the role of chemistry (including turbulent chemistry) between emissions and sampling to improve the estimation of emissions using the SOF sampling data. The Aztec made continuous measurements along the downwind side of the SOF Box at up to five heights to provide guidance on the vertical distribution of the emissions. Because of the intensive computations in LESchem, it is only possible to perform LES modeling over a limited domain size. Our LES domain is already about 45 km x 25 km, possibly the largest domain over which anybody has applied even LES, let alone LESchem. Besides, as we have seen, turbulent chemistry becomes negligible in about an hour or so downwind from the source. For studying the transport and chemistry of the industrial plumes farther downwind over mesoscale distances under the type of Lagrangian measurement conditions of our TDEV missions, the LRPM is an ideal tool, which permits much finer spatial resolution of the modeling than Eulerian OAQMs such as CMAQ, and which is much more economical as well as conducive to use of observed plume dynamics to a very substantial extent. Furthermore, it can make more detailed use of the continuous chemical measurements as diagnostic information than can the Eulerian OAQMs, as was shown in Section 2.

With reference to Figure 4.3, our plan for diagnostic modeling using LES and LRPM was as follows. LES must generate realistic IC/BC to be of use, particularly in the urban setting of the current application. Thus, we apply it in nested mode inside RAMS with addition of on-line chemistry. We have done this in the same way we added chemistry to RAMS-LES some years ago. In the current application, our plan was to use the CB05 chemical mechanism in all nested RAMS domains after testing the model for dynamics. The nesting is done in five steps between a resolution of 12.15 km and that of LES (150m), at which size, the large turbulent eddies would be explicitly resolved. The detailed application of RAMS, including generation of the IC/BC for the outermost domain, will be discussed in Section 7. The chemistry IC of the 12.15 km RAMSchem was to be derived from the runs of CMAQ performed by UH. However, we did not receive the outputs of the 12 km run of CMAQ until 27 August 2008, which was close to the end of this contract.

Our plan was also to initialize LRPM at the upwind end of the outermost RAMS domain based on CMAQ inputs to start with, and then to run it to the upwind end of the LES domain iteratively, updating the BC and the emissions along the way based on use of the surface chemistry site data as available, and the aircraft data of the upwind traverses. Such updated information would be used to improve the IC/BC for the RAMSchem runs. Such runs themselves would have been made iteratively to update the IC and the area source emissions along the way. Such refined runs of RAMSchem would have supplied the IC/BC for the

LESchem runs, which would have been run iteratively in diagnostic mode using the downwind data of the SOF and the downwind aircraft traverses and other available data (e.g., surface sites, Moody Tower etc.) to perform the TDEV analysis to estimate the best emissions from the HSC. The resulting concentration field at the downwind end of the LES domain, optimized with the TDEV-corrected emissions, would then have supplied the IC for the LRPM runs over the downwind mesoscale distance. Downwind surface and elevated emissions would be ingested during these runs. The downwind mesoscale runs of LRPM would be similar to those in TexAQS I analyses, and would be used to further check the reconciliation of the emissions with the downwind observed concentrations of the secondary products ozone and formaldehyde. Such runs would also have yielded information to assess the downwind impact of the target emissions in terms of downwind ozone.

5 THE HSC SOURCE CONFIGURATION AND THE EI DATA

Figure 5.1 shows an illustration of the source distribution in the HSC area, and locations of the eight local autoGC surface monitoring sites where speciated VOC measurements are made.

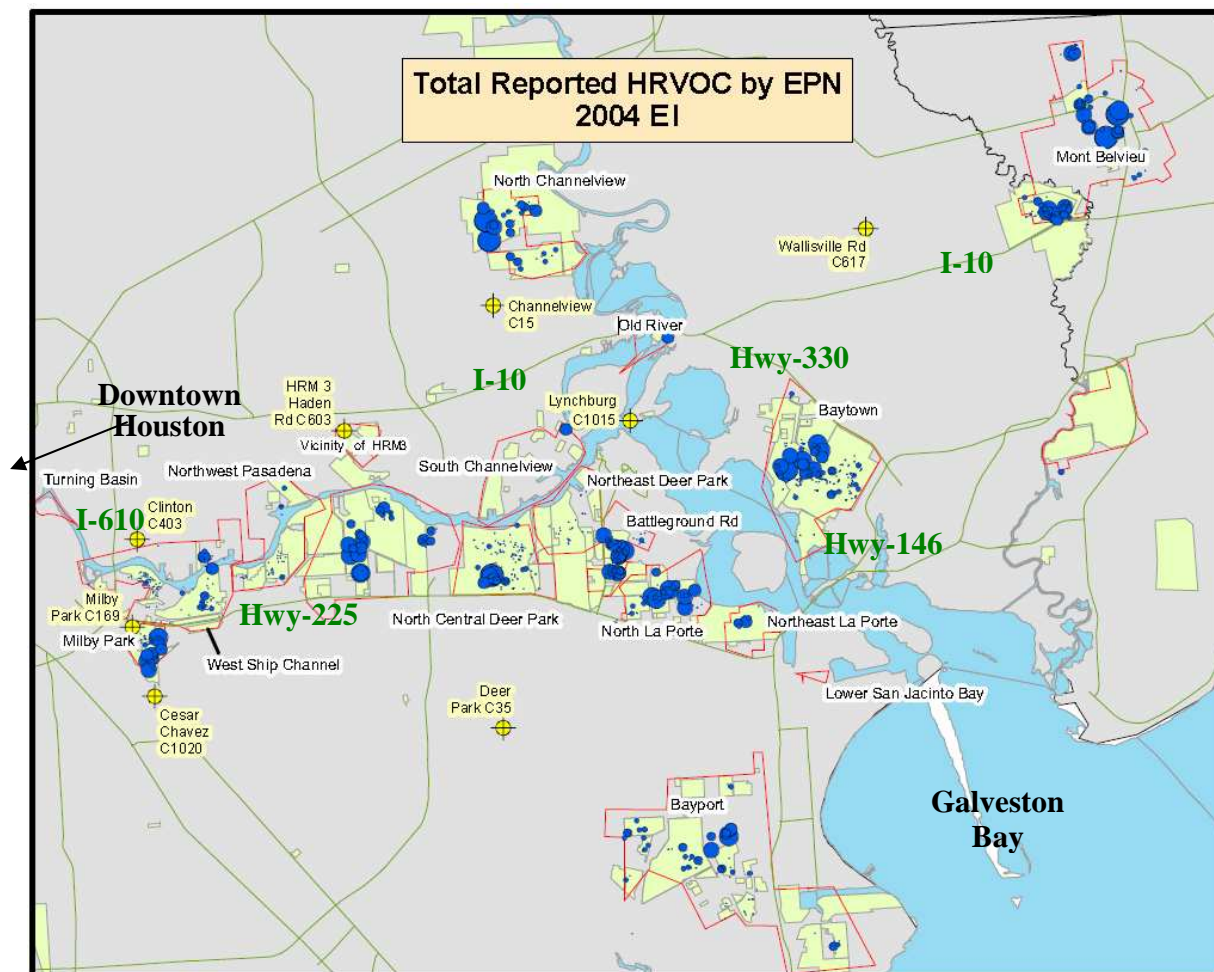


Figure 5.1 Map of the HSC area showing the main waterways, highways, a spatial distribution of the HRVOC industrial sources (solid blue circles), and the surface monitoring sites with the speciated autoGC VOC measurements (yellow circles).

The HSC is the waterway running between Galveston Bay in the SE corner of the map and downtown Houston off the map from the west-center of the map. Interstate 10 (I-10) is the main highway running a little to the north of the HSC; the eastern leg of the I-610 inner beltway runs just to the west of the main source area of the HSC; Hwy-225 runs on the south side of the HSC; and Hwys 330 and 146 form the NE and SE sides of the Baytown complex of sources. The red boundaries identify some source complexes in the HSC area. Two of the major ones, North Channelview and Mont Belvieu, are to the north of the HSC and I-10, the latter in the NE corner of the map. The complexes identified along the ship channel and mainly just south of it, from west to east, are: W. Ship Channel (north of Hwy-225), Milby Park (south of Hwy-225), NW Pasadena, Vicinity of HRM3, NC Deer Park (south of the HSC) and S. Channelview (north of the HSC), NE Deer Park, Battleground Rd., N. LaPorte, NE LaPorte, and Baytown (north of the

HSC). The Bayport source complex is south of Hwy 225 and the LaPorte area, just to the west of Galveston Bay. There are three large petroleum refineries in the HSC area: the Exxon refinery in the “Baytown” complex, the Shell refinery in the “NC Deer Park” complex, and the Lyondell refinery in the southeast part of the “W. Ship Channel” complex.

The eight local autoGC sites (yellow circles with a cross through it) are as follows (from west to east): Clinton (C403), Milby Park (C169) and Cesar Chavez (C1020) near I-610 to the west, HRM3 (C603) in the northern part of the “Vicinity of HRM3” complex, Channelview (C15) just south of the “N. Channelview” complex, Deer Park (C35) south of the “NC Deer Park” complex, Lynchburg (1015) near Lynchburg Ferry to the NE of the “NE Deer Park” and the “S. Channelview” complexes, and Wallisville Rd. (C617) to the north of I-10 between the “N. Channelview” and the “Mont Belvieu” complexes.

The Houston area point-source EIs for 2006 were received from TCEQ in the form of four sets of data files, as follows:

- (1) the Texas Acid Rain Data (Texas ARD) of large EGU and related sources, extracted from the EPA Acid Rain Program Database, mainly of NO_x and CO, mostly hourly data;
- (2) the Texas Ozone Season Day (Texas OSD) database consists of the EI data of NO_x, CO and speciated VOC for most of the industrial (NEGU) point sources not included in the Special Inventory (below), as extracted from the TCEQ STARS database --- the data are mostly daily resolution, divided into 24 equal hourly values;
- (3) the Special Hourly (day-specific) Inventory data (Special EI) of NO_x, CO and speciated VOC for selected large industrial point sources (more below), at hourly resolution; and,
- (4) the Ship data (Ship EI) of point-sources on the water channels of the HSC and Galveston Bay, with a mixed temporal resolution (some hourly data and others are daily data equally divided into hourly data).

The VOC speciation in these EIs was according to the CB05 chemical mechanism. The NO_x data were split into NO and NO₂. The temporal resolution of the data in each file is originally as pointed out above, but all data were included in the files with hourly values in gm-moles/h units.

The 2006 Special Inventory of hourly point source emissions was conducted during the 2006 intensive field study of TexAQS II from August 15 to September 15, 2006. During this period, 141 sites in the eastern half of Texas reported their hourly emissions of VOC and NO_x from predetermined industrial sources. Sources were selected for the 2006 hourly inventory based upon the following criteria: sources subject to highly reactive VOC rules, NO_x and sulfur dioxide sources equipped with continuous emissions monitors, and emissions sources located near ambient air monitoring sites.

In addition, we also received from TCEQ EI data of area sources of CO and anthropogenic and biogenic NO_x and VOC (CB05 speciation) at 2 km resolution. Since we needed area source emissions inputs to our five different gridded resolutions from 150m to 12.15 km, we also received from TCEQ area source EIs at 4 and 12 km resolutions.

All of the EI files above were processed to generate emissions based on our modeling needs. Below, we present selected plots of the spatial distribution of the emissions data aggregated for the 24 hours of 13 September 2006 from the point-source EIs for the HSC, based on our

processing (each plot is on a base map of the HSC area). Each of the sets of figures, (set one: Figure 5.2, Figure 5.4, Figure 5.6, and Figure 5.8, and for set two: Figure 5.3, Figure 5.5, Figure 5.7, and Figure 5.9), respectively, show EI data for the four species NO_x, ETH (ethene), OLE (olefins), and alkanes = ETHA (ethane) + PAR (paraffins). Each figure in the first set shows the data of each of these species by four separate emission height ranges (all heights, 0 – 50m, 50 – 100m, and 100 – 150m). Each figure in the second set shows the data of each of these species separated by the four separate EIs, viz., Acid Rain EI, Ozone Season EI, Ships EI and Special Hourly EI. The data for each source is plotted in the right location on the map of the HSC, as a circle of diameter proportional to the emission value in kg-moles/day. It may be observed that most of the data come from the Ozone Season EI, and the least from the Acid rain EI (EGUs). For each species, most emissions are from sources in the height range 0 – 50m, with decreasing numbers as the height increases. It is interesting to note that only one source of NO_x (from the Acid Rain EI) has a physical emission height greater than 100m, while there are more VOC sources in this height range (100 – 150m).

Figure 5.10, Figure 5.11, and Figure 5.12 show the area-source EI data plotted for NO_x, CO, OLE and ISOP, respectively, on our 12.15 km, 4.05 km and 150m (LES) grids. The original data for these plots were derived from TCEQ data with resolutions, respectively, of 12 km, 4 km and 2 km.

For the LESchem modeling, the emissions data would be emitted in the appropriate height layer of the model (for the point sources based on the effective stack heights) and the appropriate horizontal grid cell. For the LRPM, the area sources would be emitted in appropriate 2-km grid cells, but the very large number of point sources would have to be emitted as a manageable number of composite sources. As an example, Fig. 5.13 shows a choice of 29 composite point sources representing the HSC, TC (Texas City) and Bayport sources. TC emissions are grouped into 2 composite point sources (1 and 2), as shown, the Bayport sources into 3 composite sources (4, 5 and 6), and the HSC sources into 23 composite sources (7 – 29).

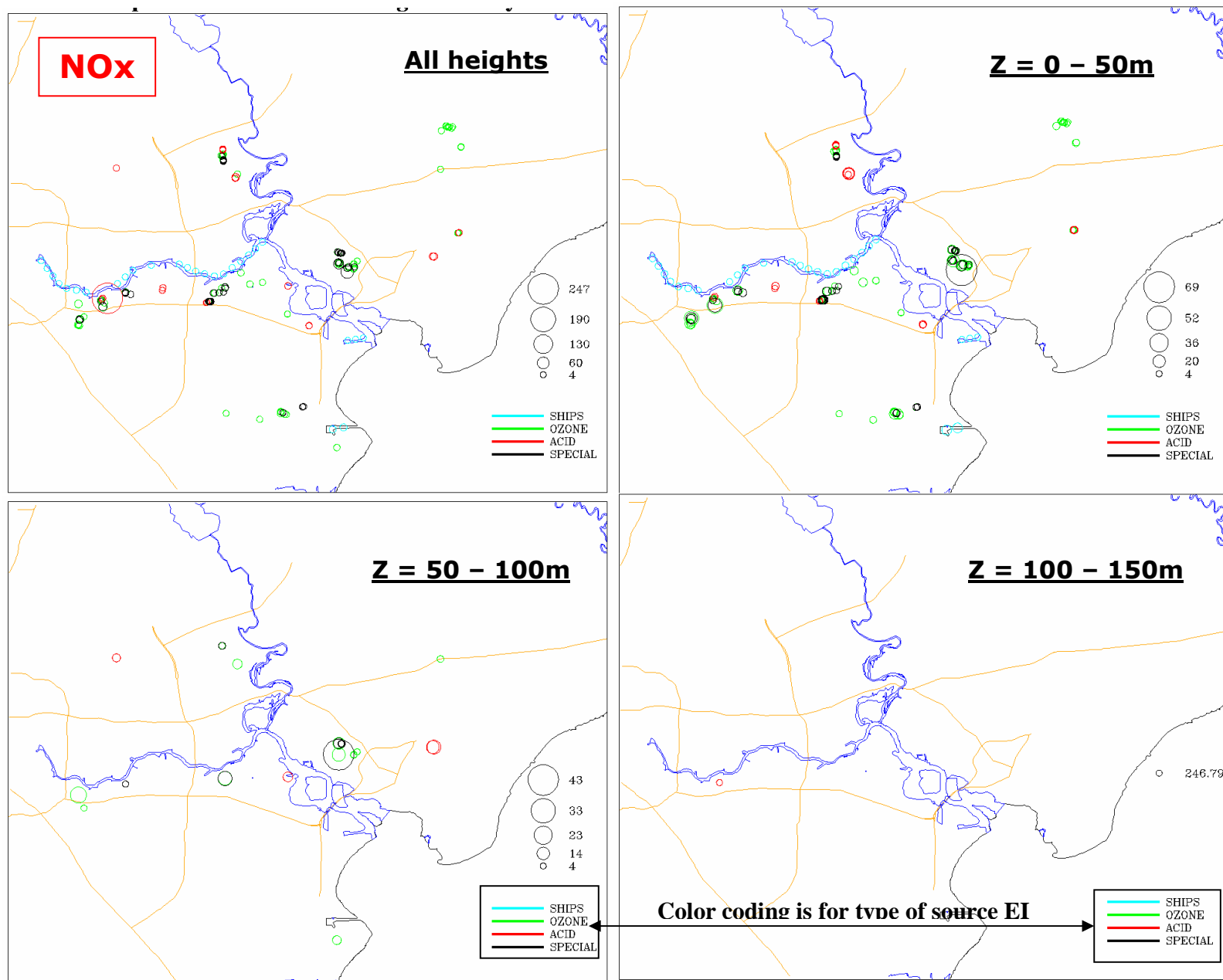


Figure 5.2 HSC – Top 200 Industrial Point Source Emissions Inventory for NO_x (kg-moles/day), by emission height.

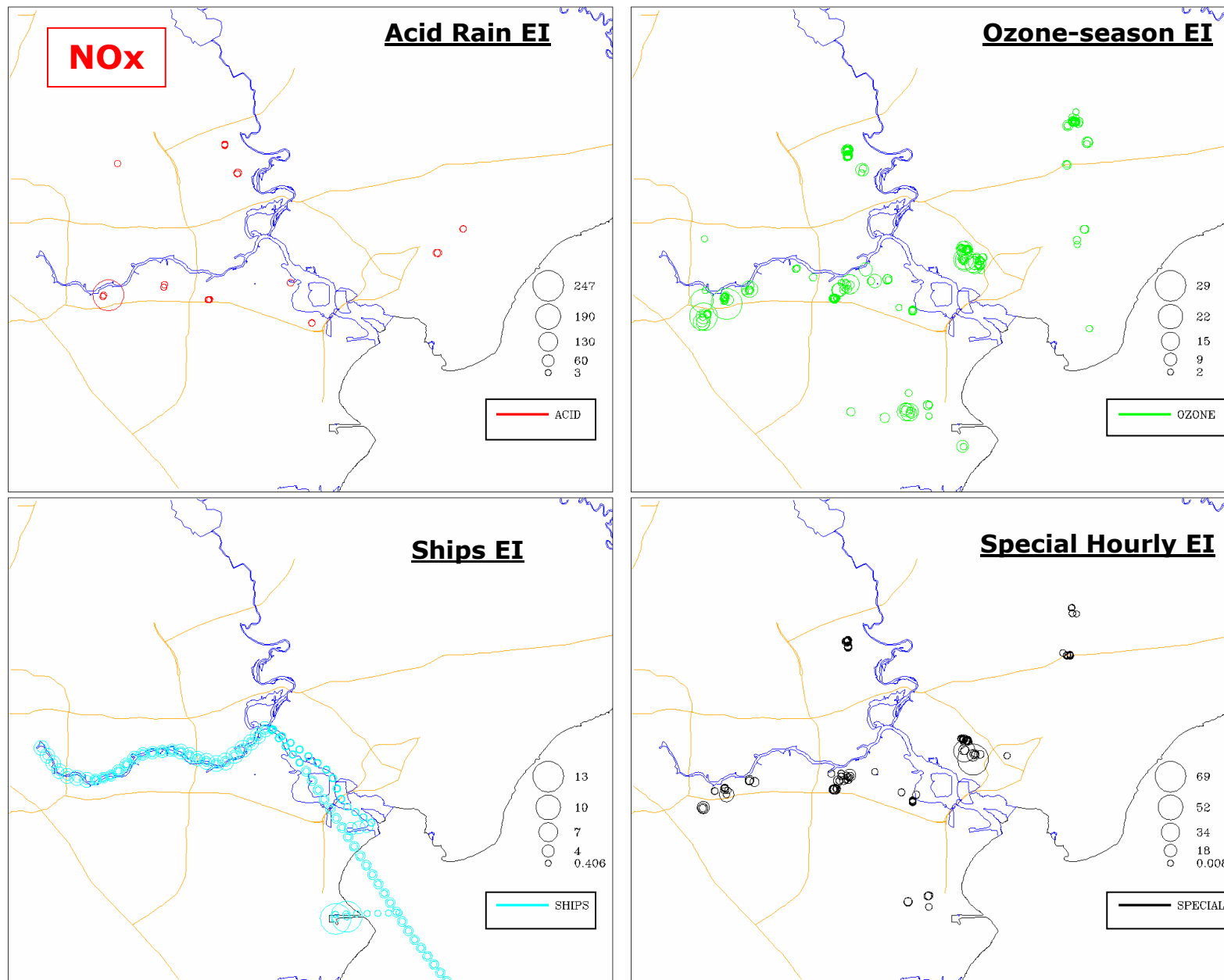


Figure 5.3 HSC – Top 200 Industrial Point Source Emissions Inventory for NOx (kg-moles/day), by type of source EI.

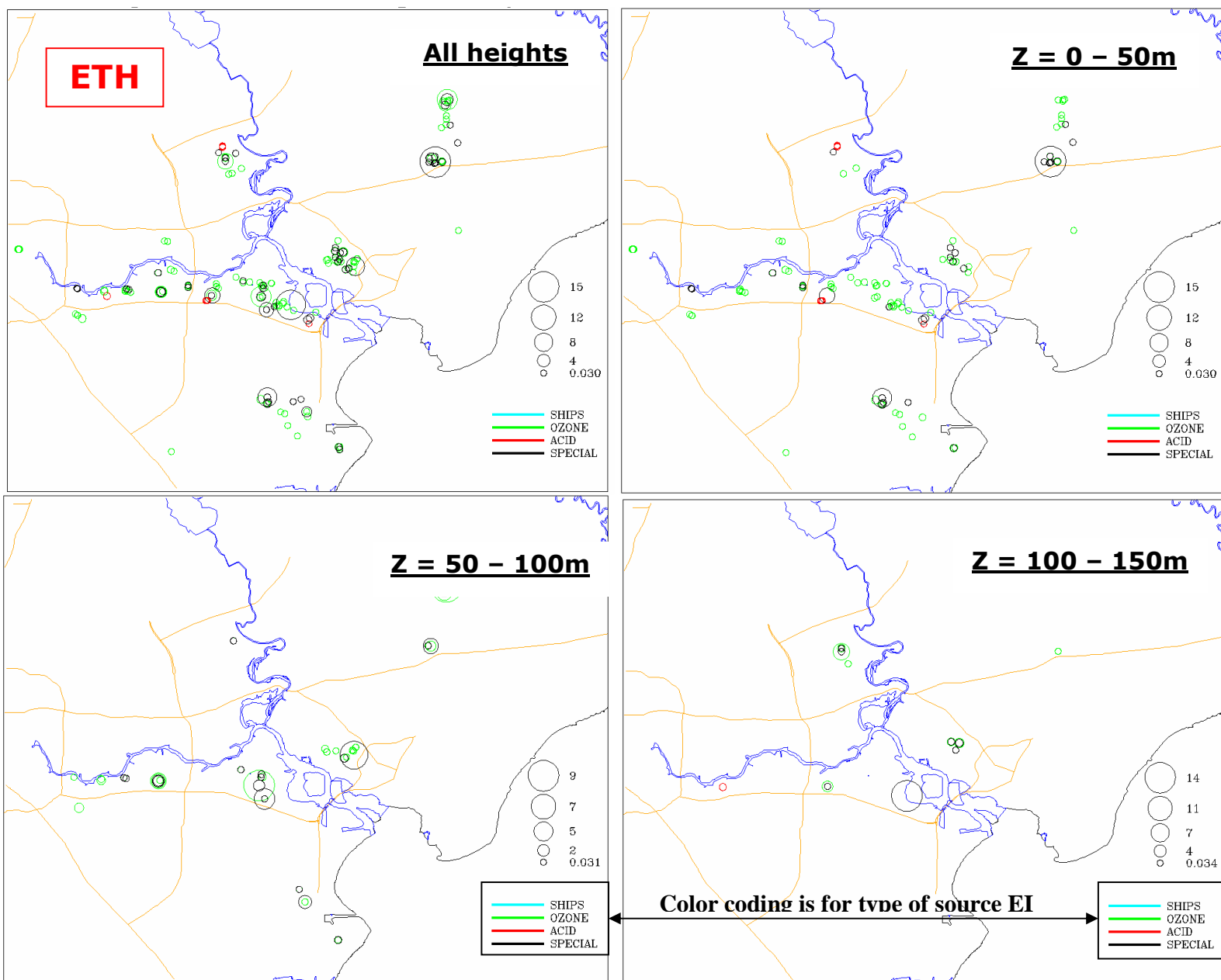


Figure 5.4 HSC – Top 200 Industrial Point Source Emissions Inventory for ETH (kg-moles/day), by emission height.

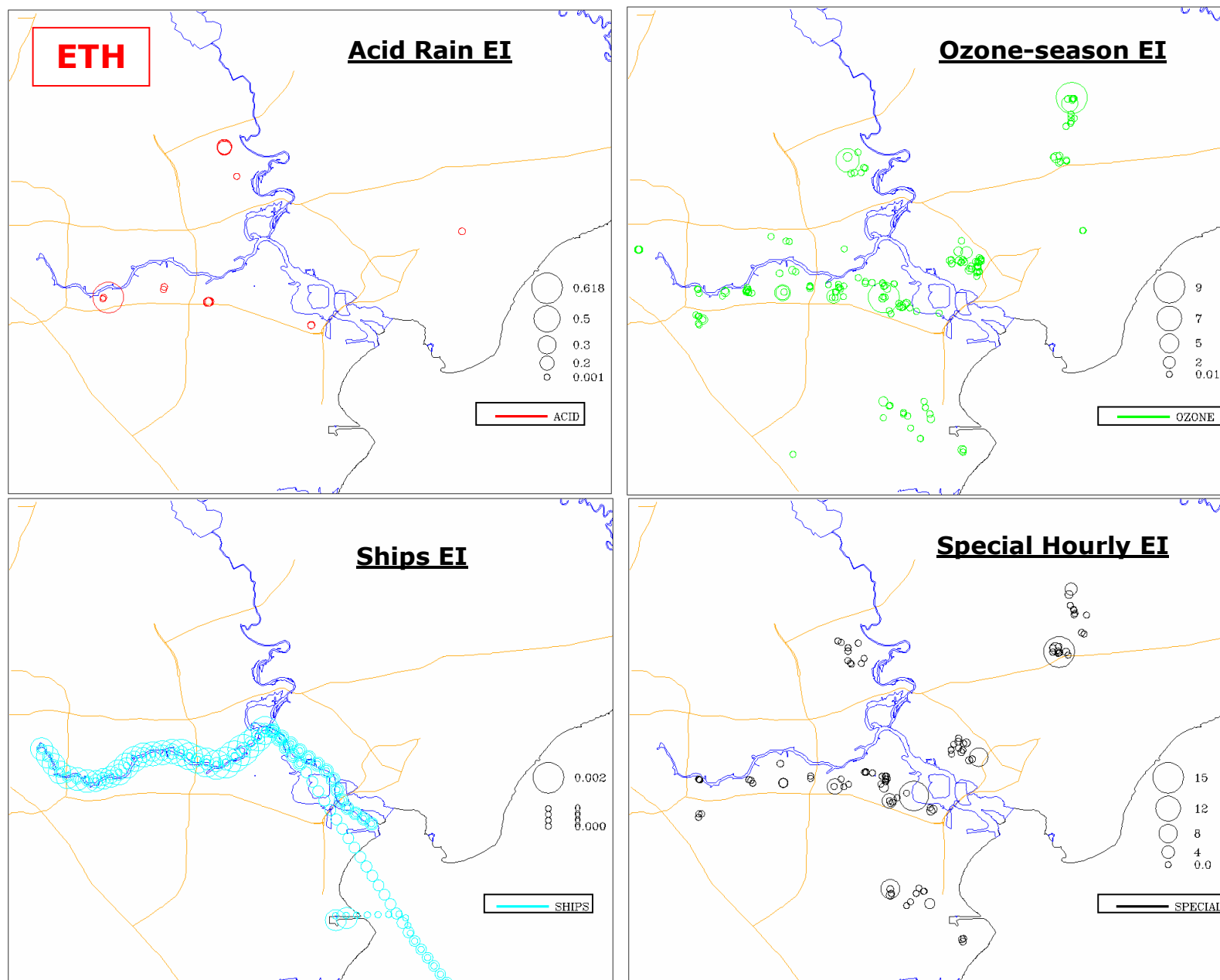


Figure 5.5 HSC – Top 200 Industrial Point Source Emissions Inventory for ETH (kg-moles/day), by type of source EI.

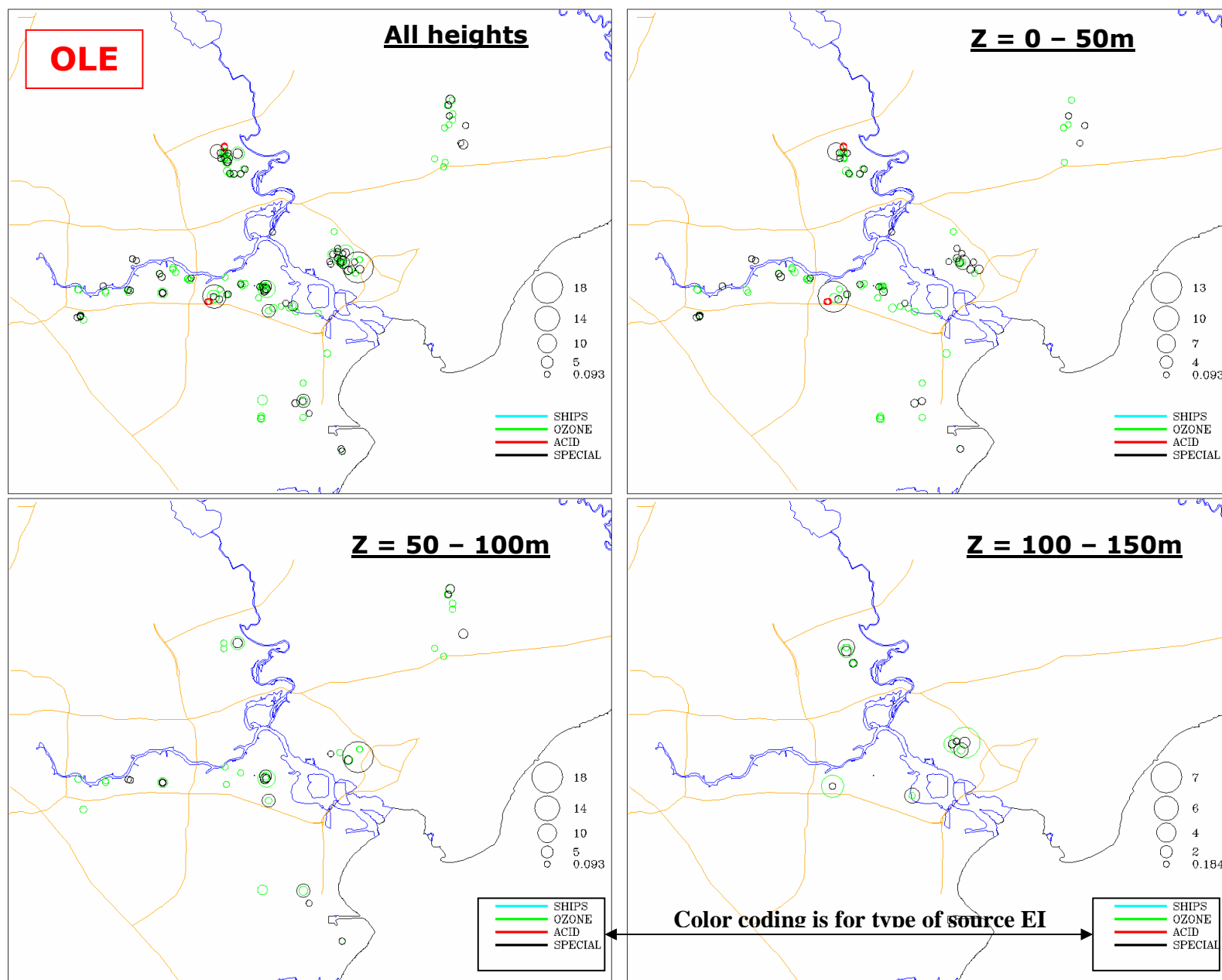


Figure 5.6 HSC – Top 200 Industrial Point Source Emissions Inventory for OLE (kg-moles/day), by emission height.

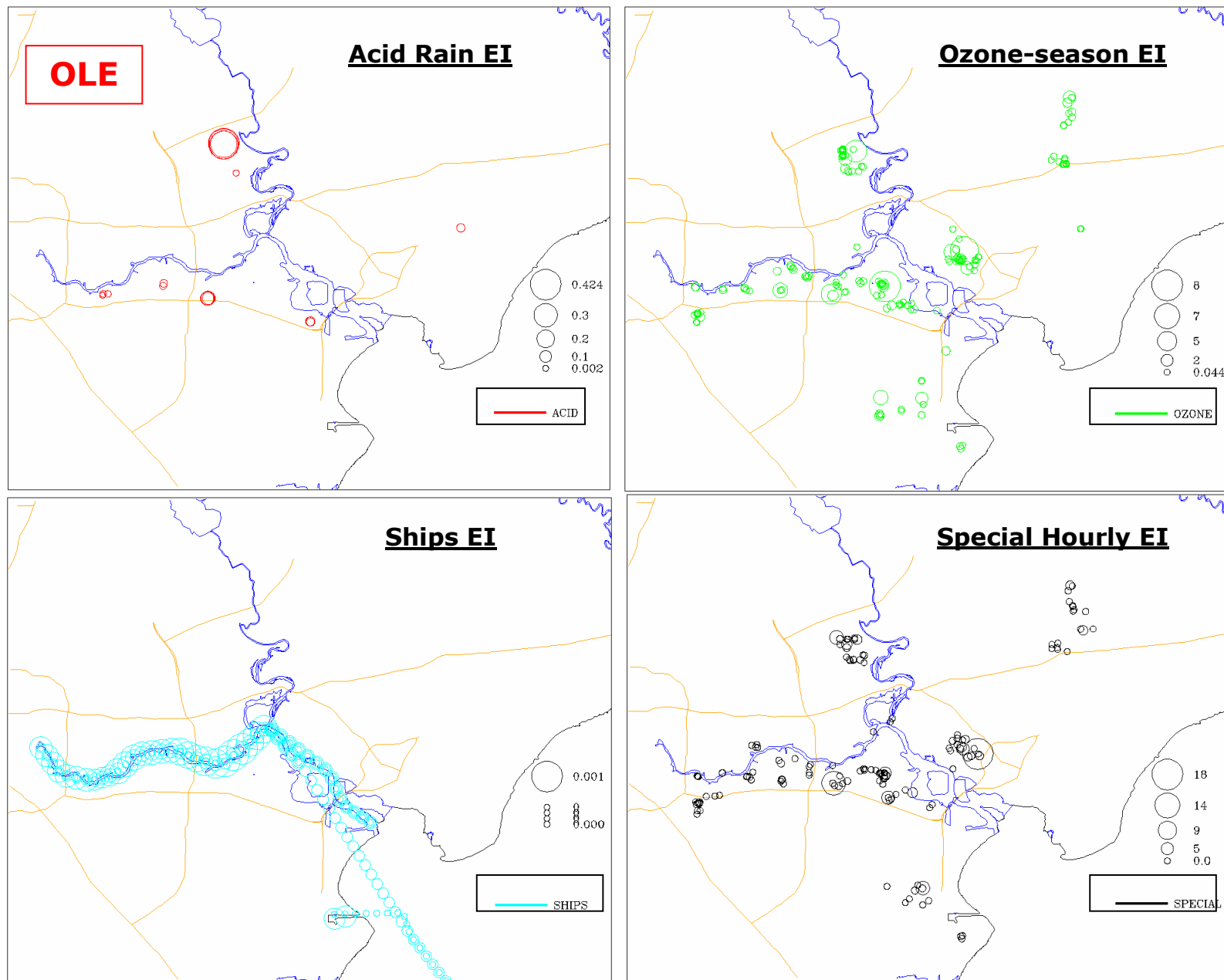


Figure 5.7 HSC – Top 200 Industrial Point Source Emissions Inventory for OLE (kg-moles/day), by type of source EI.

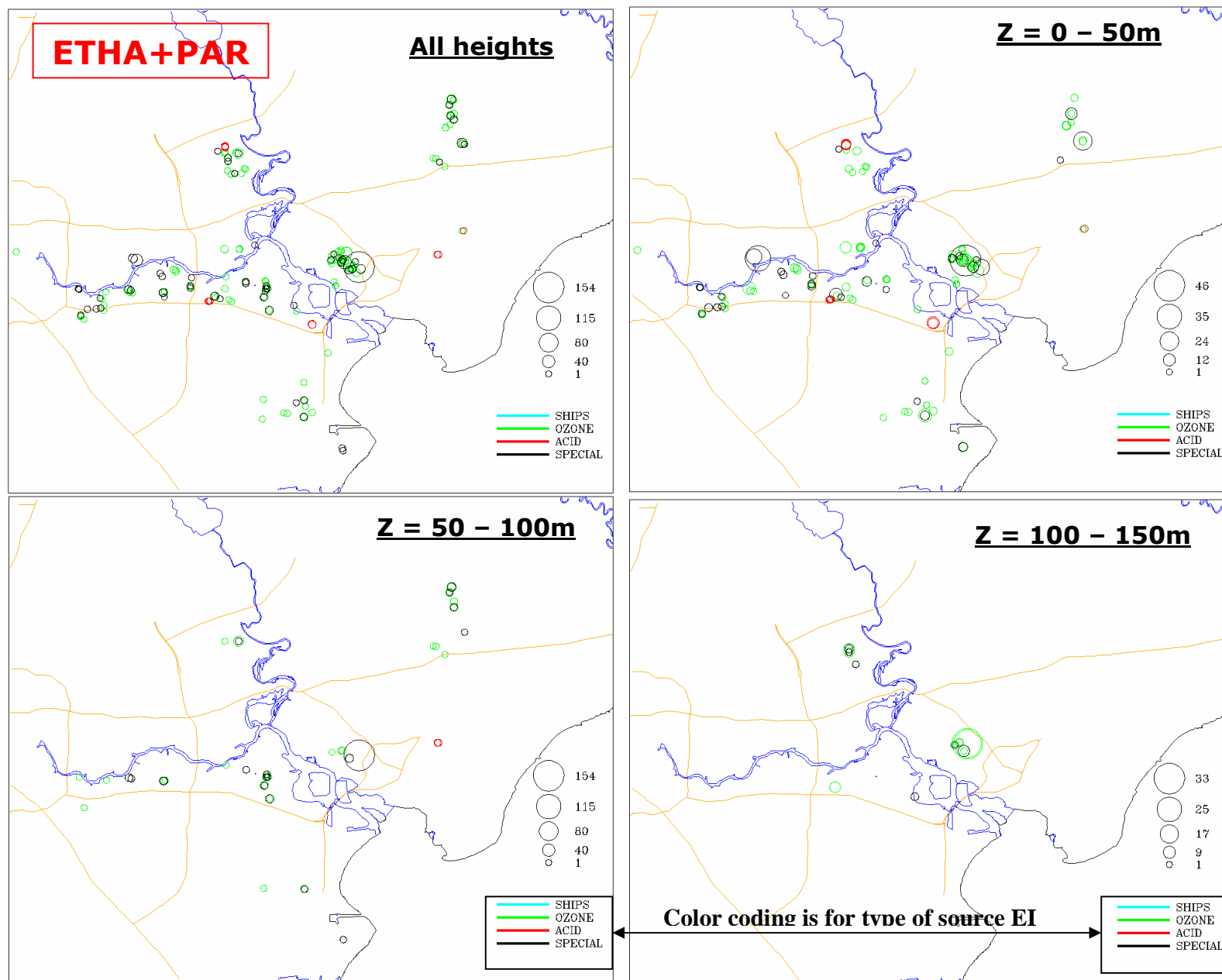


Figure 5.8 HSC – Top 200 Industrial Point Source Emissions Inventory for ETHA+PAR (kg-moles/day), by emission height.

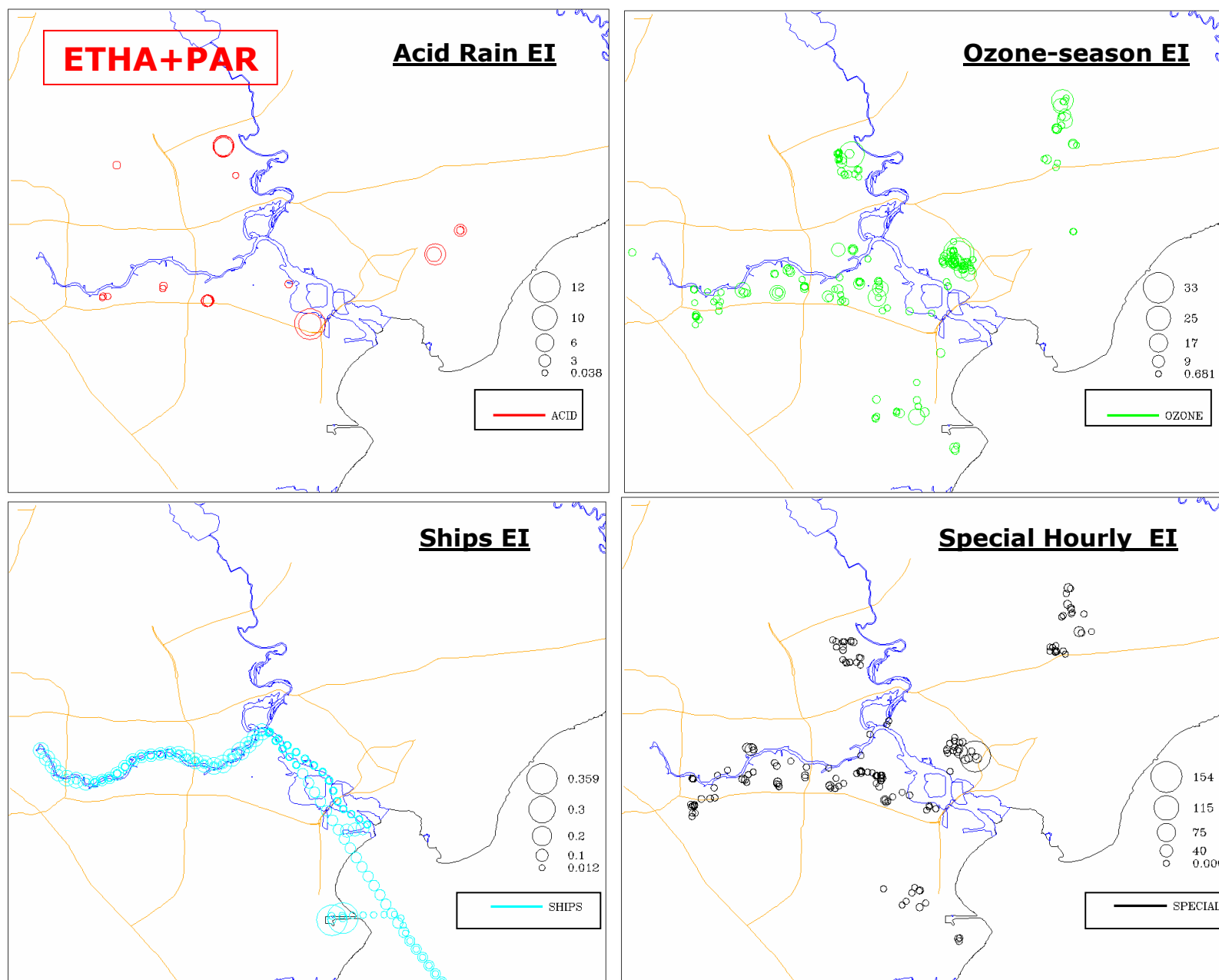


Figure 5.9 HSC – Top 200 Industrial Point Source Emissions Inventory for ETHA+PAR (kg-moles/day), by type of source EI.

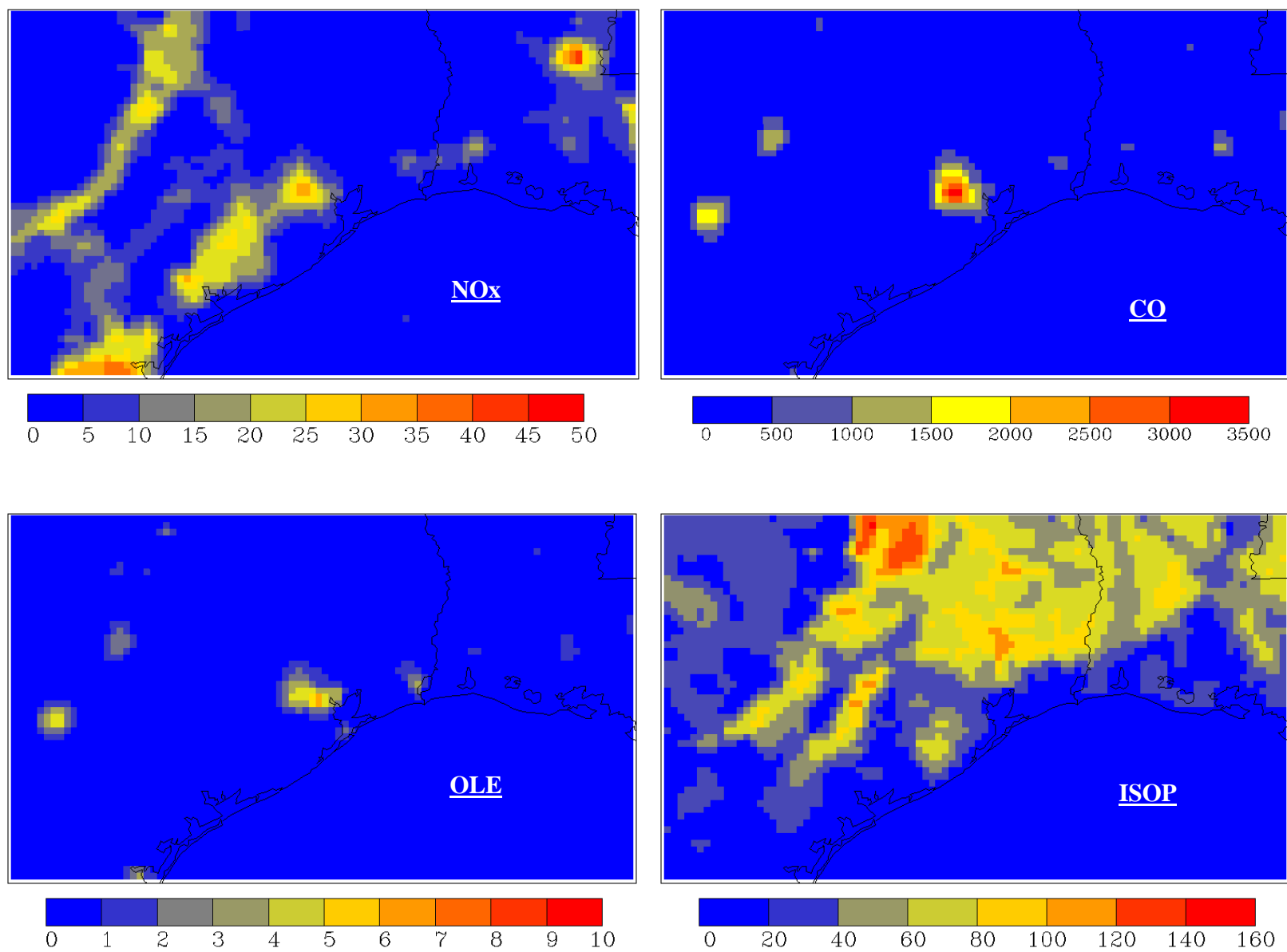


Figure 5.10 Area source emissions of NO_x, CO, OLE and ISOP (anthropogenic and biogenic) in the Houston 12.15 km grid in kg-moles/day from the TCEQ area-source EI (original data resolution = 12 km).

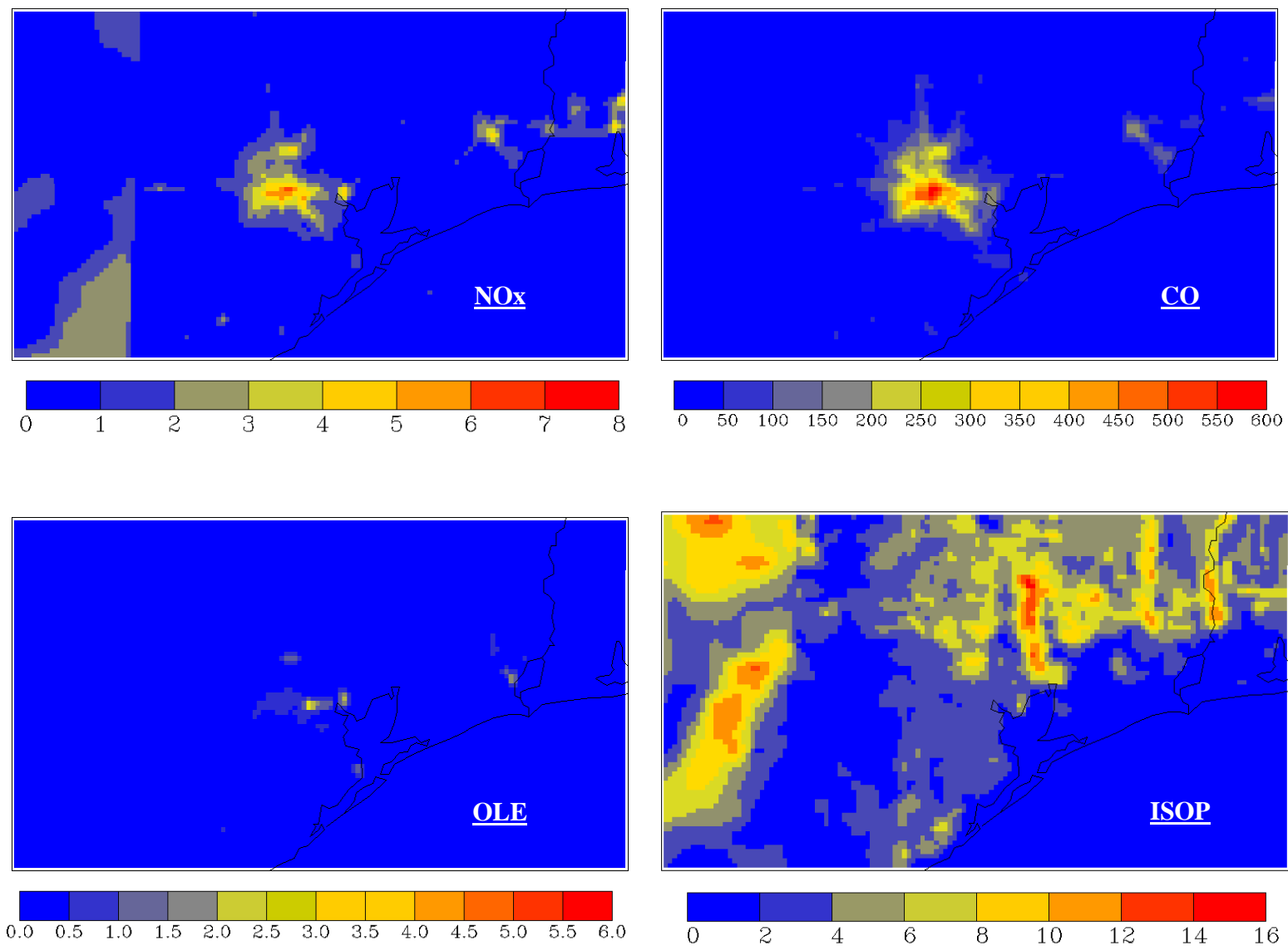


Figure 5.11 Area source emissions of NO_x, CO, OLE and ISOP (anthropogenic and biogenic) in the Houston 4.05 km grid in kg-moles/day from the TCEQ area-source EI (original data resolution = 4 km).

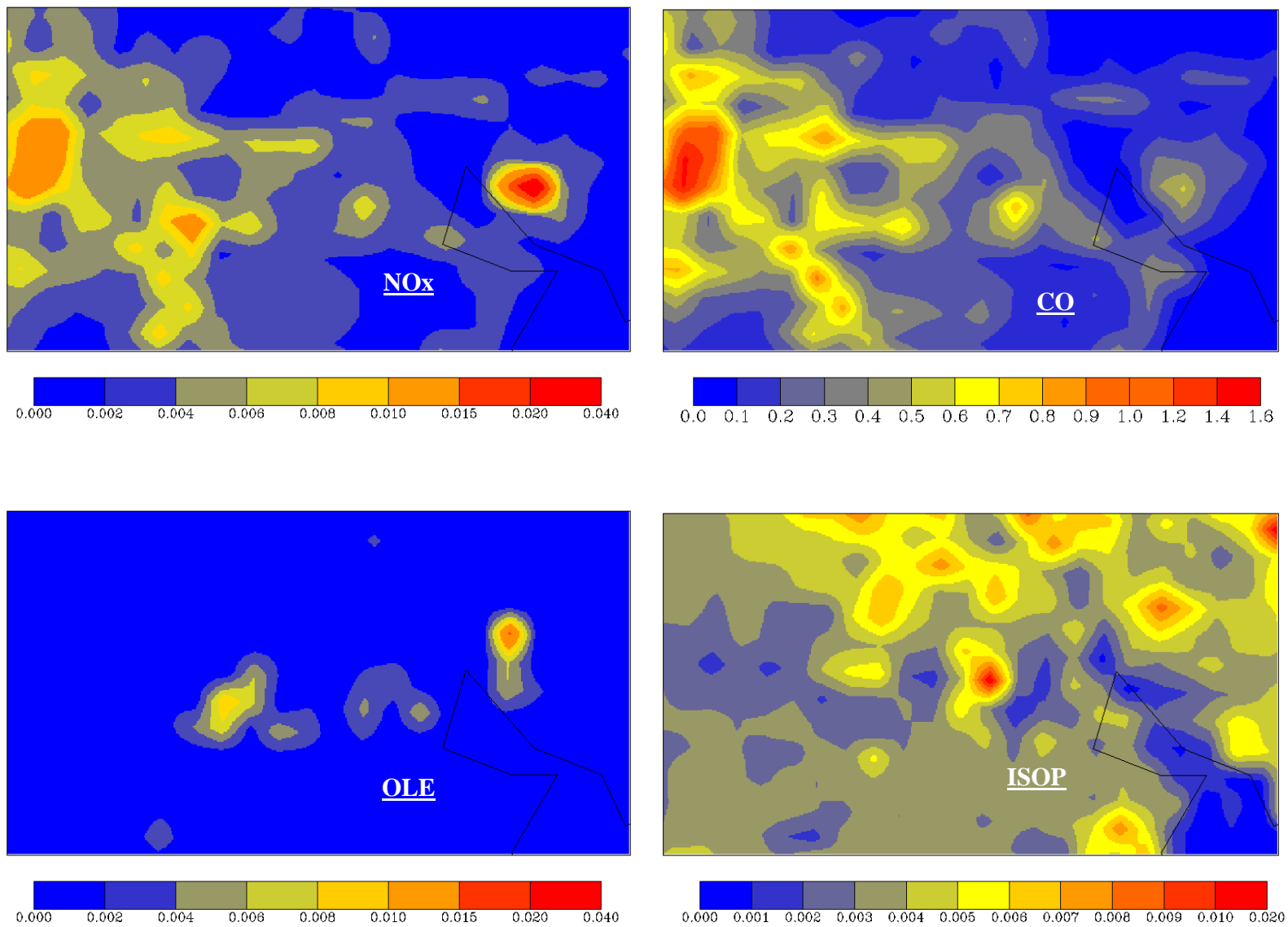


Figure 5.12 Area source emissions of NO_x, CO, OLE and ISOP (anthropogenic and biogenic) in the Houston 150m (LES) grid in kg-moles/day from the TCEQ area-source EI (original data resolution = 2 km).

Aggregated Ship Channel + Texas City Point Sources

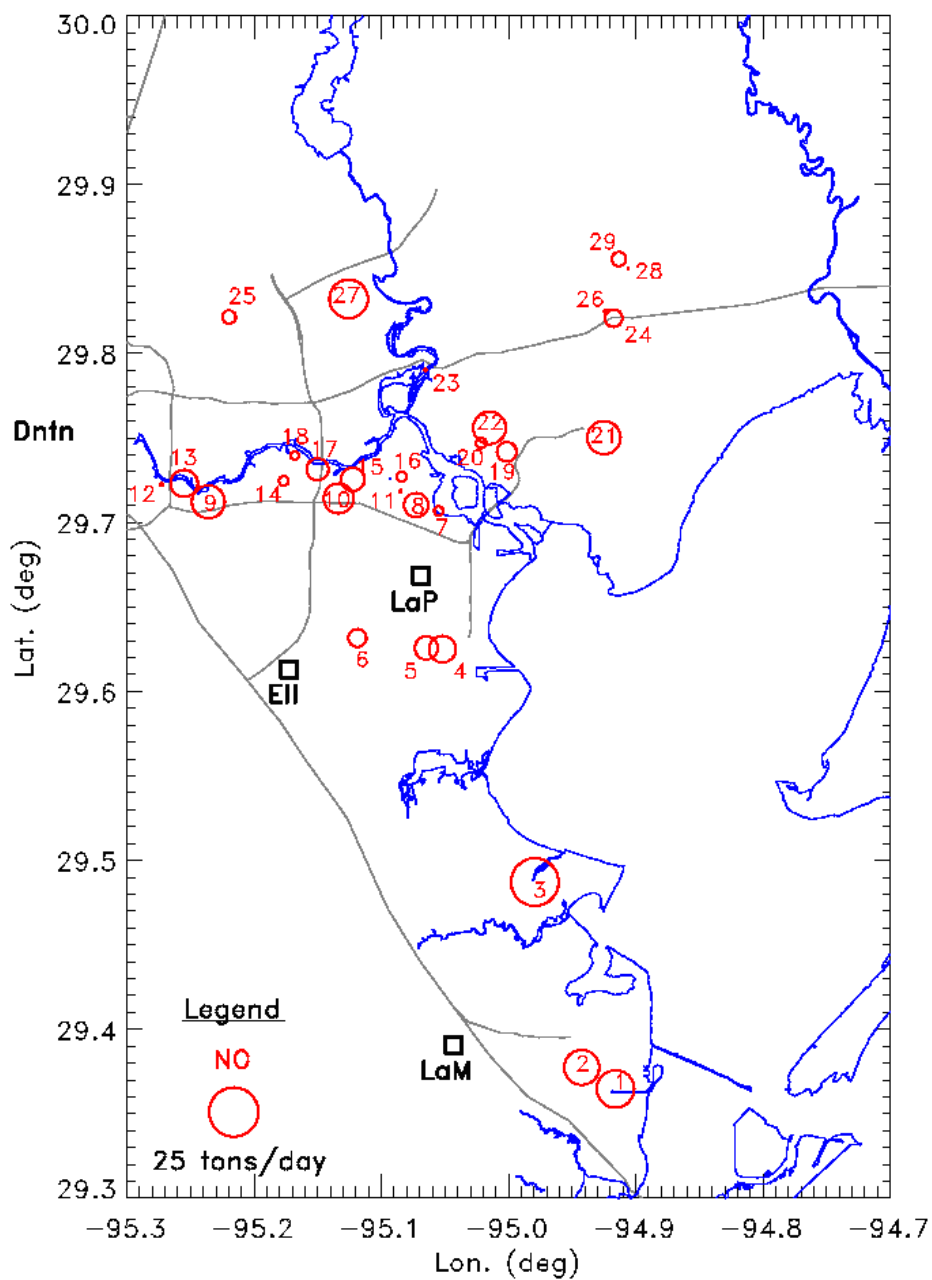


Figure 5.13 Locations (circle centers) and emission rates (proportional to circle diameters) of NO for the 29 “aggregate” or composite major point sources in the Texas City and Houston Ship Channel complexes. Also shown is the identification by a number (1 to 29) of each of these sources. The diagnostic LRPM modeling planned to be done for each of these sources.

6 THE AVAILABLE DATABASE FOR 13 SEPTEMBER 2006

13 September 2006 was selected for the first TDEV analysis in this project because it was considered to have the most comprehensive database for TDEV and downwind chemistry in TexAQS II, and because the weather on that day was right for the TDEV mission. The SOF ground vehicle was specially commissioned from Sweden to come and perform TDEV measurements for VOC species. Five daily missions of the Baylor Aztec were also dedicated for TDEV measurements in support of the SOF. Both the SOF and the Aztec participated in a coordinated TDEV study on 13 September 2006. In addition, the NOAA P3 aircraft was also deployed on that day and performed relevant complementary measurements of the HSC emissions and transport-chemistry on that day. In addition, A NOAA smart balloon was launched on that day to track the HSC plume as a Lagrangian marker, and substantial pertinent meteorological measurements were also available for that day. Also, this day was part of the one month when the Special Hourly Inventory was carried out. Furthermore, for TDEV studies, it is desirable to perform the measurements under certain conducive meteorological conditions. The most important of these is to have well-behaved flow conditions with fairly steady and uniform winds in approximately the same direction during daylight. This minimizes mixing of different air parcels with fresh emissions other than the ones being targeted for TDEV study. It also facilitates a Lagrangian study of the target emissions for downwind transport and chemistry. Ordinarily, for TDEV, it is desirable to have high clouds (well above the daytime mixing layer) locally to minimize rapid chemical depletion of the target emissions, without complicating the chemistry with aqueous-phase reactions. However, the SOF measurements require direct sunlight for optimum application, so in this study, we performed the measurements on days with minimal cloudiness.

Among the most important *in situ* chemical data needed for this study were those of the Baylor Aztec and NOAA/AL WP-3 aircraft, which made continuous as well as batch-mode measurements of a variety of chemical species pertinent to TDEV close in to the HSC sources, as well as measurements farther out for the Lagrangian study of transport-chemistry in the HSC plumes. The most important remote sensing chemical measurements were those of the Chalmers University SOF (Solar Occultation Flux) ground mobile vehicle, which continuously measured vertically integrated speciated VOC measurements by on-line FTIR analysis of the IR absorption spectra of these species. The NOAA Twin Otter aircraft flying at about 10 000 ft made continuous remote-sensing down-looking LIDAR measurements of profiles of ozone and aerosol backscatter underneath (the aerosol data are particularly useful to infer spatial variation of the mixing height) during TexAQS II, but unfortunately, on 13 September 2000, it flew in the Dallas area. Other useful chemical measurements of speciated VOC, NO_x and ozone were made at about a dozen TCEQ ground monitoring sites in the Houston area (eight of these sites were in the vicinity of the HSC) equipped with the autoGC which made continuous measurements of relevant VOC, and at the Moody Tower site of University of Houston (UH) in downtown Houston, just to the west of the HSC, where a wide variety of relevant chemical measurements were made atop a building at about 70m height above ground. Ozone sonde measurements were made in Houston by Valparaiso University.

A variety of meteorological measurements were also made. TCEQ and NWS made profiler measurements of vertical profiles of meteorological variables at a number of sites in and

near the Houston area, and TCEQ also made SODAR measurements at two sites in the HSC area. In addition, UH made rawinsonde and tetheredsonde measurements at their campus in downtown Houston, as well as tower measurements near Texas City. Basic meteorological measurements were also made at the TCEQ surface monitoring sites and at the Moody Tower site. The SOF vehicle made occasional minisonde measurements of meteorological profiles from a site near Lynchburg Ferry in the HSC and at other sites near the other sources where it made SOF measurements. These data and their use will be described more fully in Section 7. NOAA launched a smart balloon on a few days during TexAQS II and tracked its path as a Lagrangian marker of designated air parcels. One of these was launched at LaPorte to the SE of the HSC on 13 September 2006, but that data could not be obtained in validated form after the study. GOES satellite data of cloud cover and high-resolution (30m) satellite data of land cover were obtained from NASA.

Data of the hindcast runs of the regional models MM5 and CMAQ were obtained from UH. Unfortunately, the needed data of the 12-km resolution domain could not be obtained until 27 August 2008, just before this contract ended. CB05 mechanism code was obtained from EPA and tables to convert the VOC speciated measurements into CB05 speciation were obtained from TCEQ. Using these and other code developed at UAH, the measured speciated data in the aircraft and at fixed sites were converted to the CB05 speciation. Table 6-1 summarizes the various datasets compiled from various sources and processed at UAH.

Section 7 will describe the meteorological data and their use in greater detail. In the rest of this section, we describe and present the data of the SOF and the two chemical aircraft (the Baylor Aztec and the NOAA-P3).

6.1 The SOF Data

This was probably the most important set of chemical measurements performed for TDEV during TexAQS II. While the *in situ* chemical measurements in the aircraft provide very useful 3D data of chemical species, many of them continuously, the aircraft data usually have two shortcomings: the continuous data do not *usually* include speciated VOC and the data are mostly discrete in the vertical. To obtain information related to emission rates, it is necessary to estimate mass flow rates (or often erroneously called fluxes) of the target species across vertical planes close to the target sources at upwind and downwind planes. This requires as detailed and complete coverage of all mass crossing these planes for the target emission species. The sparse canister data of VOC provide detailed speciation, but not the needed spatial coverage. The Aztec instrumentation included a continuous monitor called the “Reactive Alkene Detector (RAD)” which included an uncalibrated measurement of a number of alkenes at variable sensitivities, but no quantitative information about the concentrations of individual alkenes. The P-3 included a continuous monitor for ethene and a continuous PTR-MS (Proton Transfer Reaction Mass Spectrometer) which could, presumably, give propene concentrations, but the P-3 flew only a single crosswind horizontal traverse at each downwind distance and did not provide information about vertical distribution. The SOF measurement, in principle, provided continuous information about the crosswind distribution of the vertically-integrated concentrations of selected VOC species including ethene and propene, or a rather complete coverage of the mass crossing the

Table 6-1. 13 Sep 2006 TDEV Database Compiled at UAH --- OVERVIEW

<u>1.</u>	<u>Emissions</u>		<u>Source</u>
	Area source modeling emissions in CB05 at 2 and 12 km		TCEQ
	Point-source modeling emissions in CB05		TCEQ
<u>2.</u>	<u>MET</u>		
	TCEQ - Profilers (LaPorte, Arcola etc.)		TAMU
	- SODARs in the Houston area		TCEQ
	UH	- Radiosonde	UH
		- Tethersonde	UH
		- Moody Tower	UH
	SOF	- minisonde	Chalmers U.
	UH-CRC	- Tower data	UH
<u>3.</u>	<u>Fixed Chemical sites</u>		
	Surface monitoring (including auto-GC)		TCEQ
	Moody Tower (chemistry supersite)		UH
<u>4.</u>	<u>SOF</u>		Chalmers U.
<u>5.</u>	<u>Baylor Aztec aircraft</u>	Baylor (Canister VOC data received from UH)	
<u>6.</u>	<u>NOAA WP-3 aircraft</u>		NOAA-AL
<u>7.</u>	<u>NOAA-Smart Balloon</u>	8/30, 9/13/06	NOAA-(9/13 not available)
<u>8.</u>	<u>Ozonesonde</u>		Valparaiso U.
<u>9.</u>	<u>MM5, CMAQ</u>		UH (Final received on 8/27/08)
<u>10.</u>	<u>CB05 mechanism code</u>		EPA/CMAS
	CB05 conversion tables (measurements-to-CB05)		TCEQ
<u>11.</u>	<u>LS/LU data</u>		NCDAPT
<u>12.</u>	<u>GOES satellite data of cloud cover</u>		NASA

downwind vertical plane near the sources where the emissions crossed the plane. Thus for emissions estimation, the SOF data have both the right species and the best spatial coverage.

The SOF mobile ground vehicle deployed by a team from Chalmers University of Sweden (Mellqvist et al., 2007) made continuous speciated measurement of the vertically

integrated concentrations of selected VOC by the Solar Occultation Flux method (SOF), with on-line chemical (spectral) analysis using a Fourier Transform Infrared (FTIR) spectrometer. The SOF method is based on the recording of solar broadband infrared absorption spectra (1.8 – 14 μm) of IR-absorbing species (including ethene and propene). The device is mounted in a mobile vehicle with a sun tracker. The vehicle travels on roads upwind and downwind of the target sources. Since it measures vertically integrated species concentrations, SOF measurements along roads oriented crosswind and close downwind of the target source(s) can provide the total flux of the emissions across the vertical measurement plane by integrating the data in the crosswind direction, and with appropriate wind-weighting. This flux, after subtraction of the upwind inflow based on upwind measurements, is considered as an estimate of the emissions from the target source(s). The uncertainty of the concentration measurement itself is small, but larger uncertainties result from any depletion of the measured species between emission and sampling (small if the downwind distance from the source is small), and due to error in applying wind-weighting (the largest source of error). The SOF vehicle included a GPS sonde to make local measurements of the wind profile periodically. Uncertainty in estimating the emission flux from the concentration data has been estimated at about 35%. The VOC data analysis was focused on ethene (measurement accuracy, $\epsilon \sim 3\%$), propene ($\epsilon < 25\%$, mainly due to interference of 1-butene), and total alkanes (because of interferences of the spectra of the different alkanes, a composite estimate of the alkanes class is made that is accurate to $\epsilon \sim 7\%$). Besides the SOF instrument, the SOF vehicle also deployed a mobile DOAS (Differential Optical Absorption Spectrometer), which utilizes absorption of scattered light in the UV/visible region to measure NO_2 and SO_2 .

The SOF made measurements around the HSC on ten days, with an additional 2 days around Texas City, 2 days around Sweeny, and one day around Chocolate Bayou and Freeport. On a given day, multiple measurements of the emissions from the target source were made by driving along a local SOF Box enclosing the target source(s) repeatedly. The measurements were made upwind and downwind of the source(s) in order to estimate contribution of the target emissions. The downwind measurements were typically made about 0.5 to 3 km from the source, but in some cases, they were farther downwind. Since the HSC is a large complex of sources, it was divided into eight sectors (see Figure 6.1), and the analyses provided composite emissions from individual sectors. SOF Boxes around the Mt. Belvieu complex (sector 8) and the Channelview complex (north of sector 3) were also traversed, but not on September 13. The measurements were made from August 30 through the month of September, 2006.

As a composite of multiple days of data, the SOF and DOAS results gave the hourly emissions from HSC (sectors 1 – 8 + Channelview) to be ~ 1.4 metric ton (mT) for ethene, ~ 2.2 mT for propene, ~ 15 mT for alkanes, and about 6 mT for SO_2 and NO_2 (Mellqvist et al., 2007). For ethene and propene, these are about 1-2 orders of magnitude greater than the 2004 EI (~ 6 -18 times for ethene, 15-87 times for propene), and for SO_2 and NO_2 , they are generally within a factor of 2. For the smaller complexes (TC, CB, FP, Sw), the corresponding VOC emissions were also estimated to be qualitatively similar in terms of under-estimation in the EI (12-41 times for ethene and 11-32 times for propene). The SOF data analysis by Mellqvist et al. (2007) also indicated that OH-reactivity of propene is generally greater than that of ethene in the fresh plumes from these sources. In the multiple downwind traverses from the sources, ethene and propene were found by the SOF to exhibit high variability, especially propene, and a significant

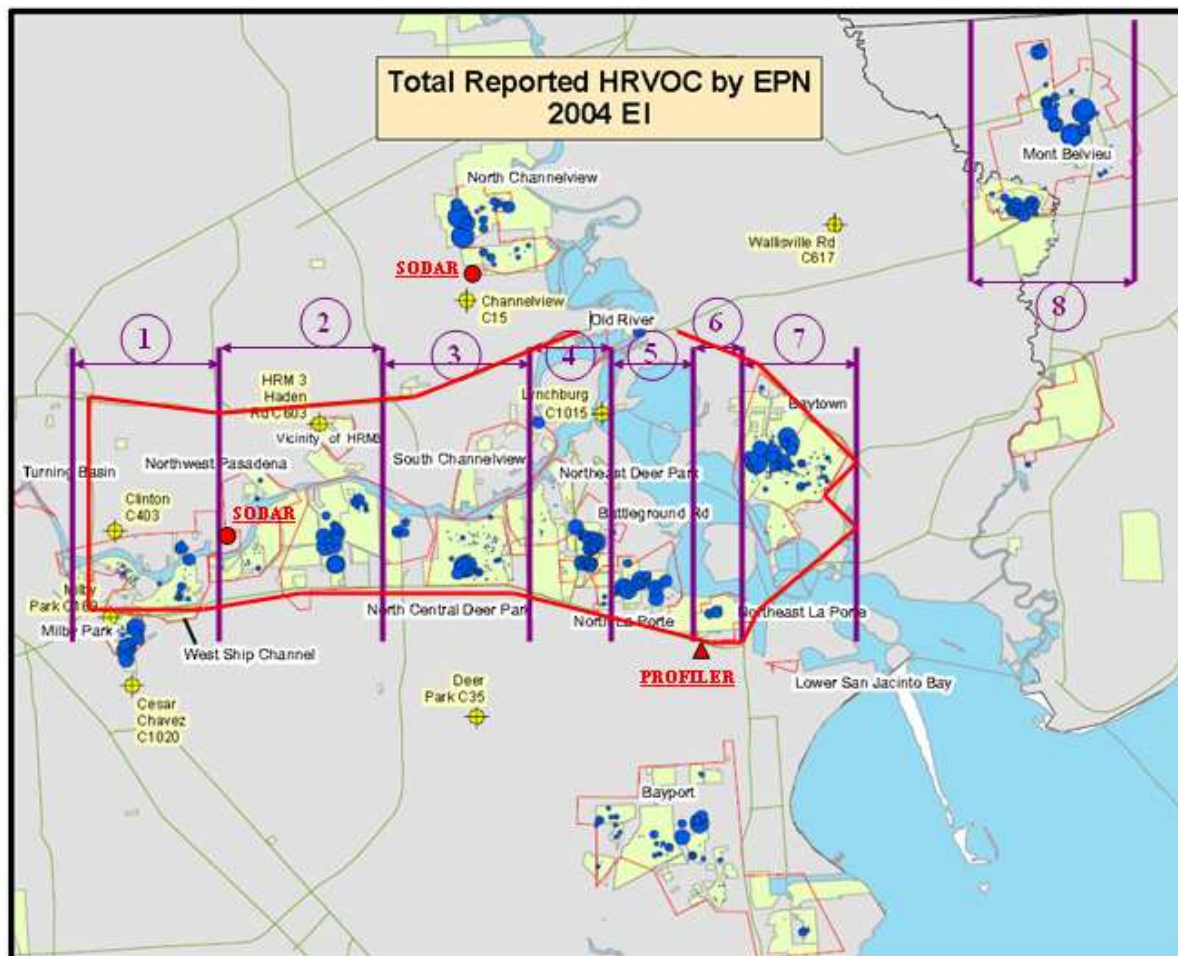


Figure 6.1 The Houston Ship Channel showing the eight SOF sectors in which the emissions were divided for analysis. Also shown is the path or “HSC SOF Box” travelled by the SOF vehicle on 13 September 2006 (red track of existing roads) for sampling emissions from sectors 1 through 7. Sector 8 in the NE of the figure bounds the Mt. Belvieu source complex, which was not sampled by the SOF on 13 September. To the north of sector 3 is the N. Channelview source complex, and to the south of sectors 5-7 is the Bayport source complex. Also shown are the locations of the LaPorte profiler (just south of sector 6) and the two sodars (Channelview, north of sector 3, and Waterworks near the western edge of sector 2 --- these provided wind data in addition to the GPS sonde launched by the SOF periodically near Lynchburg Ferry in the northern part of sector 4.

portion seemed to originate from upset releases or frequent flaring. VOC emissions from storage tanks are more dependent on evaporation, hence local meteorology. The SOF analysis by Mellqvist et al. (2007) also provides results for ethene and propene emissions from the various sectors on 13 September 2006.

On 13 September 2006, the mission plan had called for the SOF to perform measurements around the HSC SOF Box in the morning and around the TC SOF Box in the afternoon. However, due to some instrumentation problems, the morning measurements could not be performed, and measurements were made around the HSC SOF Box in the afternoon and no measurements at TC at all. Also the afternoon mission at HSC was shorter than usual, lasting only two hours, from about 1445 to 1645. In that time, there was time to go around the SOF Box only once. Table 6-2 and Figure 6.2 provide the Mission Log and Mission Activity Map for the

Table 6-2 SOF Mission Log, 13 Sep 2006
(1440 – 1645 to go around the SOF Box once)

1440 – 1455	A – B	1440-1443 on Hwy 330		
<u>Downwind Traverse</u>		1443-1455 on Hwy 201/146 south of	Sector 7	
1455 – 1547	B – C	Hwy 225	1455 – 1459 =	Sector 6
			1459 – 1503 =	Sector 5
			1503 – 1511 =	Sector 4
			1511 – 1522 =	Sector 3
			1522 – 1537 =	Sector 2
			1537 – 1547 =	Sector 1
1547 – 1607	C – D	I-610 Ferry from downwind to upwind.		
<u>Upwind Traverse</u>				
1607 – 1633	D – E	I-10 (1621-1628 ~ S. of N. Channelview complex)		
1533 – 1645	E – A	Hwy 330		

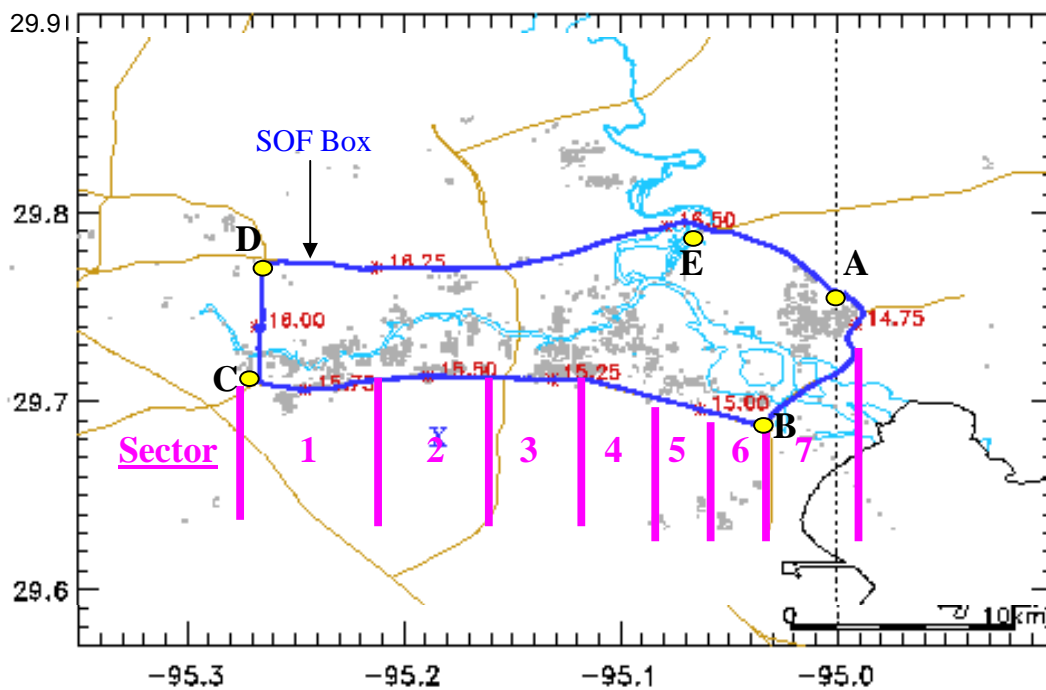


Figure 6.2 Mission activity map of the SOF on 13 September 2006, showing the seven SOF emission sectors, the HSC SOF Box (blue), and the five locations (A, B, C, D, E) along the SOF path. The Mission Log in Table above gives the times when the SOF passed each of these locations. Also shown along the SOF path are decimal times at 15-minute intervals (e.g., 14.75 near A denotes 14:45 pm). Finally, VOC sources are shown as grey dots.

SOF mission of 13 September 2006. The Map identifies locations A, B, C, D, E around the Box where the SOF passed at times given in the Mission Log. From about 1443 to 1547, the SOF made measurements downwind of the SOF Box (1443 to 1455 south of sector 7, then from 1455

to 1547, it passed south of sectors 6, 5, ... 1). It made the upwind measurements between D and A from 1607 to 1645. The map also shows the VOC sources as grey dots.

Figure 6.3 presents the ethene and propene vertically-integrated concentration data (in units of mg/m^2) of the SOF on 13 September 2006, as received from Chalmers University. Missing data are either missing or negative and not plotted. These data constitute the best information available for TDEV of ethene and propene emissions from the HSC on 13 Sep 2006. The data cannot be interpreted visually as estimates of emissions from the different sectors because of different downwind distances from the sources, which affects the intensity of the local concentration of the emitted species. Also, the wind direction has important effect on this.

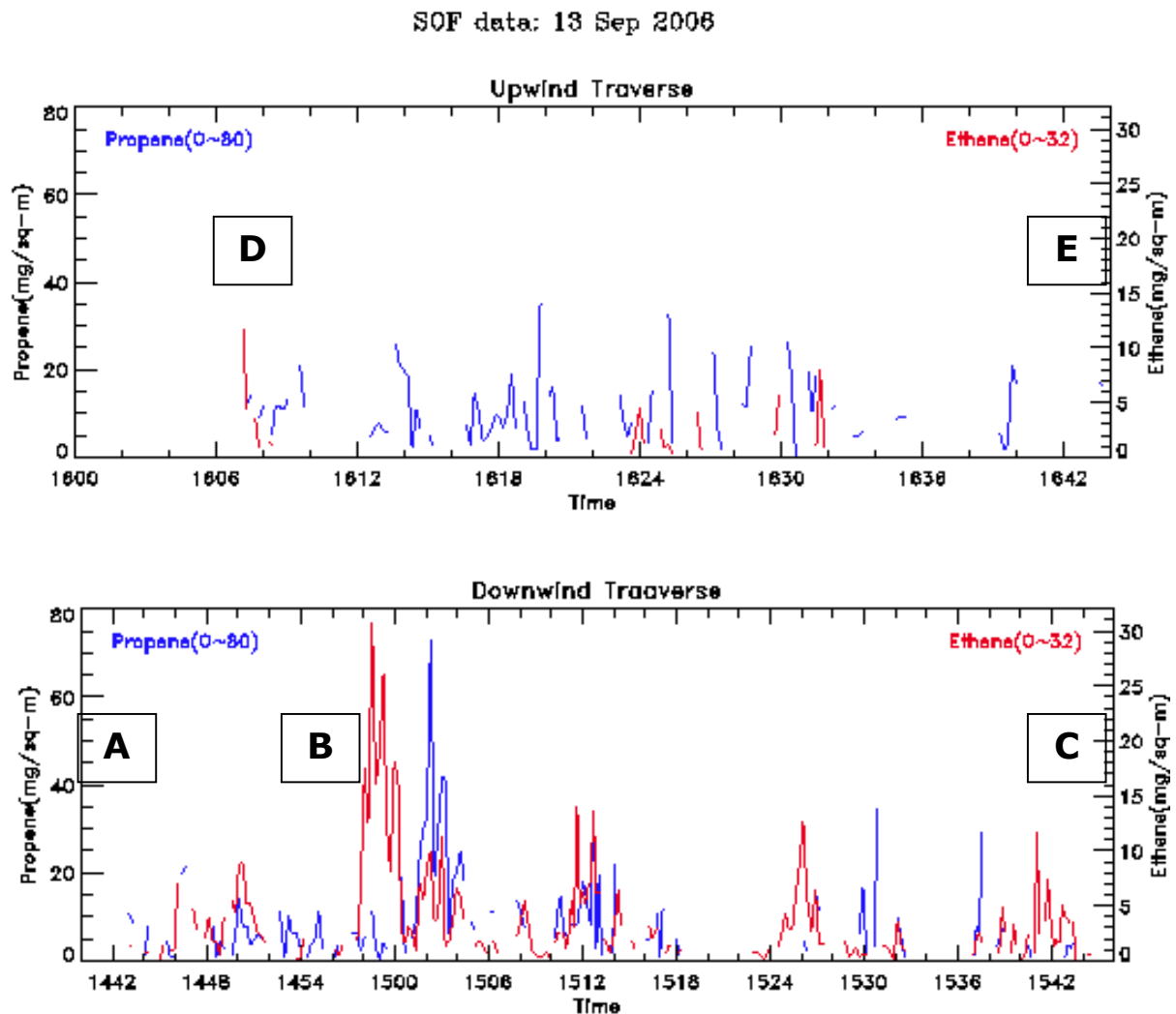


Figure 6.3 Vertically-integrated concentration data of ethene (red) and propene (blue) for the SOF mission of 13 September 2006. Also shown are the approximate times when the SOF passed the points A, B, C, D, E along the SOF path. The upper plot is for the upwind leg between D and E, and the lower plot is for the downwind leg from A to B to C.

6.2 The Aztec Data

The Aztec made continuous measurements of the following variables: O₃, NO, NO₂, NO_y, SO₂, CO, reactive alkenes (RAD), HCHO, Bscat (at 3 wavelengths), jNO₂, altitude (ALT), latitude (LAT) and longitude (LON), wind speed (WS) and direction (WD), temperature (T) and relative humidity (RH). Validated data were received from Baylor at 5s intervals. Detailed description of the measurements and validation procedures is given in Alvarez et al. (2007).

The Aztec made two flights on 13 September 2006: one in the morning from ~0747 to 1234, and the other in the afternoon from ~1446 to ~1800, after which the aircraft went on to Waco Tx. Table 6-3 and Table 6.4 present the Flight Logs of the two flights, and **Figure 6.4** and **Figure 6.5** present the corresponding Flight Maps. In the morning, the aircraft took off from EFD (Ellington Field) at ~0747, went to A to the NE of the SOF Box, made a spiral (S1), then made two long upwind traverses between B and D over plane X_{U1}, then made upwind (X_{U2}) and downwind (X_{D1}) traverses over the HSC SOF Box, with as many as five downwind traverses at X_{D1}, between about 500 and 1200 feet MSL. This should provide excellent vertical support for the SOF data. After that, it performed two long traverses at X_{D2} between Galveston Bay and west of Houston, and finally made a second up/down spiral near E before landing at 1234.

In the afternoon, the take off was at ~1446, with a ferry to the NE of the SOF Box, followed by an upwind traverse of the Box and three traverses on the downwind side (X_{D1}) between 500-1500 ft MSL. After that the aircraft made traverses at five more downwind distances (X_{D2}, X_{D3}, X_{D4}, X_{D5}, X_{D6}), providing excellent coverage for a Lagrangian transport-chemistry study over a transport range of about 70 km.

Table 6-3 and Table 6.4 present the Flight Logs of the morning and afternoon flights of the Aztec, providing detailed information about all measurement activities (traverses, spirals, etc), their times, and elevations. **Figure 6.4** and **Figure 6.5** present the corresponding Flight Maps of the morning and afternoon missions, showing, in detail, the whole flight path of each flight, with breakdown of each individual event such as traverse or spiral with clear identification of the end points of each event. The combination of each flight map and its corresponding flight log provides the detailed information about the time and location and sequence of all flight events. Each traverse and spiral is clearly identified by the sampling plane in which it occurs, its location and time, etc. Thus pinpointed, it is then meaningful to present the data of the corresponding time-series (for the traverses) or vertical profile plots (for the spirals) for each event for all variables of interest. Before presenting the time series data, we present the color-coded data of NO_y and RAD concentrations along the morning flight track in **Figure 6.6** and of ozone and formaldehyde in **Figure 6.7**. **Figure 6.8** and **Figure 6.9** present similar data of NO_y, RAD, ozone and formaldehyde along the flight track of the afternoon flight. Finally, in **Figure 6.10** through **Figure 6.25**, we present the time-series data of pertinent variables for each traverse, and the vertical profiles of the pertinent variables for each spiral, for the morning flight of the Aztec. In these plots, the times of the canister samples are identified by a heavy trace on the time axis for the duration of the sample. Also, in the plots of the traverses at X_{D1}, the plane along the downwind boundary of the SOF Box, the SOF emission sectors are also delineated. Thus, these plots comprise a data volume of the morning flight of the Aztec. **Figure 6.26** through **Figure 6.39**

present similar time series (traverses) and vertical profile plots (spirals) for the afternoon flight of the Aztec. In all the plots, missing data values of variables indicate either that the data were actually missing in the datafiles received from Baylor OR that the data were negative. We repeat, negative data have not been plotted. We wish to point out especially that a considerable amount of the RAD data were missing from the file received for the afternoon flight.

6.3 The NOAA-WP3 Data

The P-3 made an elaborate set of gas and aerosol measurements. These included continuous measurements of ethene using a laser photoacoustic spectrometer (LPAS), of a number of VOC species (other than ethene and alkanes of C<5) using the PTR-MS (Proton Transfer Reaction Mass Spectrometer), as well as formaldehyde and nitric acid. The formaldehyde measurements were made at three resolutions: 1s, 10s and 1 min. The P3 data are available to qualified users from the NOAA-ESRL website <http://www.esrl.noaa.gov/csd/tropchem/2006TexAQS/P3/index.html>, which also provides description of the platform and the instrumentation. Here, we present selected data of the P-3 for the key traverses. Table 6-5 (on p.89) presents the Flight Log for the P-3 for 13 September 2006, and Figure 6.40 (on p.90) presents the Flight Map of the P-3 flight trajectory. The P-3 took off at ~1146, made upwind-downwind measurements of the HSC and Houston downtown plumes until 1345, and then went on to Dallas for a DFW mission, and returned to the Houston area around 1730 for a 1745 landing at EFD.

In its early afternoon flight in Houston, the P-3 took off from EFD (~1146), then climbed to 3350m on a flight downwind to point A over Galveston Bay, before returning to location B upwind of HSC as it also climbed down to ~650m. Thereafter, it made an upwind traverse (AB), followed by downwind traverses DE and FG, mostly at heights of 650m and 800m, and a downwind traverse HI in which it flew in a vertical zigzag pattern between 200 and 2500m. It then flew north from I to J to K before flying off to Dallas.

Figure 6.41 presents plots of NO_y and ethylene along the flight track, and Figure 6.42 presents the same for ozone and formaldehyde at 1s resolution. Figure 6.43 through Figure 6.54 present time series data of the P-3 for the main events of the P3 flight, as follows: ferry EFD-A, ferry A-B, traverses B-C, DE, FG, HI. The traverses are all plotted from west to east; for each traverse, one plot is presented for the whole traverse, and a second plot is presented for just the segment of the plot on the east side which is for the data of the HSC plume (the west side of the plot is for the data of the downtown plume).

An important observation is that the ethylene data are missing for the most important part of the whole flight for this project --- the part of the downwind traverse just south of the HSC (D' – E; see Figs. 6.41, 6.47 and 6.48). The ethylene data of this part are the most critical for the TDEV study. The ethylene data are also missing for the part of the ferry from J – K when the aircraft was just downwind of the Texas City emission. The formaldehyde data at the 1s and 10s resolutions are quite similar, and hopefully reasonably accurate, but these are different from the data at 1min resolution.

Table 6-3 Flight Log of Flight 1 (a.m.)

Baylor Aztec, 13 Sep 2006

~0747	Take-off, EFD	
0747 - 0756	Ferry EFD – A	
075830 – 082330	Spiral S1 up near A	(~ 500' – 6000' msl)
0824 - 0832	Spiral S1 down near A	(~ 6000'–2500' msl)
0832 – 0837	A – B Upwind ferry/ traverse	(~ 2500' msl)
083730 – 0850 – 0909	B –C – D (X _{U1}): Long traverse (E to W) upwind of HSC and downtown	(~750-950' msl, except
(083915 – 0844)	Descent below bottom of down-spiral S1 partway between B and C	(~2500' – 850' msl)
0911 – 093930 msl)	D – A (X _{U1}): Long traverse (W to E)	(~950 – 1450'
093930 – 0943	Ferry, A – E	
094330 – 0953	E – F (X _{D1}): Traverse 1 on downwind side of SOF Box	(~ 500- 600' msl)
0953 – 0955	F – G, Ferry to upwind	
0956 – 100430	G – H (X _{U2}): Traverse on upwind side of SOF Box	(~ 500- 600' msl)
1006 – 1015	E – F (X _{D1}): Traverse 2 on downwind side of SOF Box	(~ 450- 650' msl)
101630 – 1026	F – E (X _{D1}): Traverse 3 on downwind side of SOF Box	(~ 650- 850' msl)
102630 – 1036	E – F (X _{D1}): Traverse 4 on downwind side of SOF Box	(~ 900-1000' msl)
103745 – 104545	F – E (X _{D1}): Traverse 5 on downwind side of SOF Box	(~1100-1200' msl)
104711 – 111645	I – J (X _{D2}): Traverse 1 (E-W) downwind of SOF Box	(~1050-1150' msl)
111940 – 115345	J – I (X _{D2}): Traverse 2 (W-E) downwind of SOF Box	(~1550-1650' msl)
1157 – 1208	Spiral up near I	(~1500' – 5800' msl)
1210 - 1226	Spiral down near I	(~5800' – 400' msl)
1226 – 1234	Ferry back to EFD and land	

Table 6-4 Flight Log of Flight 2 (p.m.)

Baylor Aztec, 13 Sep 2006

~1446 1446-1450-1455	Take-off, EFD Ferry EFD – A– A'	
1455-1459 – 1508 1508 – 1511	Upwind traverse (X_U), A'–B– C Ferry C – D	(~ 1000' msl)
1511 – 1520 1520 – 152930 1530 – 1539	D – A (X_{D1}): Traverse downwind of HSC A – D (X_{D1}): Traverse downwind of HSC D – A (X_{D1}): Traverse downwind of HSC	(~ 500' msl) (~1000' msl) (~1500' msl)
1542 – 1552 1553 – 160445	E' – F (X_{D2}): Traverse F – E (X_{D2}): Traverse	(~1500' msl) (~1500' msl)
1604 – 1617 1617 – 1625 1625 – 1628	Spiral S3 up at E Spiral S3 down at E E – G, Ferry	(~1500-5500' msl) (~5500-1500' msl)
162824 – 1639	G – H (X_{D3}): Traverse	(~1500' msl)
1639 – 1642	H – I, Ferry	
1642 – 165645	I – J (X_{D4}): Traverse	(~1500' msl)
165645 – 1700	J – K, Ferry	
1700 – 1714	K – L (X_{D5}): Traverse	(~1500' msl)
1715 – 1718	L – M, Ferry	
1718 – 1737	M – N (X_{D6}): Traverse	(~1500' msl)
1737 – 1745 – 1800 –	Ferry, N – O– P – on to Waco	

AZTEC: 13 Sep 2006, Flight 1 (a.m.)

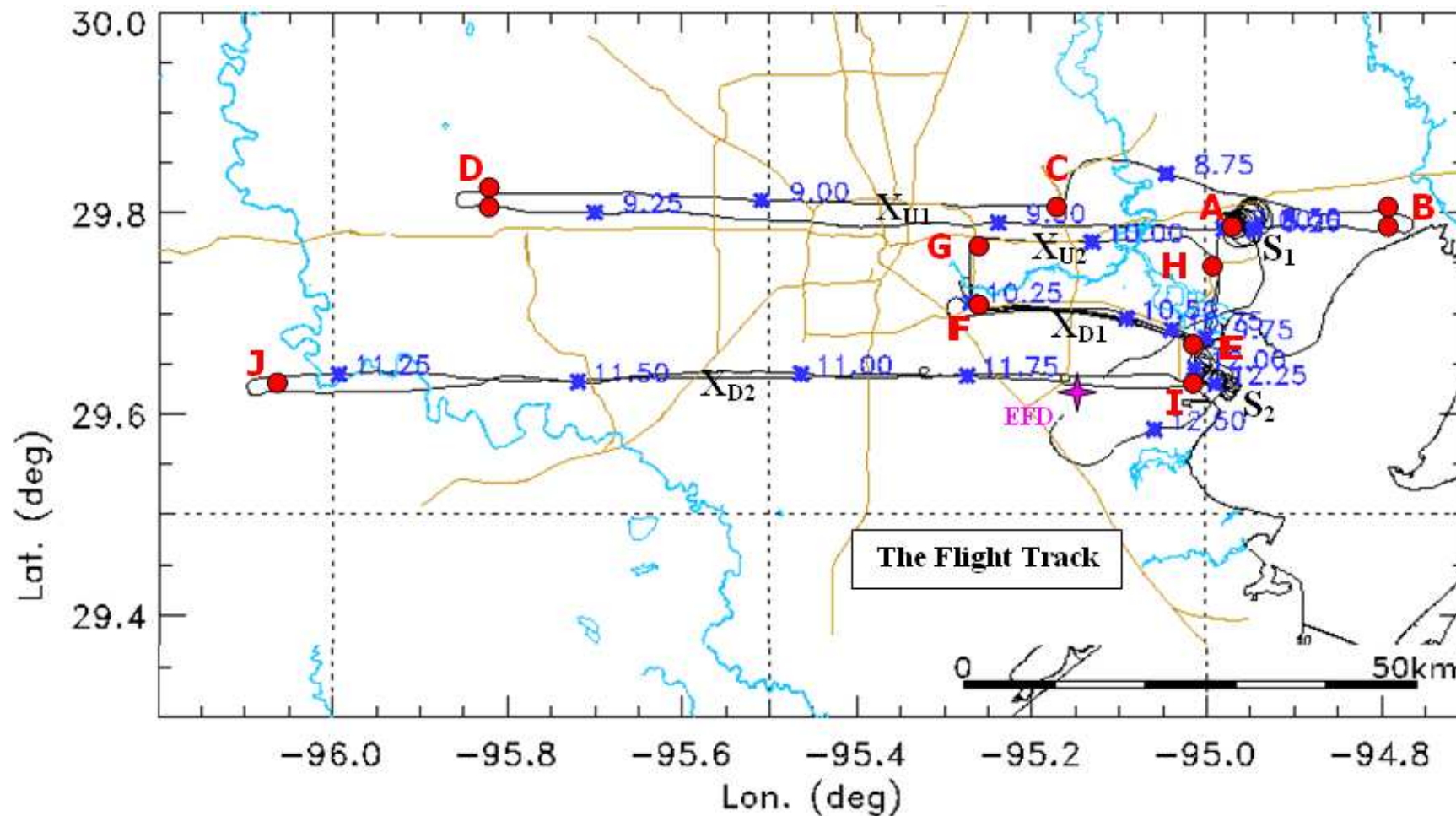


Figure 6.4 Flight map for the a.m. flight of the Aztec. The map shows end points of critical events (e.g., traverses) as letters (red); spirals are marked as S1, S2...(green); the base airport (EFD = Ellington Field); identifiers of sampled planes upwind (X_{U1} , ...) or downwind of HSC (X_{D1} , X_{D2} , ...); and, decimal times along the flight path (blue)

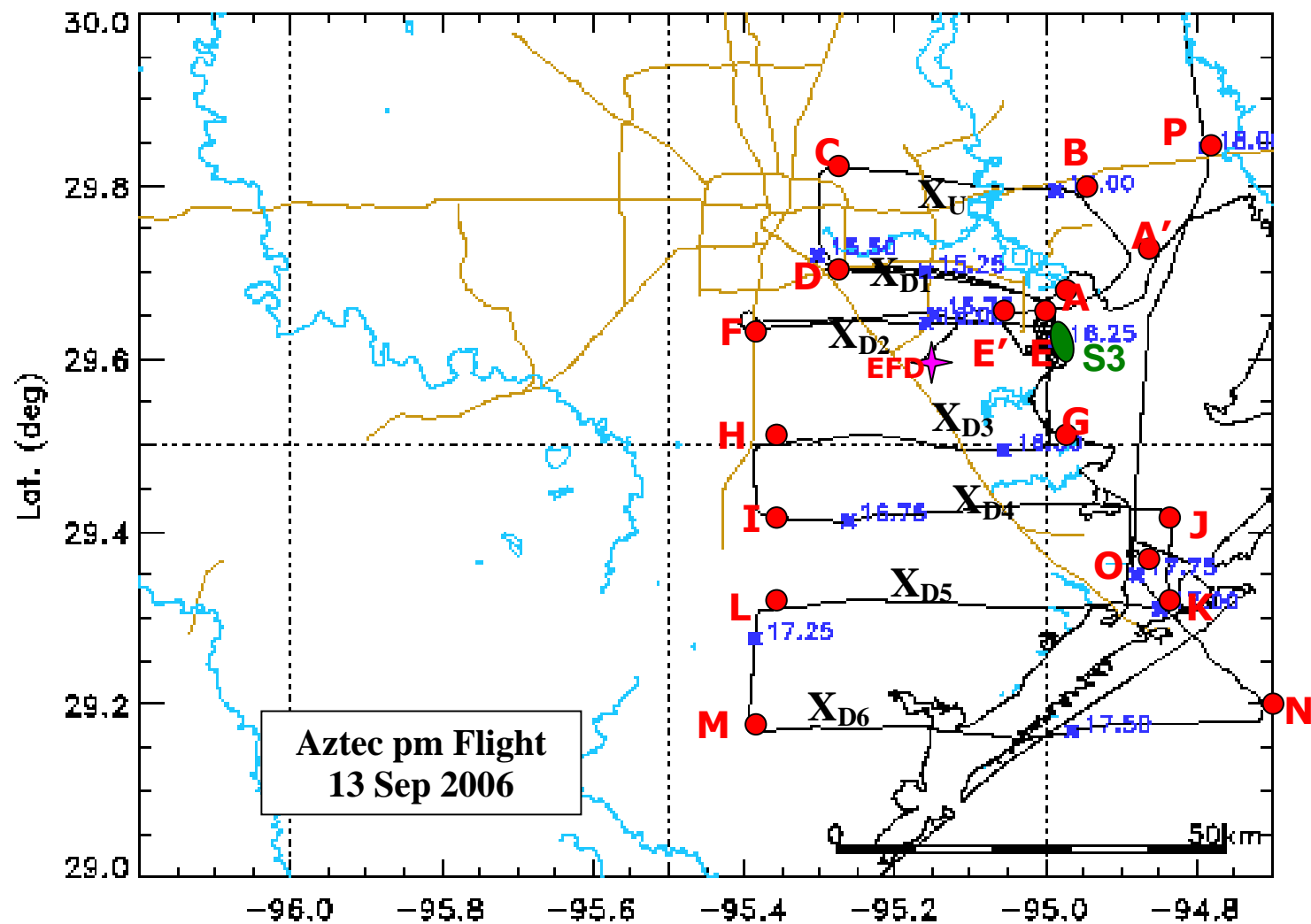


Figure 6.5 Flight map for the p.m. flight of the Aztec. The map shows end points of critical events (e.g., traverses) as letters (red); spirals are marked as S3 (green); the base airport (EFD = Ellington Field); identifiers of sampled planes upwind (X_{U1} , ...) or downwind of HSC (X_{D1} , X_{D2} , ...); and, decimal times along the flight path (blue) .

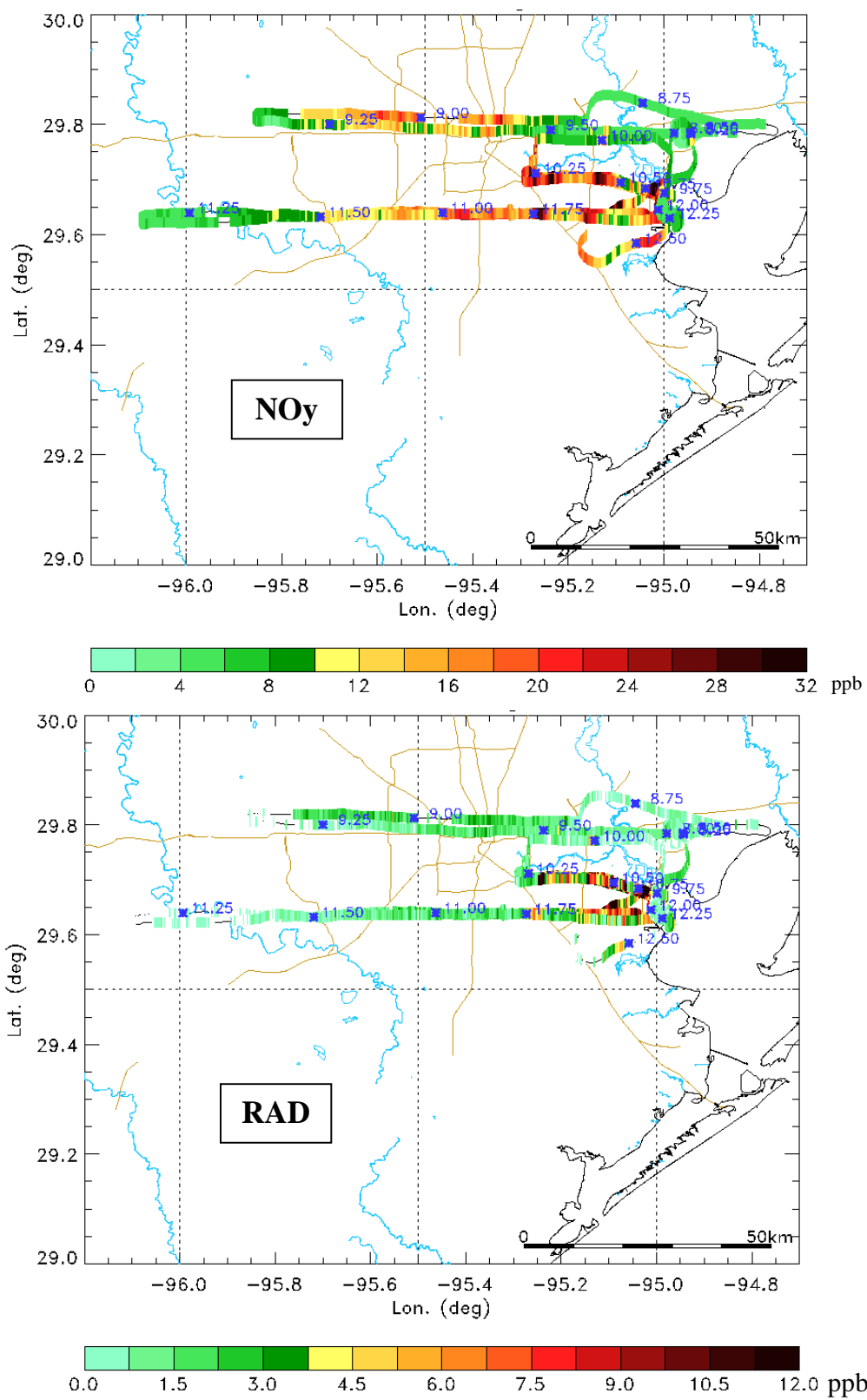


Figure 6.6 Map of NOy (upper plot) and RAD (lower plot) concentrations plotted along the Aztec flight track in the morning flight of 13 September 2006

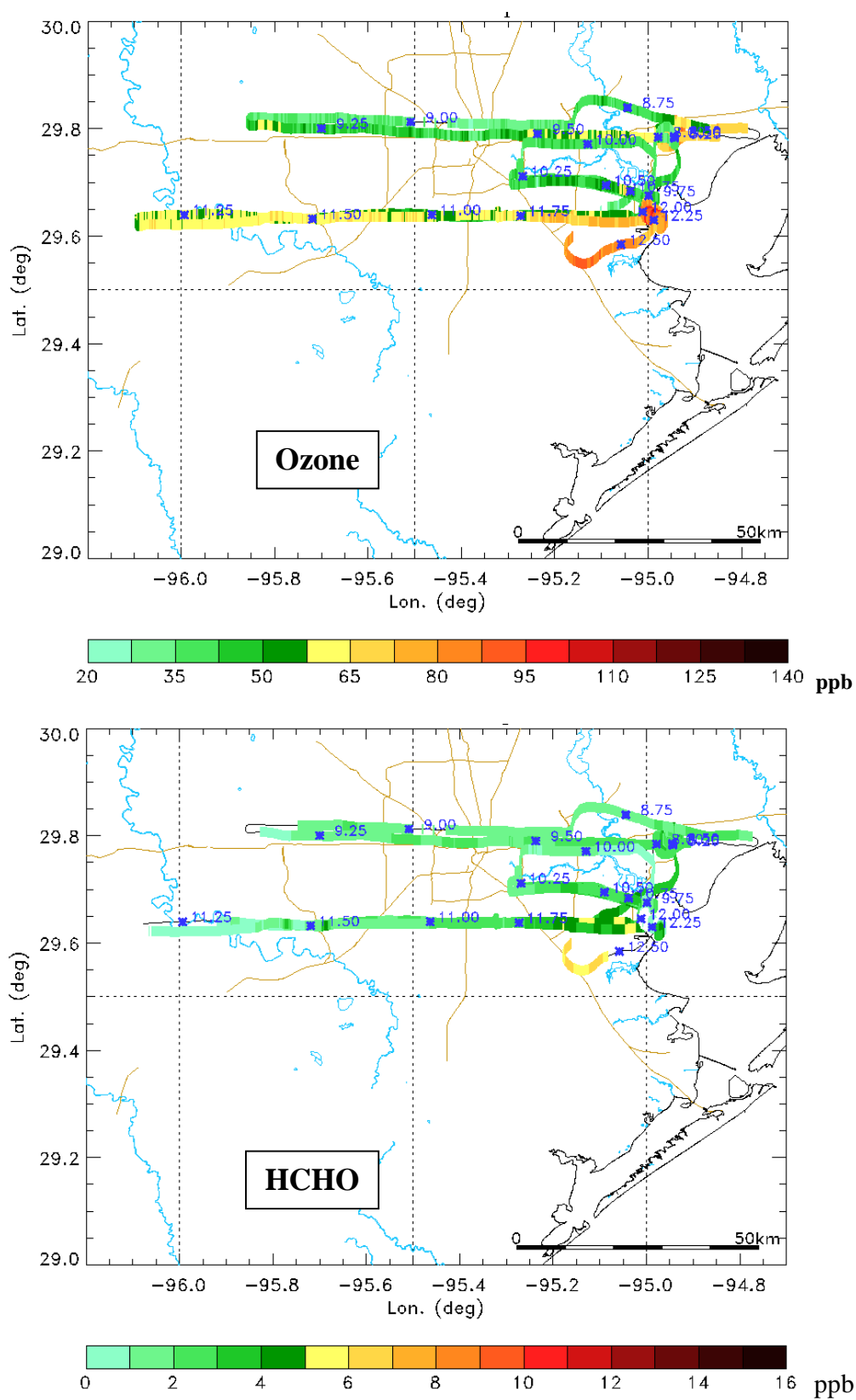


Figure 6.7 Map of ozone (upper plot) and formaldehyde (lower plot) concentrations plotted along the Aztec flight track in the morning flight of 13 September 2006

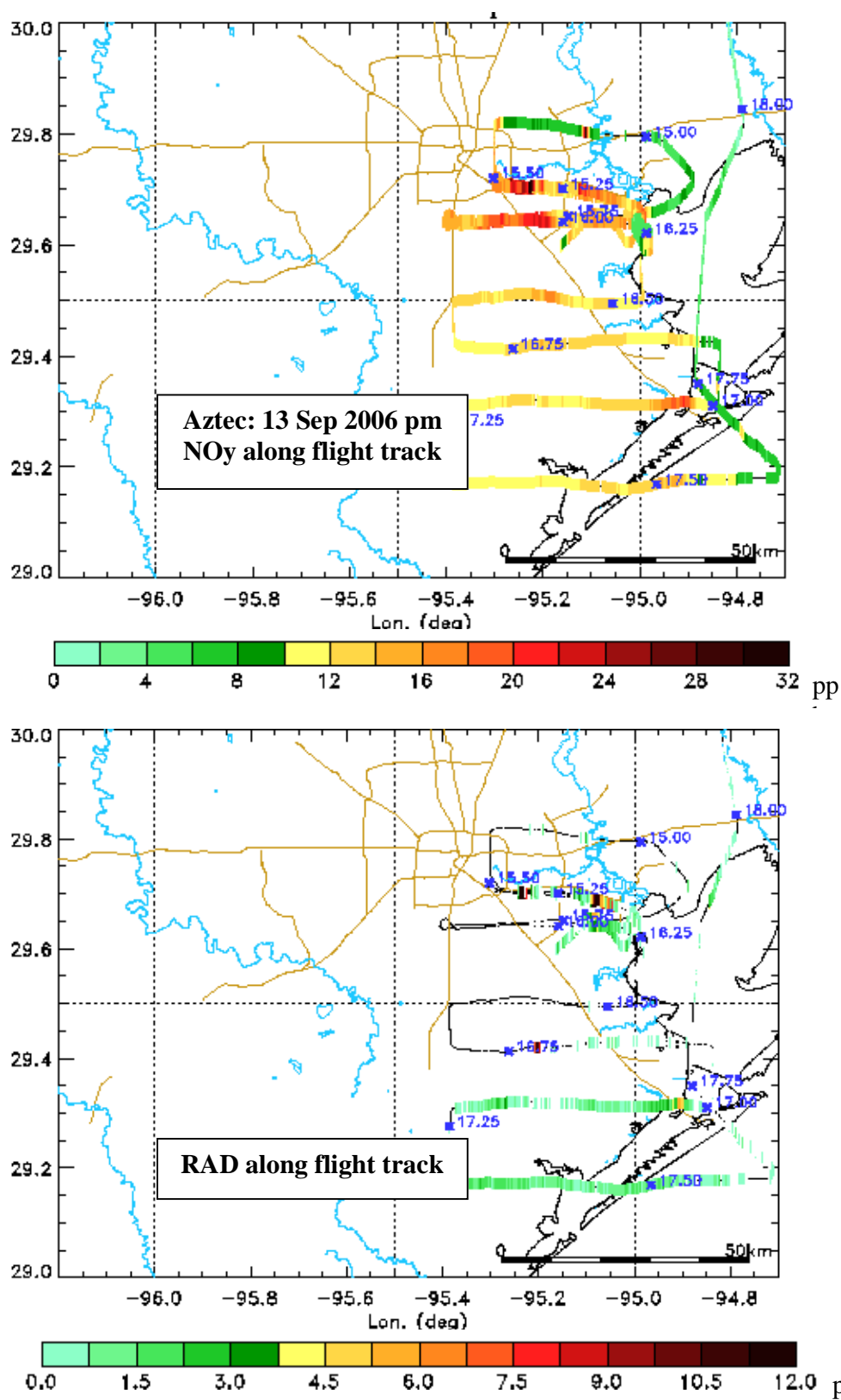


Figure 6.8 Map of NOy (upper plot) and RAD (lower plot) concentrations plotted along the Aztec flight track in the afternoon flight of 13 September 2006

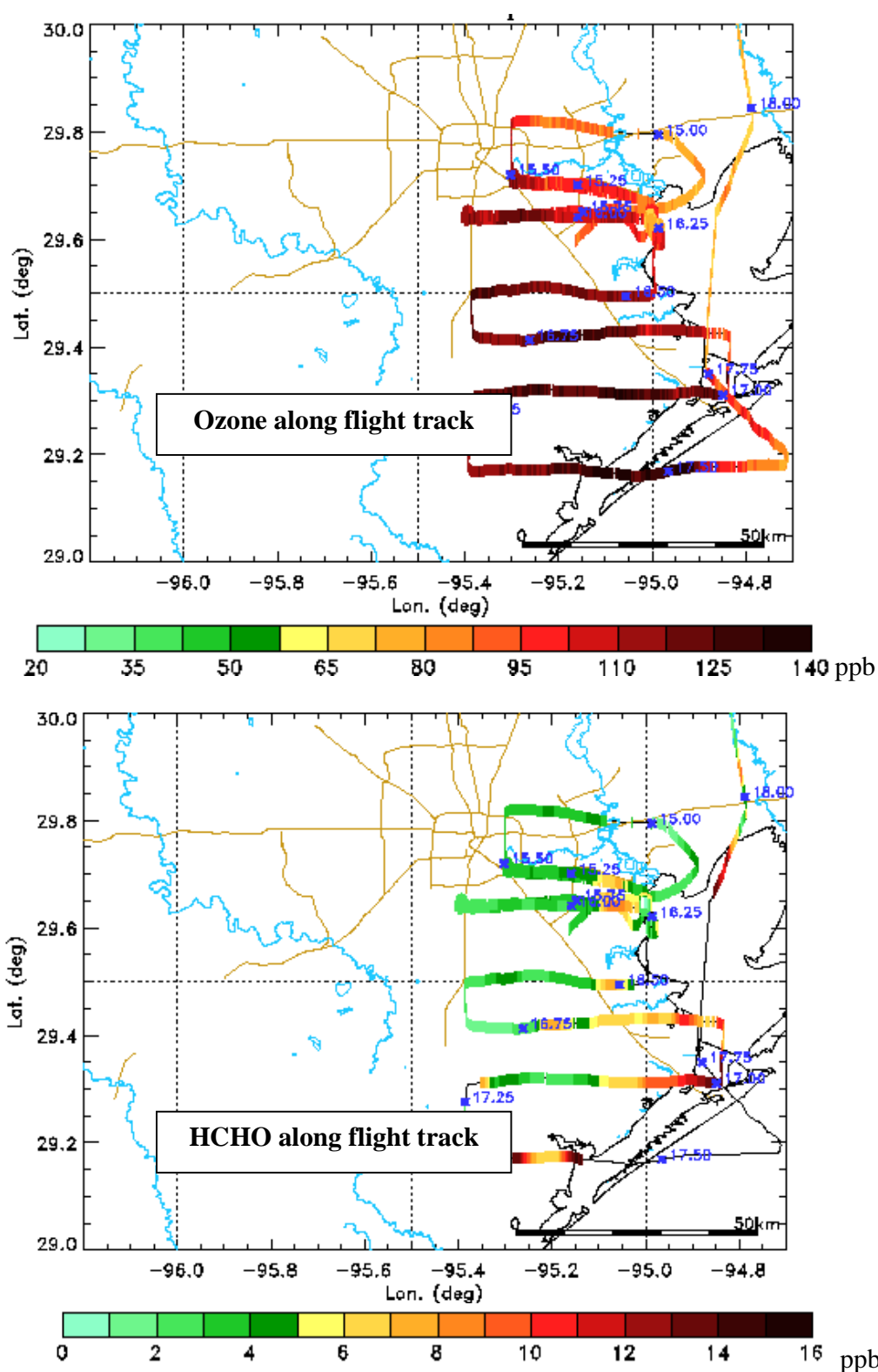


Figure 6.9 Map of ozone (upper plot) and formaldehyde (lower plot) concentrations plotted along the Aztec flight track in the afternoon flight of 13 September 2006

BAYLOR – AZTEC data: 13 Sep 2006 (a.m)

Upward Spiral S1:075830–082330

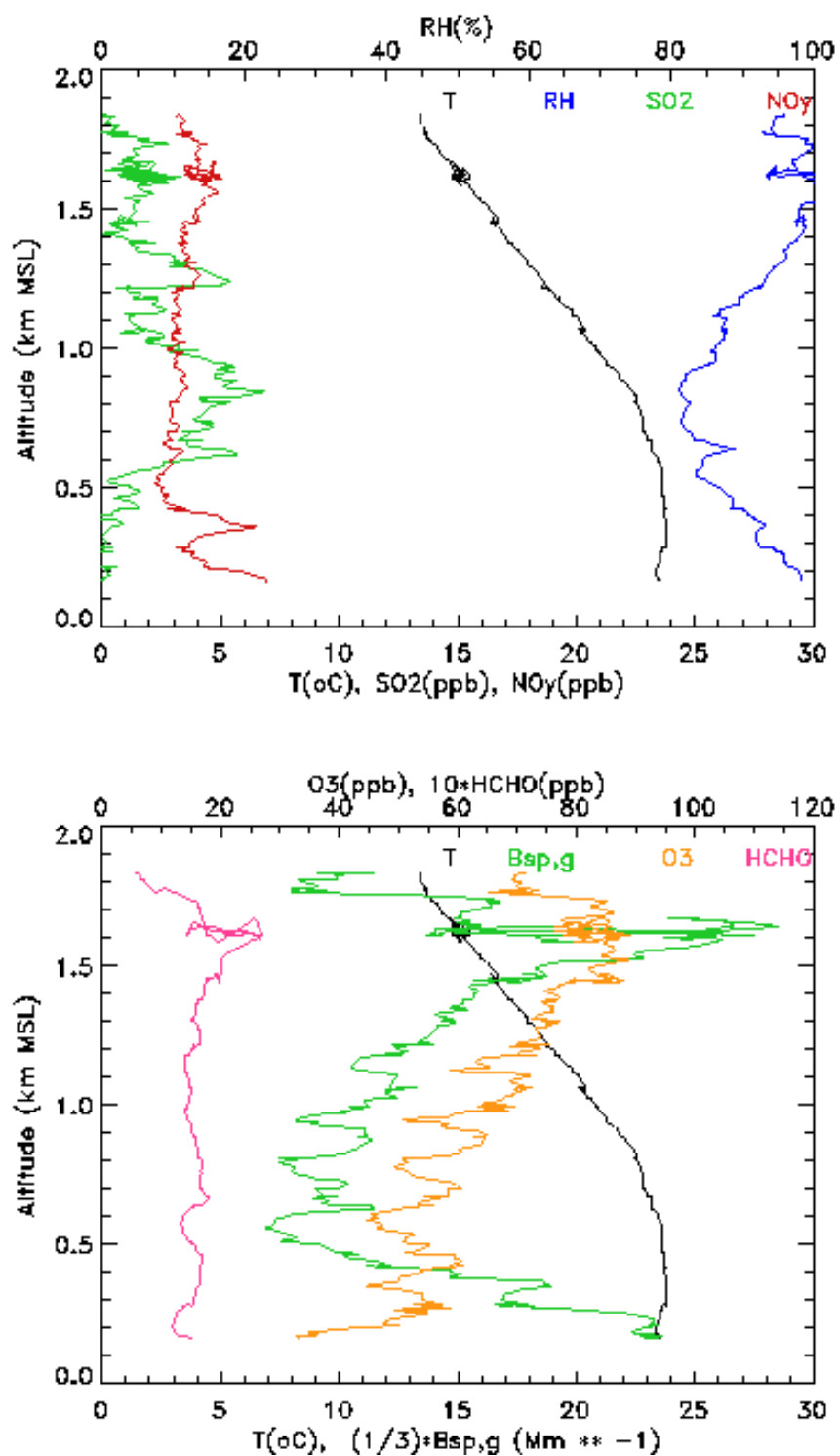


Figure 6.10 Data of Aztec up-spiral S1 near location A in the morning flight, showing the data for T (black trace), RH (blue), NOy (red) and SO2 (green) in the upper plot and of T (black), O3 (orange), HCHO (pink) and Bsp,green wavelength (green) in the lower plot.

BAYLOR – AZTEC data: 13 Sep 2006 (a.m)

Downward Spiral S1:082400–083200

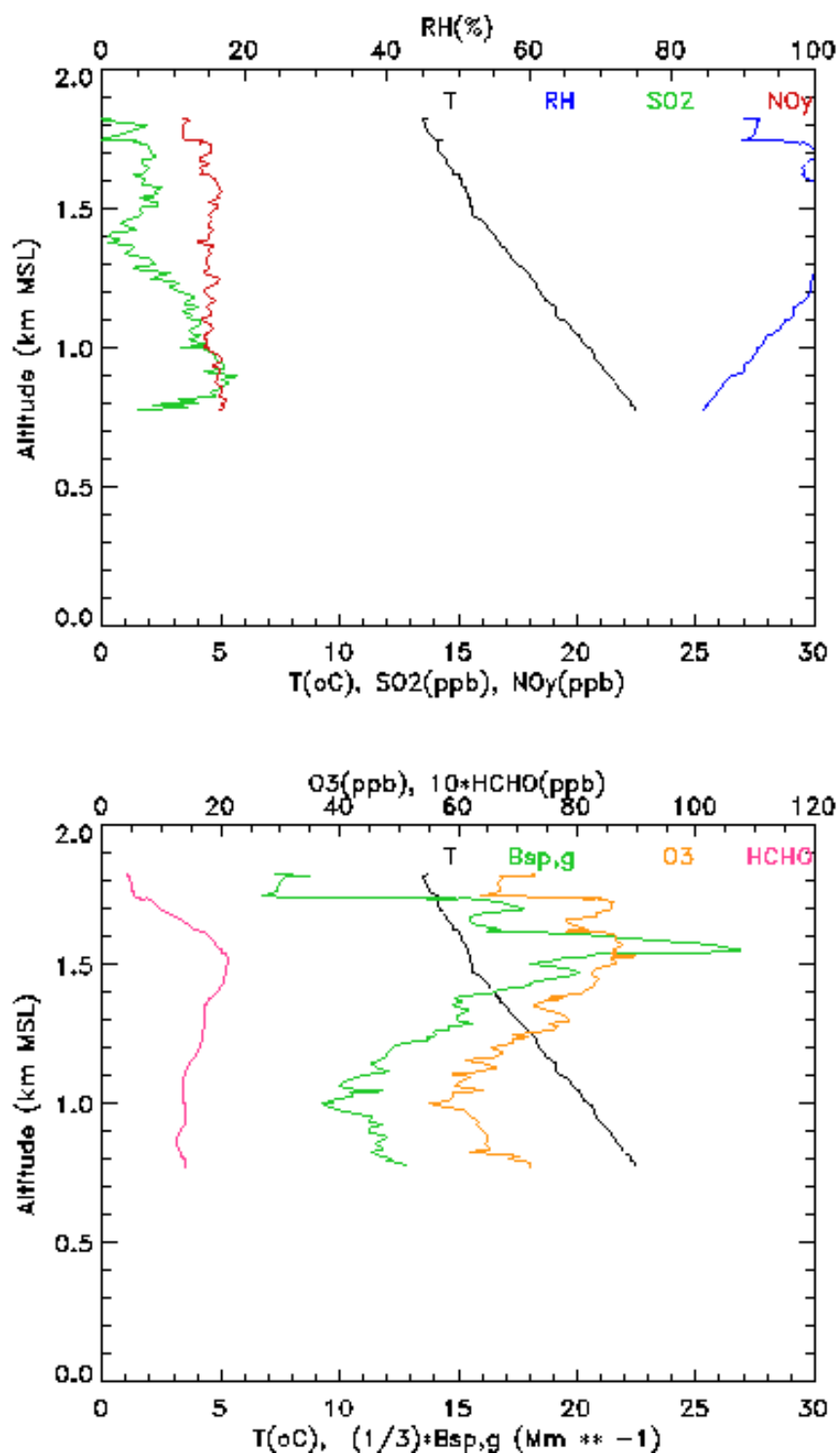


Figure 6.11 Data of Aztec down-spiral S1 in the morning flight, showing the data for T (black trace), RH (blue), NOy (red) and SO2 (green) in the upper plot and of T (black), O3 (orange), HCHO (pink) and Bsp.green wavelength (green) in the lower plot.

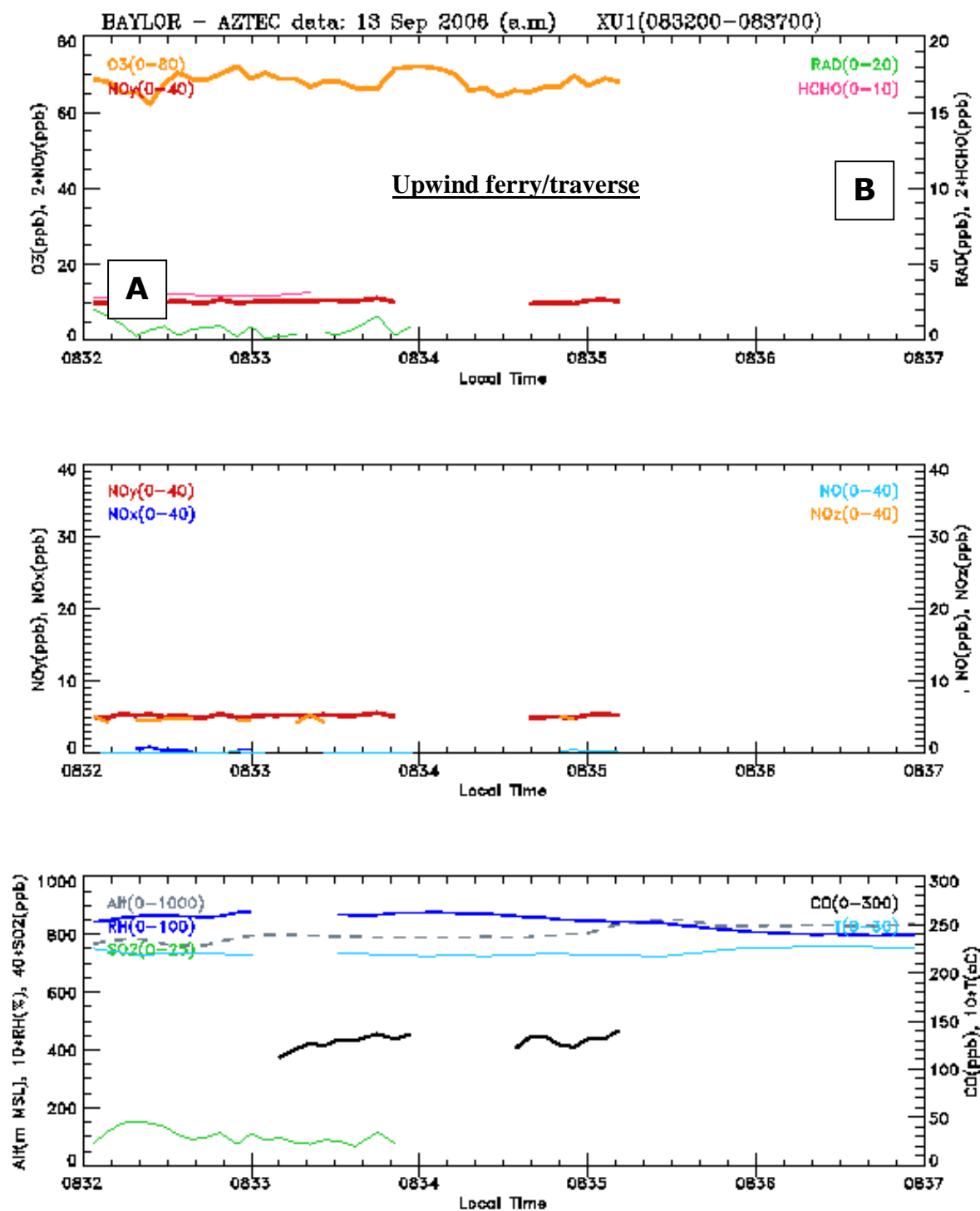


Figure 6.12 Data of Aztec upwind ferry/traverse (A – B) in the morning flight, showing the data of :
 NO_y (red), RAD (green), HCHO (pink), and ozone (orange) in the upper panel;
 NO_y (red), NO_x (blue), NO (light blue), and NO_z (orange) in the middle panel; and,
 ALT (broken black), CO (black), RH (dark blue), T (light blue), and SO₂ (green) .

BAYLOR – AZTEC data: 13 Sep 2006 (a.m)

Descent :083915–084400

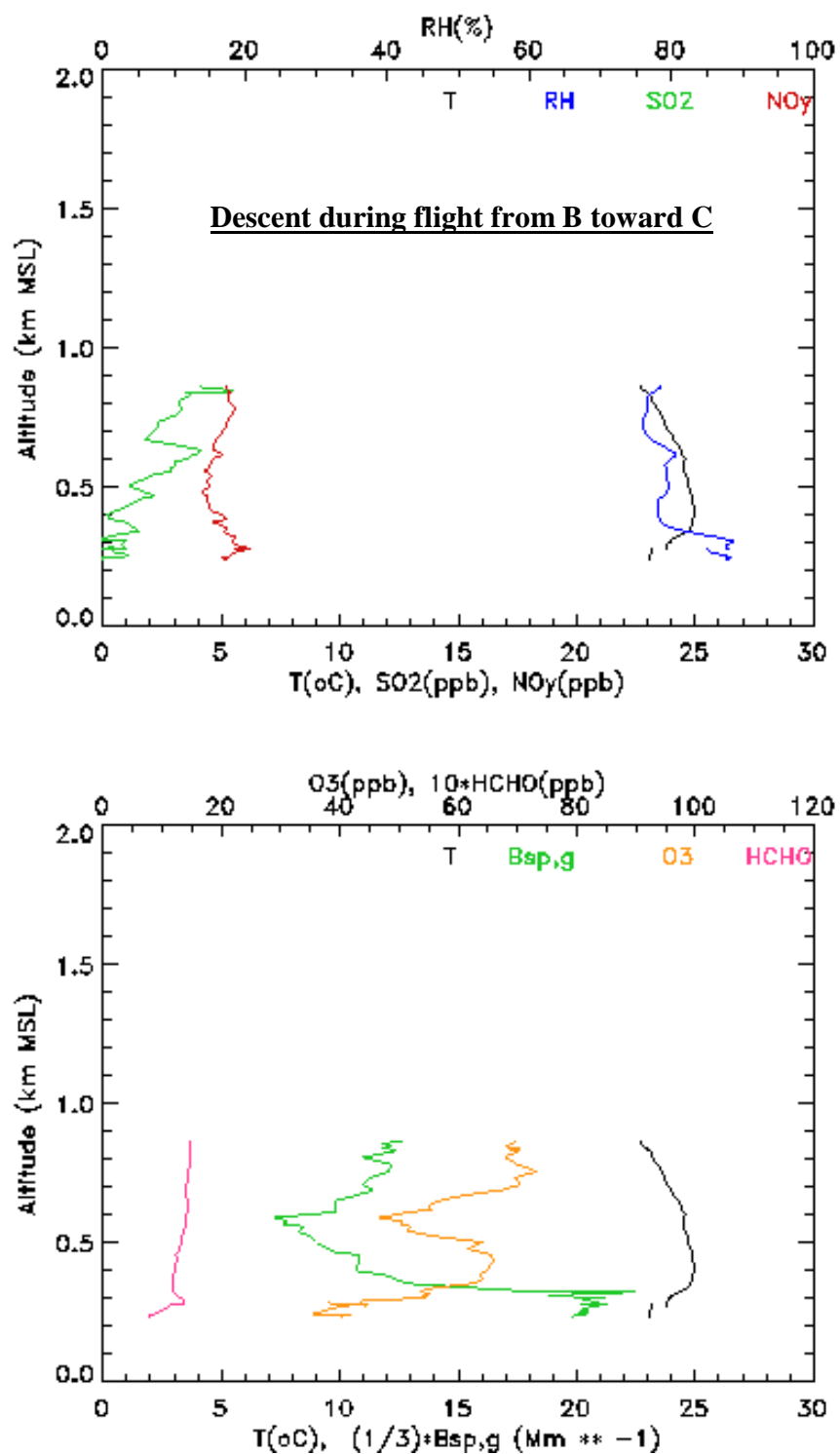


Figure 6.13 Data of Aztec descent flight pathways between B and C in the morning flight, below the level of the down-spiral S1, showing the data for T (black trace), RH (blue), NOy (red) and SO2 (green) in the upper plot and of T (black), O3 (orange), HCHO (pink) and Bsp,green wavelength (green).

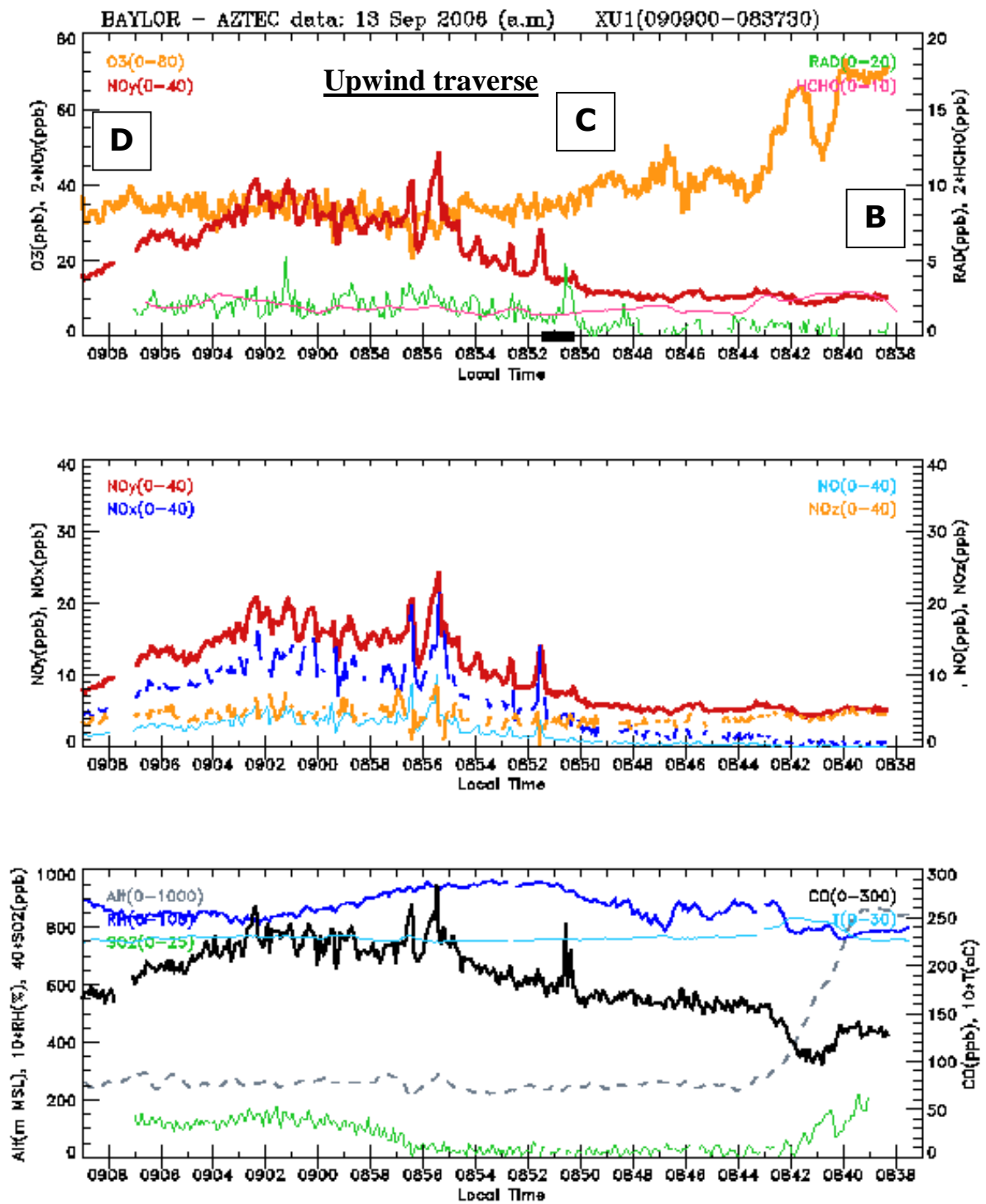


Figure 6.14 Data of Aztec upwind traverse (B-C-D) in the morning flight, showing the data of :
 NO_y (red), RAD (green), HCHO (pink), and ozone (orange) in the upper panel;
 NO_y (red), NO_x (blue), NO (light blue), and NO_z (orange) in the middle panel; and,
 ALT (broken black), CO (black), RH (dark blue), T (light blue), and SO₂ (green) .
 As with all traverse data, the plots are from west to east (in this case, back in time from D to C to B).
 Note also, the dark black marking between 0850 and 0852 along the time axis: this is an indication of a canister
 sample having been made during that time-frame.

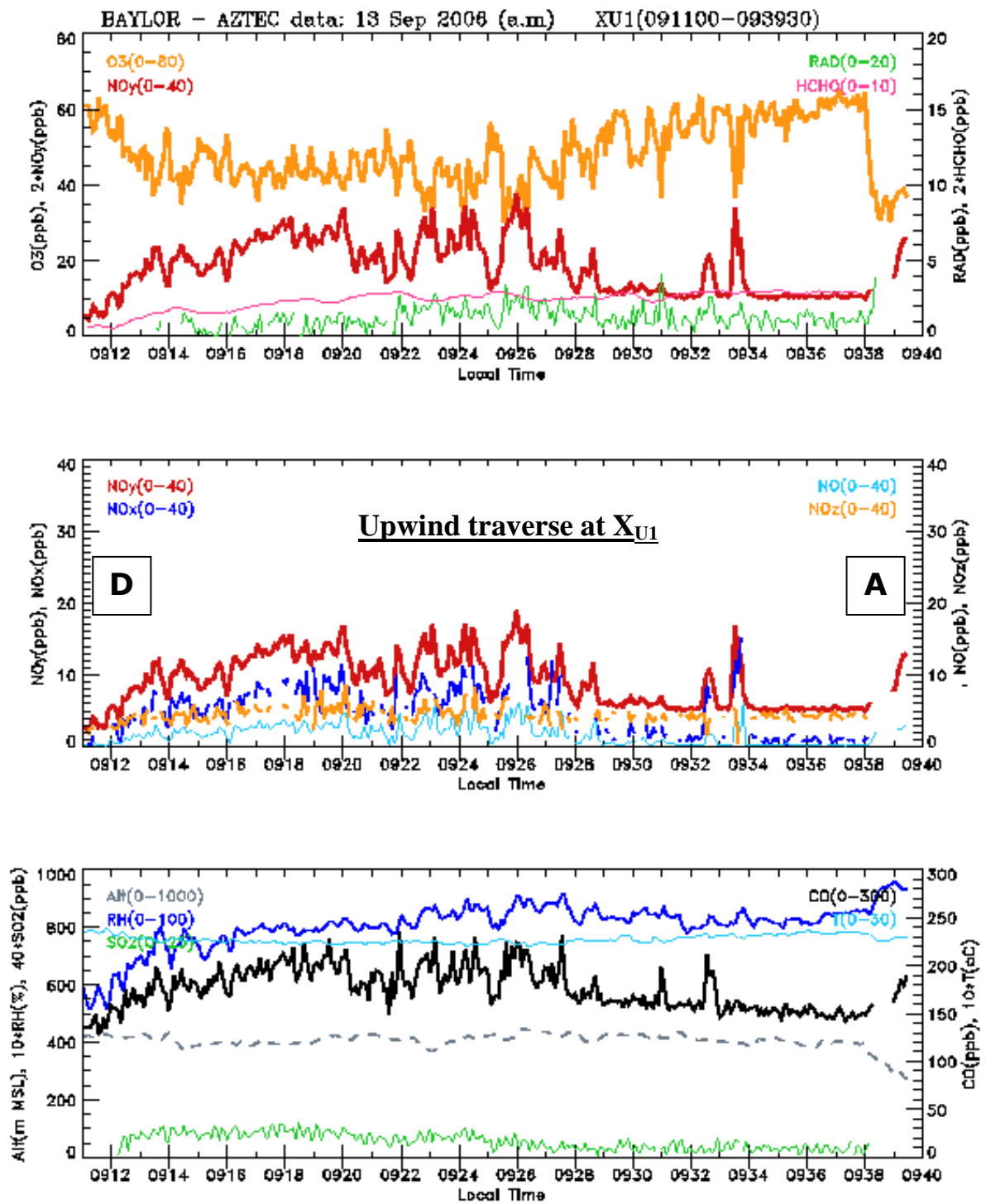


Figure 6.15 Data of Aztec upwind return traverse (D-A) in the morning flight, showing the data of :
 NO_y (red), RAD (green), HCHO (pink), and ozone (orange) in the upper panel;
 NO_y (red), NO_x (blue), NO (light blue), and NO_z (orange) in the middle panel; and,
 ALT (broken black), CO (black), RH (dark blue), T (light blue), and SO₂ (green) .
 As with all traverse data, the plots are from west to east (in this case, forward in time from D to A).

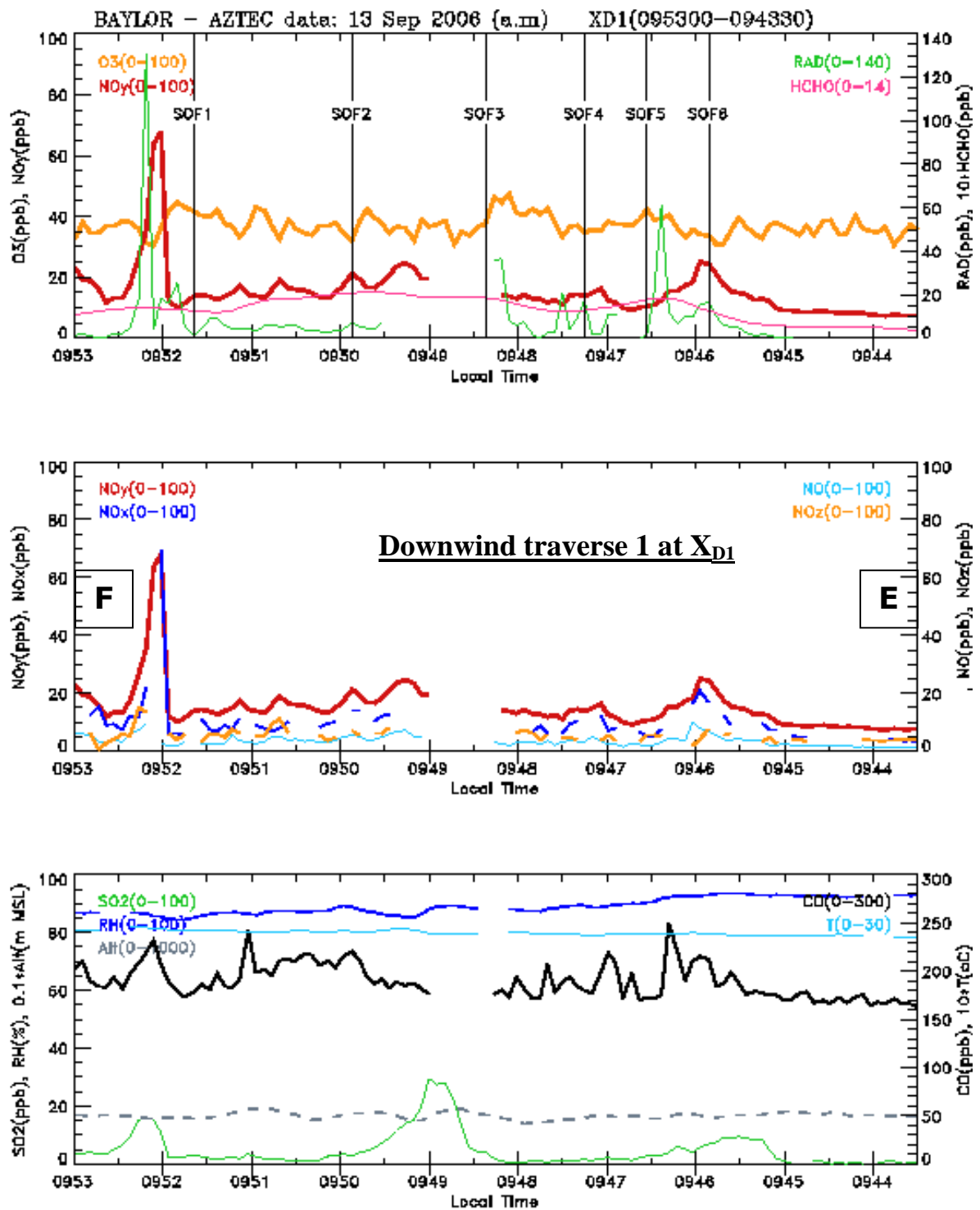


Figure 6.16 Data of Aztec downwind traverse (E-F) in the morning flight at X_{D1} , showing the data of :
 NO_y (red), RAD (green), $HCHO$ (pink), and ozone (orange) in the upper panel;
 NO_y (red), NO_x (blue), NO (light blue), and NO_z (orange) in the middle panel; and,
 ALT (broken black), CO (black), RH (dark blue), T (light blue), and SO_2 (green) .
 As with all traverse data, the plots are from west to east (in this case, forward in time from D to A).
 In the top panel, the vertical lines denote the right hand boundary of the SOF emission sector indicated.
 Thus, the part between SOF1 and SOF2 indicates the SOF sector 2.

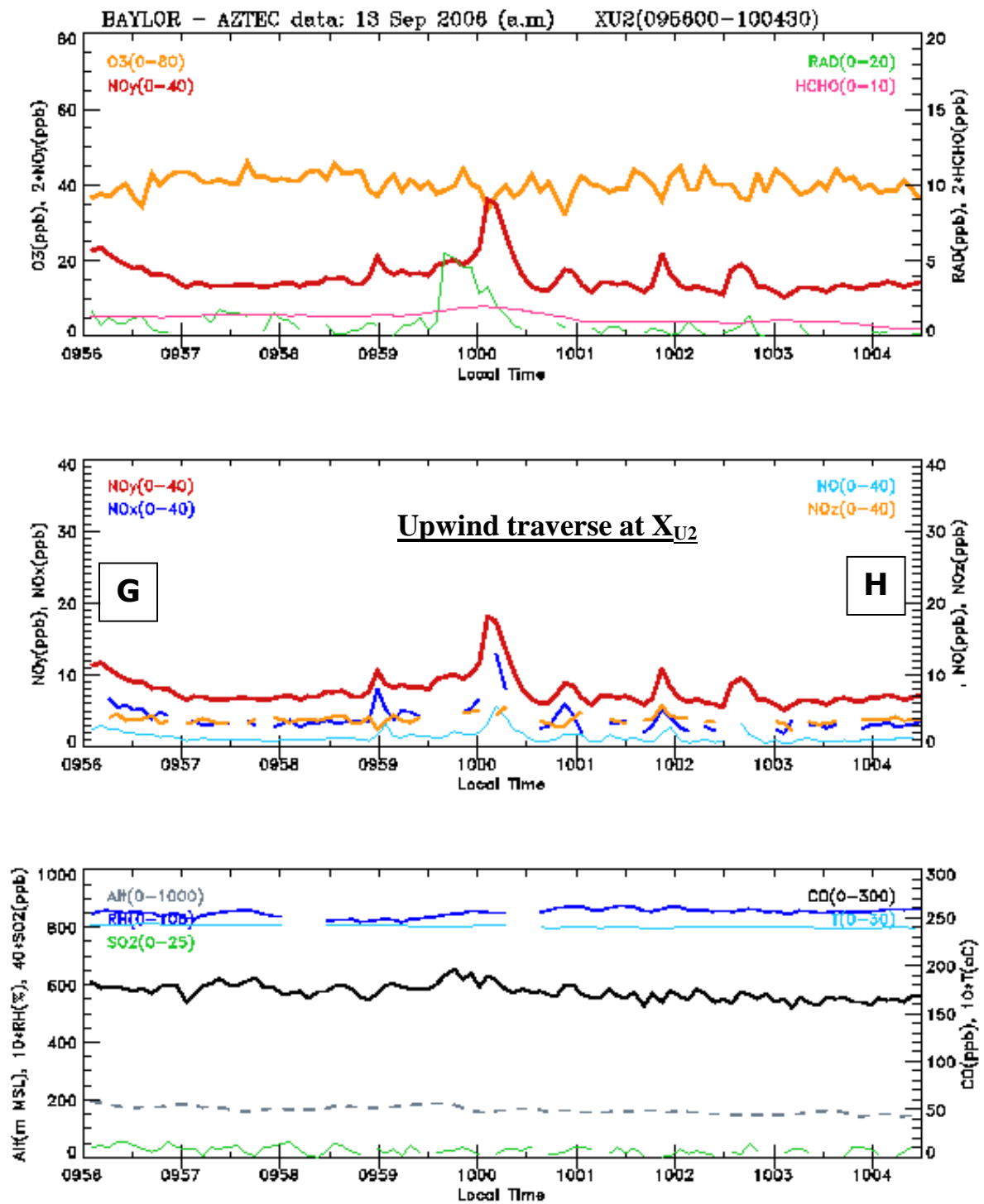


Figure 6.17 Data of Aztec upwind traverse (G-H) in the morning flight at X_{U2} , showing the data of :
 NO_y (red), RAD (green), HCHO (pink), and ozone (orange) in the upper panel;
 NO_y (red), NO_x (blue), NO (light blue), and NO_z (orange) in the middle panel; and,
 ALT (broken black), CO (black), RH (dark blue), T (light blue), and SO₂ (green) .
 As with all traverse data, the plots are from west to east.

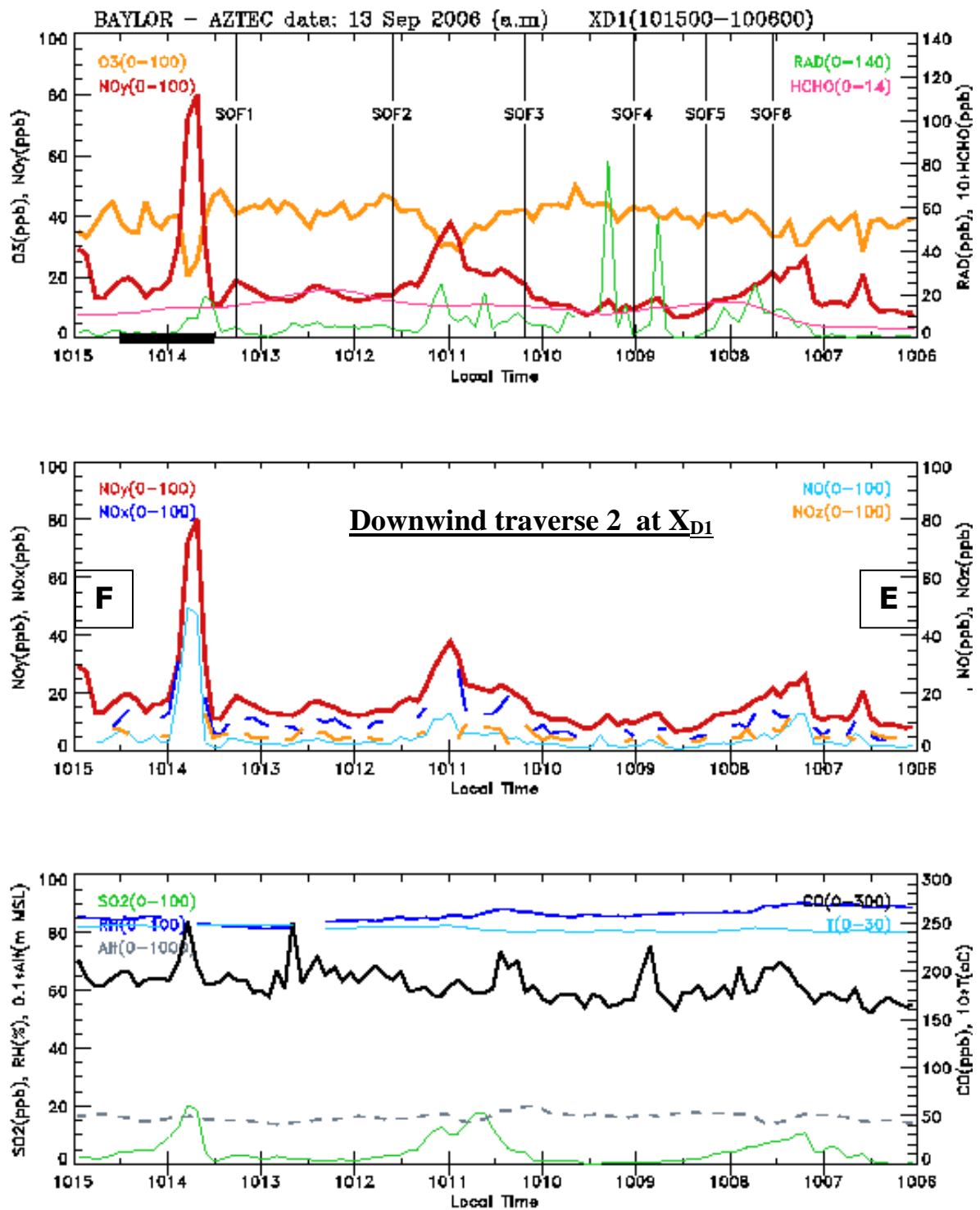


Figure 6.18 Data of Aztec downwind traverse (E-F) in the morning flight at X_{D1}, showing the data of :
 NO_y (red), RAD (green), HCHO (pink), and ozone (orange) in the upper panel;
 NO_y (red), NO_x (blue), NO (light blue), and NO_z (orange) in the middle panel; and,
 ALT (broken black), CO (black), RH (dark blue), T (light blue), and SO₂ (green) .

As with all traverse data, the plots are from west to east.

In the top panel, the vertical lines denote the right hand boundary of the SOF emission sector indicated, and the heavy line on the time axis near 1014 denotes the time of a canister sample.

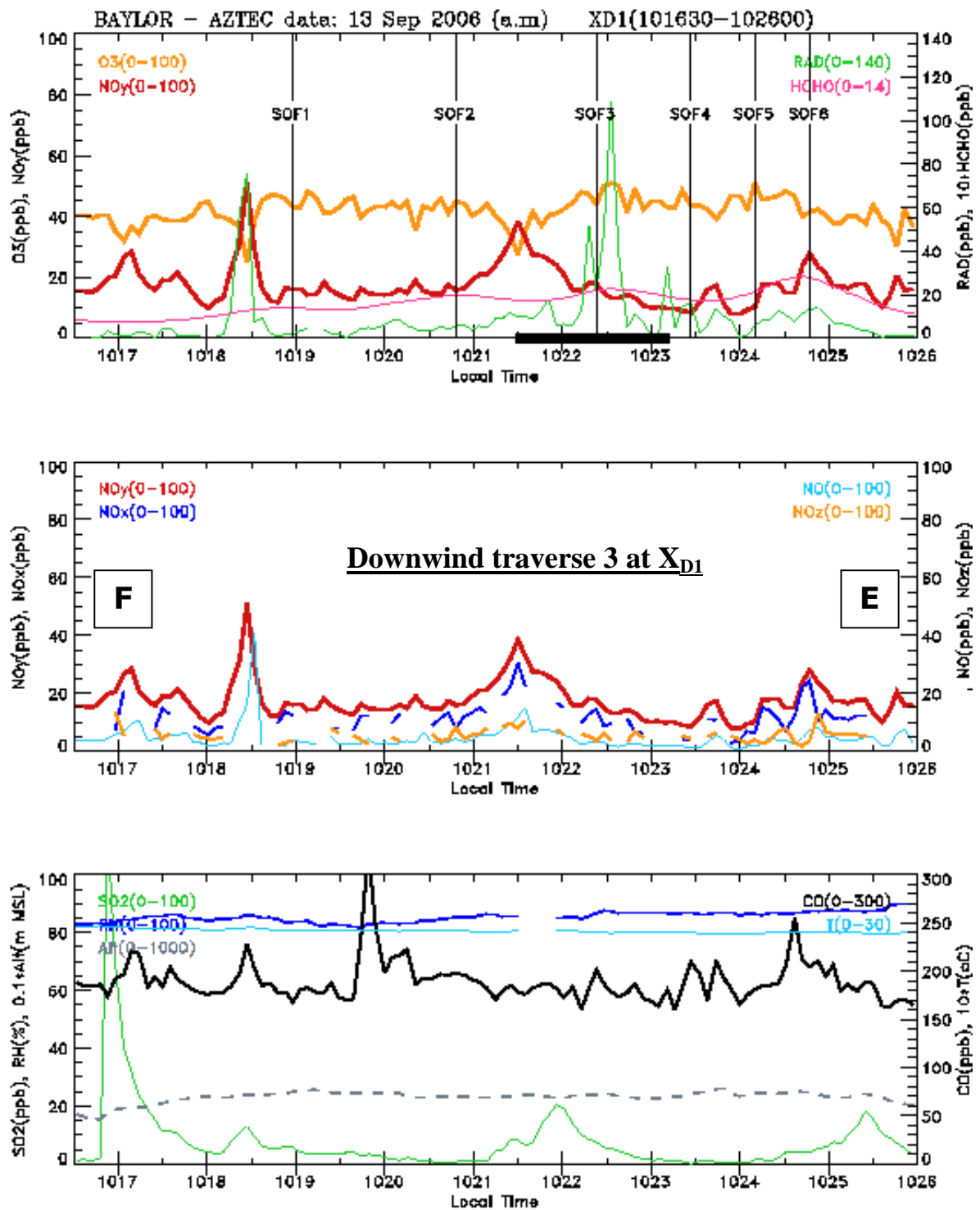


Figure 6.19 Data of Aztec downwind traverse in the morning flight at X_{D1}, showing the data of :

NO_y (red), RAD (green), HCHO (pink), and ozone (orange) in the upper panel;
 NO_y (red), NO_x (blue), NO (light blue), and NO_z (orange) in the middle panel; and,
 ALT (broken black), CO (black), RH (dark blue), T (light blue), and SO₂ (green) .

As with all traverse data, the plots are from west to east.

In the top panel, the vertical lines denote the right hand boundary of the SOF emission sector indicated,
 and the heavy line on the time axis near 1022-23 denotes the time of a canister sample.

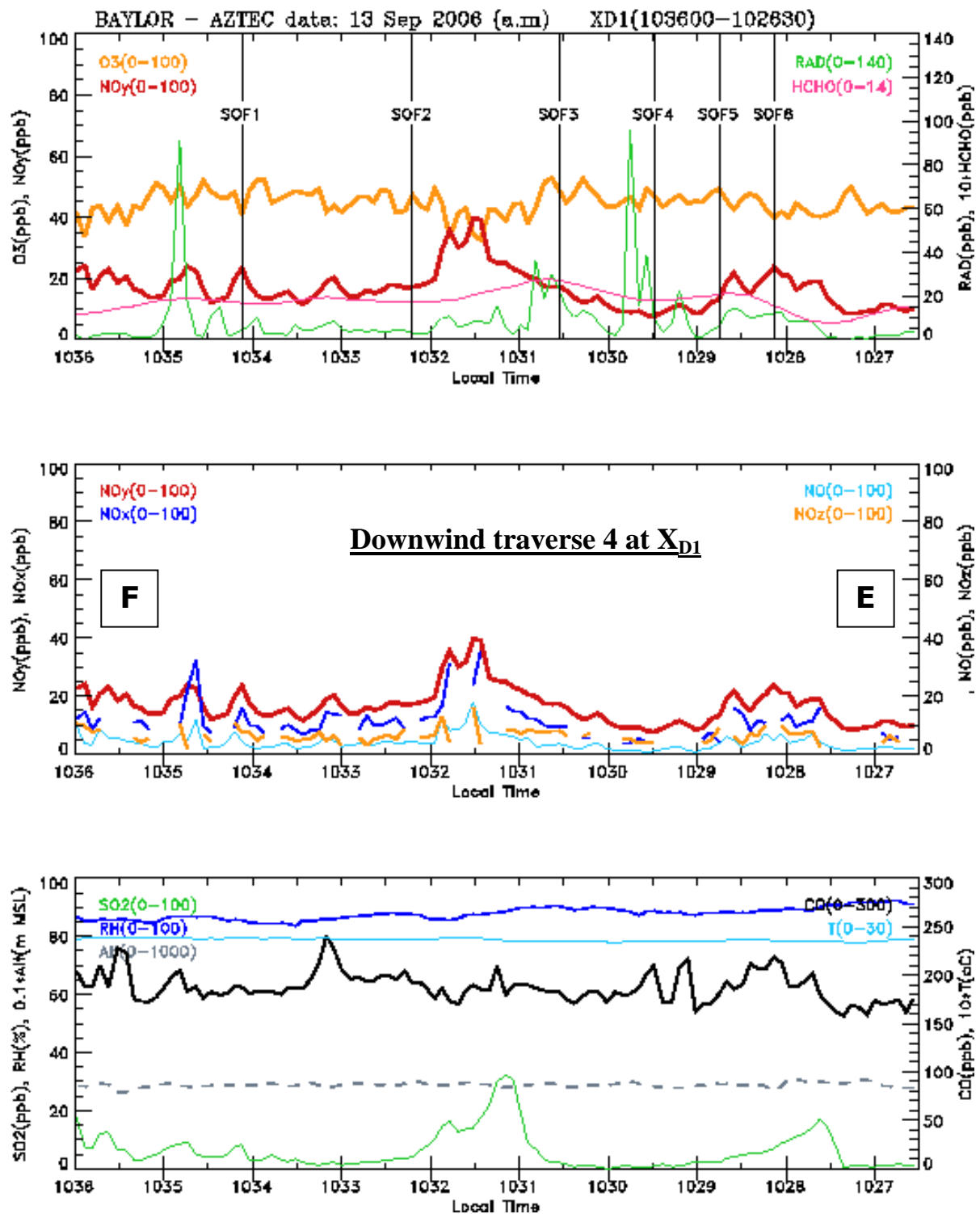


Figure 6.20 Data of Aztec downwind traverse in the morning flight at X_{D1} , showing the data of :
 NOy (red), RAD (green), HCHO (pink), and ozone (orange) in the upper panel;
 NOy (red), NOx (blue), NO (light blue), and NOz (orange) in the middle panel; and,
 ALT (broken black), CO (black), RH (dark blue), T (light blue), and SO2 (green) .

As with all traverse data, the plots are from west to east.

In the top panel, the vertical lines denote the right hand boundary of the SOF emission sector indicated.

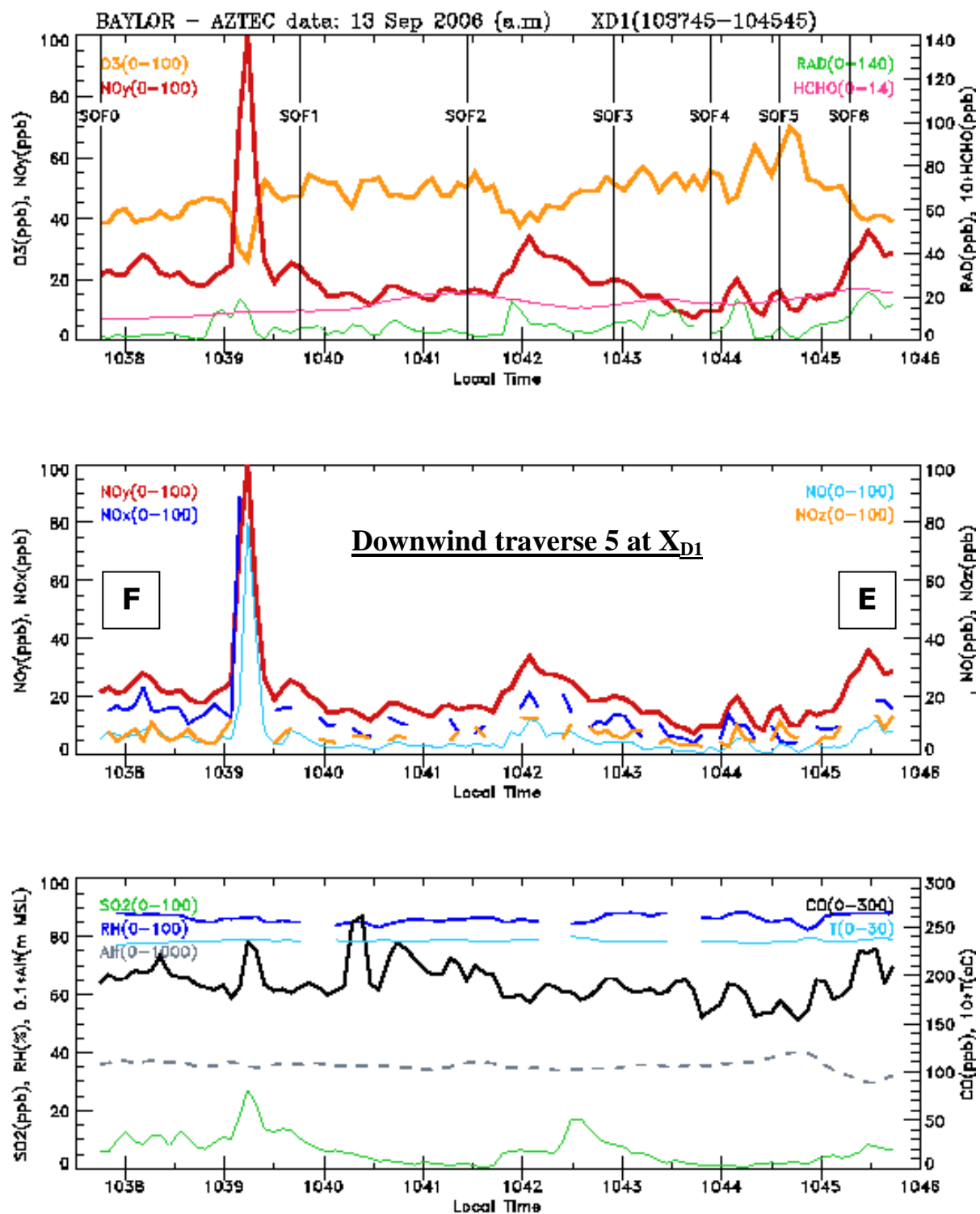


Figure 6.21 Data of Aztec downwind traverse in the morning flight at X_{D1}, showing the data of :
 NO_y (red), RAD (green), HCHO (pink), and ozone (orange) in the upper panel;
 NO_y (red), NO_x (blue), NO (light blue), and NO_z (orange) in the middle panel; and,
 ALT (broken black), CO (black), RH (dark blue), T (light blue), and SO₂ (green) .
 As with all traverse data, the plots are from west to east.
 In the top panel, the vertical lines denote the right hand boundary of the SOF emission sector indicated.

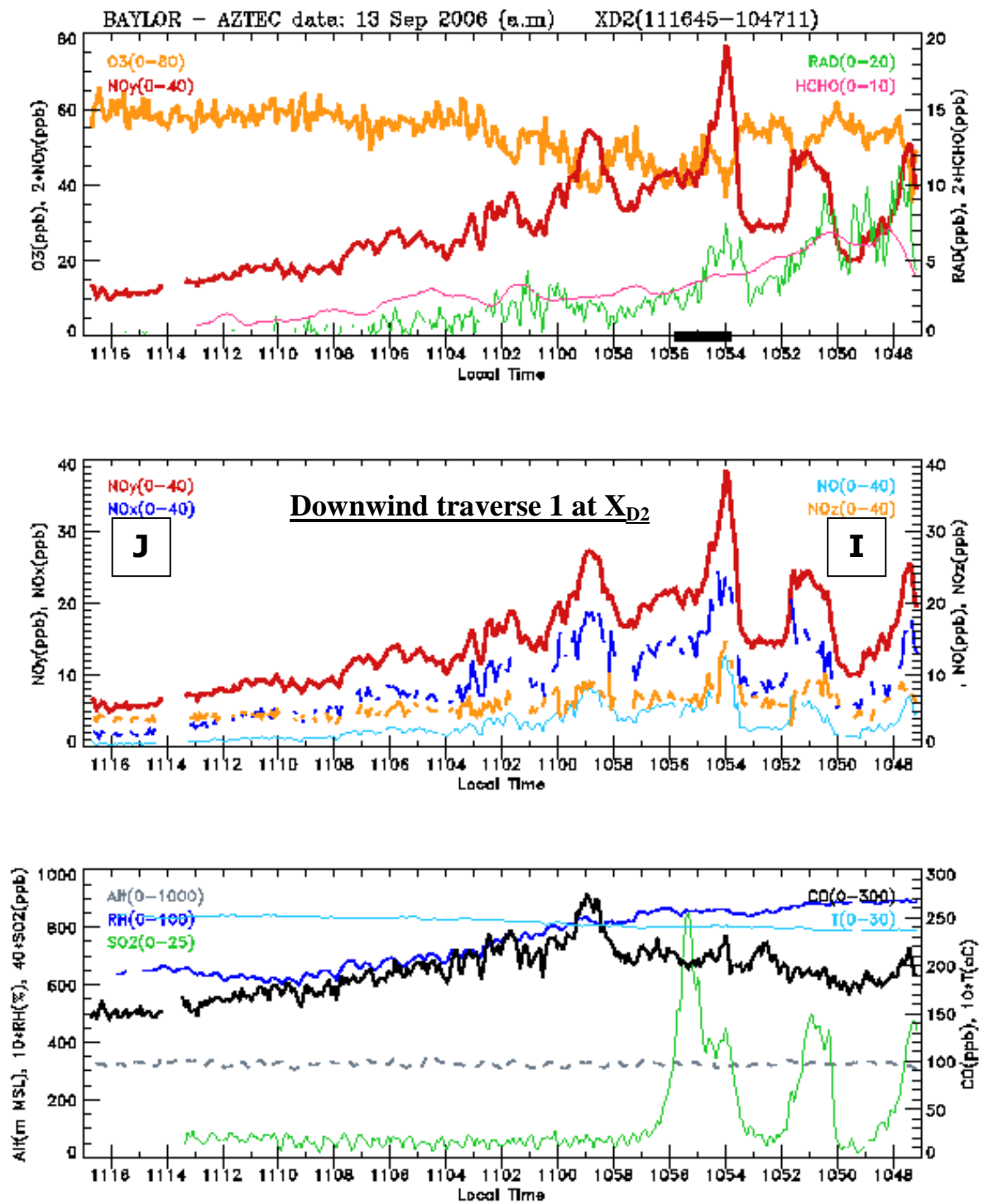


Figure 6.22 Data of Aztec downwind traverse 1 at X_{D2} in the morning flight, showing the data of :
 NO_y (red), RAD (green), HCHO (pink), and ozone (orange) in the upper panel;
 NO_y (red), NO_x (blue), NO (light blue), and NO_z (orange) in the middle panel; and,
 ALT (broken black), CO (black), RH (dark blue), T (light blue), and SO₂ (green) .
 As with all traverse data, the plots are from west to east.

The heavy trace on the time axis between 1054 and 1056 denotes time of a canister sample.

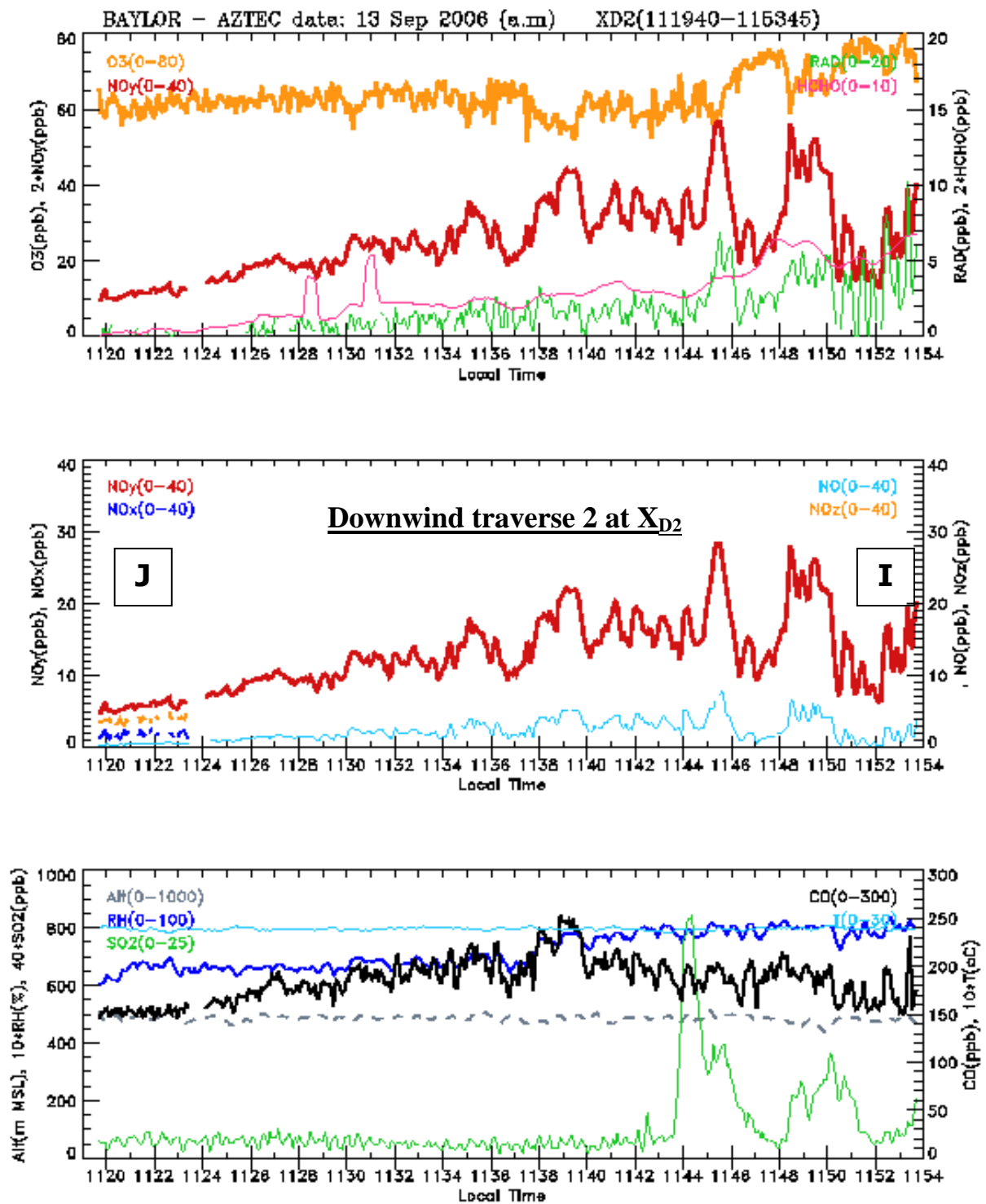


Figure 6.23 Data of Aztec downwind traverse 2 at X_{D2} in the morning flight, showing the data of :
 NO_y (red), RAD (green), $HCHO$ (pink), and ozone (orange) in the upper panel;
 NO_y (red), NO_x (blue), NO (light blue), and NO_z (orange) in the middle panel; and,
 ALT (broken black), CO (black), RH (dark blue), T (light blue), and SO_2 (green) .
 As with all traverse data, the plots are from west to east.

BAYLOR – AZTEC data: 13 Sep 2006 (a.m)

Upward Spiral S2:115700–120800

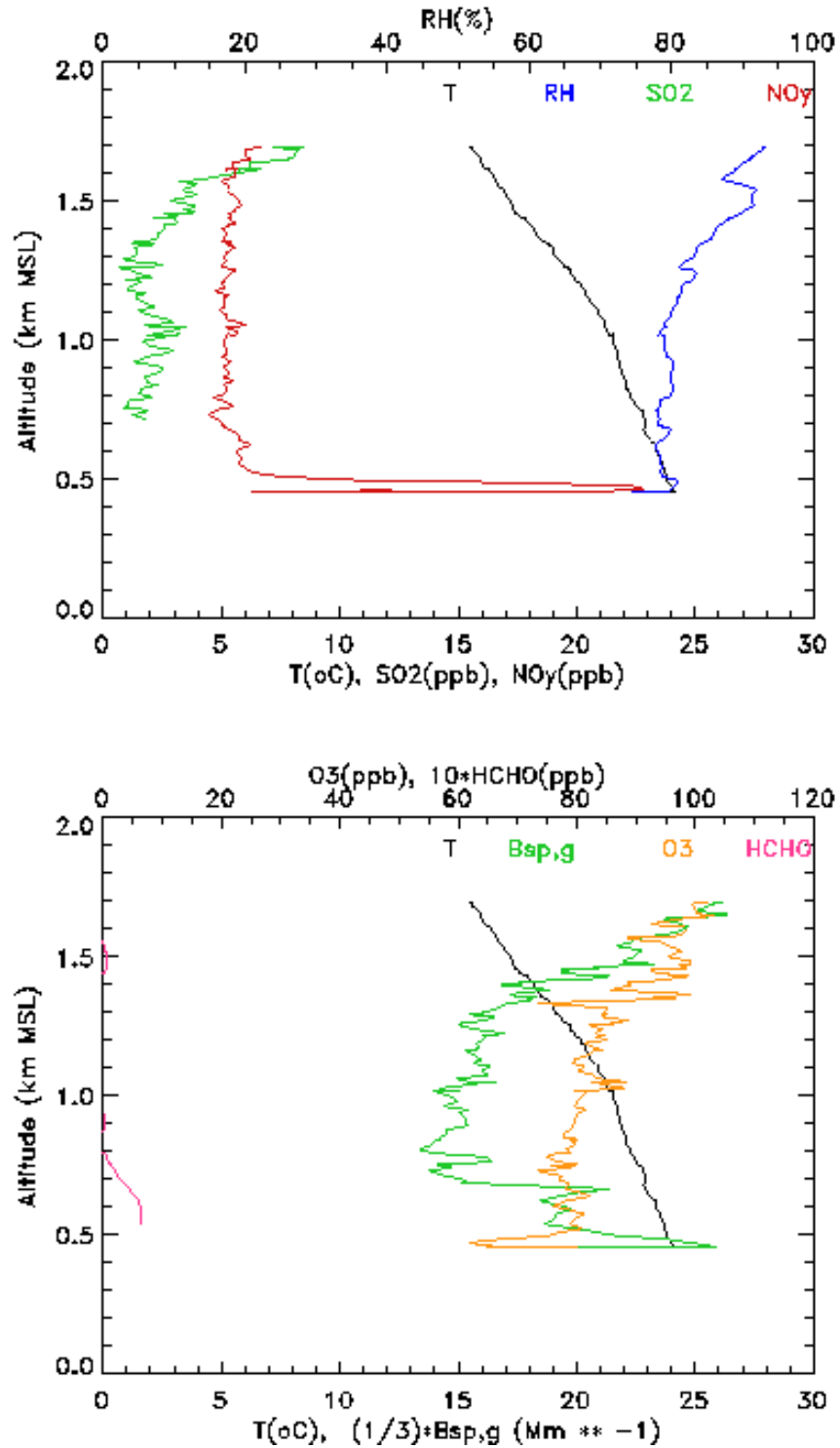


Figure 6.24 Data of Aztec up-spiral S2 in the morning flight, showing the data for T (black trace), RH (blue), NOy (red) and SO2 (green) in the upper plot and of T (black), O3 (orange), HCHO (pink) and Bsp,green wavelength (green) in the lower plot.

BAYLOR – AZTEC data: 13 Sep 2006 (a.m)

Downward Spiral S2:121000–122600

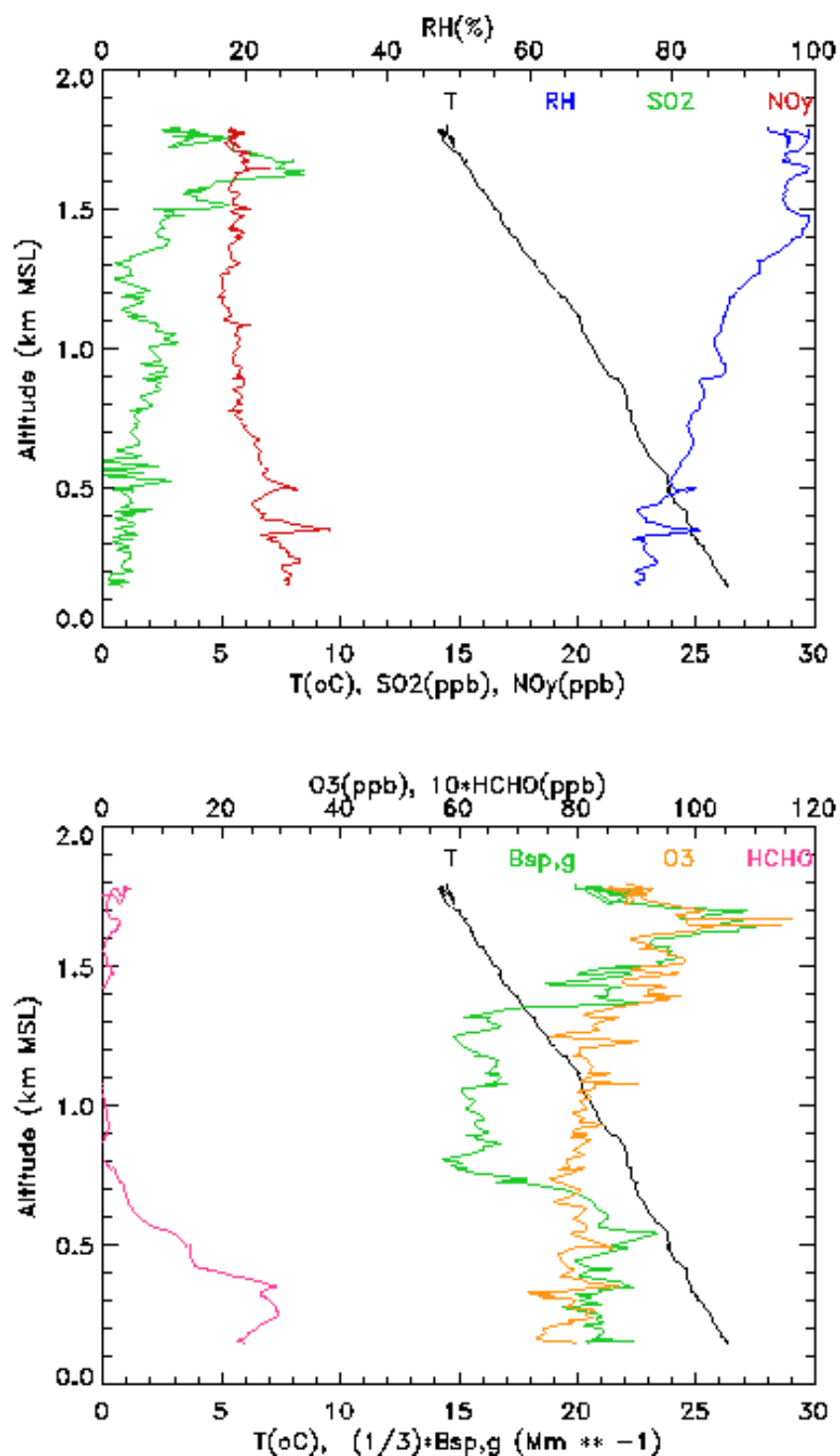


Figure 6.25 Data of Aztec down-spiral S2 in the morning flight, showing the data for T (black trace), RH (blue), NOy (red) and SO2 (green) in the upper plot and of T (black), O3 (orange), HCHO (pink) and Bsp.green wavelength (green) in the lower plot.

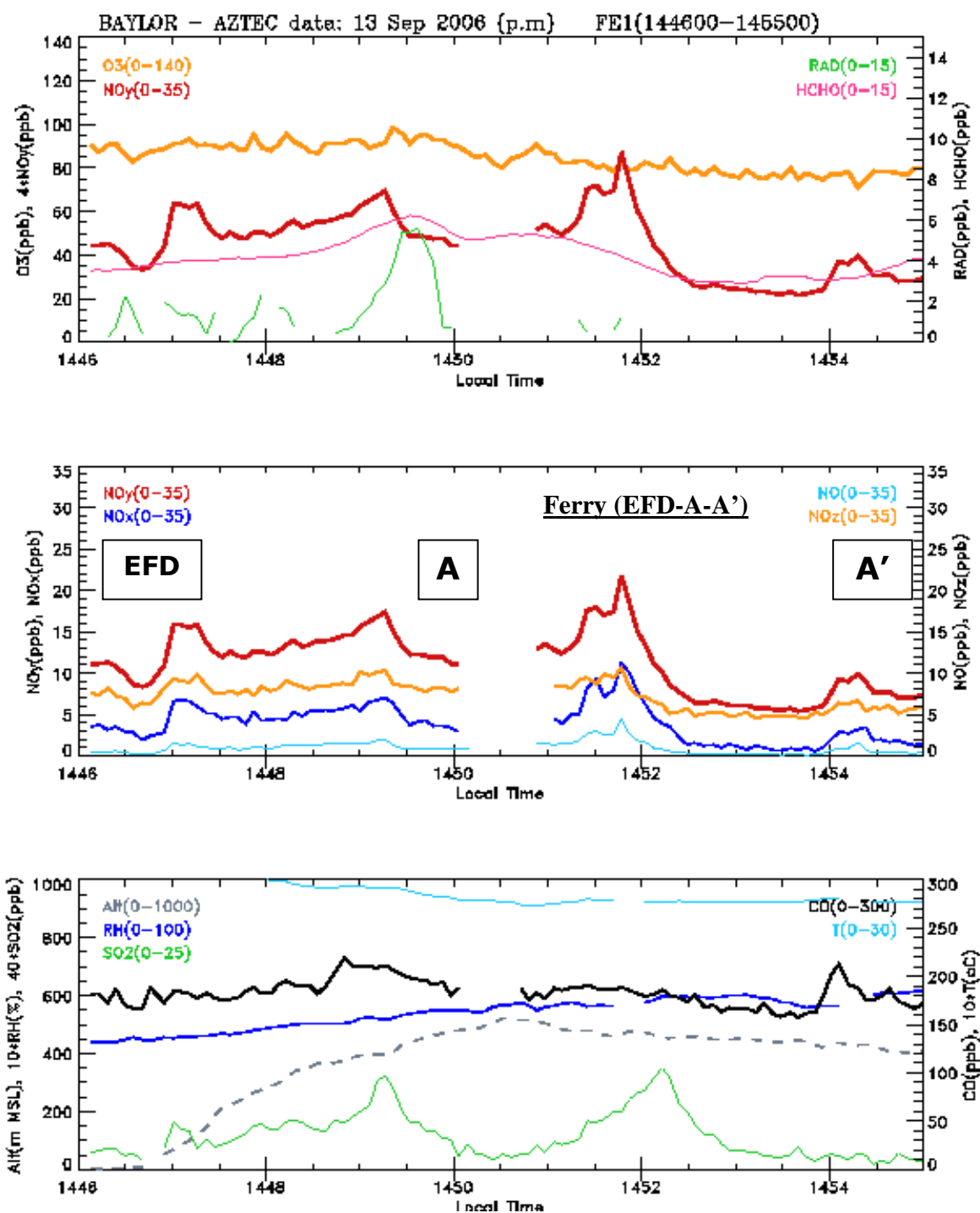


Figure 6.26 Time series data of Aztec in the afternoon flight:
 NO_y (red), RAD (green), HCHO (pink), and ozone (orange) in the upper panel;
 NO_y (red), NO_x (dark blue), NO (light blue), and NO_z (orange) in the middle panel; and,
 ALT (broken black), CO (solid black), RH (dark blue), T (light blue), and SO₂ (green) in the lower panel.

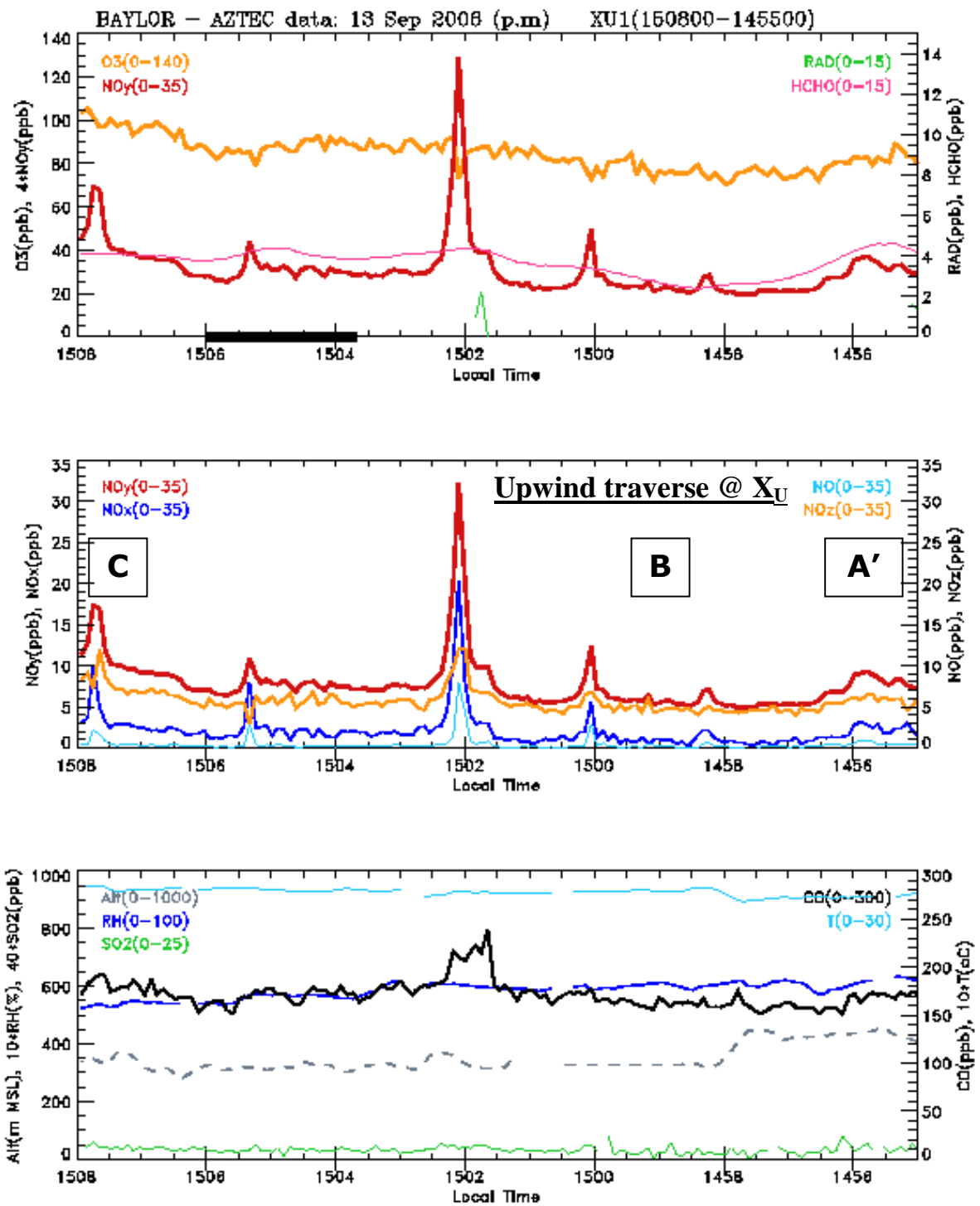


Figure 6.27 Time series data of Aztec in the afternoon flight:

NO_y (red), RAD (green), HCHO (pink), and ozone (orange) in the upper panel;

NO_y (red), NO_x (dark blue), NO (light blue), and NO_z (orange) in the middle panel; and, ALT (broken black), CO (solid black), RH (dark blue), T (light blue), and SO₂ (green) in the lower panel.

As with all traverse data, the plots are from west to east.

In the top panel, the heavy line on the time axis around 1504-1506 denotes the time of a canister sample.

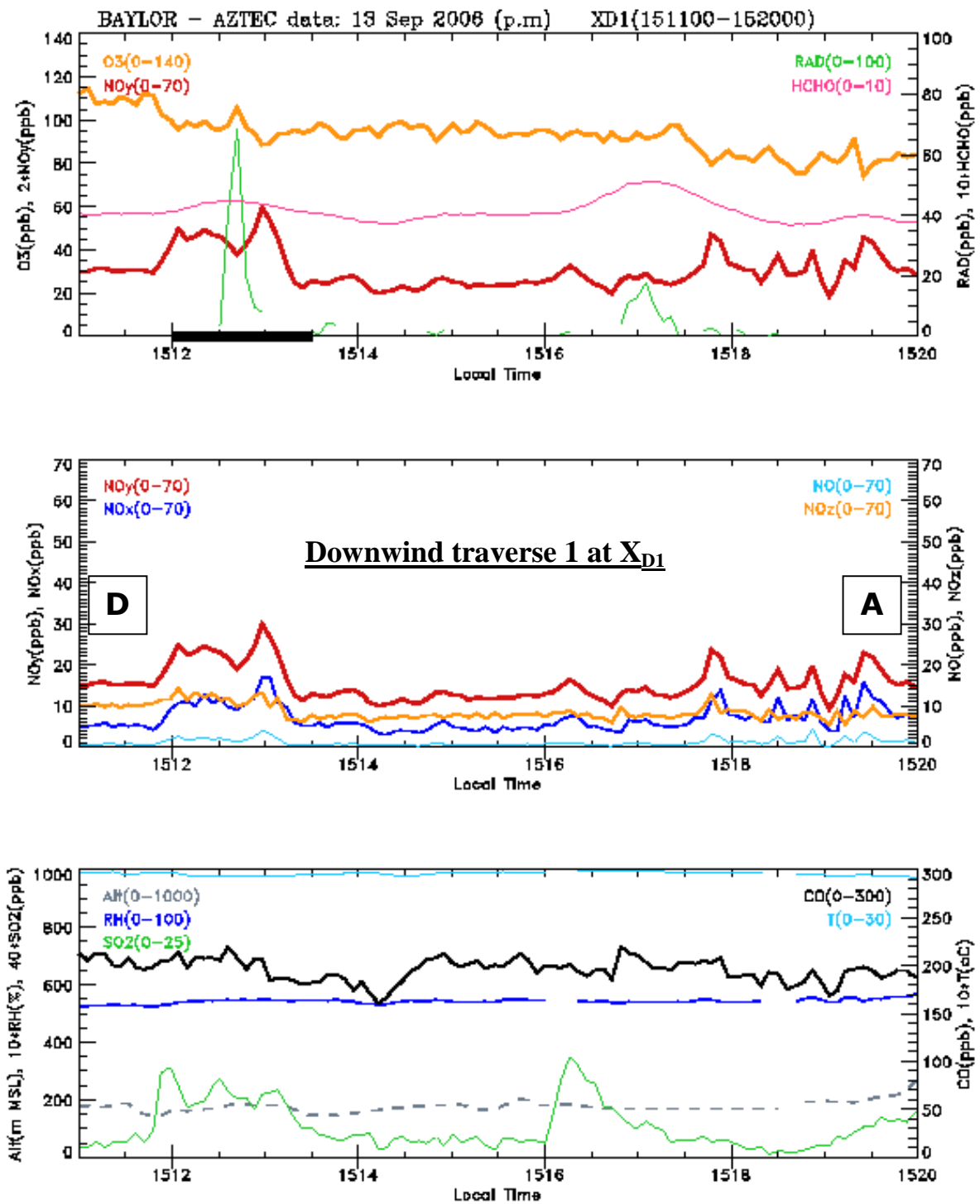


Figure 6.28 Time series data of Aztec in the afternoon flight:
 NO_y (red), RAD (green), HCHO (pink), and ozone (orange) in the upper panel;
 NO_y (red), NO_x (dark blue), NO (light blue), and NO_z (orange) in the middle panel; and,
 ALT (broken black), CO (solid black), RH (dark blue), T (light blue), and SO₂ (green) in the lower panel .
 As with all traverse data, the plots are from west to east. In the top panel,
 the heavy line on the time axis near 1512-1513:30 denotes the time of a canister sample.

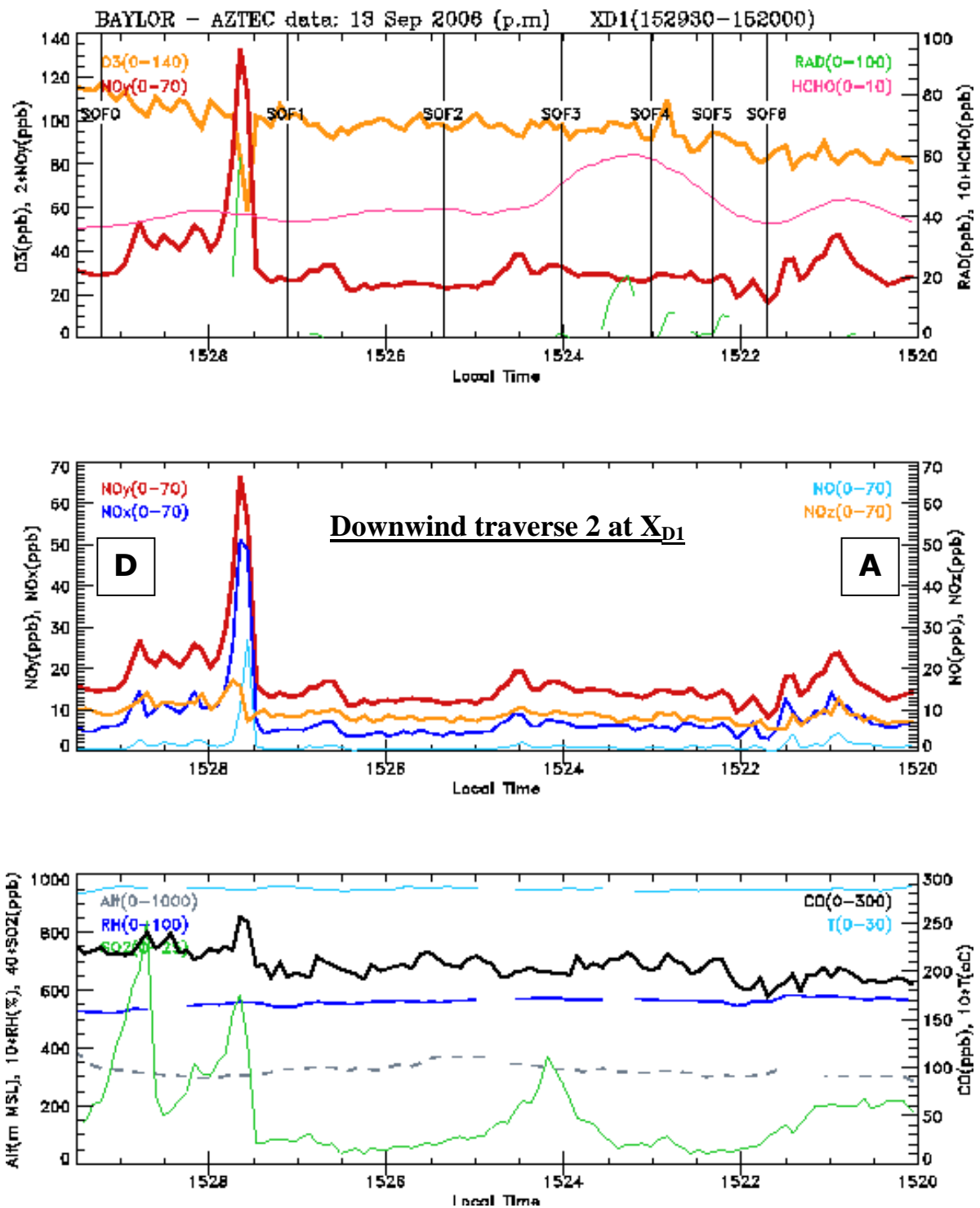


Figure 6.29 Time series data of Aztec in the afternoon flight:
 NO_y (red), RAD (green), HCHO (pink), and ozone (orange) in the upper panel;
 NO_y (red), NO_x (dark blue), NO (light blue), and NO_z (orange) in the middle panel; and,
 ALT (broken black), CO (solid black), RH (dark blue), T (light blue), and SO₂ (green) in the lower panel .
 As with all traverse data, the plots are from west to east. In the top panel, the vertical lines denote
 the time of passage of the right hand boundary of the SOF emission sector indicated.

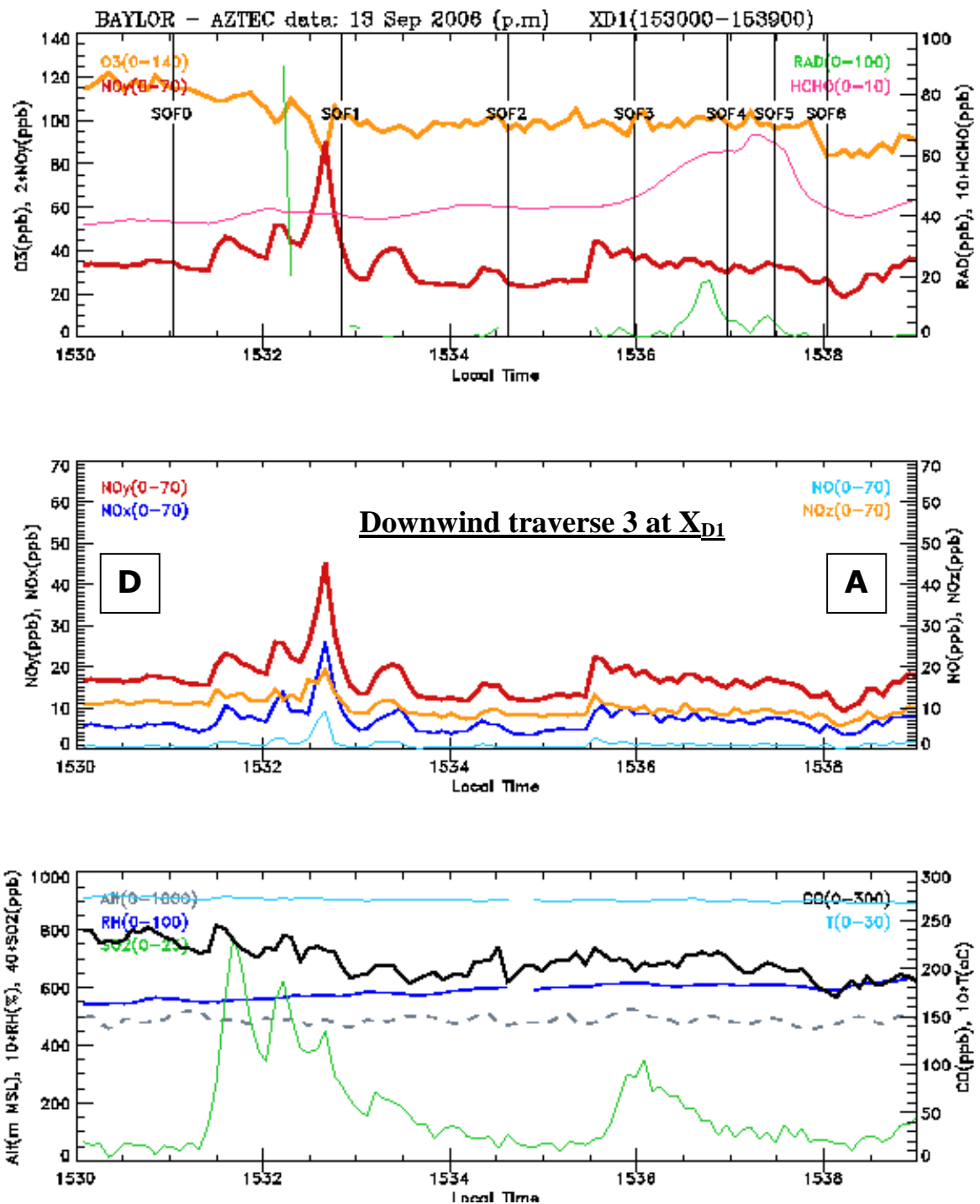


Figure 6.30 Time series data of Aztec in the afternoon flight:
 NO_y (red), RAD (green), HCHO (pink), and ozone (orange) in the upper panel;
 NO_y (red), NO_x (dark blue), NO (light blue), and NO_z (orange) in the middle panel; and,
 ALT (broken black), CO (solid black), RH (dark blue), T (light blue), and SO₂ (green) in the lower panel .
 As with all traverse data, the plots are from west to east. In the top panel, the vertical lines denote
 the passage of the right hand boundary of the SOF emission sector indicated.

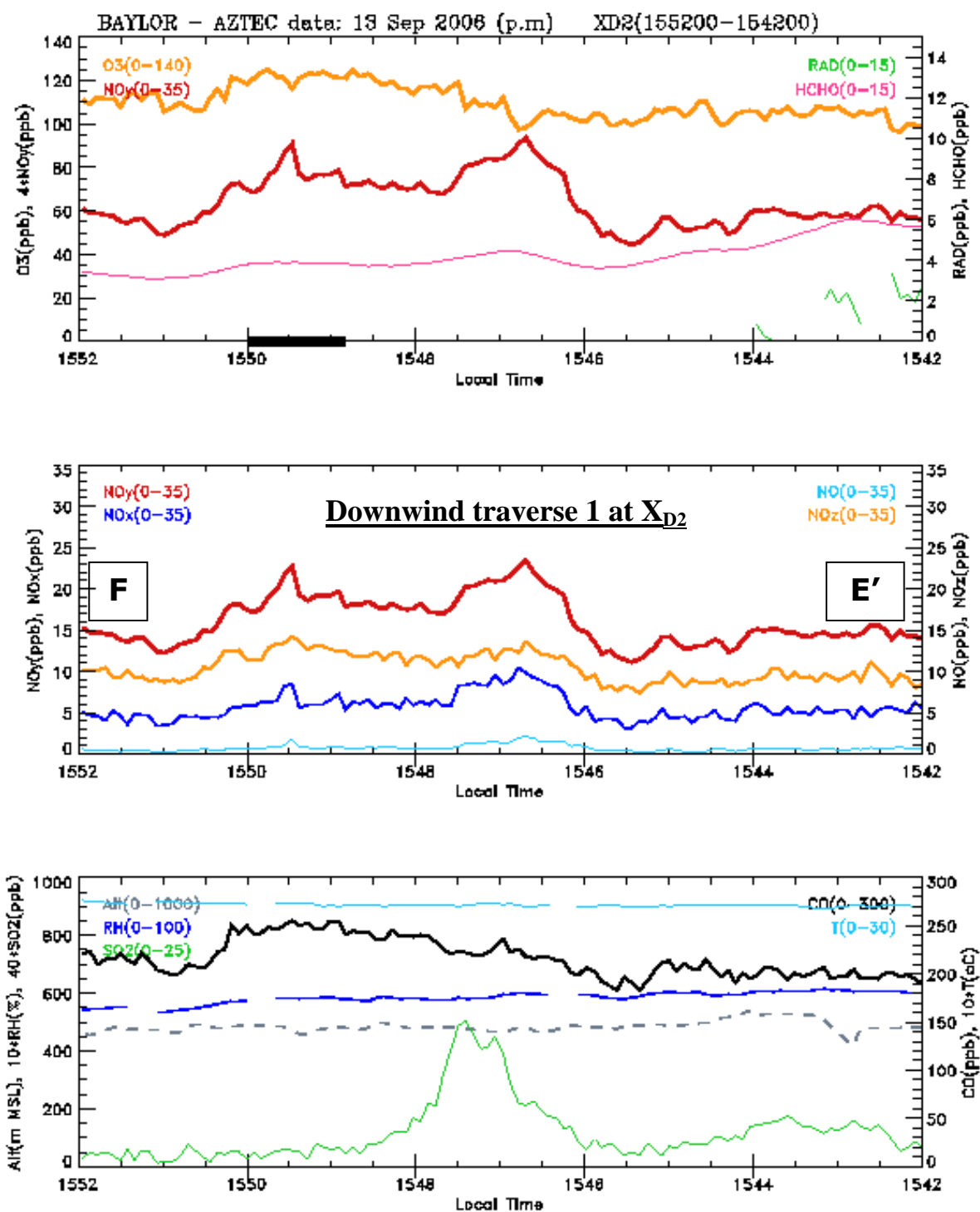


Figure 6.31 Time series data of Aztec in the afternoon flight:

NO_y (red), RAD (green), HCHO (pink), and ozone (orange) in the upper panel;

NO_y (red), NO_x (dark blue), NO (light blue), and NO_z (orange) in the middle panel; and,

ALT (broken black), CO (solid black), RH (dark blue), T (light blue), and SO₂ (green) in the lower panel.

As with all traverse data, the plots are from west to east.

In the top panel, the heavy line on the time axis between 1548:40 and 1550 denotes the time of a canister sample.

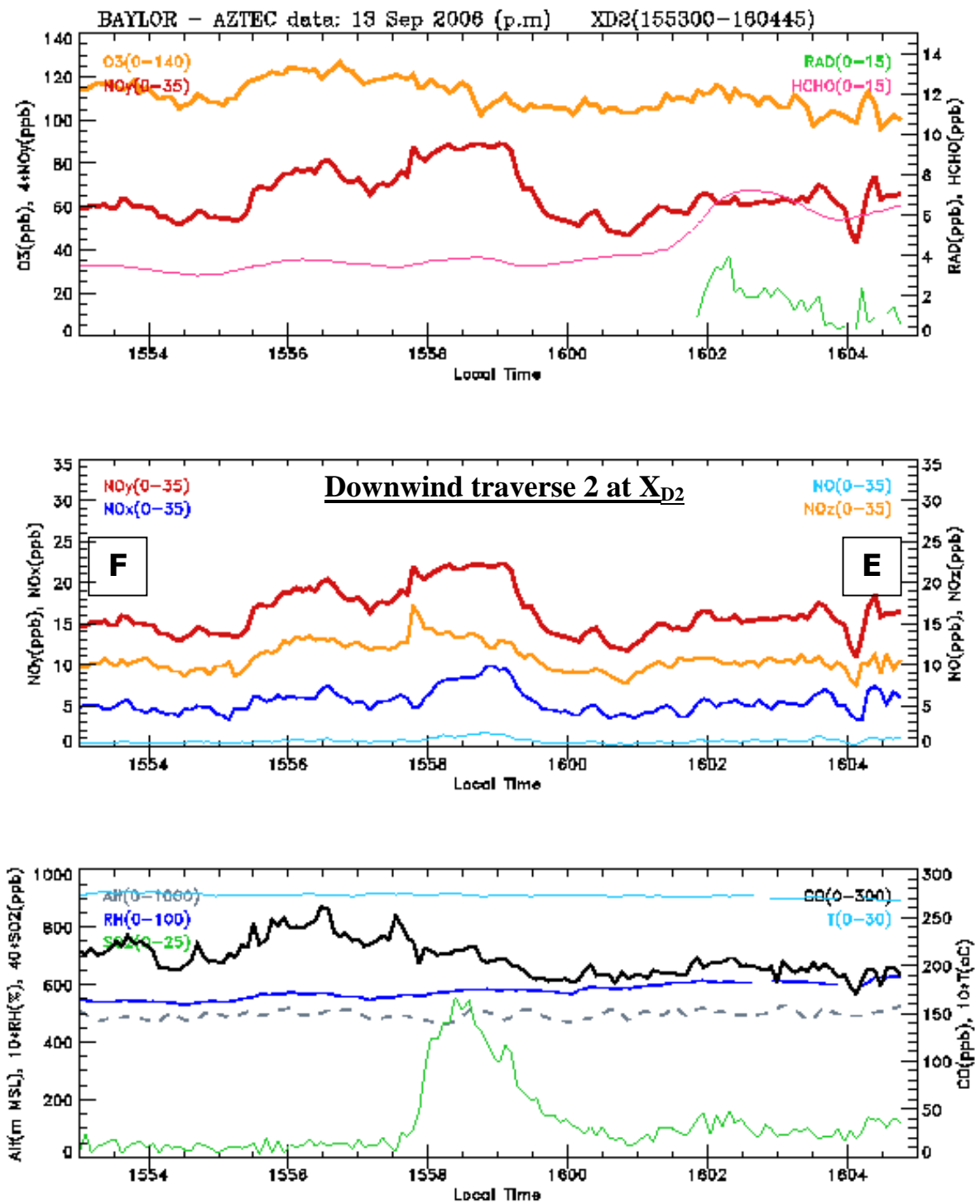


Figure 6.32 Time series data of Aztec in the afternoon flight:
 NO_y (red), RAD (green), HCHO (pink), and ozone (orange) in the upper panel;
 NO_y (red), NO_x (dark blue), NO (light blue), and NO_z (orange) in the middle panel; and,
 ALT (broken black), CO (solid black), RH (dark blue), T (light blue), and SO₂ (green) in the lower panel .
 As with all traverse data, the plots are from west to east.

BAYLOR – AZTEC data: 13 Sep 2006 (p.m)

Upward Spiral S2:160400–161700

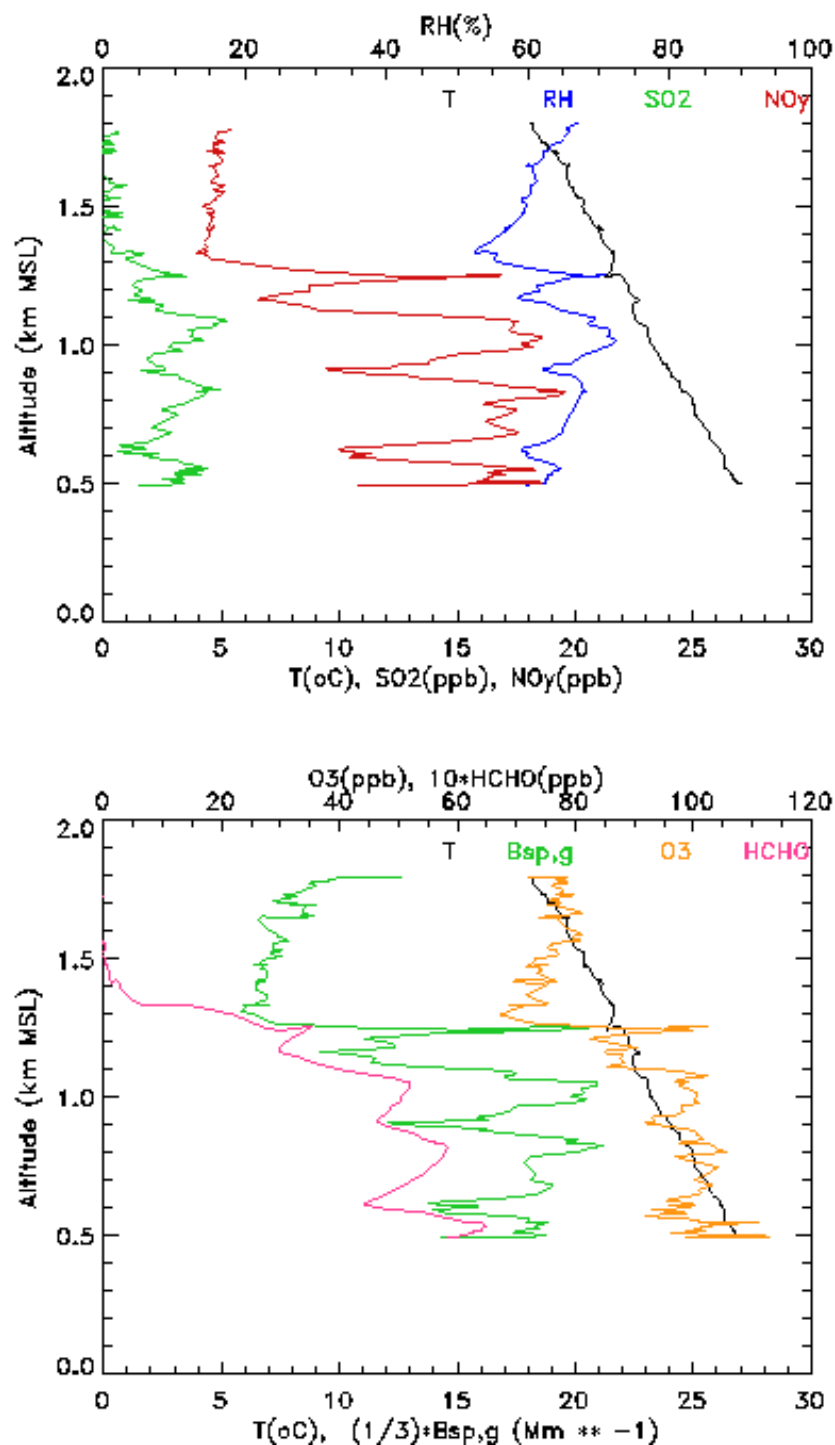


Figure 6.33 Data of Aztec up-spiral S3 near location E in the afternoon flight, showing the data for T (black trace), RH (blue), NOy (red) and SO2 (green) in the upper plot and of T (black), O3 (orange), HCHO (pink) and Bsp.green wavelength (green) in the lower plot.

BAYLOR – AZTEC data: 13 Sep 2006 (p.m)

Downward Spiral S2:161700–162500

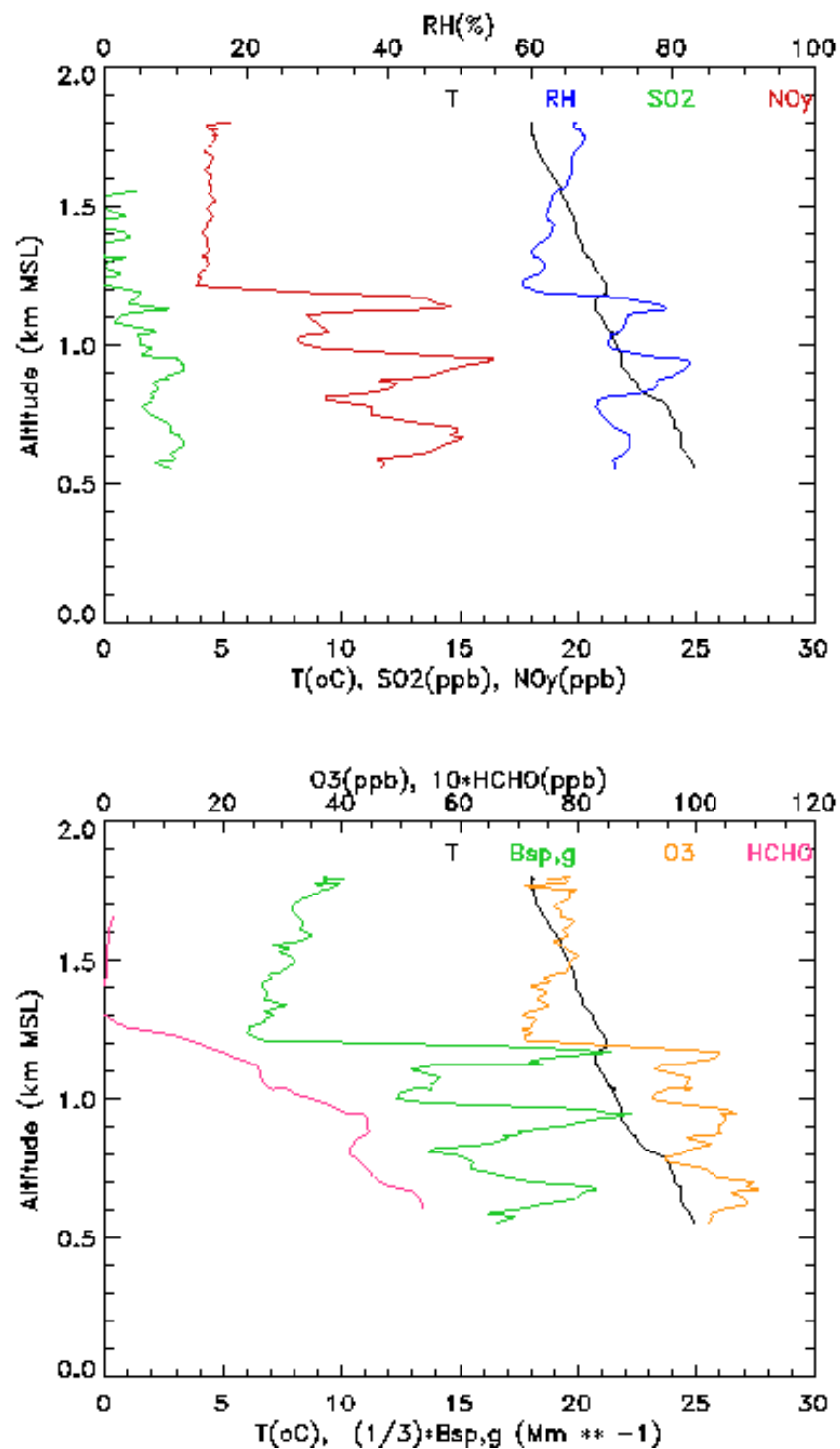


Figure 6.34 Data of Aztec down-spiral S3 near location E in the afternoon flight, showing the data for T (black trace), RH (blue), NOy (red) and SO2 (green) in the upper plot and of T (black), O3 (orange), HCHO (pink) and Bsp,green wavelength (green) in the lower plot.

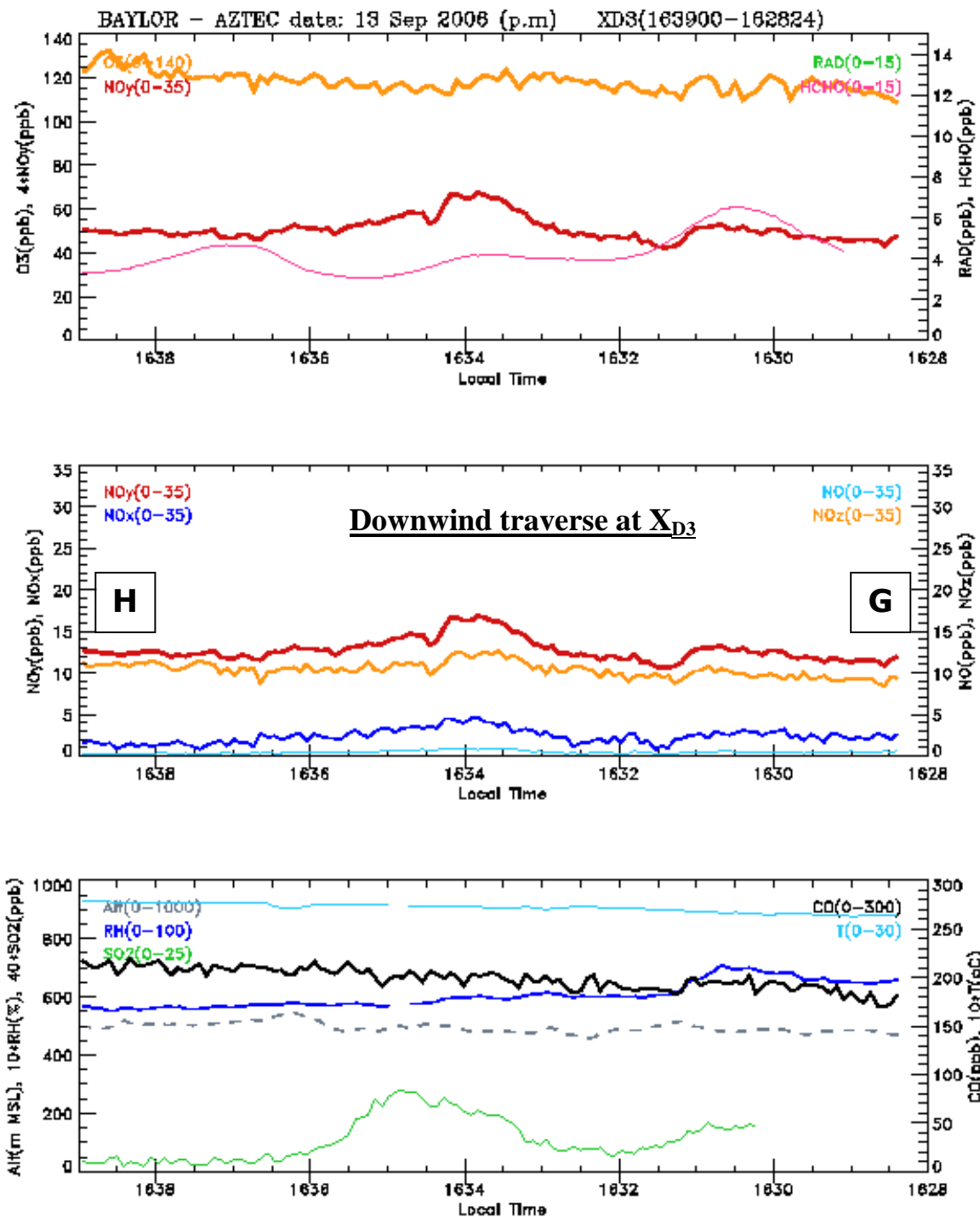


Figure 6.35 Time series data of Aztec in the afternoon flight:
 NO_y (red), RAD (green), HCHO (pink), and ozone (orange) in the upper panel;
 NO_y (red), NO_x (dark blue), NO (light blue), and NO_z (orange) in the middle panel; and,
 ALT (broken black), CO (solid black), RH (dark blue), T (light blue), and SO₂ (green) in the lower panel .
 As with all traverse data, the plots are from west to east.

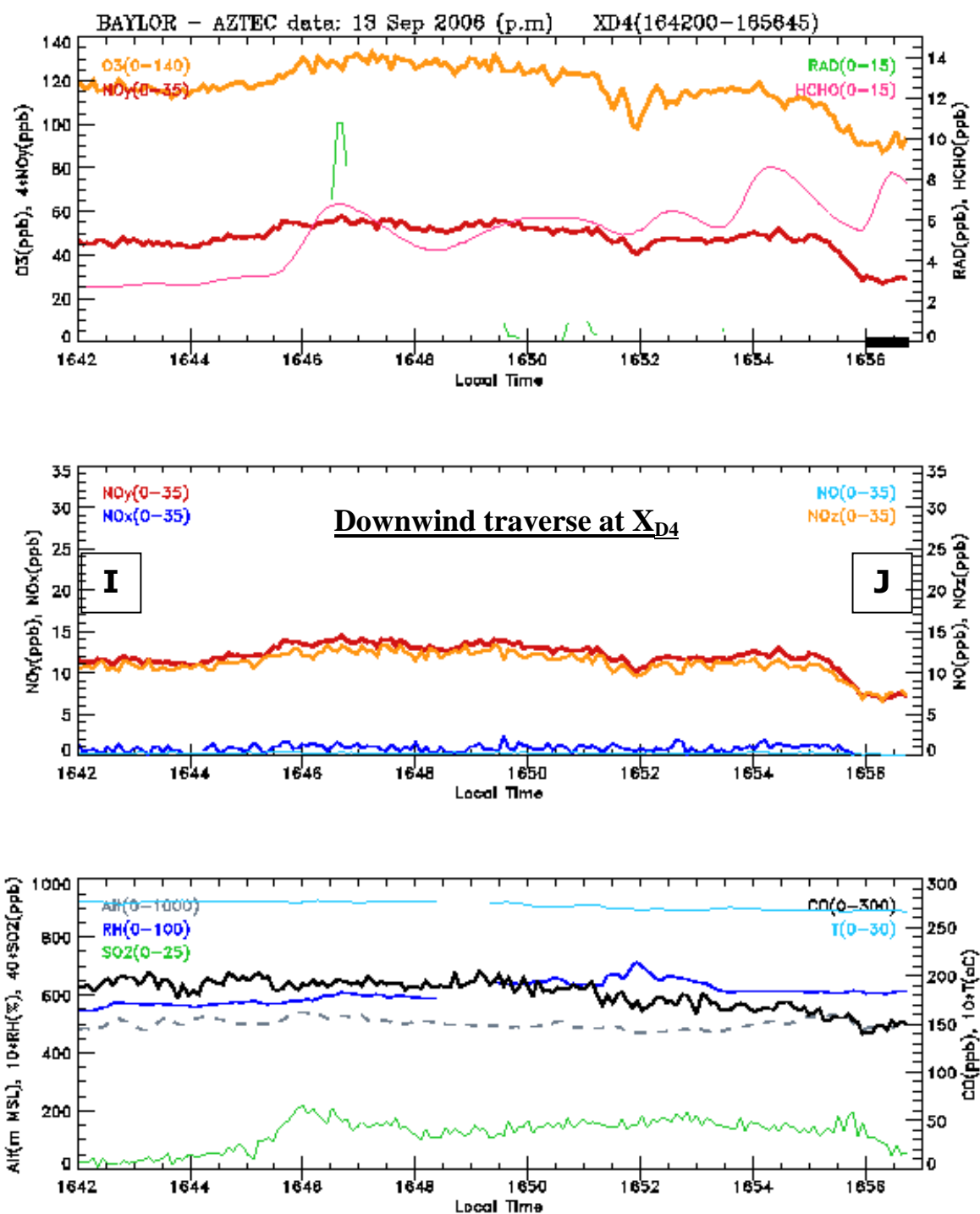


Figure 6.36 Time series data of Aztec in the afternoon flight:
 NO_y (red), RAD (green), HCHO (pink), and ozone (orange) in the upper panel;
 NO_y (red), NO_x (dark blue), NO (light blue), and NO_z (orange) in the middle panel; and,
 ALT (broken black), CO (solid black), RH (dark blue), T (light blue), and SO₂ (green) in the lower panel.
 As with all traverse data, the plots are from west to east. In the top panel, the heavy line on the time axis
 between 1548:40 and 1550 denotes the time of a canister sample.

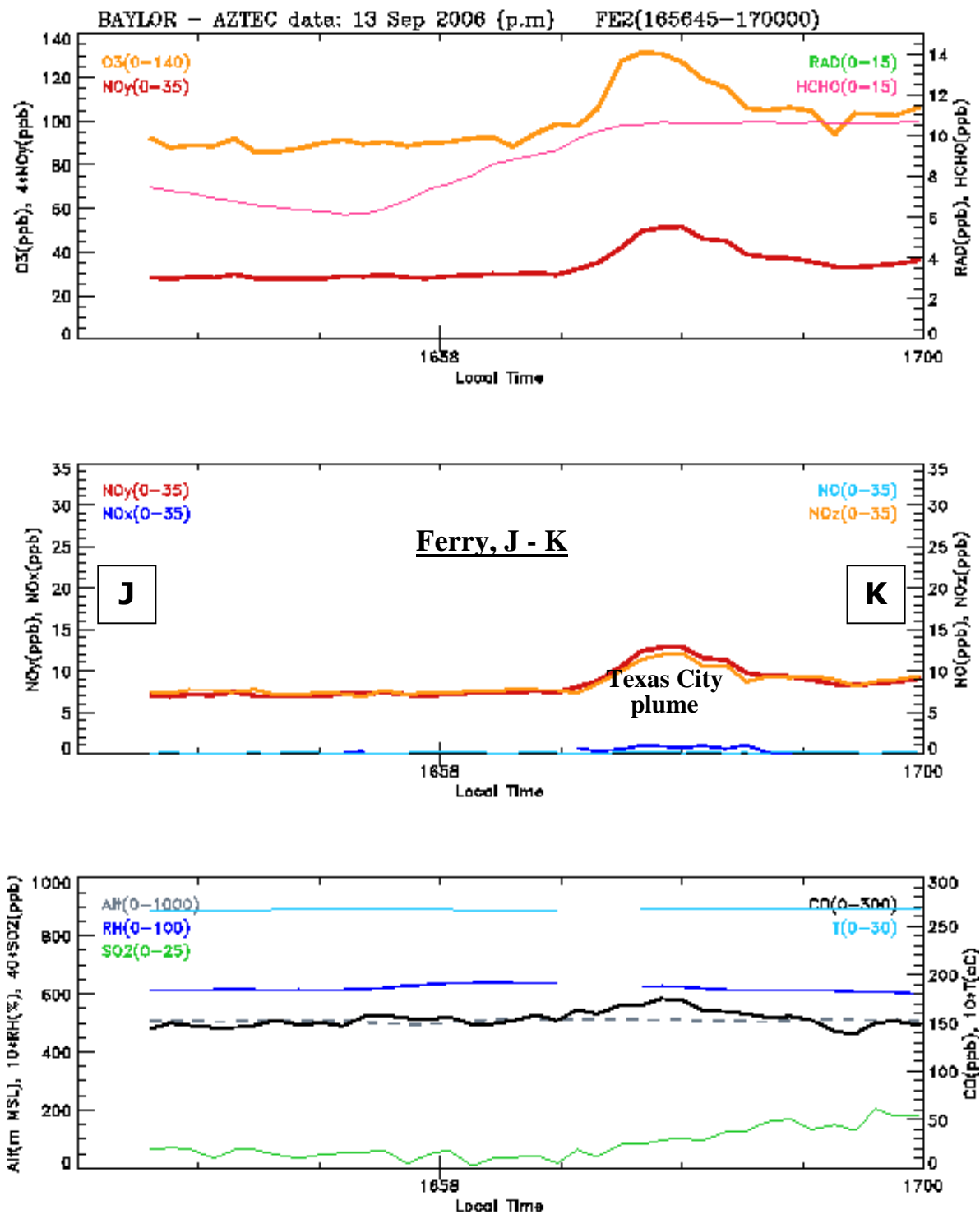


Figure 6.37 Time series data of Aztec in the afternoon flight:
 NO_y (red), RAD (green), HCHO (pink), and ozone (orange) in the upper panel;
 NO_y (red), NO_x (dark blue), NO (light blue), and NO_z (orange) in the middle panel; and,
 ALT (broken black), CO (solid black), RH (dark blue), T (light blue), and SO₂ (green) in the lower panel.

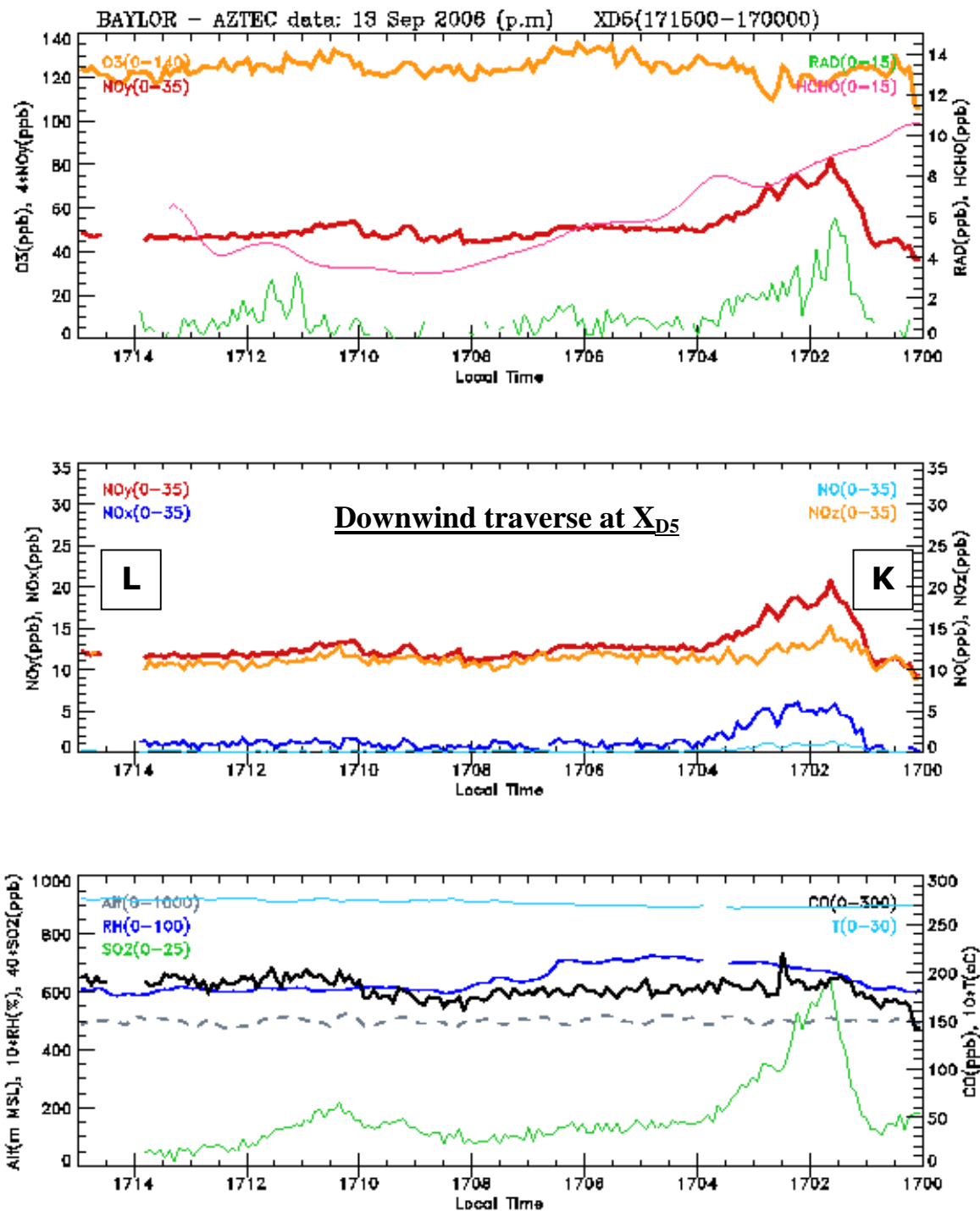


Figure 6.38 Time series data of Aztec in the afternoon flight:
 NO_y (red), RAD (green), HCHO (pink), and ozone (orange) in the upper panel;
 NO_y (red), NO_x (dark blue), NO (light blue), and NO_z (orange) in the middle panel; and,
 ALT (broken black), CO (solid black), RH (dark blue), T (light blue), and SO₂ (green) in the lower panel .
 As with all traverse data, the plots are from west to east.

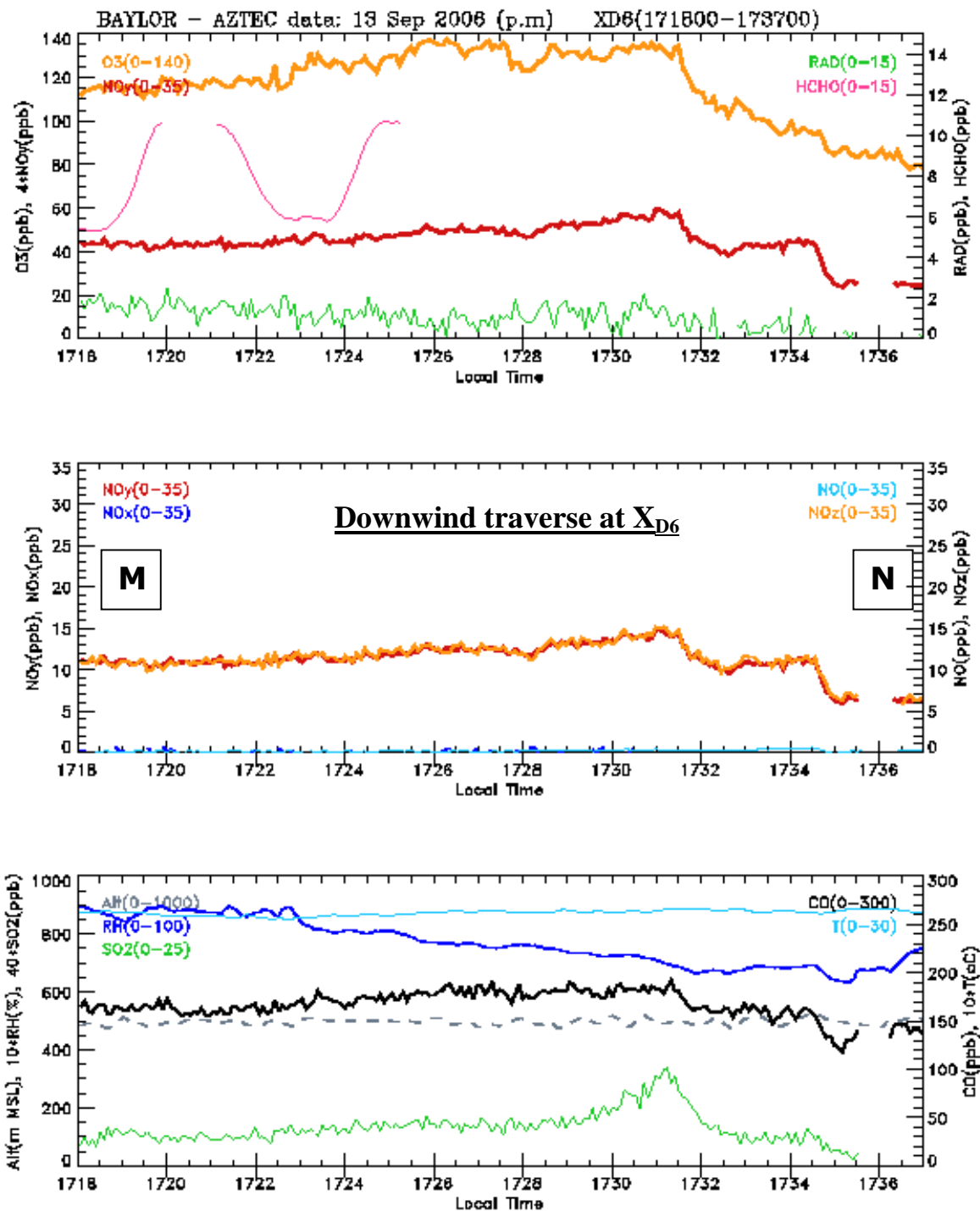


Figure 6.39 Time series data of Aztec in the afternoon flight:
 NO_y (red), RAD (green), HCHO (pink), and ozone (orange) in the upper panel;
 NO_y (red), NO_x (dark blue), NO (light blue), and NO_z (orange) in the middle panel; and,
 ALT (broken black), CO (solid black), RH (dark blue), T (light blue), and SO₂ (green) in the lower panel.
 As with all traverse data, the plots are from west to east.

Table 6-5 NOAA WP-3 Flight Log, 13 Sep 2006
Houston Component

~1146	Take-off, EFD
1146 – 1200	Ferry EFD – A (Climb from ground to ~3350m, 1146-1157)
1200 – 1214	Ferry continued A – B (Climb down, ~3350m to 650m, 1207 – 1213)
1214 – 122645	Long traverse B – C (X_U) upwind of HSC (~800m) & downtown (~ 1000m msl)
1227 – 122845	Ferry C – D
1229 – 124230	Long traverse D – E (X_{D1}) just downwind of downtown (~650m) & downwind of HSC (~800m)
124230 – 124530	Ferry E – F (~650m)
124540 – 125830	Long traverse F – G (X_{D2}) downwind of HSC & downtown (~650m)
125830 – 130515	Ferry G – H (~650m)
130515 – 132215	Long traverse H – I (X_{D3}) downwind of downtown & HSC (@ heights zig-zagging between ~200 and 2500 m msl)
132215 – 1330 – 1345	Ferry from I – J – K, then on to Dallas

Return Leg from Dallas (in Houston area)

1730 – 1735 – 1740 - 1745	Ferry L – M – N - EFD
---------------------------	-----------------------

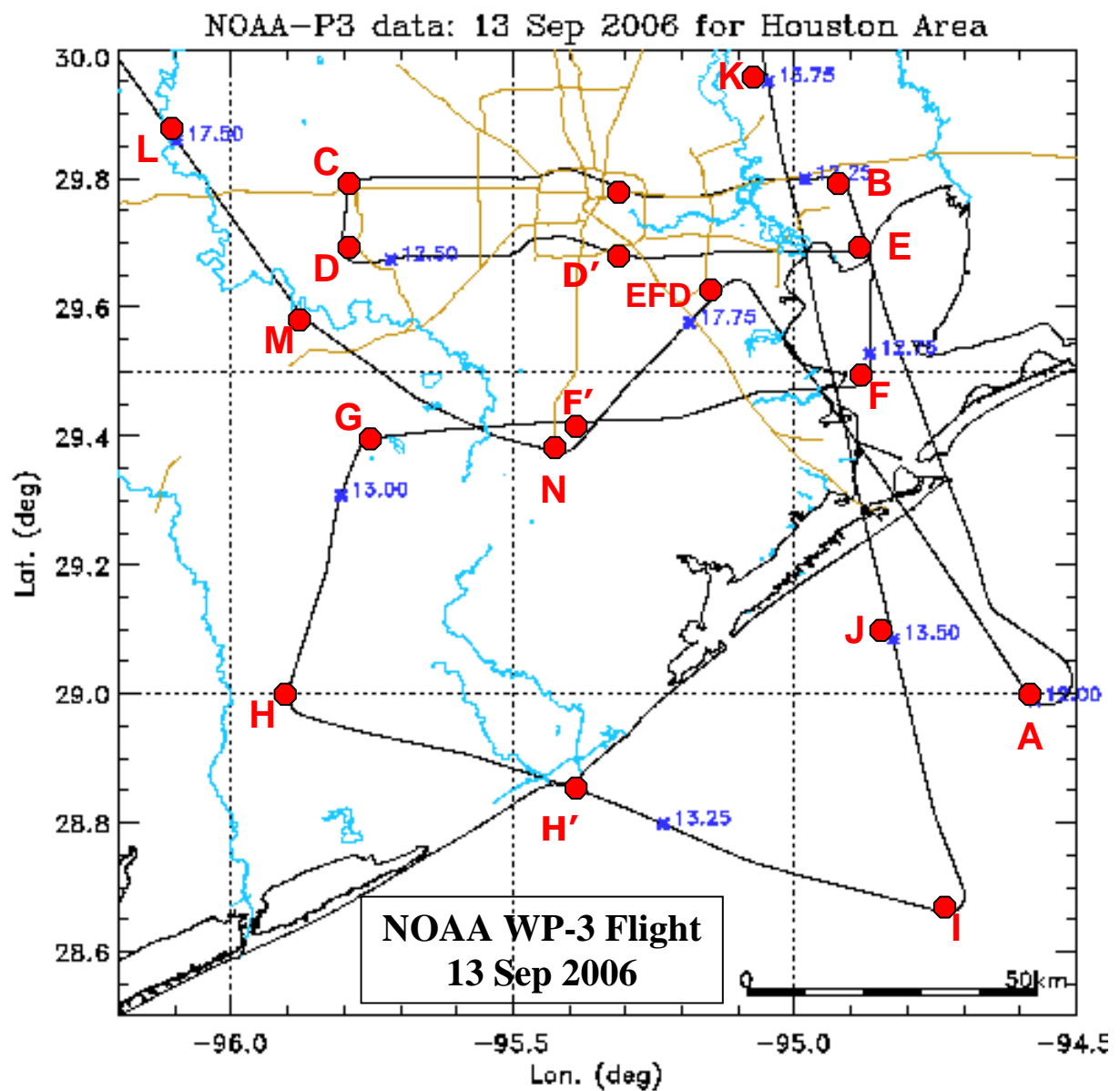


Figure 6.40 Flight track of the NOAA-P3 during the Houston portion of its flight on 13 September 2006.

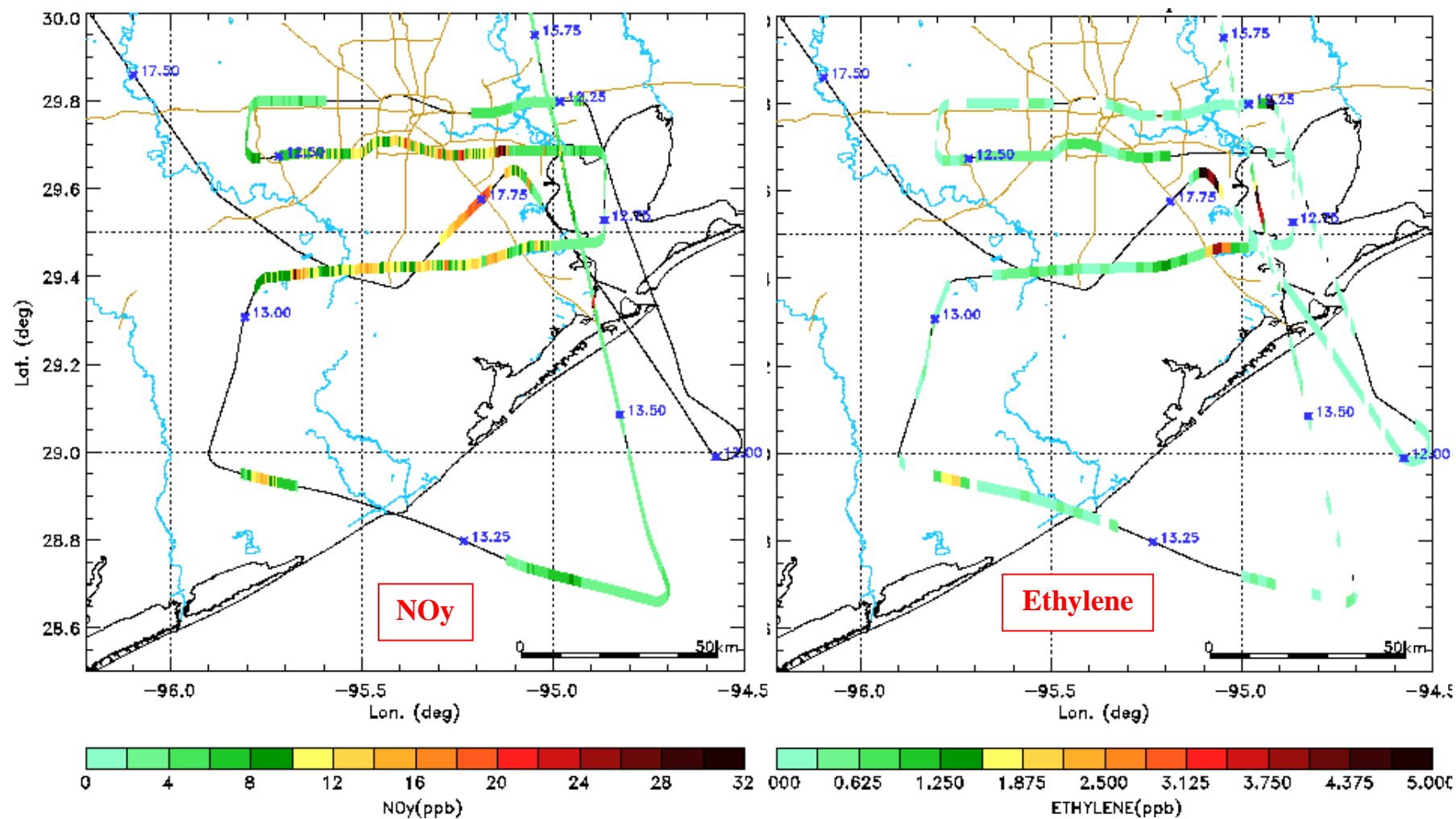


Figure 6.41 Maps of the NOAA P-3 flight of 13 September 2006 with concentrations of NOy and ethylene plotted along the flight track.

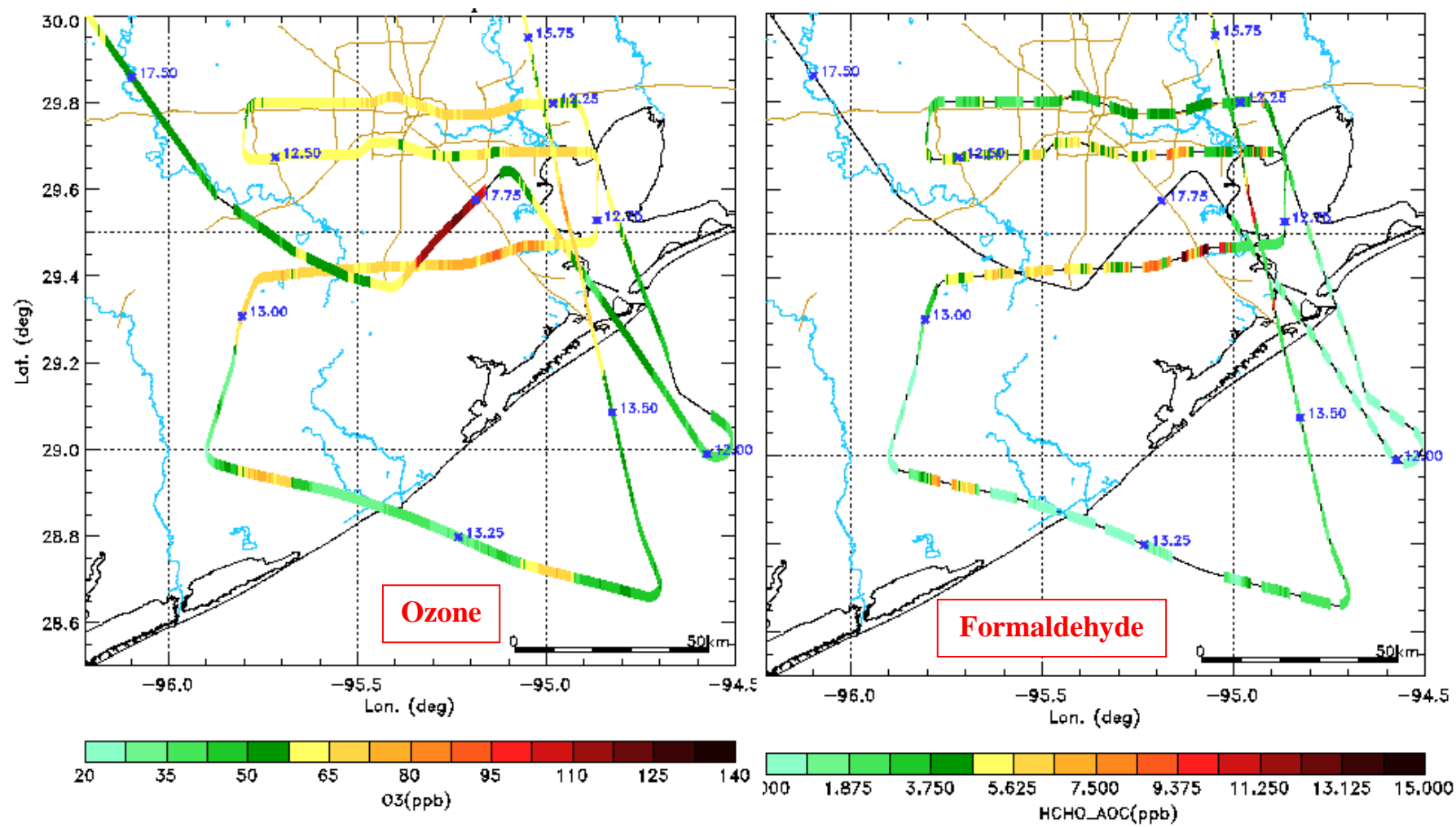


Figure 6.42 Maps of the NOAA P-3 flight of 13 September 2006 with concentrations of ozone and formaldehyde (1s resolution) plotted along the flight track.

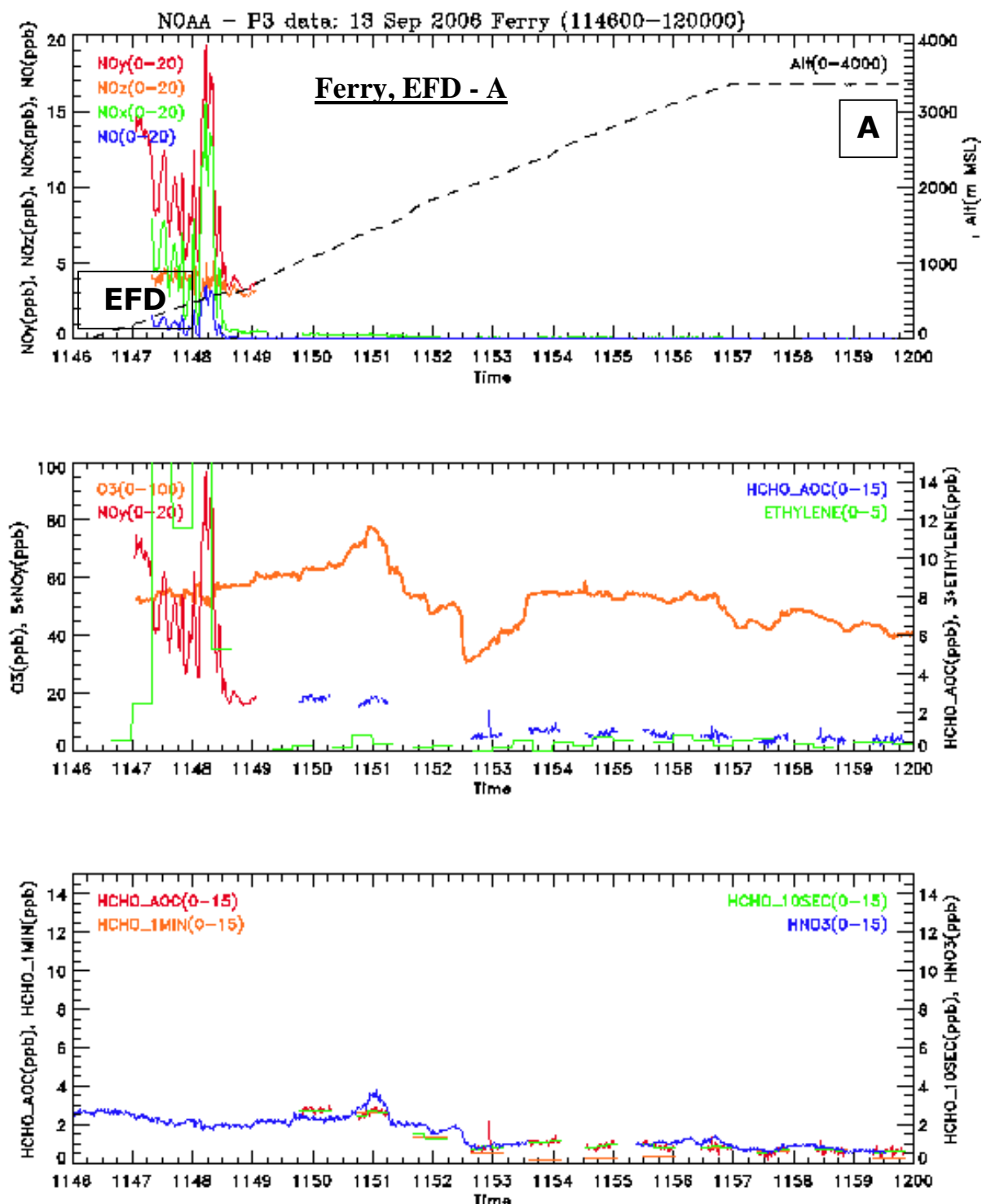


Figure 6.43 Time series data of the P-3 flight of 13 September 2006.
 Upper panel: NOy (red), NOx (green), NO (dark blue), NOz (orange) and ALT (broken black);
 Middle panel: NOy (red), ethylene (green), ozone (orange), and HCHO_1s (blue); and,
 Lower panel: HNO3 (blue), HCHO_1s (red), HCHO_10s (green), HCHO_1min (orange).

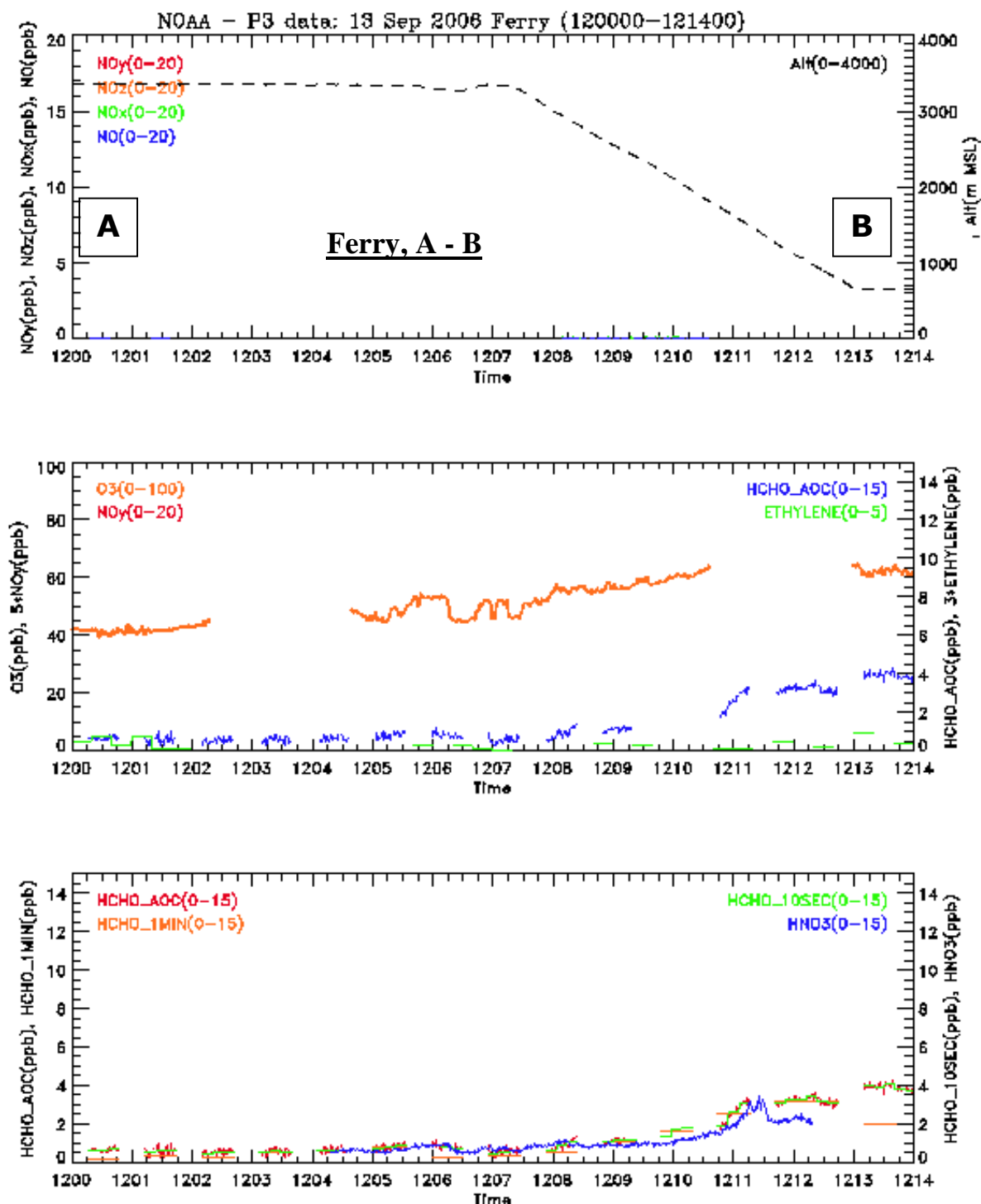


Figure 6.44 Time series data of the P-3 flight of 13 September 2006.

Upper panel: NOy (red), NOx (green), NO (dark blue), NOz (orange) and ALT (broken black);

Middle panel: NOy (red), ethylene (green), ozone (orange), and HCHO_1s (blue); and,

Lower panel: HNO3 (blue), HCHO_1s (red), HCHO_10s (green), HCHO_1min (orange).

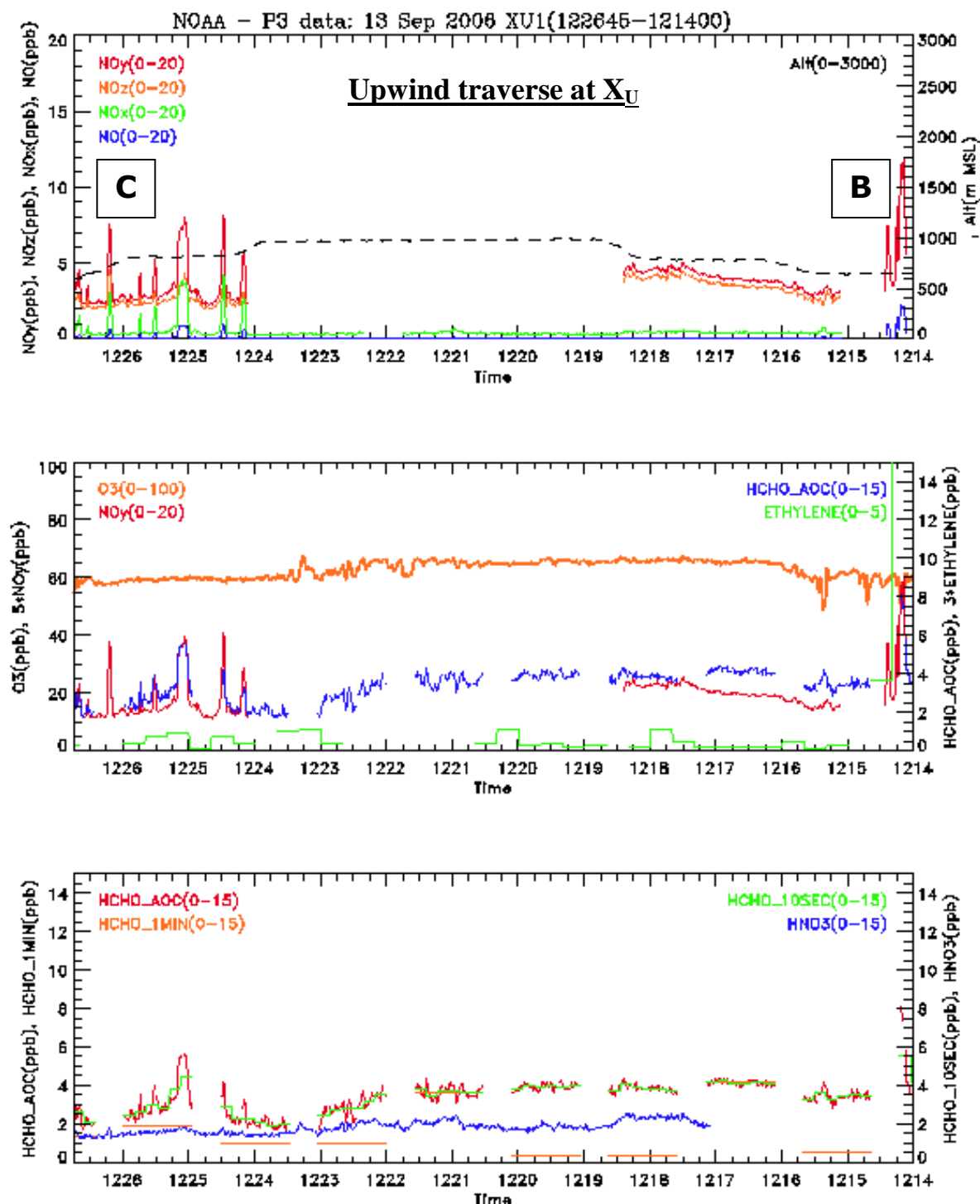


Figure 6.45 Time series data of the P-3 flight of 13 September 2006.

Upper panel: NOy (red), NOx (green), NO (dark blue), NOz (orange) and ALT (broken black);

Middle panel: NOy (red), ethylene (green), ozone (orange), and HCHO_1s (blue); and,

Lower panel: HNO3 (blue), HCHO_1s (red), HCHO_10s (green), HCHO_1min (orange).

All traverse data are from west to east.

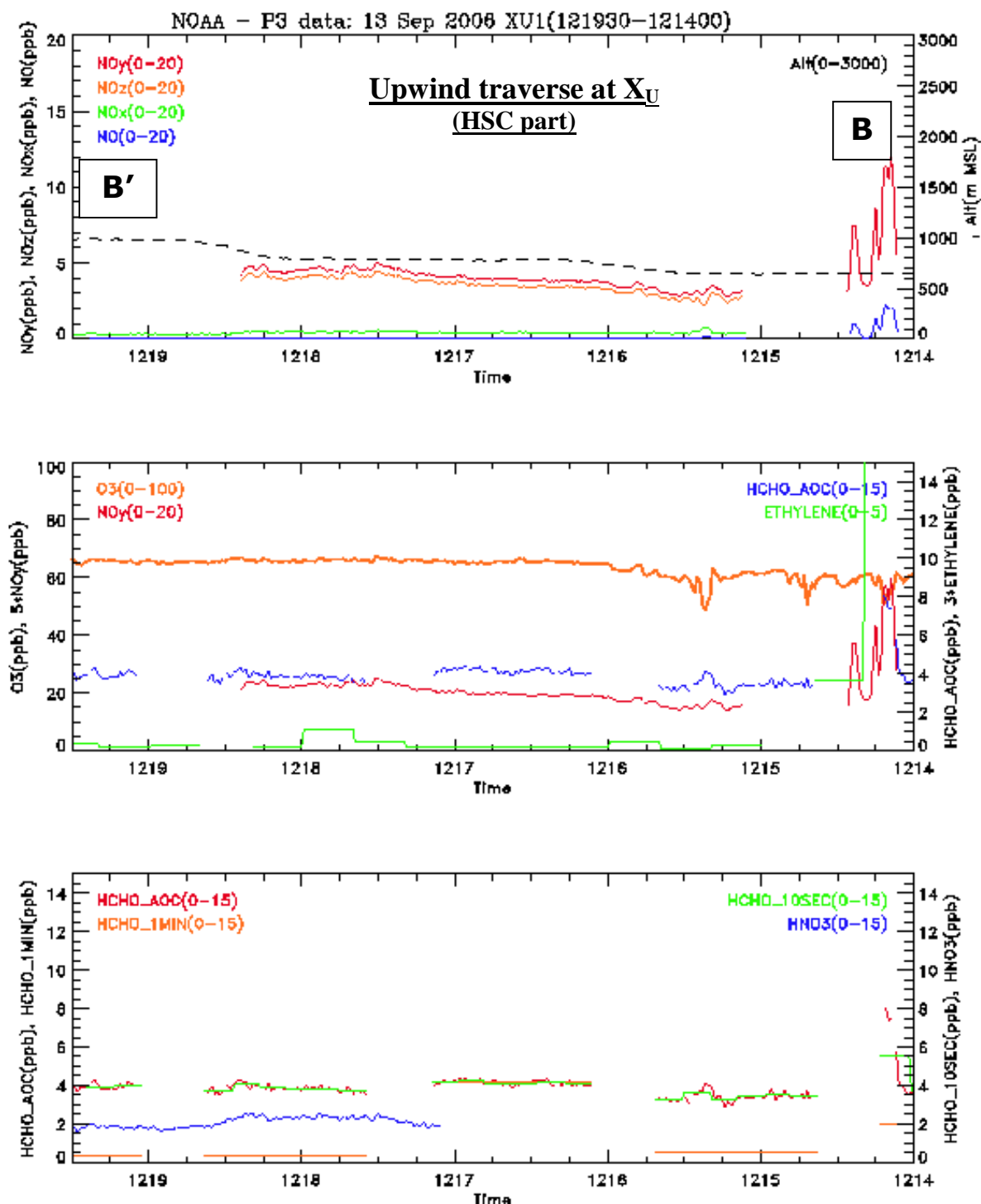


Figure 6.46 Time series data of the P-3 flight of 13 September 2006.

Upper panel: NO_y (red), NO_x (green), NO (dark blue), NO_z (orange) and ALT (broken black);

Middle panel: NO_y (red), ethylene (green), ozone (orange), and HCHO_1s (blue); and,

Lower panel: HNO₃ (blue), HCHO_1s (red), HCHO_10s (green), HCHO_1min (orange).

All traverse data are from west to east.

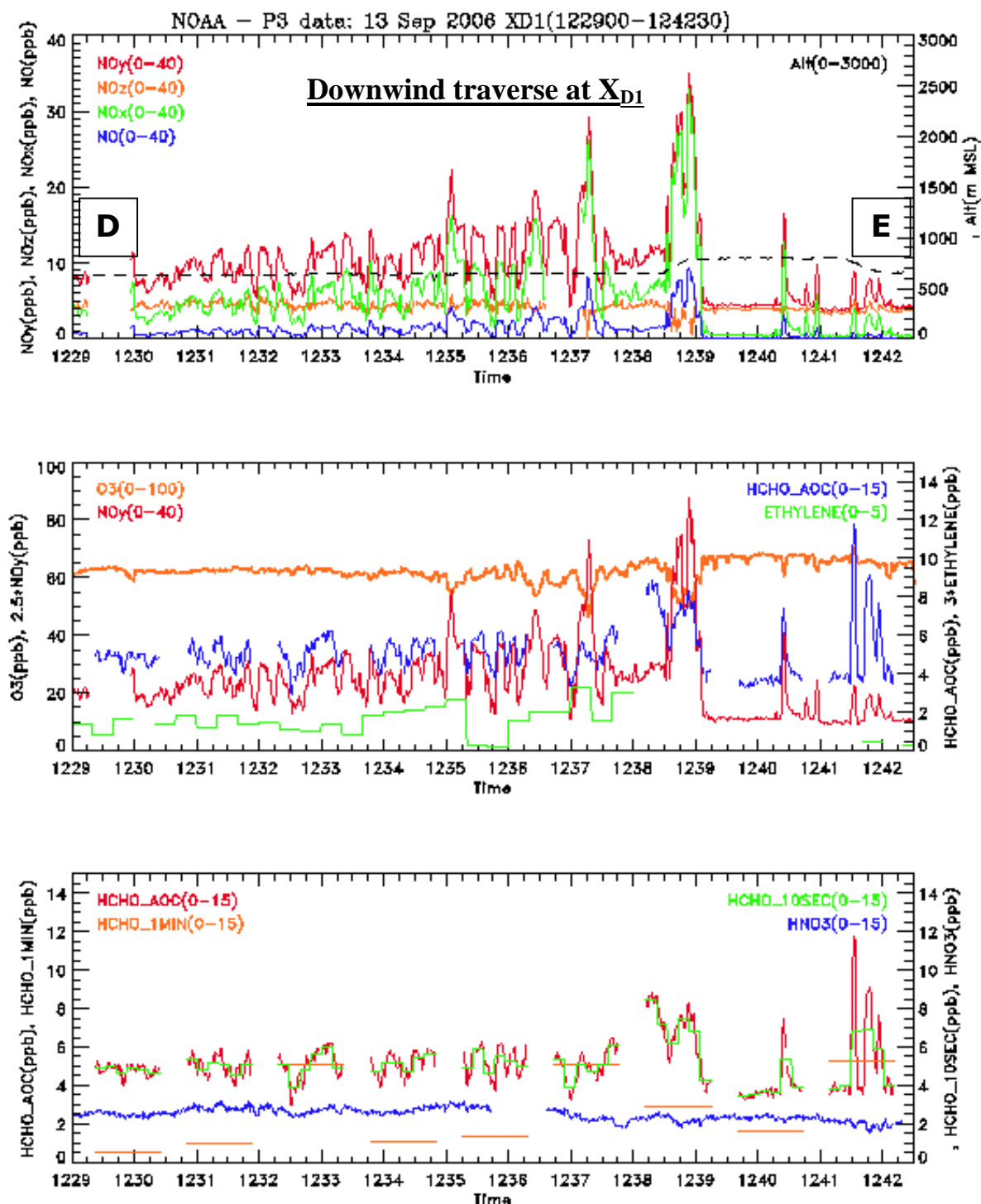


Figure 6.47 Time series data of the P-3 flight of 13 September 2006.

Upper panel: NO_y (red), NO_x (green), NO (dark blue), NO_z (orange) and ALT (broken black);

Middle panel: NO_y (red), ethylene (green), ozone (orange), and HCHO_1s (blue); and,

Lower panel: HNO₃ (blue), HCHO_1s (red), HCHO_10s (green), HCHO_1min (orange).

All traverse data are from west to east.

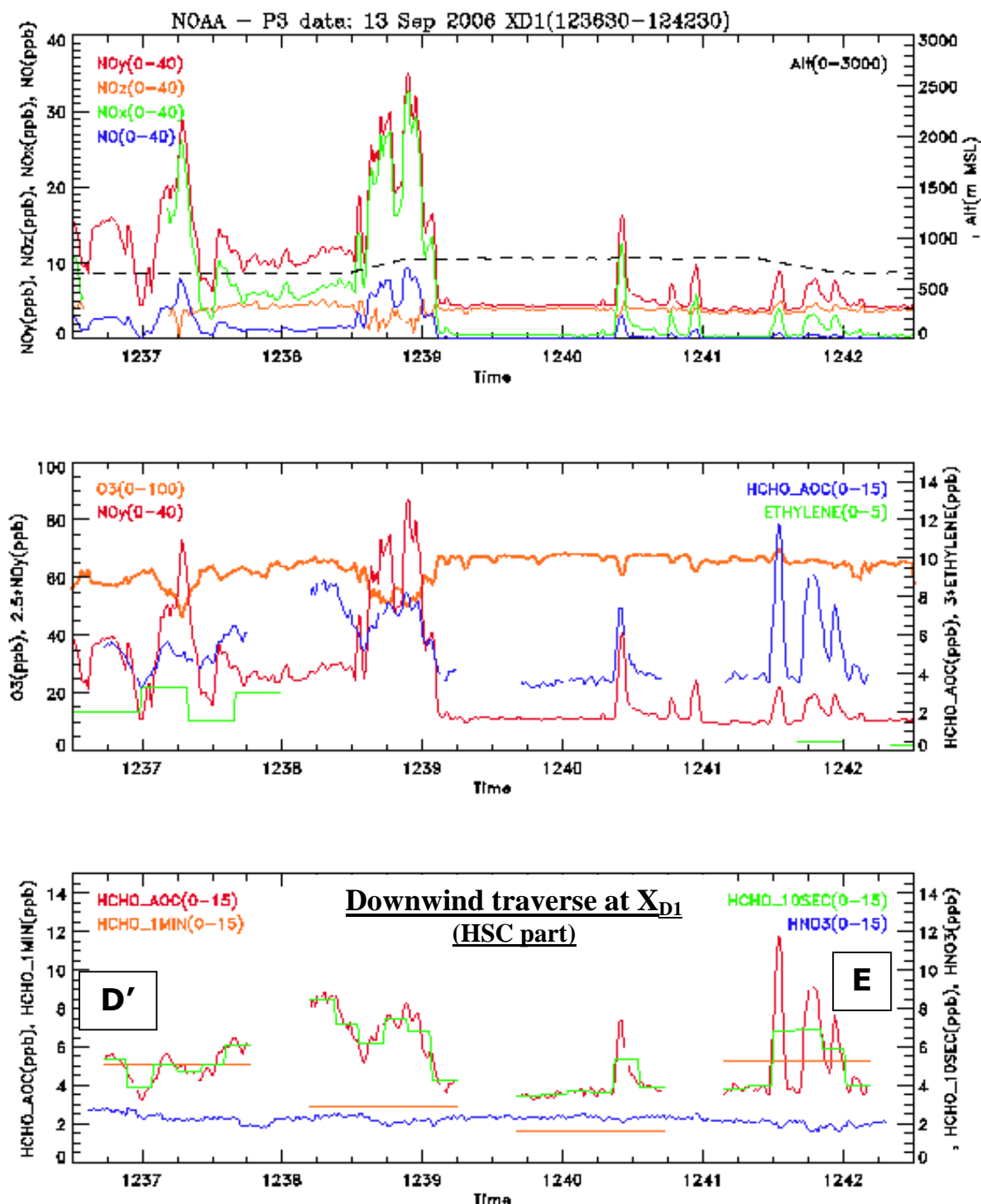


Figure 6.48 Time series data of the P-3 flight of 13 September 2006.
 Upper panel: NOy (red), NOx (green), NO (dark blue), NOz (orange) and ALT (broken black);
 Middle panel: NOy (red), ethylene (green), ozone (orange), and HCHO_1s (blue); and,
 Lower panel: HNO3 (blue), HCHO_1s (red), HCHO_10s (green), HCHO_1min (orange).
 All traverse data are from west to east.

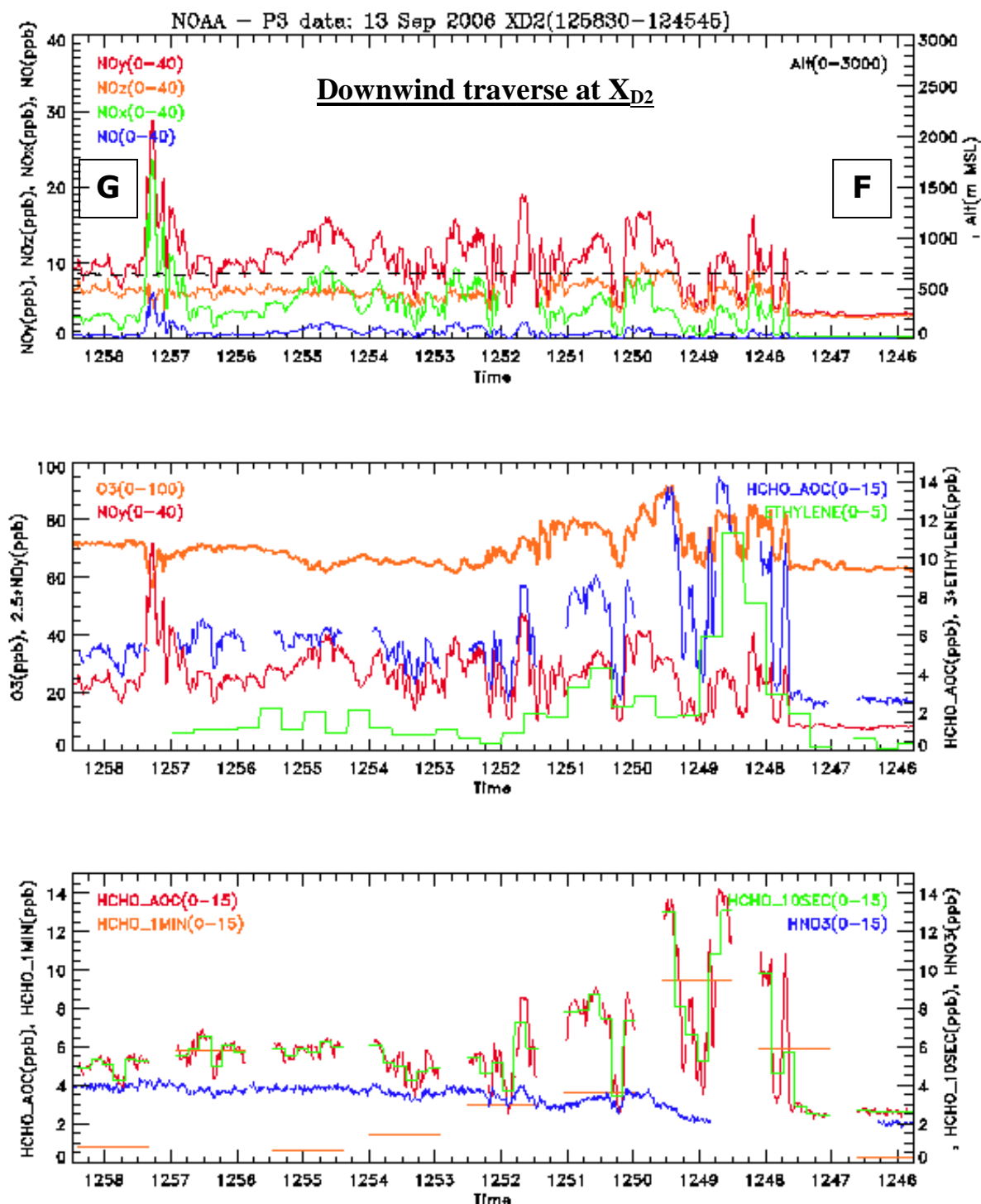


Figure 6.49 Time series data of the P-3 flight of 13 September 2006.

Upper panel: NOy (red), NOx (green), NO (dark blue), NOz (orange) and ALT (broken black);

Middle panel: NOy (red), ethylene (green), ozone (orange), and HCHO_1s (blue); and,

Lower panel: HNO3 (blue), HCHO_1s (red), HCHO_10s (green), HCHO_1min (orange).

All traverse data are from west to east.

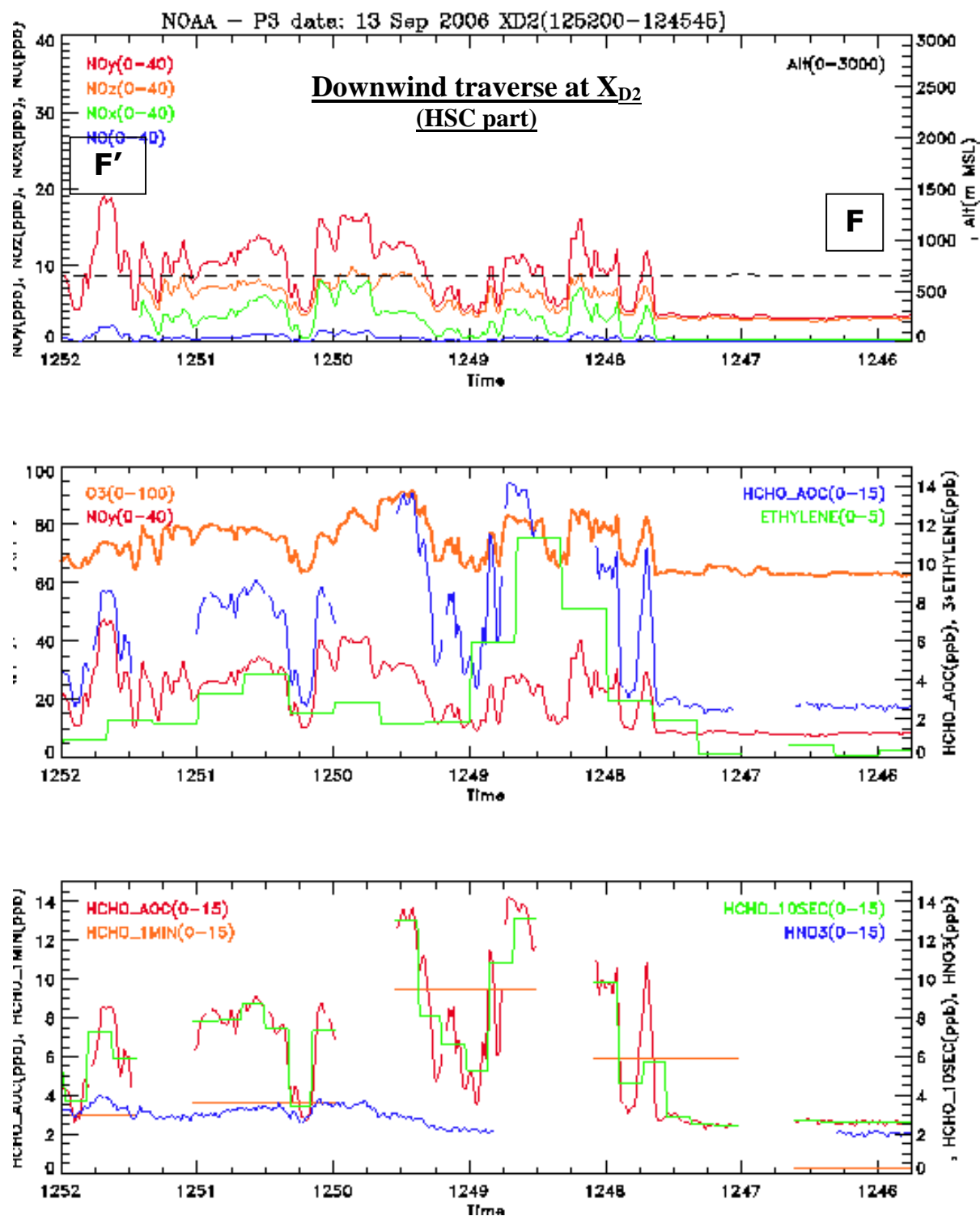


Figure 6.50 Time series data of the P-3 flight of 13 September 2006.

Upper panel: NOy (red), NOx (green), NO (dark blue), NOz (orange) and ALT (broken black);

Middle panel: NOy (red), ethylene (green), ozone (orange), and HCHO_1s (blue); and,

Lower panel: HNO₃ (blue), HCHO_1s (red), HCHO_10s (green), HCHO_1min (orange).

All traverse data are from west to east.

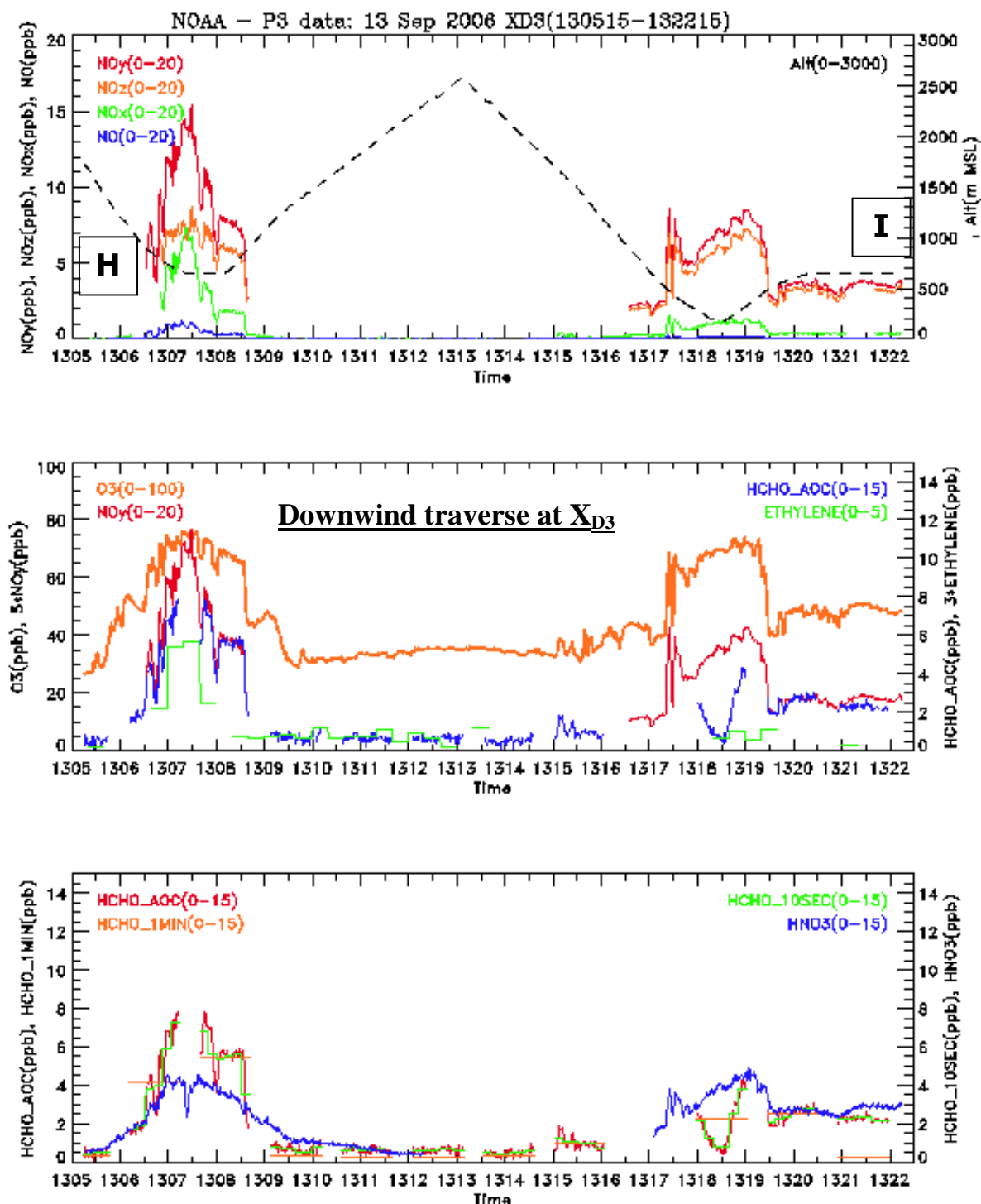


Figure 6.51 Time series data of the P-3 flight of 13 September 2006.

Upper panel: NOy (red), NOx (green), NO (dark blue), NOz (orange) and ALT (broken black);

Middle panel: NOy (red), ethylene (green), ozone (orange), and HCHO_1s (blue); and,

Lower panel: HNO3 (blue), HCHO_1s (red), HCHO_10s (green), HCHO_1min (orange).

All traverse data are from west to east.

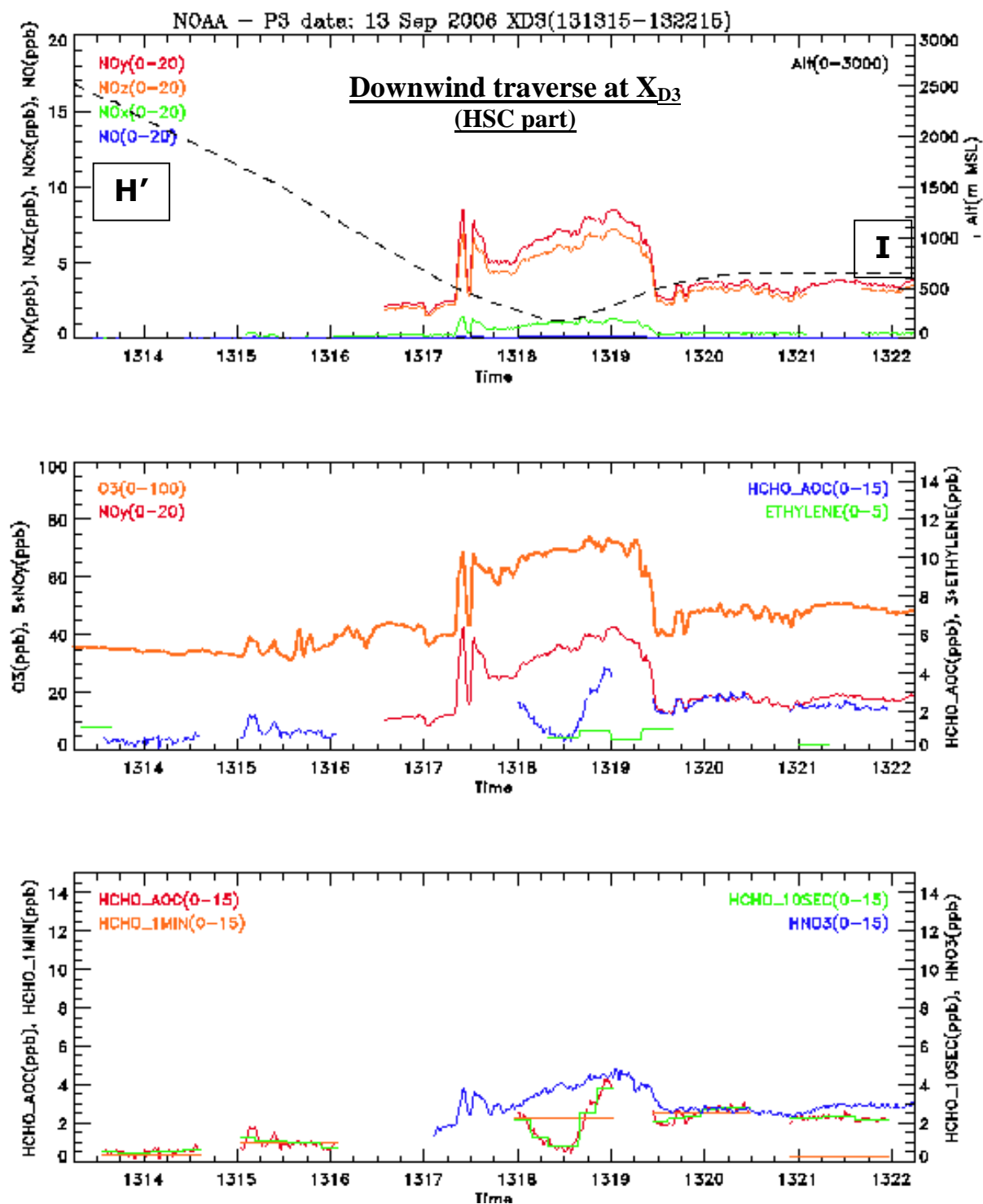


Figure 6.52 Time series data of the P-3 flight of 13 September 2006.
 Upper panel: NOy (red), NOx (green), NO (dark blue), NOz (orange) and ALT (broken black);
 Middle panel: NOy (red), ethylene (green), ozone (orange), and HCHO_1s (blue); and,
 Lower panel: HNO3 (blue), HCHO_1s (red), HCHO_10s (green), HCHO_1min (orange).
 All traverse data are from west to east.

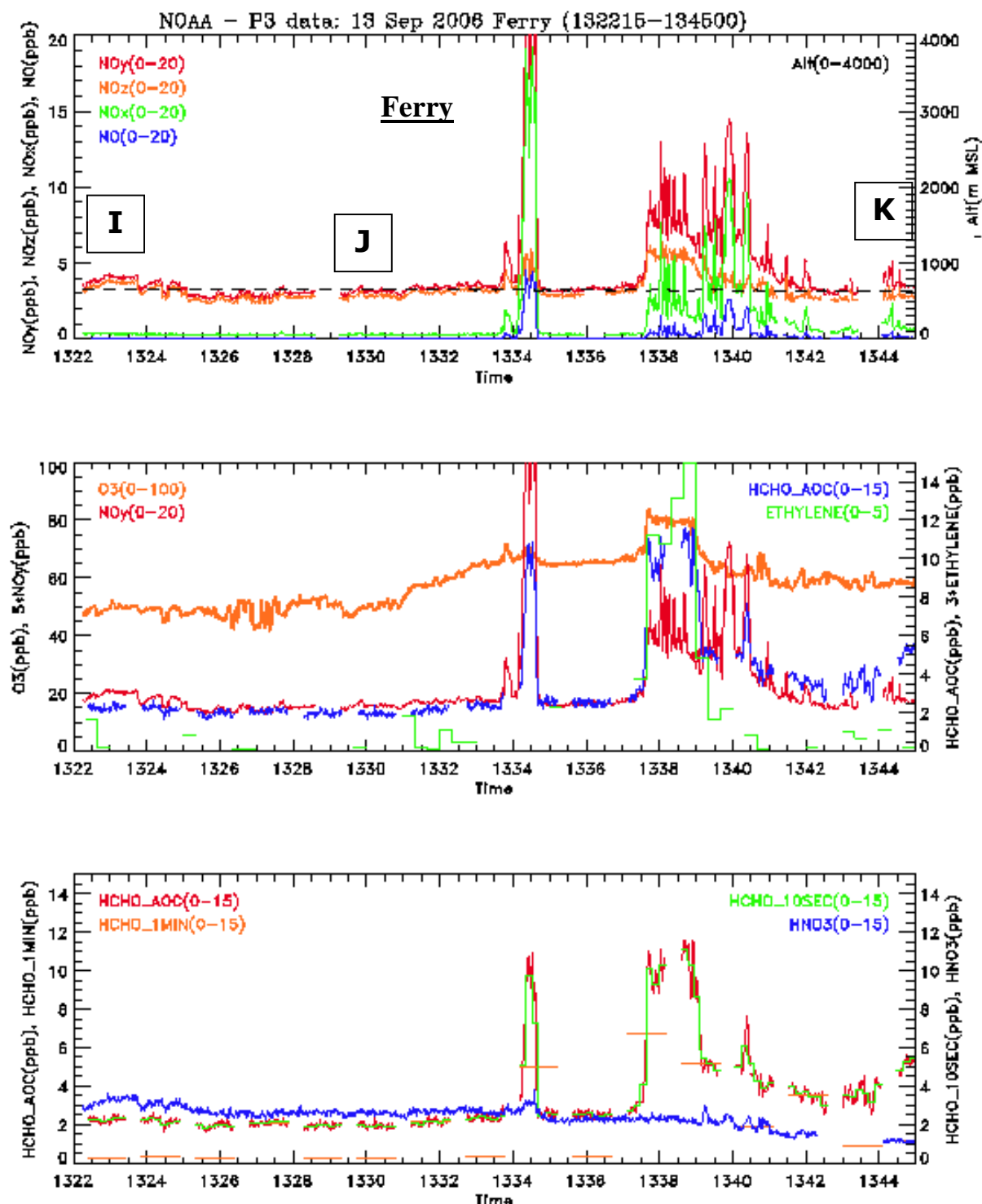


Figure 6.53 Time series data of the P-3 flight of 13 September 2006.
 Upper panel: NOy (red), NOx (green), NO (dark blue), NOz (orange) and ALT (broken black);
 Middle panel: NOy (red), ethylene (green), ozone (orange), and HCHO_1s (blue); and,
 Lower panel: HNO3 (blue), HCHO_1s (red), HCHO_10s (green), HCHO_1min (orange).
 All traverse data are from west to east.

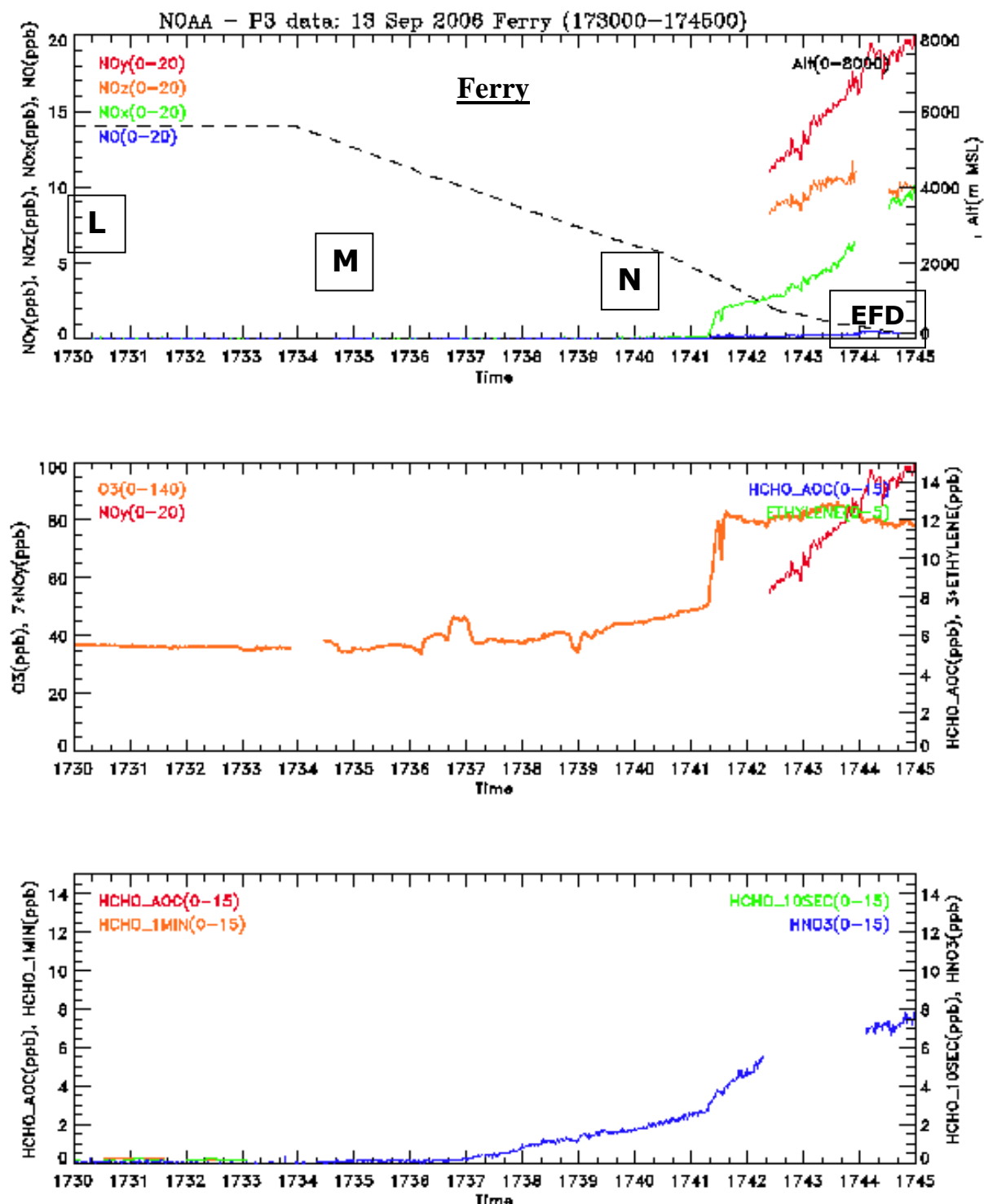


Figure 6.54 Time series data of the P-3 flight of 13 September 2006.
 Upper panel: NOy (red), NOx (green), NO (dark blue), NOz (orange) and ALT (broken black);
 Middle panel: NOy (red), ethylene (green), ozone (orange), and HCHO_1s (blue); and,
 Lower panel: HNO3 (blue), HCHO_1s (red), HCHO_10s (green), HCHO_1min (orange).
 All traverse data are from west to east.

7 DIAGNOSTIC DATA ANALYSIS

7.1 Introduction

Smog chemistry depends on reactant concentrations, which in turn, particularly for point-source plumes, and especially in the near-source regime, depend strongly on plume dynamics. The accuracy of simulation of near-source plume chemistry thus depends strongly on model spatial-temporal resolution and on the simulation of the dynamics. That is why, in this project, the emphasis was on LES and LRPM, and on an attempt to simulate the meteorology and plume dynamics at high resolution. Also, since this project was focused on TDEV based on diagnostic modeling, i.e., on comparison of model results with field data collected continuously at high resolution (e.g., SOF and the aircraft), the model results had to be accurate enough for such comparison. One of our findings has turned out to be that, given the spatial-temporal coverage of the field data, and time limitations imposed by the contracts, our high resolution model results were simply not accurate enough for such high resolution comparison even at the meteorological and dynamical level. Much of our modeling effort was focused on an attempt to optimize the dynamical simulations. This section describes such effort.

Section 7.2 gives an overview of the RAMS model application. Section 7.3 describes the required input data. Section 7.4 describes the synoptic situation for 13 September 2006. Section 7.5 discusses the primary landuse classifications that relate to the modeling effort. Section 7.6 gives an overview of the profiler data. Section 7.7 compares the control and soil moisture model runs with observations. Section 7.8 compares the model wind profiles with the observed wind profiles. Section 7.9 compares the model mixing heights against the observed values. Section 7.10 gives a summary of the major issues raised by this modeling study. Section 7.11 provides conclusions and Section 7.12 outlines some suggestions based on this study.

7.2 Description of RAMS Model Application

7.2.1 Overview of model application

The Regional Atmospheric Modeling System (RAMS) (Pielke et al. 1992) was chosen to perform the meteorological simulations in the Houston area for this component of the TexAQS-II project because our LES model is the RAMS-LES. Version 6.0 was used (with June 8, 2007 updates) as obtained from the vendor website (<http://atmet.com/>). A description of the history of the development of this three-dimensional primitive equation model can be found in the User's Guide which is available at the source website. The RAMS model has been applied over a broad range of circulations and horizontal mesh sizes. Examples of recent published work include Zhong and Fast (2003) who compared a nested RAMS simulation against other models, and Gopalakrishnan and Avissar (2000) who used the RAMS model in a Large Eddy Simulation (LES) mode with a horizontal resolution of 120 m and cyclic boundary conditions to study the impact of surface properties on dispersion. The work attempted in this project was in one sense a reflection of both the studies just cited in that we employed a nested simulation centered over the Houston Ship Channel (HSC), with the innermost grid having a LES resolution of 150 m. The LES resolution of the interior grid was required to realistically simulate the transport and dispersion of the large point sources near the HSC area. Our previous work had also linked the RAMS-LES model with detailed atmospheric chemistry in the model UAH-LESchem.

7.2.2 Nested grid setup and model options chosen

Table 7-1 describes the 5 nested grids used for this modeling exercise with the outermost grid having a horizontal resolution of about 12 km and an innermost (LES) grid having a horizontal resolution of 150 m. The vertical coordinate in RAMS is a terrain-following σ_H system defined in Eq. (1), where H is a scale height of about 12 km at which the sigma-h levels are flat, E is the terrain height above mean sea level (MSL), and Z is the three-dimensional height field (MSL). Table 7.2 gives the σ_H values used for all the grids. The vertical grid is a staggered grid, with the mesh size increasing by 12% in each succeeding cell upwards, until it reaches a size of 1 km. Thereafter, it is held constant at 1 km. About twenty levels exist below σ_H values of 1 km and with the maximum layer thicknesses of 1 km being attained at about σ_H of 9 km. Table 7-3 shows some of the selections required in the “RAMSIN” file which controls the model simulations. Of those parameters listed, perhaps the most important were the choices for the vertical eddy diffusion. For all of the grid meshes except for the LES grid, the Mellor and Yamada (1982) scheme was chosen which is a so-called level 2.5 scheme. For the LES 150-m grid the Deardorff (1980) scheme was chosen since the horizontal and vertical dimensions of the grid cells in the boundary layer have comparable size.

Table 7-1 Nested grid arrangement for RAMS-LES simulations over the Houston Ship channel. NX is the number of west-east grid points, NY is the number of north-south grid points, NZ is the number of vertical levels, and DX is the horizontal grid mesh size in meters.

Grid Number	NX	NY	NZ	DX
1	64	38	40	12,150
2	92	53	40	4,050
3	137	77	40	1,350
4	200	113	40	450
5	296	164	40	150

$$(1) \quad \sigma_h = \frac{H(Z - E)}{(H - E)}$$

Table 7-2 Sigma-h grid for horizontal wind components and scalars. Levels are labeled by Grid Cell Number (GCN) from 1 (below ground) to 40 (top of model domain). Sigma-h values corresponding to each GCN are in the columns to the right of the GCN values.

GCN	sigma-h	GCN	sigma-h	GCN	sigma-h	GCN	sigma-h
1	-9.18	11	322.46	21	1352.48	31	4551.58
2	9.72	12	381.15	22	1534.78	32	5117.77
3	30.88	13	446.89	23	1738.95	33	5751.90
4	54.59	14	520.52	24	1967.63	34	6462.13
5	81.14	15	602.98	25	2223.74	35	7257.58
6	110.88	16	695.34	26	2510.59	36	8151.70
7	144.18	17	798.78	27	2831.86	37	9129.59
8	181.48	18	914.63	28	3191.69	38	10133.27
9	223.26	19	1044.39	29	3594.69	39	11133.27
10	270.05	20	1189.72	30	4046.05	40	12133.27

Table 7-3 Selected model parameters and their values chosen for the HSC modeling.

MODEL PARAMETER	SPECIFIED VALUE(S)
Map Projection	Polar Stereographic, Centered over HSC
Time Step	30 s for 12-km grid
Thickness of Lowest Model Layer	~ 20 m
Ratio of Consecutive Model Layer Thicknesses	1.12
Maximum Model Layer Thickness	1000 m
Minimum Nudging Time Scale (12-km grid, lateral boundaries)	300 s
Maximum Nudging Time Scale (12-km grid, center of domain)	3600 s
Resolution of Default Land Use Data	30 s (about 1 km)
Resolution of Default NDVI Data	30 s (about 1 km)
Resolution of Default Soil Data	2 minutes (about 3 km)
Resolution of Default SST Data	1 degree (about 100 km)
Resolution of Default Terrain Data	30 s (about 1 km)
Shortwave Radiation Parameterization	Chen and Cotton (1983)
Longwave Radiation Parameterization	Chen and Cotton (1983)
Vertical Eddy Diffusion (all grids except interior grid)	Mellor and Yamada (1982)
Vertical Eddy Diffusion (interior grid)	Deardorff (1980)
Water Complexity	water vapor, no clouds, no precipitation

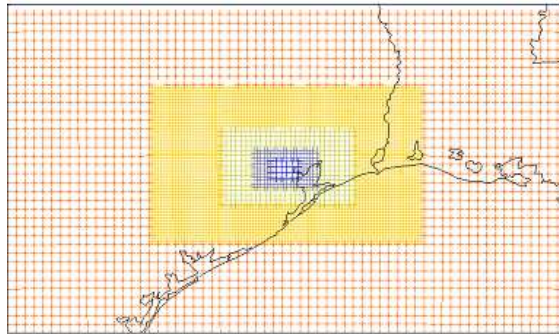


Figure 7.1 Current nested-grid arrangement for the LES-CHEM simulations for the Houston ship channel. Grid number (as in Table 7-1), horizontal resolution, and color are as follows: (1, 12.15-km, red), (2, 4.05-km, orange), (3, 1.35-km, green), (4, 450-m, dull-blue), and (5, 150-m, bright blue). Not all the grid points are plotted.

Figure 7.1 shows the nested grid arrangement described in Table 7-1 with horizontal grid resolutions of 12.150 km (orange), 4.05 km (yellow), 1.35 km (green), 450 m (light blue), and 150 m (dark blue). Nudging towards the observed analyses was only performed on the outermost (12.150 km) grid via a quadratic weight function with the highest nudging done near the borders and decreasing toward the center. Nudging was not done on the other grids because the horizontal and/or temporal resolution of the observed data was not sufficient.

7.3 Required input data

The National Oceanic and Atmospheric Administration (NOAA) National Center for Environmental Prediction (NCEP) North American Mesoscale Model (NAM) analysis data was used to provide the so-called “first-guess” fields for the RAMS initialization. This data was obtained from the NOAA National Operational Model Archive and Distribution System (NOMADS) (the front page for this site is at <http://nomads.ncdc.noaa.gov>). The RAMS ISentropic ANalysis (ISAN) package was used to create the initial states for each of the grids and to provide nudging fields for the coarse 12.150-km grid. Fields of the horizontal wind components, temperature, water vapor mixing ratio, and pressure are interpolated horizontally

and vertically from the NAM grid locations to two types of RAMS grids. The two RAMS grids share the same horizontal structure but differ in the vertical grid. One is a σ_H grid and the other is an isentropic (levels of constant potential temperature) grid. The final analysis for each grid column uses the isentropic values exclusively for higher levels, the σ_H values exclusively for levels near the ground, and a linear combination of the two for the transition zone between the two zones. Five types of upper-air data were available to modify the first-guess NAM fields: 1) standard National Weather Service (NWS) rawinsondes, 2) special rawinsondes taken at the University of Houston, 3) Radar Wind Profiler (RWP) soundings of wind speed and wind direction, 4) Radio Acoustic Sounding System (RASS) soundings of virtual temperature, and 5) mini-sodar soundings of wind speed and wind direction. Types 1-4 were utilized – time did not allow type 5 to be utilized. The default RAMS ISAN code did not allow for time interpolation of the model first-guess fields (the NAM data for our application). Substantial time was required to make the code changes to the ISAN system to allow for time interpolation to hourly values which in turn allowed the use of the (mainly) hourly RWP and RASS hourly-averaged soundings. The special sounding data was interpolated vertically and temporally to be consistent with the ISAN package. All the sounding data was used in a Barnes analysis scheme (e.g., Koch et al 1983 and the references therein) to modify the first-guess fields within ISAN. The standard airways hourly NWS surface observations were used in three ways. In the first, they were used within the ISAN package to modify the first-guess fields close to the surface. In the second, they were utilized to create observed analyses using the Barnes scheme which were used to verify the RAMS simulations on the 12.15-km grid and to provide a means to examine the weather over the period of interest. The third way was to provide a moisture correction to the RASS profiles in order to obtain a temperature profile from the virtual temperature profile observations. Figure 7.2 provides a plot of the locations of the various upper-air data locations in the Houston area (upper), and in southeast Texas (lower). Figure 7.3 shows the locations of the standard NWS hourly observations within the RAMS 12.15-km domain.

The ISAN package uses climatological values for soil moisture and the water skin temperature. It also imposes a horizontally homogeneous vertical profile of offsets from the lowest atmospheric temperature to initialize the soil temperature. The NAM model values of soil moisture and temperature and water Sea Surface Temperature (SST) were used in place of the default values for all model grids.

The last major dataset which was incorporated in the RAMS system was a change in the land surface type information. The ISAN package for RAMS uses land surface type information that has a horizontal resolution of about 1 km. That was not sufficient resolution for our 450-m and 150-m grids. The land surface type specification is needed because it plays a major role in the generation of atmospheric turbulence, which in turn plays an important role in the transport and diffusion of atmospheric pollutants. We used the National Land Cover Dataset (NLCD) which is based on 2001 Landsat thematic mapper imagery consisting of 21 categories of land cover information at an original resolution of 30-m (Homer et al. 2004). The NLCD data had to be transformed to the RAMS polar stereographic map projection and the expected RAMS surface characteristics categories. To accomplish this required 3 steps. In the first step, one of our colleagues utilized existing GIS software to map the raw NLCD data onto a 100-m Lambert Conformal grid. The choice of the Lambert Conformal grid was determined by the scope of other local projects that were using this data. The second step involved the use and modification

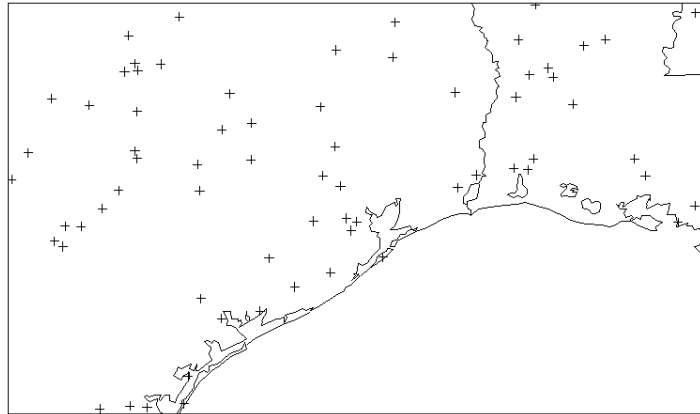


Figure 7.3 Locations of National Weather Service hourly surface observations of temperature and water vapor mixing ratio at a height of 2-m, and wind direction and wind speed at a height of 10-m. Grid domain is the 12.15-km RAMS grid.

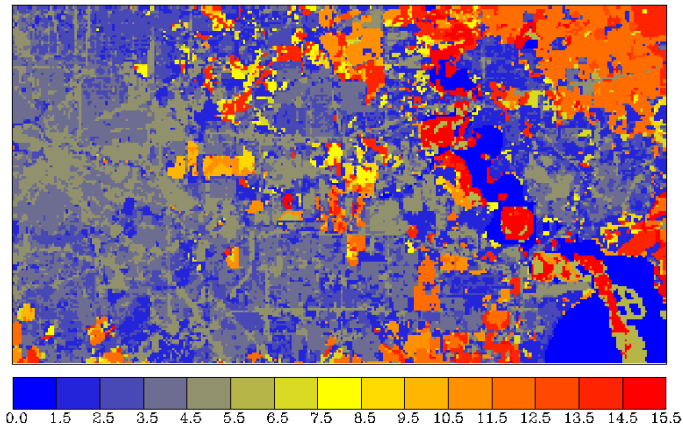


Figure 7.4 NLCD data on the 150-m RAMS grid with a polar stereographic map projection. Categories 1-15 correspond to, respectively: (1) open water, (2) developed, open space, (3) developed, low intensity, (4) developed, medium intensity, (5) developed, high intensity, (6) barren land rock/sand/clay, (7) deciduous forest, (8) evergreen forest, (9) mixed forest, (10) shrub/scrub, (11) grassland/herbaceous, (12) pasture/hay, (13) cultivated crops, (14) woody wetlands, and (15) emergent herbaceous wetlands.

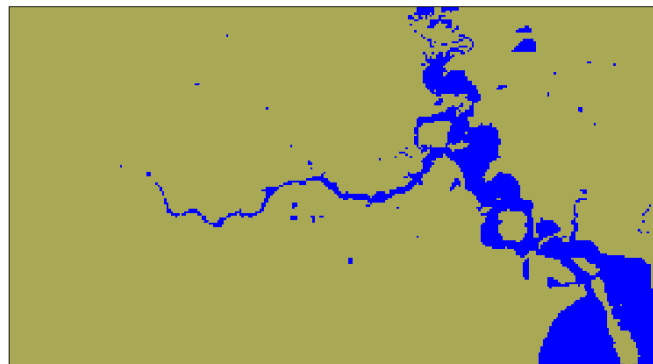


Figure 7.5 Land fraction as derived from the NLCD on the 150-m RAMS grid. Grid cells with 50% or more water surface are colored blue, all others are colored green.

7.4 Synoptic Situation on 13 September 2006

7.4.1 *Large-scale and preliminary aspects*

Figure 7.6 shows the surface analyses for the continental United States at 1200 UTC for the mornings of 12-14 September 2006 which bracket the model simulation time period of interest of 12-h starting at 1200 UTC 13 September 2006. At 1200 UTC 12 September a cold front was seen approaching southeast Texas. By 1200 UTC 13 September, the cold front has passed the Houston area and was analyzed over northern portions of the Gulf of Mexico. A large area of high pressure covered much of the central and southern Plains with a center over northern Oklahoma. By the next day, at 1200 UTC 14 September, the cold front remained analyzed over the Gulf of Mexico but with the high pressure moving northeastward to the Great Lakes region. Figure 7.7 shows precipitation estimates for the 6-h periods ending at 00, 06, 12, and 18 UTC 13 September 2006 and 00 UTC 14 September 2006. Precipitation amounts on the order of 30 mm or less fell on significant portions of the 12.15-km RAMS domain including parts of the northern, southwestern, and eastern sections. For the period 1200 UTC 13 September through 0000 UTC 14 September precipitation over land was mainly confined to the Texas Gulf coastal areas southwest of Houston including locations near Matagorda Bay and Corpus Christi and a separate area of heavier amounts over southeastern Louisiana late in the afternoon. For much of the day significant convection was occurring over parts of the Gulf Of Mexico, especially over the extreme southern portions of the 12.15-km grid domain. Figure 7.8 shows the Geostationary Operational Environmental Satellite (GOES) derived insolation for a mid-morning time of 1500 UTC and a mid-afternoon time of 2100 UTC. The morning view shows that apart from a small area of clouds west of Houston, the entire 12.15 km domain was clear except for the southern edge of the domain mainly over the Gulf of Mexico and eastern Louisiana. The afternoon view shows the same domain clear except for the same areas mentioned in the precipitation discussion with clouds maintaining their presence along the extreme southern edge of the 12.15 km domain. With the predominant northerly flow behind the cold frontal passage early on 13 September most of the 12.15-km model grid was cloud and precipitation free. For this reason as well as the additional computational demands, and the difficult challenge of simulating clouds and precipitation correctly, our model simulation has the cloud and precipitation physics “turned off”. It is possible, however, that convective inflows and/or outflows over the Gulf of Mexico affected portions of the land domain as will be discussed in the next section.

7.4.2 *Discussion of the observed analyses on the 12.15-km grid*

A Barnes analysis scheme (Koch et al 1983) was used to create analyses of 2-m temperature and water vapor mixing ratio, and 10-m winds, on the 12.15-km grid from the standard hourly airways data. These observed analyses were used for two purposes. The first, as used in this section, was to use them to obtain an idea of the near-surface weather features which affected the domain for our period of interest. The second use was to compare the RAMS model simulated values with the same variables to assess model performance on the 12.15 grid as will be discussed in section 7.7.2. For this section, as given in Figure 7.9 - Figure 7.11, observed plots of these analyses are shown for the times 1500, 1800, and 2100 UTC 13 September 2006 and 0000 UTC 14 September 2006 for the winds at 10-m, water vapor mixing ratio at 2-m, and then temperatures at 2-m, respectively.

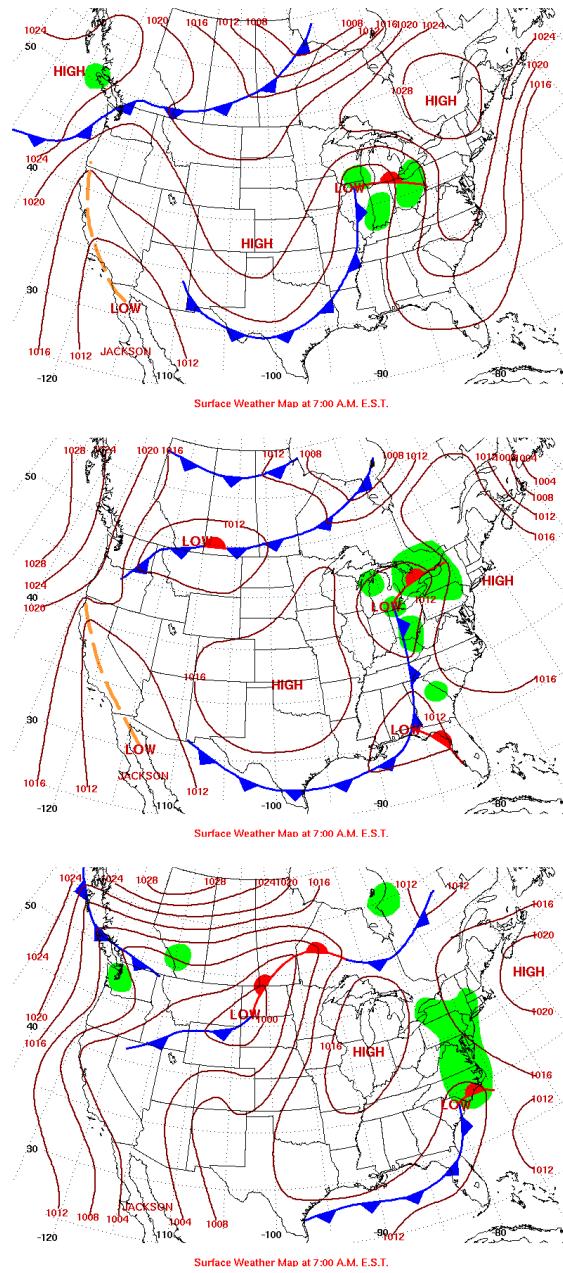


Figure 7.6 Surface weather maps for 1200 UTC for 12, 13, and 14 September 2006 (top, middle, and bottom, respectively). Maps are taken from <http://www.hpc.ncep.noaa.gov/dailywxmap/>.

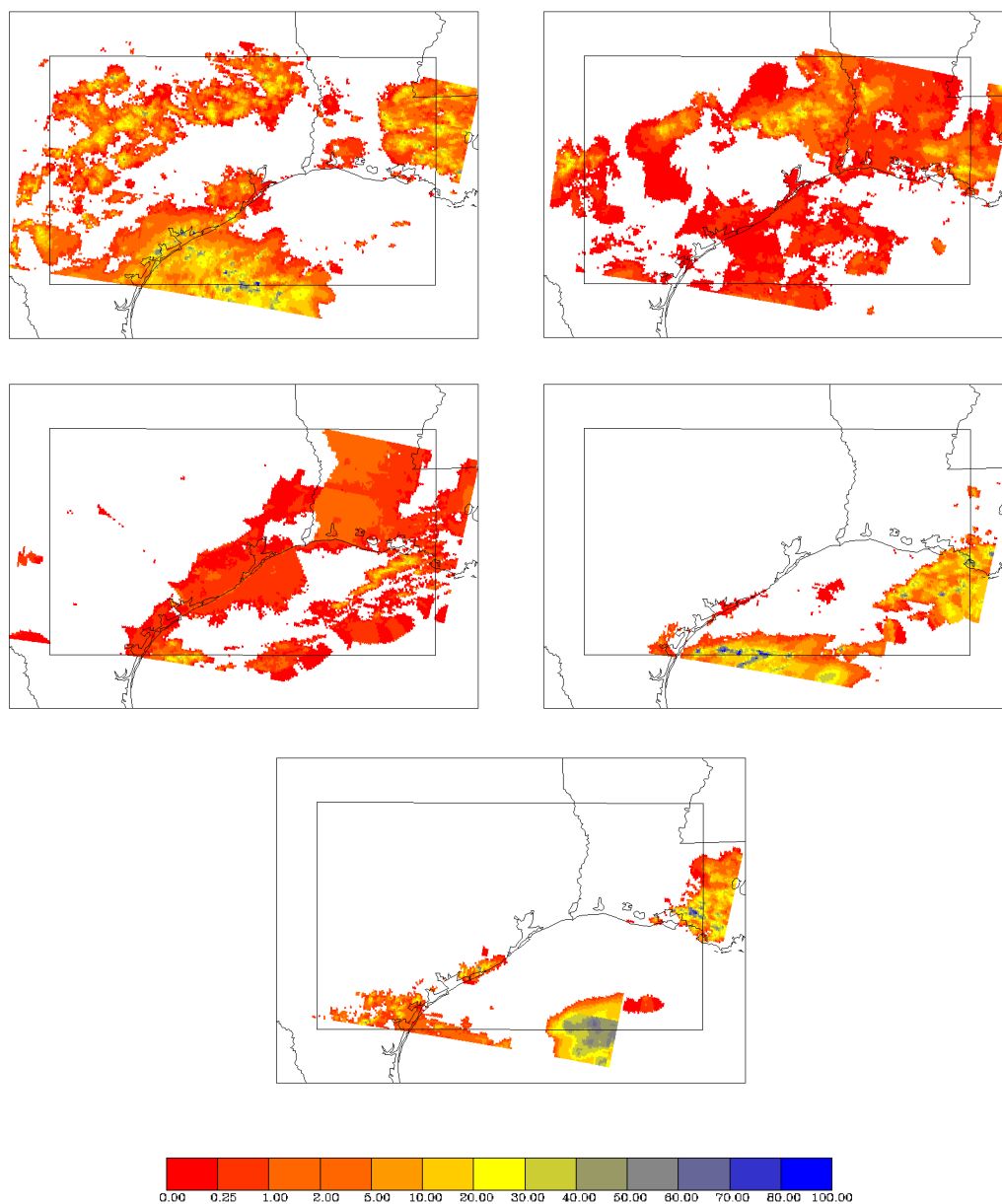


Figure 7.7 Stage IV 4-km precipitation estimates from the National Oceanic and Atmospheric Administration (NOAA) (<http://www.emc.ncep.noaa.gov/mmb/ylin/pcpanl/stage4/>) in units of mm for 6-h periods ending at 00 , 06, 12, and 18 UTC 13 September 2006 (top left, top right, middle left, and middle right, respectively) and 00 UTC 14 September 2006 (bottom). Outline of 12.15 km RAMS grid is superimposed inside each plot.

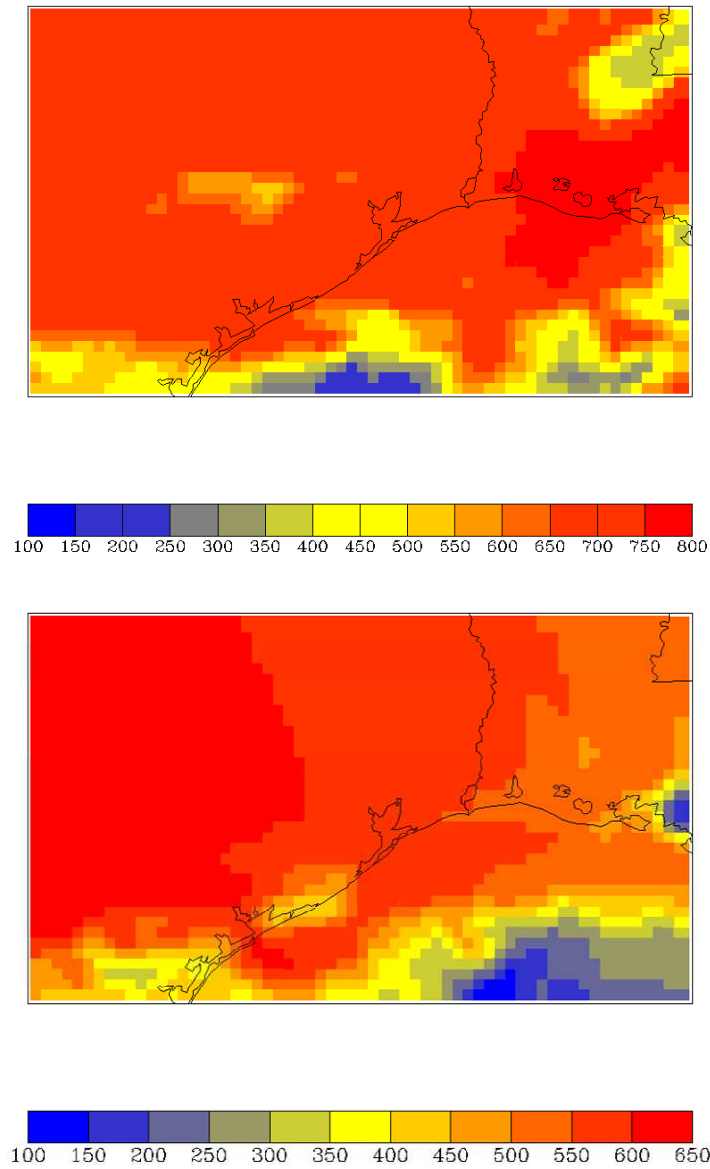


Figure 7.8 GOES-derived downward surface insolation in W m^{-2} for 1500 UTC (top) and 2100 UTC (bottom) for 13 September 2006.

Figure 7.9 shows that the predominant flow pattern at 10-m during the day on 13 September was north to northeast flow with generally decreasing wind speeds as evening approached. However, there were also some significant mesoscale features which will be briefly discussed. At 1500 UTC, a band of relatively strong winds of $5\text{--}6\text{ m s}^{-1}$ existed over the western portion of the domain. This area saw a decrease in wind speeds at the other times shown. An interesting convergence zone was observed over southeastern portions of Louisiana, with northwesterly flow to the west of the zone and light southwesterly flow to east. This would seem to hint that either the frontal zone was not as far into the Gulf of Mexico as indicated by the surface analyses in Figure 7.6, or that a weak wave was moving along the front. At 1800 UTC the latter convergence zone had shifted westward over southern Louisiana. By 2100 UTC this same zone had once again shifted back east. By the final time at 0000 UTC the wind direction over this same area in Louisiana had now shifted to the northeast. This complex sequence of events was likely due to some combination of a weak wave moving along the frontal zone in the Gulf of Mexico along with mesoscale circulations related to the convection occurring over southeastern Louisiana and the Gulf of Mexico. At this same time of 0000 UTC, southerly onshore flow is seen in the Texas coastal area from Galveston Bay southwestward to Corpus Christi. This feature could either be a sea breeze circulation or it could possibly be convective outflow from the convection occurring for most of the day over parts of the Gulf of Mexico over the southern parts of the domain.

The water vapor mixing ratio plots in Figure 7.10 show a large northwest to southeast gradient with low values to the north and the highest values along the Gulf coast. By 0000 UTC 14 September 2006, the minimum values in the northerly flow at the northern edge of the domain were near 4 g kg^{-1} , while the maximum values along the coast were near 18 g kg^{-1} . The higher values along the coast, even with northerly flow, are the result of a frontal zone which had not progressed very far south over the Gulf of Mexico, and also the result of some areas receiving significant rainfall the previous day which increased evaporation on the following day.

Figure 7.11 shows the same time sequence of analyses for 2-m temperature in $^{\circ}\text{F}$. Temperatures mainly in the 70's reached highs by the afternoon in the low to mid 90's. The plot for 0000 UTC shows the lower temperatures over the Texas coastal area from Galveston Bay southwestward to Corpus Christi in conjunction with the clouds and precipitation in that area, and the same for extreme southeastern Louisiana.

7.5 Landuse Characteristics

Figure 7.12 shows the main landuse types for the 12.15-km grid. A large area north of Houston consists of evergreen needleleaf forest. Apart from the water and urban areas, the remaining large area consists mainly of a crop/mixed farming/grassland regime. The forest area was especially important for our modeling period since the HSC is downwind of the forest area with the mainly northerly winds which occurred.

Figure 7.13 illustrates the possible refinement of the variations of the urban type when the NLCD data was used. It shows the different areas which have low, medium, and high intensity of development. Particularly in the high-intensity plot, one can recognize the roadways around the HSC where the SOF travelled on this day.

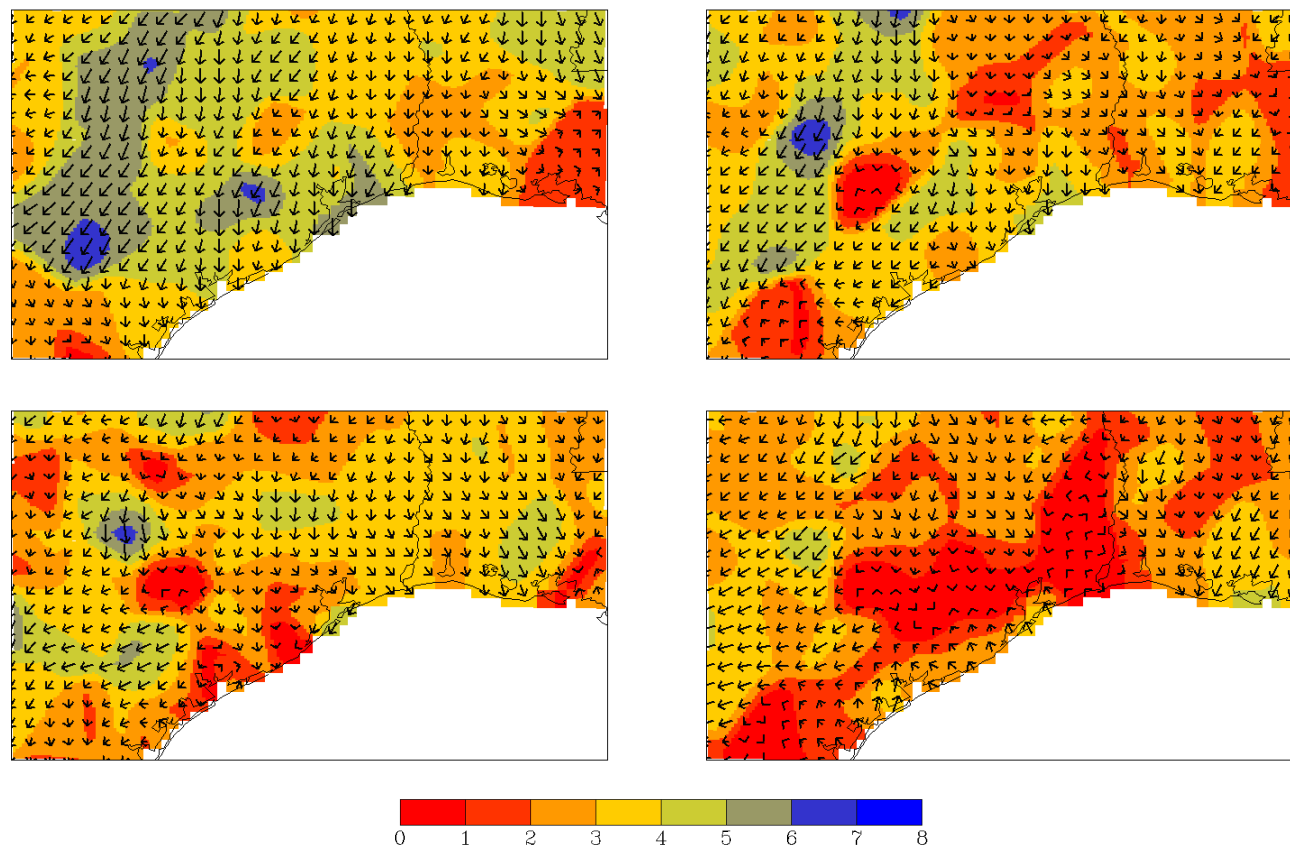


Figure 7.9 Observed analyses of 10-m winds on the 12.15 km grid. Panels correspond to: 1) upper-left, 1500 UTC 13 September 2006; 2) upper-right, 1800 UTC 13 September 2006; 3) lower-left, 2100 UTC 13 September 2006, and 4) lower-right, 0000 UTC 14 September 2006. Wind speeds are in m s^{-1} and plotted according to the color bar.

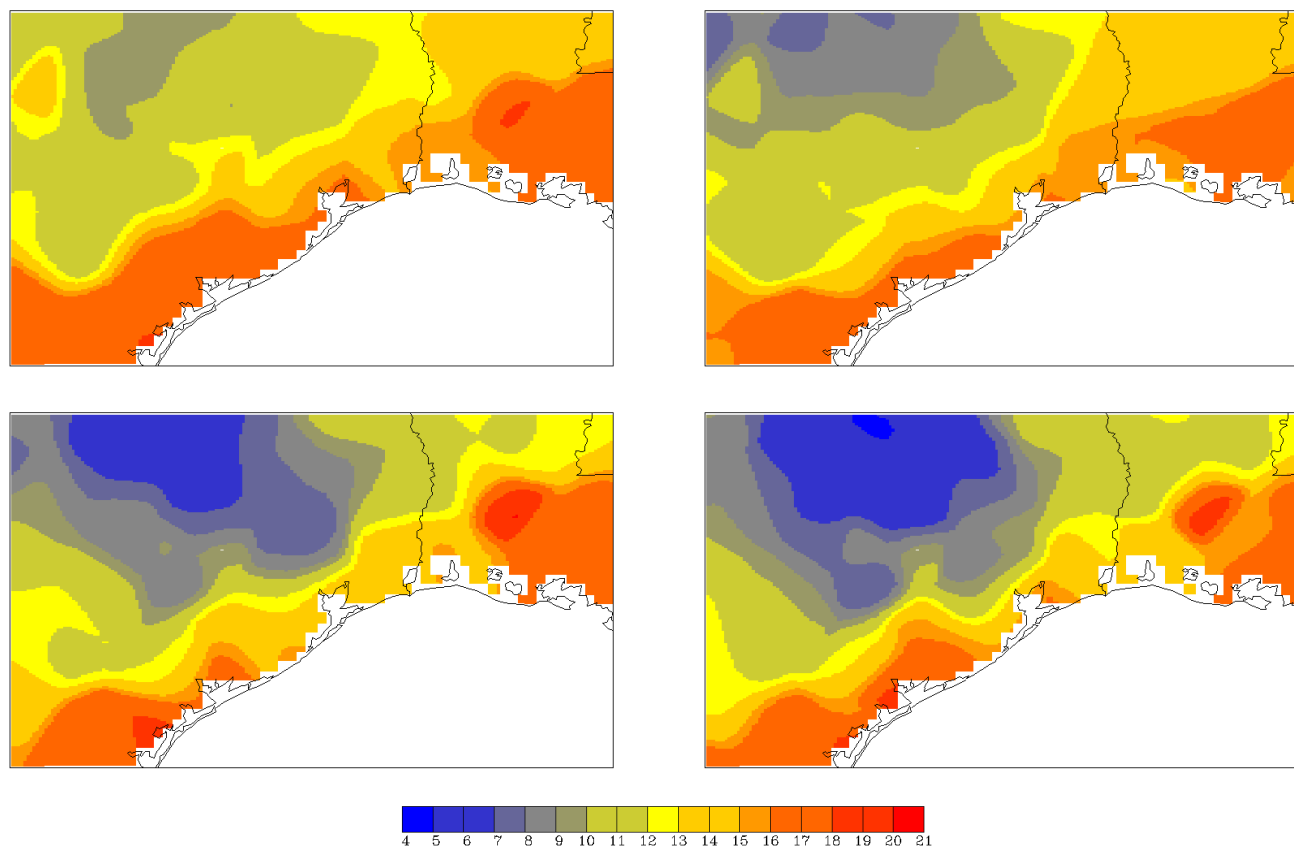


Figure 7.10 Observed analyses of 2-m water vapor mixing ratio on the 12.15 km grid. Panels correspond to: 1) upper-left, 1500 UTC 13 September 2006; 2) upper-right, 1800 UTC 13 September 2006; 3) lower-left 2100 UTC 13 September 2006, and 4) lower-right, 0000 UTC 14 September 2006. Mixing ratios are in g kg^{-1} and plotted according to the color bar.

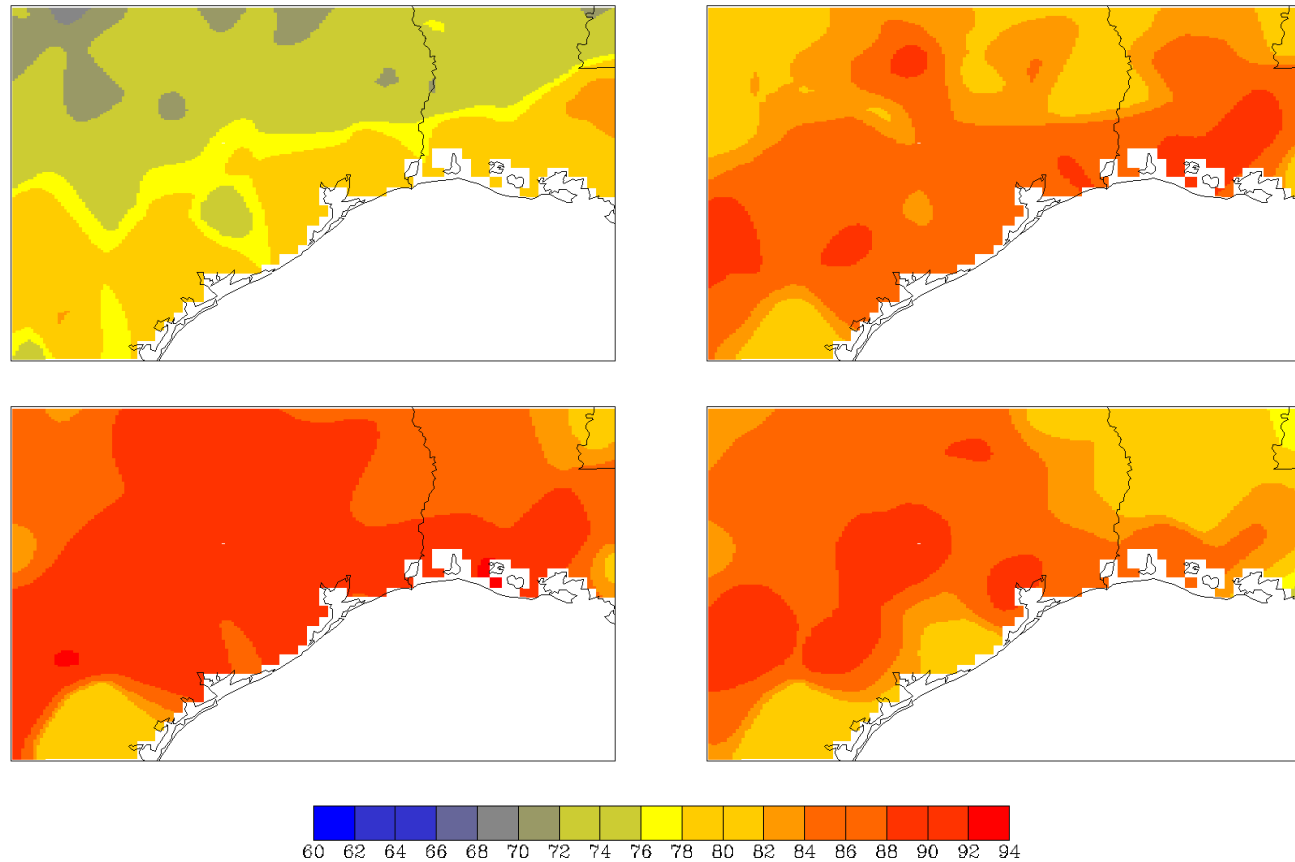


Figure 7.11 Observed analyses of 2-m temperature on the 12.15 km grid. Panels correspond to: 1) upper-left, 1500 UTC 13 September 2006; 2) upper-right, 1800 UTC 13 September 2006; 3) lower-left 2100 UTC 13 September 2006, and 4) lower-right, 0000 UTC 14 September 2006. Temperatures are in °F and plotted according to the color bar.

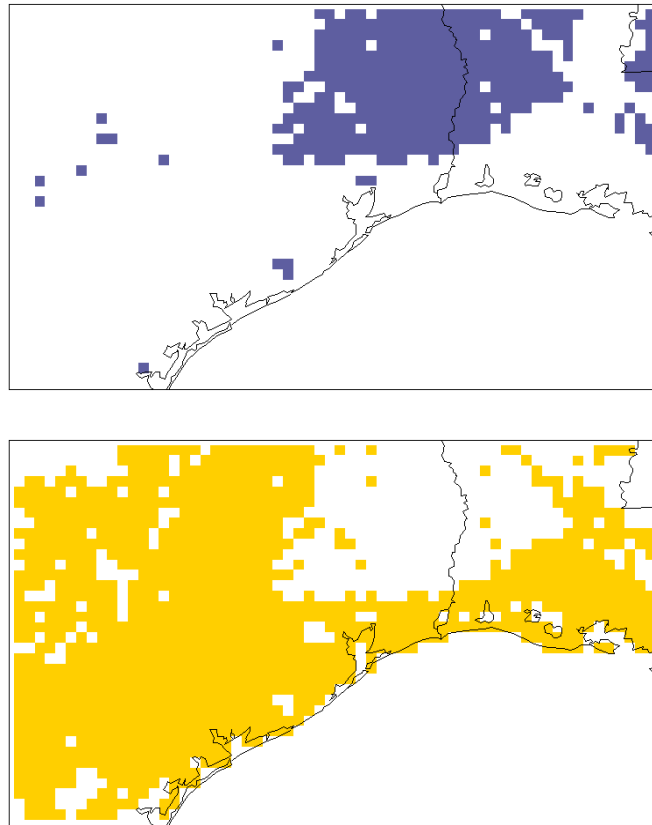


Figure 7.12 Predominant landuse types for the 12.15-km grid excluding water and urban areas. Evergreen needleleaf forest (top). Crop/mixed farming/grassland (bottom).

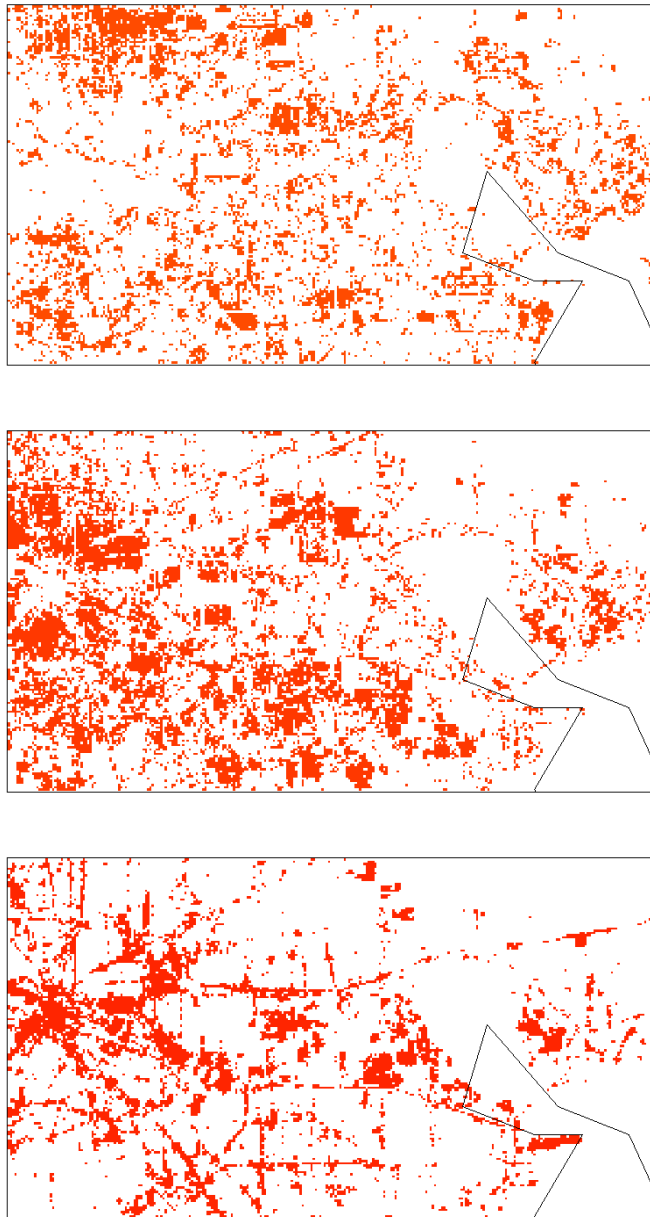


Figure 7.13 Developed land use types for the 150-m grid from the National Land Cover Data (NLCD). Low intensity (top), medium intensity (middle), and high intensity (bottom).

7.6 Overview of profiler data

7.6.1 Data sources

Figure 7.14 shows the locations of the various upper-air/sounder/profiler data available for this project. Superimposed on the map are also the colored outlines of the five nested grids used in the RAMS simulations. Table 7-4 gives the site name, operator, instrument type, variables measured, data frequency, and the use status with respect to this modeling effort.

Five data types are represented in Table 7-4: 1) Radar Wind Profiler (RWP), 2) Radio Acoustic Sounding System (RASS), 3) SOnic Detection And Ranging (SODAR), 4) mini-SODAR, and 5) rawinsondes. With a few exceptions the RWP instrument provided approximately hour-averaged wind profiles. The RASS instrument gives 5-minute averaged profiles of virtual temperature which are available every hour and essentially are instantaneous data. Depending on location the SODAR instrument gave either 10-minute or 30-minute averaged wind profiles. The mini-SODARS gave wind profiles every 5 minutes. Finally, the rawinsondes were available every 12-h and gave profiles of all variables. Further discussion of the RWP, SODAR, and RASS data is given by Knoderer and MacDonald (2007).

Section 7.3 gives an overview of how the data were implemented in the RAMS ISAN initialization scheme. The files created by ISAN are utilized in the RAMS package in two modes. The first is to provide the grid specific initial states of horizontal wind, temperature, pressure, and water vapor mixing ratio. The second use is to provide analysis nudging fields for the coarse 12.15-km grid. Nudging was not performed on the other grids because the data does not have the spatial and horizontal resolution necessary to improve the model performance. The files for these two modes are identical. The only difference is that the initial state files are used only at the start time whereas the nudging process uses the hourly analyses continuously in the nudging process on the coarse grid.

The use status flags in Table 7-4 have values of 1-5 and indicate if the location was utilized and in what capacity. Most sites have a value of “1” which means they were utilized in the ISAN package and were within one or more of the model grids so that the model fields could be compared against the observed values. The Calaveras Lake site had a use flag of “2” which indicates there were no data available for the required modeling period. The two mini-sodar sites (Channelview and Waterworks) have a use flag of “3” because time did not allow their incorporation into the ISAN system. Three sites (Sonora RASS, Sonora RWP, and the Jayton RWP) were outside of the radius of influence of the Barnes analyses scheme and therefore were not used. Finally, two sites (Cleburne RWP and Palestine RWP) were within the radius of influence of the 12.15-km grid and therefore affected the analyses but since they were outside the borders of the coarse grid the model simulation could not be compared with the observed values.

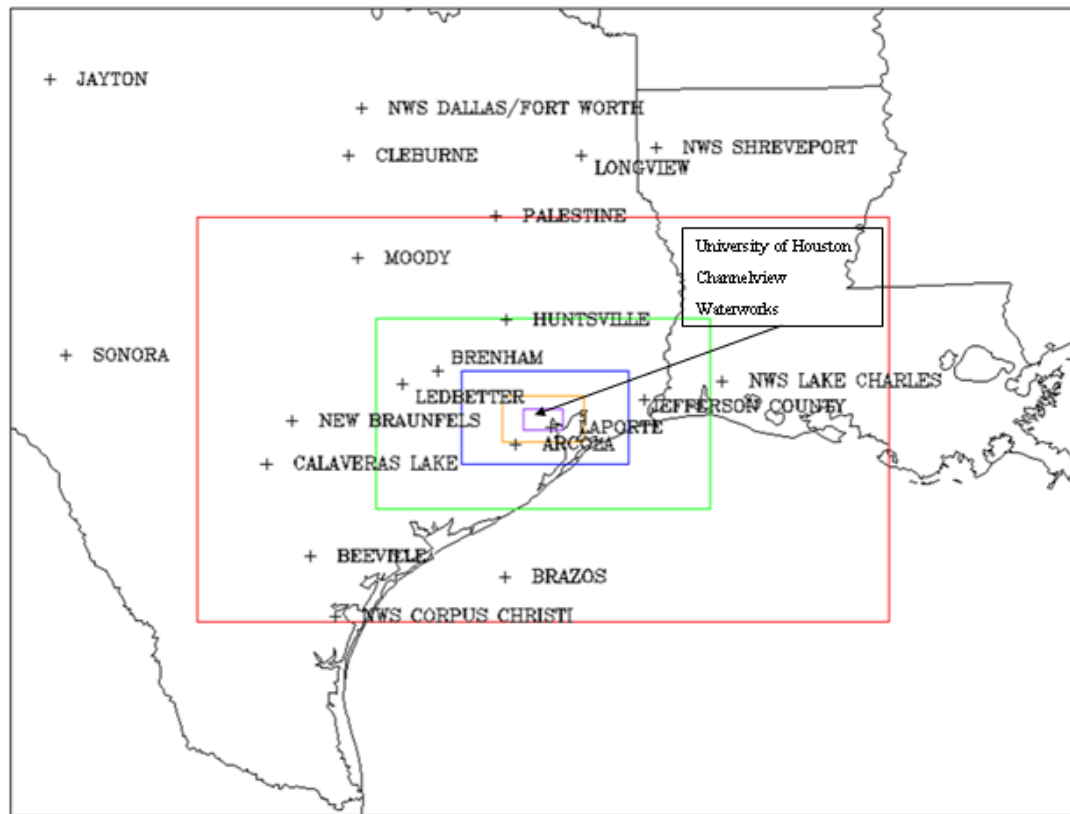


Figure 7.14 Locations for sounding data used in this project. The five model grids are outlined by the following colors: 1) 12.15 km, red; 2) 4.05 km, green; 3) 1.35 km, blue; 4) 450 m, gold, and 5) 150 m, purple. Site location names are plotted to the right of the location indicated by “+”. An additional three sites located in the 150-m grid are labeled by the offset box with the arrow.

Table 7-4 Summary of profiler/sounder/rawinsonde data used in this modeling exercise. Operator and variable abbreviations are given to the right of the table. Use flags indicate how the data was used. The column labeled “Freq.” indicates the predominant frequency at which the data was available (“m” stands for minutes, “h” stands for hours). See the text for additional details. Some data in this table taken from Knoderer and MacDonald (2007).

Site Name	Operator	Type	Variables	Freq.	Use
Channelview	TCEQ	Mini-Sodar	Z, WD, WS	5 m	3
Waterworks	TCEQ	Mini-Sodar	Z, WD, WS	5 m	3
Arcola	NOAA PSD	RASS	Z, Tv	60 m	1
Beeville	NOAA PSD	RASS	Z, Tv	60 m	1
Brazos	STI	RASS	Z, Tv	60 m	1
Brenham	NOAA PSD	RASS	Z, Tv	60 m	1
Huntsville	NOAA PSD	RASS	Z, Tv	60 m	1
Longview	NOAA PSD	RASS	Z, Tv	60 m	1
Moody	NOAA CSD	RASS	Z, Tv	60 m	1
New Braunfels	STI	RASS	Z, Tv	60 m	1
Sonora	NOAA PSD	RASS	Z, Tv	60 m	4
Corpus Christi	NWS	Rawinsonde	Z, T, Td, WD, WS, P	12 h	1
Dallas/Fort Worth	NWS	Rawinsonde	Z, T, Td, WD, WS, P	12 h	1
Lake Charles	NWS	Rawinsonde	Z, T, Td, WD, WS, P	12 h	1
Shreveport	NWS	Rawinsonde	Z, T, Td, WD, WS, P	12 h	1
University of Houston	University of Houston	Rawinsonde	Z, T, Td, WD, WS, P	12 h	1
Arcola	NOAA PSD	RWP	Z, WD, WS	60 m	1
Beeville	NOAA PSD	RWP	Z, WD, WS, M	60 m	1
Brazos	STI	RWP	Z, WD, WS	60 m	1
Brenham	NOAA PSD	RWP	Z, WD, WS, M	60 m	1
Cleburne	TCEQ	RWP	Z, WD, WS	30 m	5
Huntsville	NOAA PSD	RWP	Z, WD, WS, M	60 m	1
Jayton	NOAA NPN	RWP	Z, WD, WS	60 m	4
Jefferson County	TCEQ	RWP	Z, WD, WS, M	30 m	1
Laporte	TCEQ	RWP	Z, WD, WS, M	60 m	1
Ledbetter	NOAA NPN	RWP	Z, WD, WS	60 m	1
Longview	NOAA PSD	RWP	Z, WD, WS, M	60 m	1
Moody	NOAA CSD	RWP	Z, WD, WS	60 m	1
New Braunfels	STI	RWP	Z, WD, WS, M	60 m	1
Palestine	NOAA NPN	RWP	Z, WD, WS	60 m	5
Sonora	NOAA PSD	RWP	Z, WD, WS	60 m	4
Brazos	STI	SODAR	Z, WD, WS	10 m	1
Calaveras Lake	TCEQ	SODAR	Z, WD, WS	30 m	2

Operator Abbreviations

NOAA-PSD	National Oceanic and Atmospheric Administration - Physical Science Division
NOAA-CSD	National Oceanic and Atmospheric Administration - Chemical Science Division
STI	Sonoma Technology Incorporated
TCEQ	Texas Commission on Environmental Quality
NOAA-NPN	National Oceanic and Atmospheric Administration – National Profiler Network
NWS	National Weather Service

Variable Abbreviations

Z	height
WD	wind direction
WS	wind speed
T	temperature
Tv	virtual temperature
Td	dew point temperature
P	pressure
M	mixing height

Use Flags

- 1-used in initialization and compared with model simulation
- 2 – no data for 13 September
- 3- did not implement
- 4 – outside radius of influence for 12.15-km grid
- 5 – used in initialization but not compared with model simulation
- outside of model 12.15-km grid

7.6.2 Overview of sounding characteristics

Figure 7.16 - Figure 7.18 give hourly plots of wind direction and speed obtained from the 15 Radar Wind Profiler (RWP) instruments. Figure 7.19 - Figure 7.22 are skew-T plots of the four National Weather Service rawinsondes for the times of 1200 UTC 13 September 2006 and 0000 UTC 14 September 2006. Figure 7.23 is the skew-T plot of the University of Houston rawinsondes for same times. Figure 7.24 - Figure 7.27 are examples of the RASS temperature soundings which were available in general every 10 minutes but here are only shown for the same times as the rawinsondes.

In terms of wind behavior at least three patterns were observed when examining the RWP wind data for the lowest 1-km layer. These spatial groupings of stations are illustrated in Figure 7.15. The most common pattern (the red-shaded area in Figure 7.15) was a generally consistent northerly flow (comprising hourly wind directions from northwest to northeast) with a typical trend of decreasing wind speeds and a more northeast wind direction as the day progressed. This pattern was observed to some degree at Brenham, Huntsville, Jefferson County, Moody, New Braunfels, Ledbetter, Longview, Cleburne, and Palestine locations. While they do not have the time resolution of the RWP data the NWS rawinsonde sites at Dallas, Shreveport, and Lake Charles also had behavior similar to this group. The second group (the yellow-shaded areas in Figure 7.15) had generally light and variable winds for the entire day. Two separate areas had this behavior: one area to the northwest comprising the Jayton and Sonora sites, and a second area near the Texas coast south of Houston which included the Arcola and Brazos sites. The final group (the green-shaded area in Figure 7.15) displayed northerly flow early in the day but transitioned to southeasterly flow at a time from early to late afternoon. The Laporte and Beeville RWP sites demonstrated this behavior as well as the NWS Corpus Christi rawinsonde location. These patterns are consistent with the synoptic discussion given in section 7.4. Group one consists of an area sufficiently behind the cold front to have consistent northerly flow. Group two consists of an areas either far removed from the cold frontal zone or very near it with relatively weak and variable winds. Group three illustrates the onshore flow observed from the analyses of the surface observations in the Texas coastal area from Galveston Bay southwestward to Corpus Christi. As noted before, this flow pattern was likely the result of either a sea breeze circulation or convective outflow from a convective system in the Gulf of Mexico.

The NWS Dallas and Shreveport sites and the University of Houston rawinsonde sites revealed the dry air being advected southward with low-level water vapor mixing ratios near 5 g kg^{-1} by 0000 UTC. The other rawinsonde sites had low-level mixing ratios of 15 g kg^{-1} or higher.

Figure 7.24 - Figure 7.27 are examples of the RASS temperature soundings. The original RASS data give profiles of virtual temperature. In order for these to be used in the RAMS ISAN package the virtual temperatures had to be converted to temperatures. This was accomplished by obtaining an estimate of the 2-m water mixing ratio at the RASS sounding location using a Barnes analysis with the standard airways hourly observations at the locations shown in Figure 7.3. The assumption was then made that this mixing ratio was representative of the entire RASS sounding and the correction made as in Eq. (2),

$$(2) \quad T_e(z) = T_v(z) / (1 + 0.61 r_s)$$

where $T_e(z)$ is the estimated temperature as a function of height, $T_v(z)$ is the observed RASS virtual temperature, and r_s is the estimated 2-m water vapor mixing ratio in kg kg^{-1} . The RASS plots in Figure 7.24 - Figure 7.27 show this estimated temperature curve. The general patterns seen in these plots were stable layers near the surface at 1200 UTC and near adiabatic lapse rates at 0000 UTC. The only exception is the Brazos site, which being over water, had near-neutral lapse rates for both times.

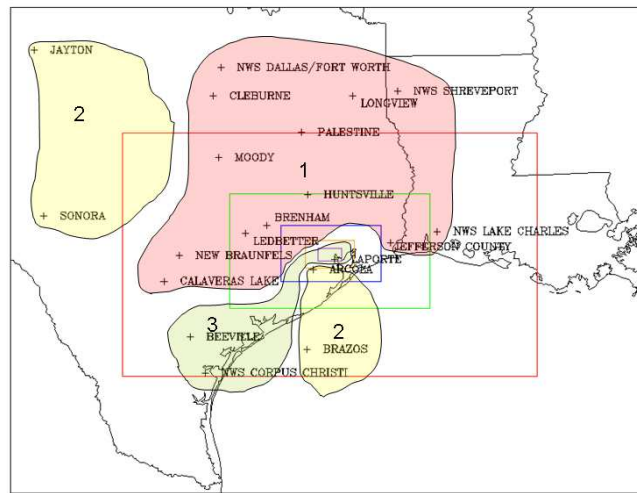


Figure 7.15 Groups of observation locations with similar wind behavior in the lowest 1-km for the period 1200 UTC 13 September 2006 to 0000 UTC 14 September 2006. The red area is group number 1, the yellow areas are group number two, and the green area is group number three. See the text for additional details.

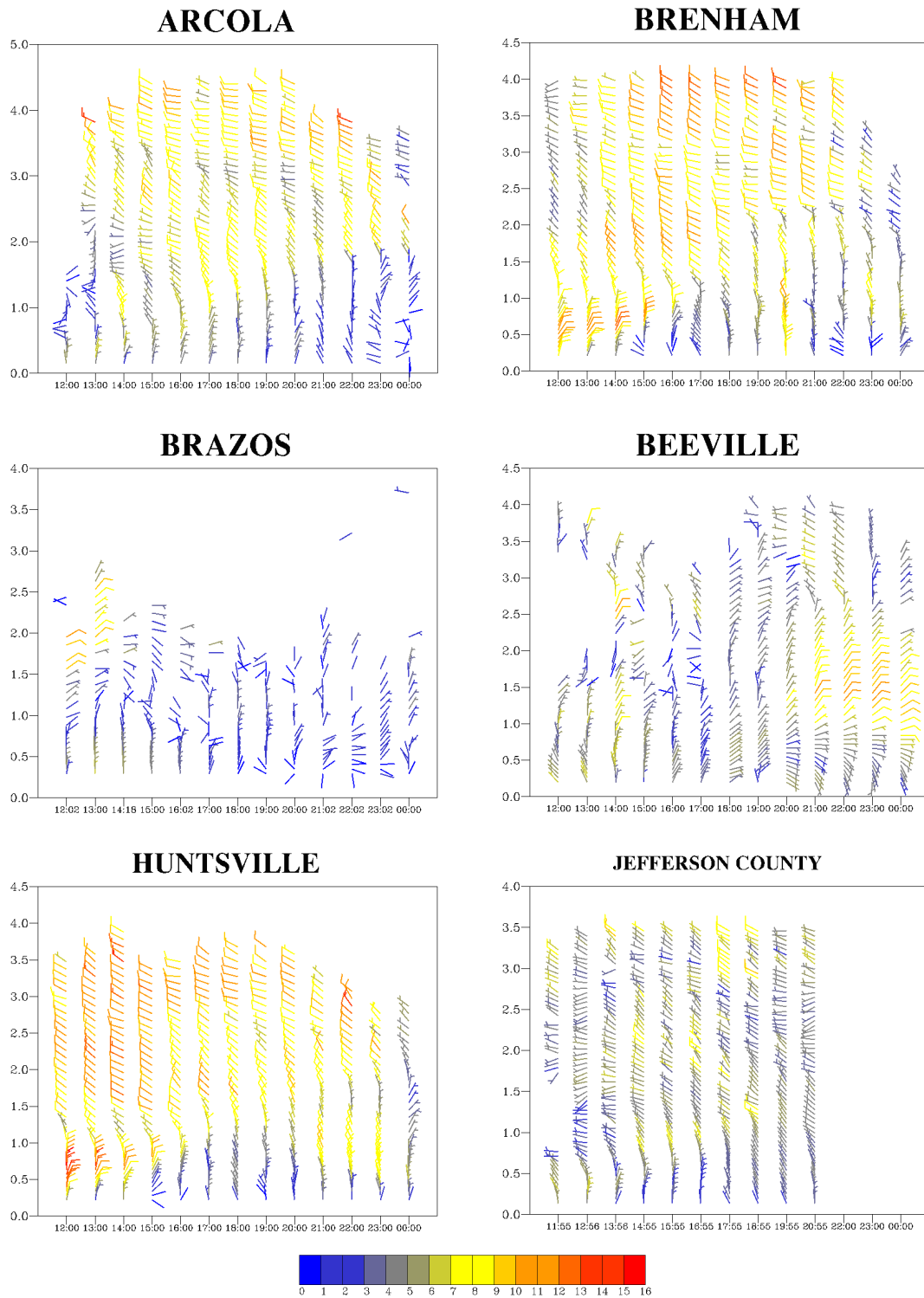


Figure 7.16 Time height sections for various profiler locations which are indicated at the top of each plot. Full barbs represent 10 m s^{-1} and half barbs represent 5 m s^{-1} . Wind speeds in m s^{-1} for each wind vector are color coded as in the color bar at the bottom. The z-axis is the height in km above the local terrain. The x-axis is the UTC time.

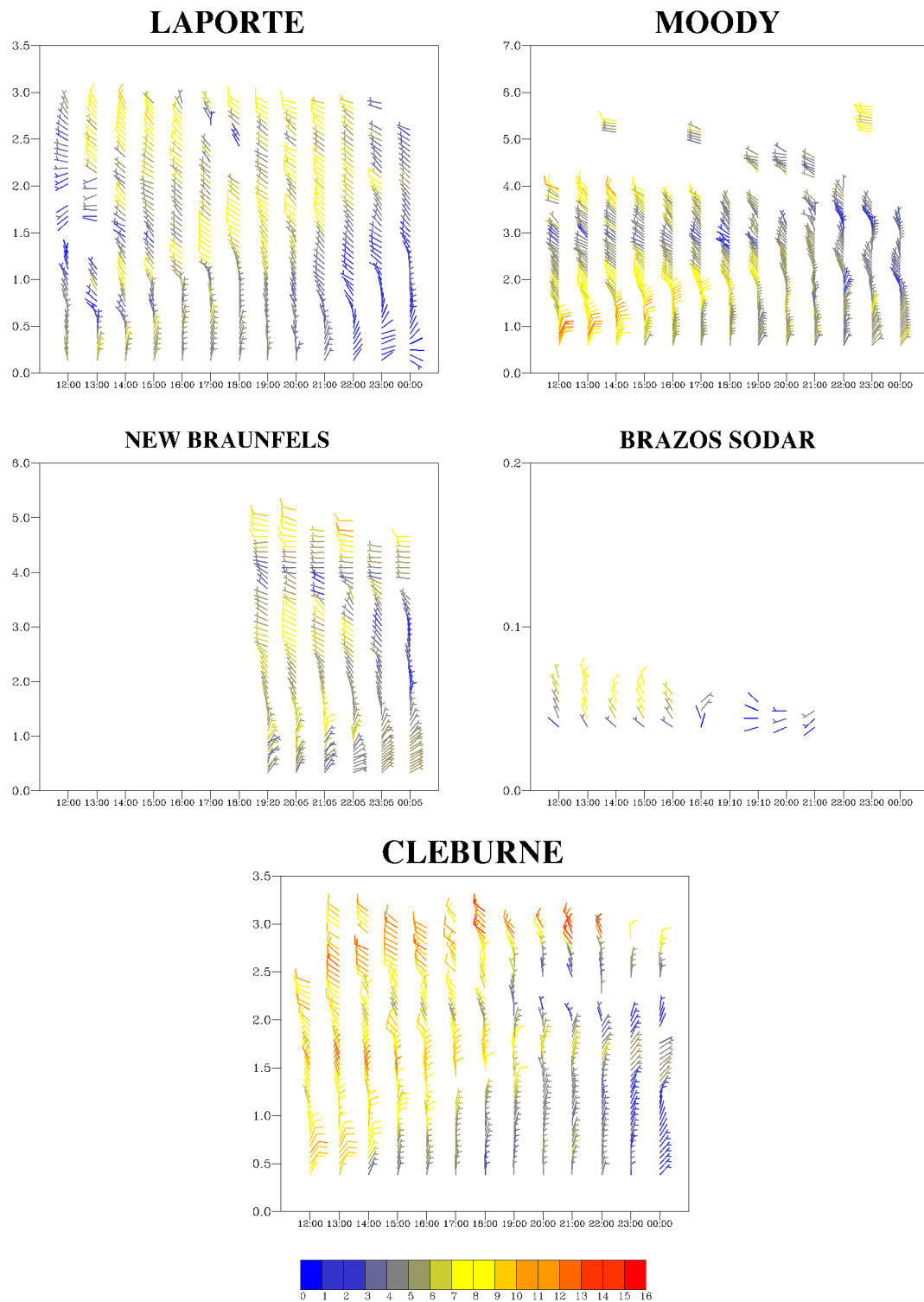


Figure 7.17 Time height sections for various profiler locations which are indicated at the top of each plot. Full barbs represent 10 m s⁻¹ and half barbs represent 5 m s⁻¹. Wind speeds in m s⁻¹ for each wind vector are color coded as in the color bar at the bottom. The z-axis is the height in km above the local terrain. The x-axis is the UTC time.

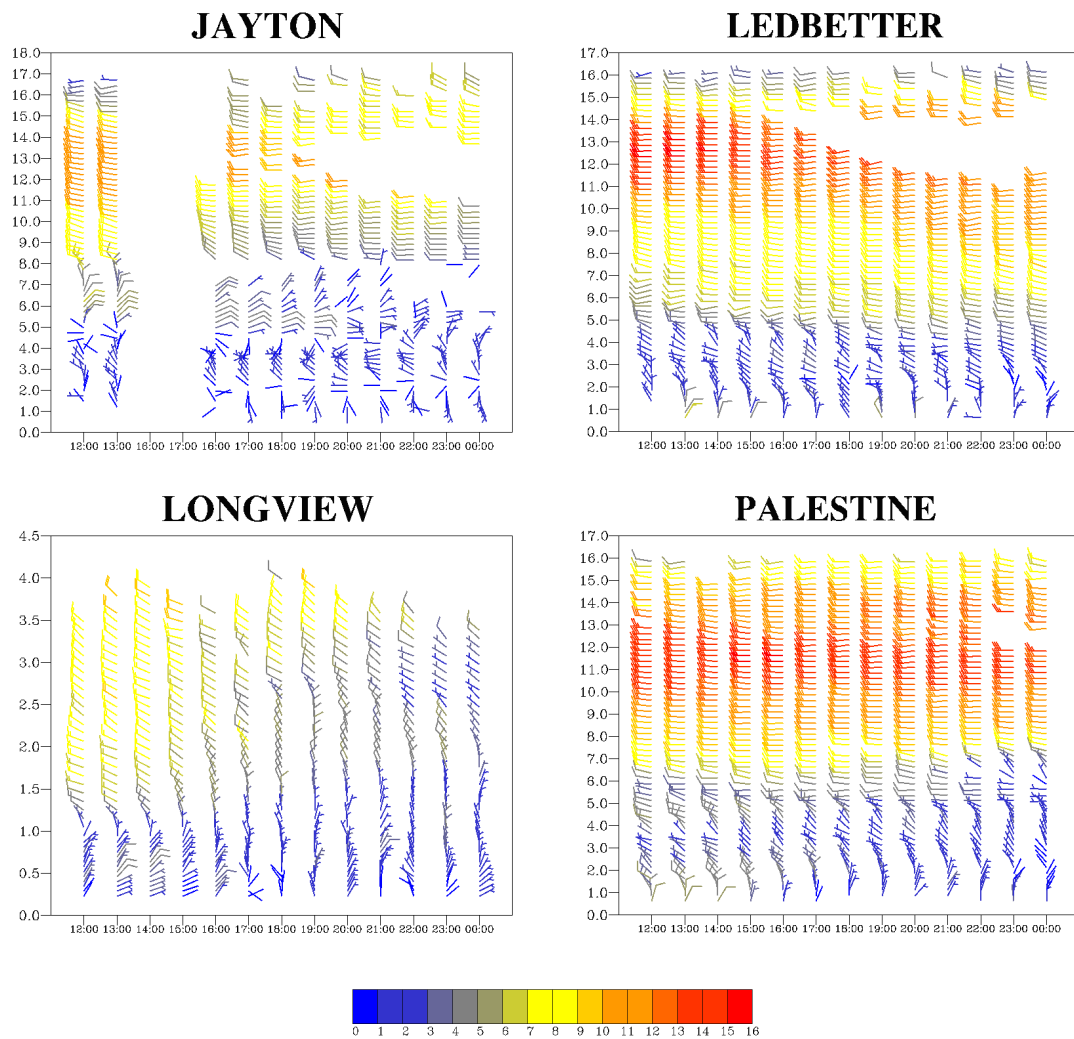


Figure 7.18 Time height sections for various profiler locations which are indicated at the top of each plot. Full barbs represent 10 m s^{-1} and half barbs represent 5 m s^{-1} . Wind speeds in m s^{-1} for each wind vector are color coded as in the color bar at the bottom. The z-axis is the height in km above the local terrain. The x-axis is the UTC time.

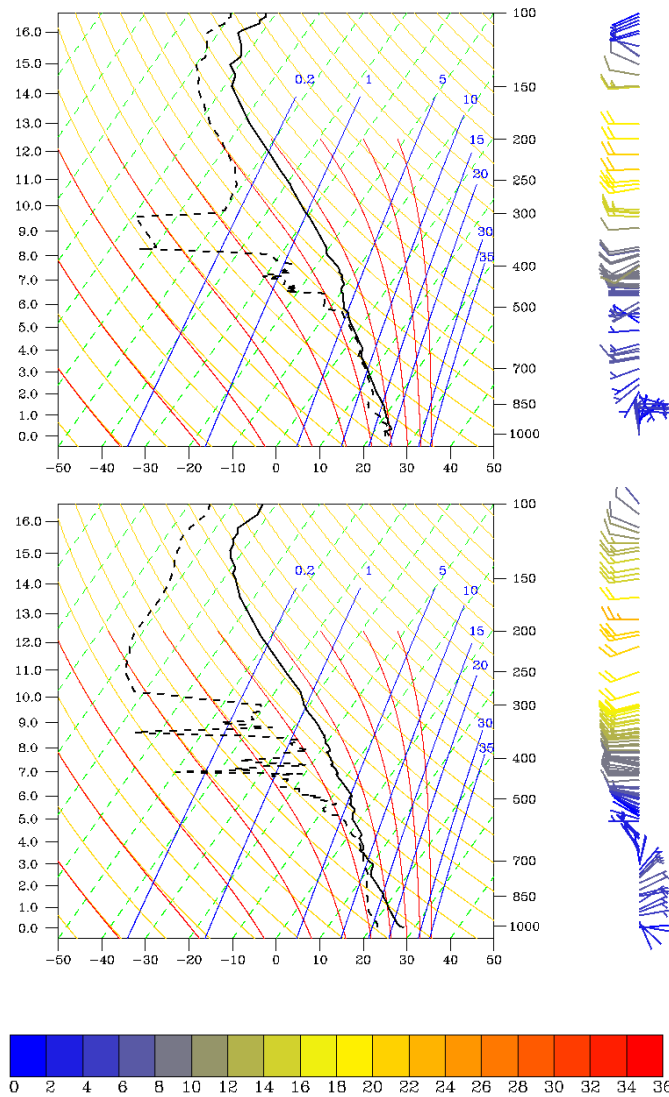


Figure 7.19 Skew-t plots for the NWS site at Corpus Christi, Texas for 1200 UTC 13 September 2006 (top) and 0000 UTC 14 September 2006 (bottom). Height above MSL in km is plotted on the left vertical axis, while pressure in mb is plotted on the right vertical axis. Temperature in $^{\circ}\text{C}$ is plotted along the horizontal axis. Dry adiabats are the gold lines and the moist adiabats are the red lines. Isotherms are the green dashed lines. Lines of constant water vapor mixing ratio are in blue and labeled in g kg^{-1} . The black solid line is the temperature sounding curve, and the black dashed line is the dew point sounding curve. Wind speeds are indicated by color and barbs. Wind speeds are plotted in m s^{-1} according to the color bar at the bottom. A half barb corresponds to 5 m s^{-1} and a full barb corresponds to 10 m s^{-1} .

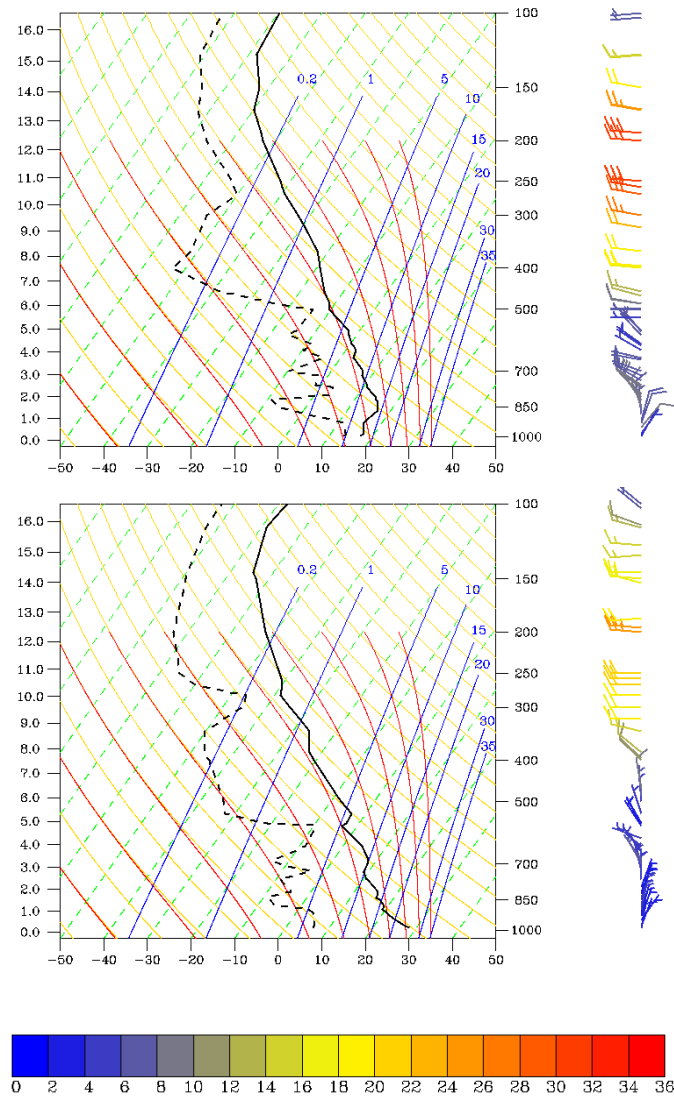


Figure 7.20 Skew-t plots for the NWS site at Dallas/Fort Worth, Texas for 1200 UTC 13 September 2006 (top) and 0000 UTC 14 September 2006 (bottom). Height above MSL in km is plotted on the left vertical axis, while pressure in mb is plotted on the right vertical axis. Temperature in $^{\circ}\text{C}$ is plotted along the horizontal axis. Dry adiabats are the gold lines and the moist adiabats are the red lines. Isotherms are the green dashed lines. Lines of constant water vapor mixing ratio are in blue and labeled in g kg^{-1} . The black solid line is the temperature sounding curve, and the black dashed line is the dew point sounding curve. Wind speeds are indicated by color and barbs. Wind speeds are plotted in m s^{-1} according to the color bar at the bottom. A half barb corresponds to 5 m s^{-1} and a full barb corresponds to 10 m s^{-1} .

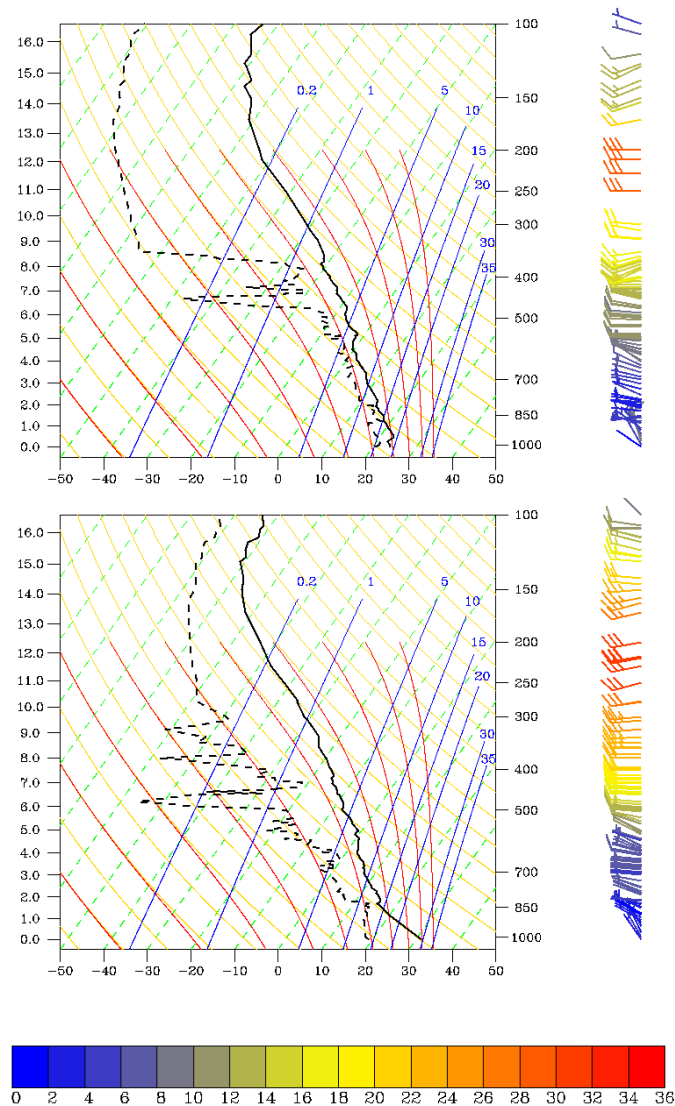


Figure 7.21 Skew-t plots for the NWS site at Lake Charles, Louisiana for 1200 UTC 13 September 2006 (top) and 0000 UTC 14 September 2006 (bottom). Height above MSL in km is plotted on the left vertical axis, while pressure in mb is plotted on the right vertical axis. Temperature in $^{\circ}\text{C}$ is plotted along the horizontal axis. Dry adiabats are the gold lines and the moist adiabats are the red lines. Isotherms are the green dashed lines. Lines of constant water vapor mixing ratio are in blue and labeled in g kg^{-1} . The black solid line is the temperature sounding curve, and the black dashed line is the dew point sounding curve. Wind speeds are indicated by color and barbs. Wind speeds are plotted in m s^{-1} according to the color bar at the bottom. A half barb corresponds to 5 m s^{-1} and a full barb corresponds to 10 m s^{-1} .

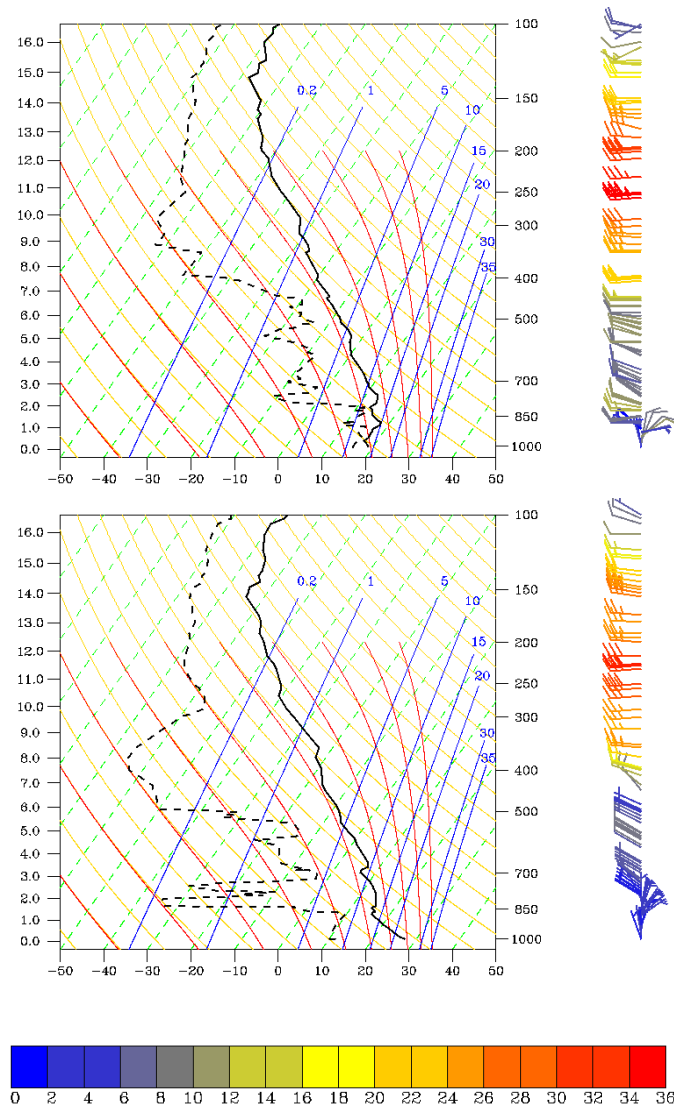


Figure 7.22 Skew-t plots for the NWS site at Shreveport, Louisiana for 1200 UTC 13 September 2006 (top) and 0000 UTC 14 September 2006 (bottom). Height above MSL in km is plotted on the left vertical axis, while pressure in mb is plotted on the right vertical axis. Temperature in $^{\circ}\text{C}$ is plotted along the horizontal axis. Dry adiabats are the gold lines and the moist adiabats are the red lines. Isotherms are the green dashed lines. Lines of constant water vapor mixing ratio are in blue and labeled in g kg^{-1} . The black solid line is the temperature sounding curve, and the black dashed line is the dew point sounding curve. Wind speeds are indicated by color and barbs. Wind speeds are plotted in m s^{-1} according to the color bar at the bottom. A half barb corresponds to 5 m s^{-1} and a full barb corresponds to 10 m s^{-1} .

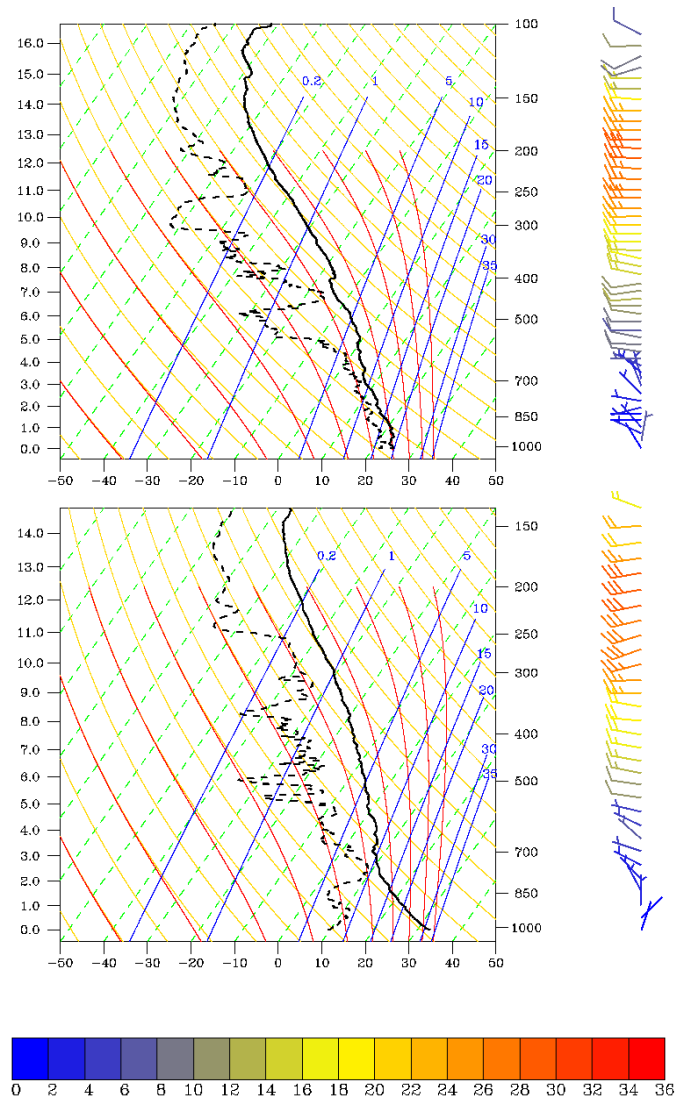


Figure 7.23 Skew-t plots for the University of Houston site for 1200 UTC 13 September 2006 (top) and 0000 UTC 14 September 2006 (bottom). Height above MSL in km is plotted on the left vertical axis, while pressure in mb is plotted on the right vertical axis. Temperature in $^{\circ}\text{C}$ is plotted along the horizontal axis. Dry adiabats are the gold lines and the moist adiabats are the red lines. Isotherms are the green dashed lines. Lines of constant water vapor mixing ratio are in blue and labeled in g kg^{-1} . The black solid line is the temperature sounding curve, and the black dashed line is the dew point sounding curve. Wind speeds are indicated by color and barbs. Wind speeds are plotted in m s^{-1} according to the color bar at the bottom. A half barb corresponds to 5 m s^{-1} and a full barb corresponds to 10 m s^{-1} . Sounding was truncated at 100 mb.

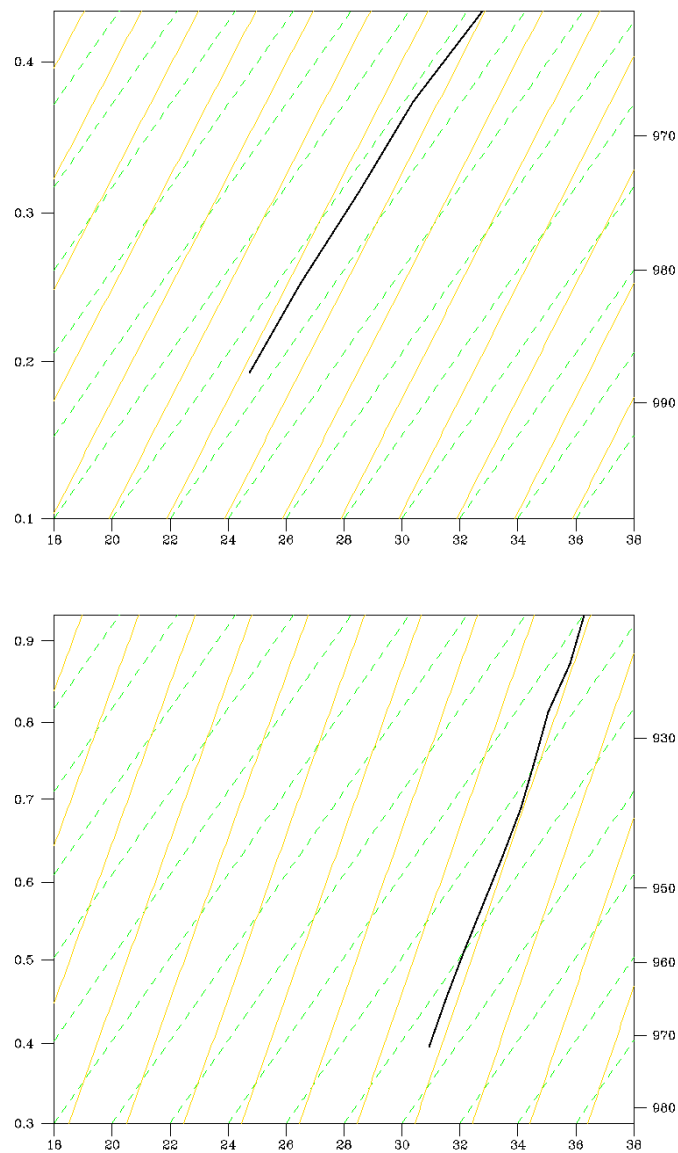


Figure 7.24 Skew-t plots for the Brenham RASS data for 1200 UTC 13 September 2006 (top) and 0000 UTC 14 September 2006 (bottom). Height above MSL in km is plotted on the left vertical axis, while pressure in mb is plotted on the right vertical axis. Temperature in °C is plotted along the horizontal axis. Dry adiabats are the gold lines and the isotherms are the green dashed lines. Original virtual temperature data was converted to an estimate of temperature using 2-m observed analyses of water vapor mixing ratio. This estimated temperature sounding is plotted as a solid black line.

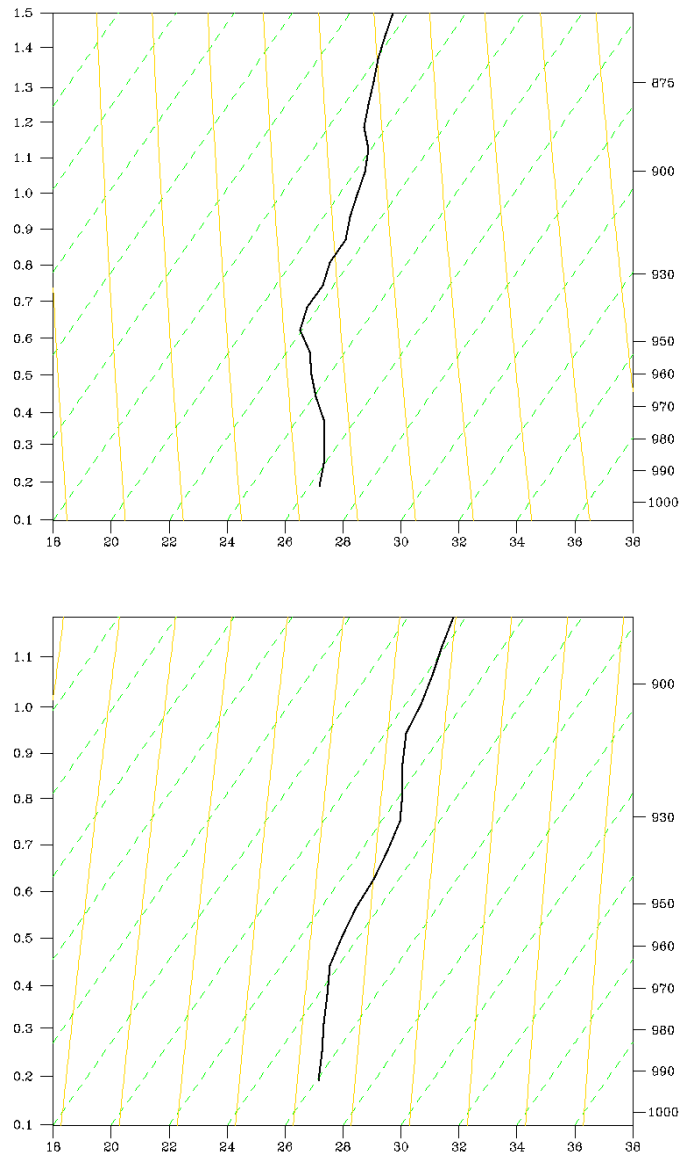


Figure 7.25 Skew-t plots for the Brazos RASS data for 1200 UTC 13 September 2006 (top) and 0000 UTC 14 September 2006 (bottom). Height above MSL in km is plotted on the left vertical axis, while pressure in mb is plotted on the right vertical axis. Temperature in °C is plotted along the horizontal axis. Dry adiabats are the gold lines and the isotherms are the green dashed lines. Original virtual temperature data was converted to an estimate of temperature using 2-m observed analyses of water vapor mixing ratio. This estimated temperature sounding is plotted as a solid black line.

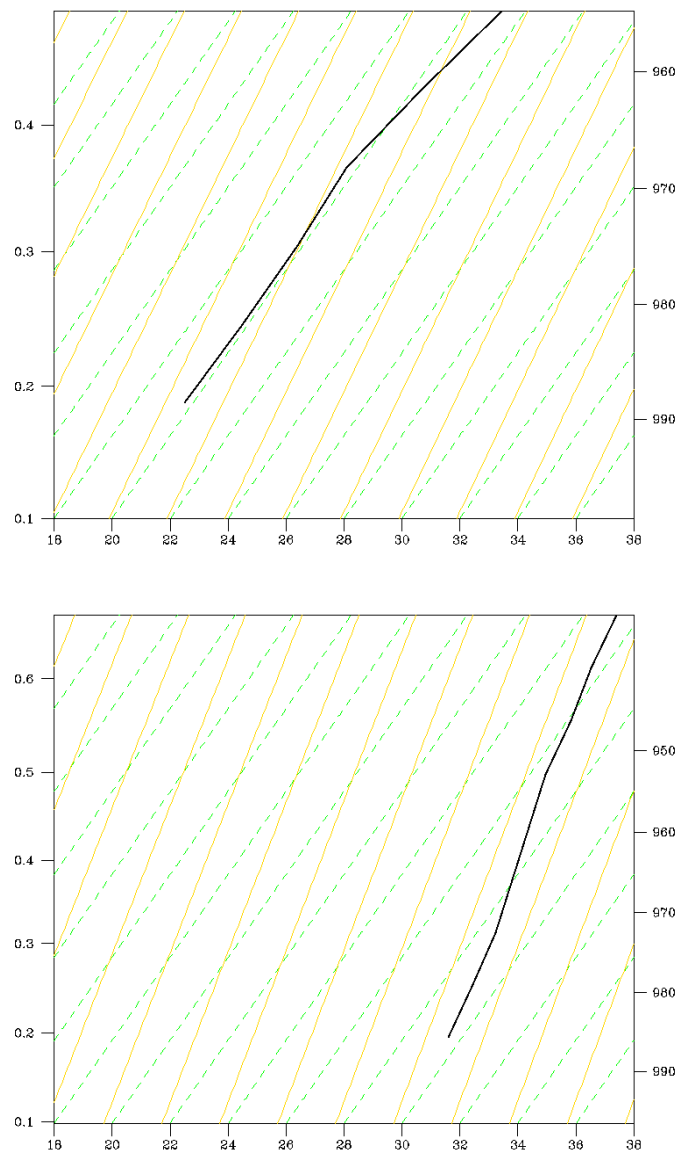


Figure 7.26 Skew-t plots for the Huntsville RASS data for 1200 UTC 13 September 2006 (top) and 0000 UTC 14 September 2006 (bottom). Height above MSL in km is plotted on the left vertical axis, while pressure in mb is plotted on the right vertical axis. Temperature in °C is plotted along the horizontal axis. Dry adiabats are the gold lines and the isotherms are the green dashed lines. Original virtual temperature data was converted to an estimate of temperature using 2-m observed analyses of water vapor mixing ratio. This estimated temperature sounding is plotted as a solid black line.

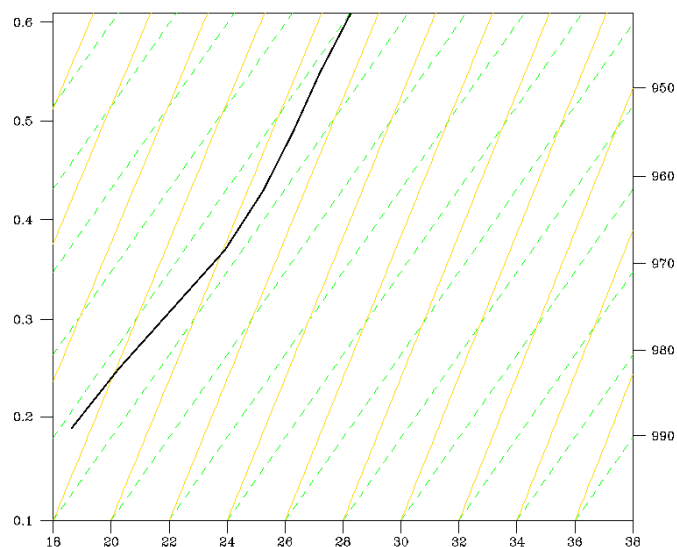


Figure 7.27 Skew-t plots for the Longview RASS data for 1200 UTC 13 September 2006 (top) and 0000 UTC 14 September 2006 (bottom). Height above MSL in km is plotted on the left vertical axis, while pressure in mb is plotted on the right vertical axis. Temperature in °C is plotted along the horizontal axis. Dry adiabats are the gold lines and the isotherms are the green dashed lines. Original virtual temperature data was converted to an estimate of temperature using 2-m observed analyses of water vapor mixing ratio. This estimated temperature sounding is plotted as a solid black line.

7.7 Control and Soil Moisture Simulations for the 12.15-km Grid

7.7.1 *Soil moisture adjustment procedures*

The so-called “control run” used the soil moisture derived from the NCEP NAM model analysis data. To compare the performance of this control run on the 12.15-km grid the 2-m temperatures (T_{2M}) and water vapor mixing ratios (Q_{2M}) were compared to observations. The model T_{2M} and Q_{2M} values were diagnosed by similarity theory using the first model level values above the ground and other quantities. An observed analysis of T_{2M} and Q_{2M} was obtained by using the hourly observations as shown in Figure 7.3 in a Barnes analysis scheme to obtain estimates of the observed values at each grid point of the RAMS 12.15-km grid. The temperature and mixing ratio bias (model minus analyzed observed value) at each grid point for a given time is defined by Eqs. (3) and (4), respectively. The average biases over all grid points and all times are given by Eqs. (5) and (6), where N_G is the total number of grid points considered over all the hourly model times. The root mean square error (RMSE) is defined using the same quantities as in Eqs. (7) and (8).

$$(3) \quad E_T = T_{2M}(\text{model}) - T_{2M}(\text{observed})$$

$$(4) \quad E_Q = Q_{2M}(\text{model}) - Q_{2M}(\text{observed})$$

$$(5) \quad \bar{E}_T = \frac{\sum E_T}{N_G}$$

$$(6) \quad \bar{Q}_T = \frac{\sum Q_T}{N_G}$$

$$(7) \quad T_{\text{RMSE}} = \sqrt{\frac{\sum E_T E_T}{N_G}}$$

$$(8) \quad Q_{\text{RMSE}} = \sqrt{\frac{\sum E_Q E_Q}{N_G}}$$

Table 7-5 shows the bias and rmse statistics for the 12-h control run. It shows an overall wet and cool bias. This seemed to be the result of soil moisture being initialized too moist. The NAM soil moisture values are related to NAM soil model thickness values, which are larger than the ones used in RAMS. The NAM top soil model thickness is 10 cm whereas in this RAMS simulation it was 5 cm. Land surface schemes are very sensitive to the soil moisture gradient near the soil-atmosphere interface. Based on these issues it seemed reasonable to develop a means to adjust the initial soil moisture to decrease the biases and rmse of temperature and water vapor.

Table 7-5 Bias (BIAS) and root mean square error (RMSE) for temperature and water vapor mixing ratio at 2-m (T_{2M} and Q_{2M} , respectively) for the control run on the 12.15-km grid using hourly data for the 12-h simulation. Temperature is in units of °F and mixing ratio is in units of g kg⁻¹.

	T_{2M}	Q_{2M}
BIAS	-0.3	2.1
RMSE	2.7	2.7

The desired changes in initial soil moisture were modeled by linear relationships as in Eqs. (9) and (10),

$$(9) \quad -E_T = \frac{\partial E_T}{\partial S_M} \Delta S_M$$

$$(10) \quad -E_Q = \frac{\partial E_Q}{\partial S_M} \Delta S_M$$

where $-E_T$ and $-E_Q$ are the negative of the biases defined in Eqs. (3) and (4), the partial derivatives are the error gradient terms which are the slopes of the changes in error relative to changes in soil moisture (to be defined momentarily), and ΔS_M is the desired change in soil moisture to bring the bias to near zero. If for example, there was a 3 °F warm bias at a given grid point at a given time, then what is needed is a 3 °F cooling to correct this error. This is the reason for the negative of the bias values being used. In order to calculate the error gradient terms, a 6-h run was made with only the 12.15-km grid activated where the initial soil moisture at all soil model levels was reduced by 50% at each grid point. With this run the error gradient terms are defined as in Eqs. (11) and (12).

$$(11) \quad \frac{\partial E_T}{\partial S_M} = \frac{E_T(\text{control}) - E_T(50\%)}{S_M(\text{control}) - S_M(50\%)}$$

$$(12) \quad \frac{\partial E_Q}{\partial S_M} = \frac{E_Q(\text{control}) - E_Q(50\%)}{S_M(\text{control}) - S_M(50\%)}$$

With this information in Eqs. (9) and/or (10) can be solved for the desired soil moisture adjustment ΔS_M . The spatial details of the control run will be discussed in section 7.7.2, but while there was an overall cool bias, it seemed that the major forest area north of Houston (see top panel in Figure 7.12) and areas in the western portion of the 12.15-km grid were too warm while the area near to the Houston area was too cool. In general terms, increasing soil moisture increases evaporation which increases the near-surface mixing ratio and decreases the temperature. Likewise decreasing soil moisture decreases evaporation which decreases the near-surface mixing ratio and increases the temperature. Table 7.6 shows the four possible scenarios (labeled with numbers 1-4) between the temperature and mixing ratio bias regimes. Only two of the

Table 7-6 Contingency table of options to handle 2-m temperature and mixing ratio biases and their consistency status.

	Wet Bias	Dry Bias
Warm Bias	Category 1: $E_T > 0$, $E_Q > 0$ Decrease soil moisture, decrease mixing ratio, increase temperature [INCONSISTENT]	Category 2: $E_T > 0$, $E_Q < 0$ Increase soil moisture, increase mixing ratio, decrease temperature [CONSISTENT]
Cool Bias	Category 3: $E_T < 0$, $E_Q > 0$ Decrease soil moisture, decrease mixing ratio, increase temperature [CONSISTENT]	Category 4: $E_T < 0$, $E_Q < 0$ Increase soil moisture, increase mixing ratio, decrease temperature [INCONSISTENT]

categories provide an opportunity to simultaneously correct the bias by only adjusting the one variable of soil moisture. A plot of the four categories for the 12.15-km grid for the control run is shown in Figure 7.28. It shows that the predominant modes were category one (too warm and too wet) and category three (too cool and too wet). There were two main areas displaying the category one behavior. One was the large forested area north of Houston, and the other was a large area in the western part of the domain which extended south to the Gulf coast.

Equations (10) and (12) were chosen to create the soil moisture adjustment for all situations except for the category one area north of Houston. There the temperature scheme represented by Eqs. (9) and (11) was utilized with the philosophy of decreasing the warm bias at the expense of allowing an increase in the wet bias. This was justified by the fact, that in general, forested areas should be cooler than surrounding areas with the same environmental conditions (e.g., see Luvall and Holbo 1989) and the fact that few surface observations were available in the major forested area north of Houston to accurately ascertain actual conditions there. With this modeling philosophy, as will be discussed in the next section, a large part of the western region with category one conditions will have an increase in the magnitude of the warm temperature bias since soil moisture was decreased there. The final step in the soil moisture calculations was to calculate an adjustment factor S_f as in Eq. (13), which was the way the initial soil moisture conditions were modified within the model and which is plotted in Figure 7.29. As just discussed, the forest area north of

$$(13) \quad S_f = \left[S_M(\text{control}) + \Delta S_M \right] / S_M(\text{control})$$

Houston was moistened in order to reduce the warm bias, so that region has S_f values greater than one. In general, areas close to the coast had S_f values close to one. Otherwise the S_f factors were less than one to dry the category three areas.

7.7.2 Comparison of 12.15-km grid control and soil moisture adjustment simulations

The summary statistics for the control and soil moisture adjustment simulations (hereafter referred to as “CNTRL” and “SOILM”, respectively) are given in Table 7-7. The cool bias of -0.3°F in the CNTRL run was replaced by a warm bias of 1.3°F in the SOILM run. As will be seen in the discussion of the spatial patterns, this warm bias was almost exclusively the result of drying the regions in the western part of the domain which exhibited a warm and wet bias in the CNTRL run. The temperature RMSE also increased from 2.7°F for the CNTRL run to 3.2°F for the SOILM run. Both the bias and the RMSE for the mixing ratio were reduced by 25% or more. Very little difference was observed in the statistics between the two runs for the wind direction or wind speed.

Table 7-7 Summary statistics for the bias (BIAS) (model minus observed) and rmse (RMSE) for the control (CNTRL) and soil moisture adjustment (SOILM) simulations for the 12.15-km grid for the 12-h simulation from 1200 UTC 13 September 2006 to 0000 UTC 14 September 2006. The temperature and water vapor mixing ratio at 2-m are labeled as “T2M” and “Q2M” respectively, while the wind direction and wind speed at 10-m are labeled as “WDIR10M” and “WSPD10M”, respectively. The temperature units are $^{\circ}\text{F}$, the mixing ratio units are g kg^{-1} , the wind direction units are degrees, and the wind speed units are m s^{-1} .

	T2M		Q2M		WDIR10M		WSPD10M	
	CNTRL	SOILM	CNTRL	SOILM	CNTRL	SOILM	CNTRL	SOILM
BIAS	-0.34	1.28	2.05	1.06	6.22	7.29	-0.20	-0.20
RMSE	2.74	3.22	2.72	1.99	35.00	35.57	2.49	2.49

Figure 7.30 shows the temperature bias for the CNTRL and SOILM runs. It shows a warm bias in the CNTRL run for the forested area north of Houston, and for portions of the western and southwestern areas of the domain. At the same time it showed a cool bias of -2 to -5°F in and near to the HSC area. As expected, the SOILM run shows an improvement in the temperature bias for the forest area north of Houston and the HSC area itself, but an increase in the warm bias over a large area of the western part of the domain. The RMSE temperature plot in Figure 7.31 shows similar behavior, with the RMSE increasing to values near 8°F over the extreme southwestern portion of the domain.

Figure 7.32 shows the water vapor mixing ratio bias for the CNTRL and SOILM runs. The CNTRL run shows a consistent wet bias of 1 to 6 g kg^{-1} . The SOILM run had bias values mainly in the $\pm 1 \text{ g kg}^{-1}$ range but with a larger wet bias in the forested area north of Houston which was by design. The RMSE mixing ratio plot in Figure 7.33 shows in a similar manner the reduction in the RMSE for much of the domain.

The same type of plots for wind direction are given by Figure 7.34 and Figure 7.35, and for wind speed are given by Figure 7.36 and Figure 7.37. Those plots showed very little difference between the CNTRL and SOILM simulations for the wind variable errors. The RMSE plot for wind direction in Figure 7.35 was significant for several reasons. While there was very little difference between the CNTRL and SOILM simulations, the plot does show features which were related to the synoptic discussion in section 7.4 and the landuse importance

in section 7.5. There were basically four areas which had RMSE for the wind direction of 60° or more. The first was the HSC area and then southwestward along the Gulf coast. Part of this area had the onshore flow late in the day which was either a sea breeze event or outflow from convection to the south over the Gulf of Mexico. Parts of this same area also had showers and thunderstorms late in the day as well. The second area is an extension of the latter area but extends north of the HSC into the large forest area. The third and fourth areas are relatively isolated pockets of large RMSE of wind direction over the extreme southwestern and eastern locations of the domain. These are likely due to the convective activity in those areas. To the extent this is true, since both the CNTRL and SOILM simulations had cloud and precipitation processes inactivated, these runs had no ability to reproduce those circulations and therefore the large RMSE values which were observed. This plot will also have value when the model winds are compared to the radar wind profilers in section 7.8.

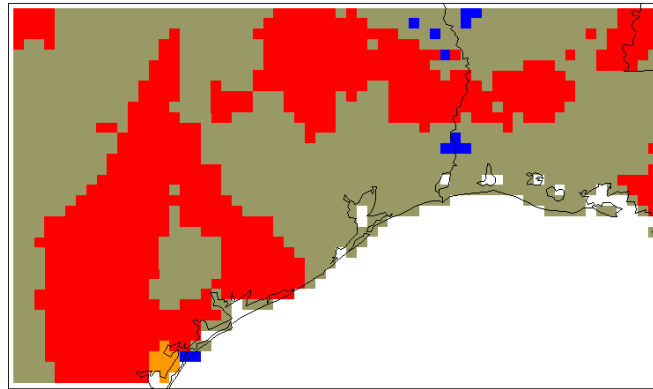


Figure 7.28 Plot of categories related to model biases at 2-m for temperature and mixing ratio. Bias values are defined by model values minus the observed. Red areas have model values which are too warm and too wet. Yellow areas have model values which are too warm and too dry. Green areas have model values which are too cool and too wet. Blue areas have model values which are too cool and too dry.

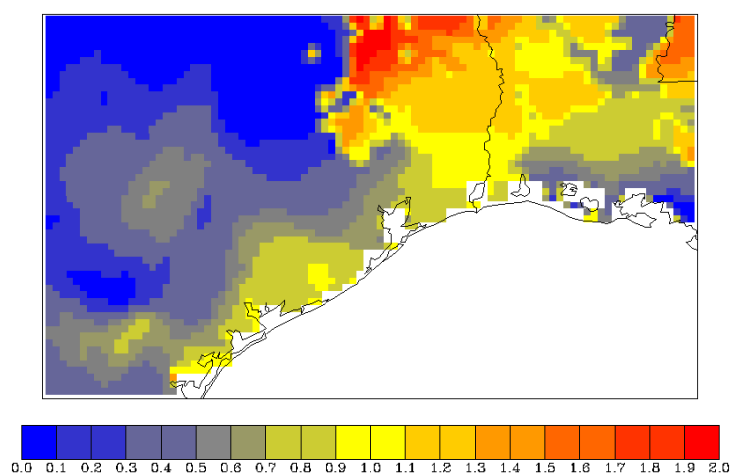


Figure 7.29 Soil moisture adjustment factor used to adjust the initial soil moisture of the control run for the 12.15-km grid. Values less than one indicate a drying of the soil whereas values greater than one indicate a moistening of the soil. The maximum values for the plot have been truncated to 2.0

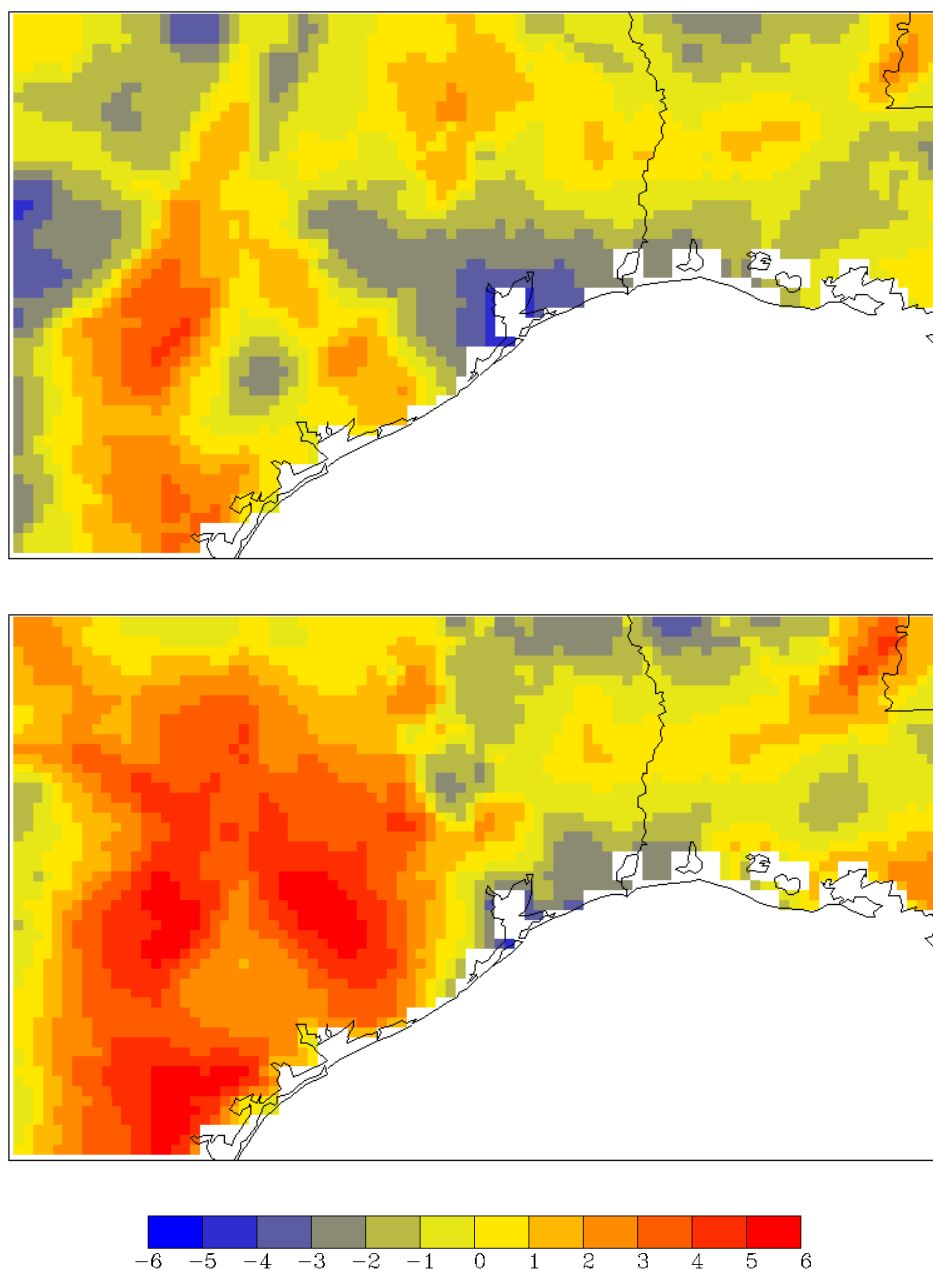


Figure 7.30 Average bias (RAMS model minus analyzed observations) in units of °F for temperatures at 2-m for the 12.15 km horizontal resolution grid for the control simulation (top) and the adjusted soil moisture simulation (bottom). Simulation period was for 12 h starting at 1200 UTC 13 September 2006. Instantaneous hourly model data and hourly observations were used.

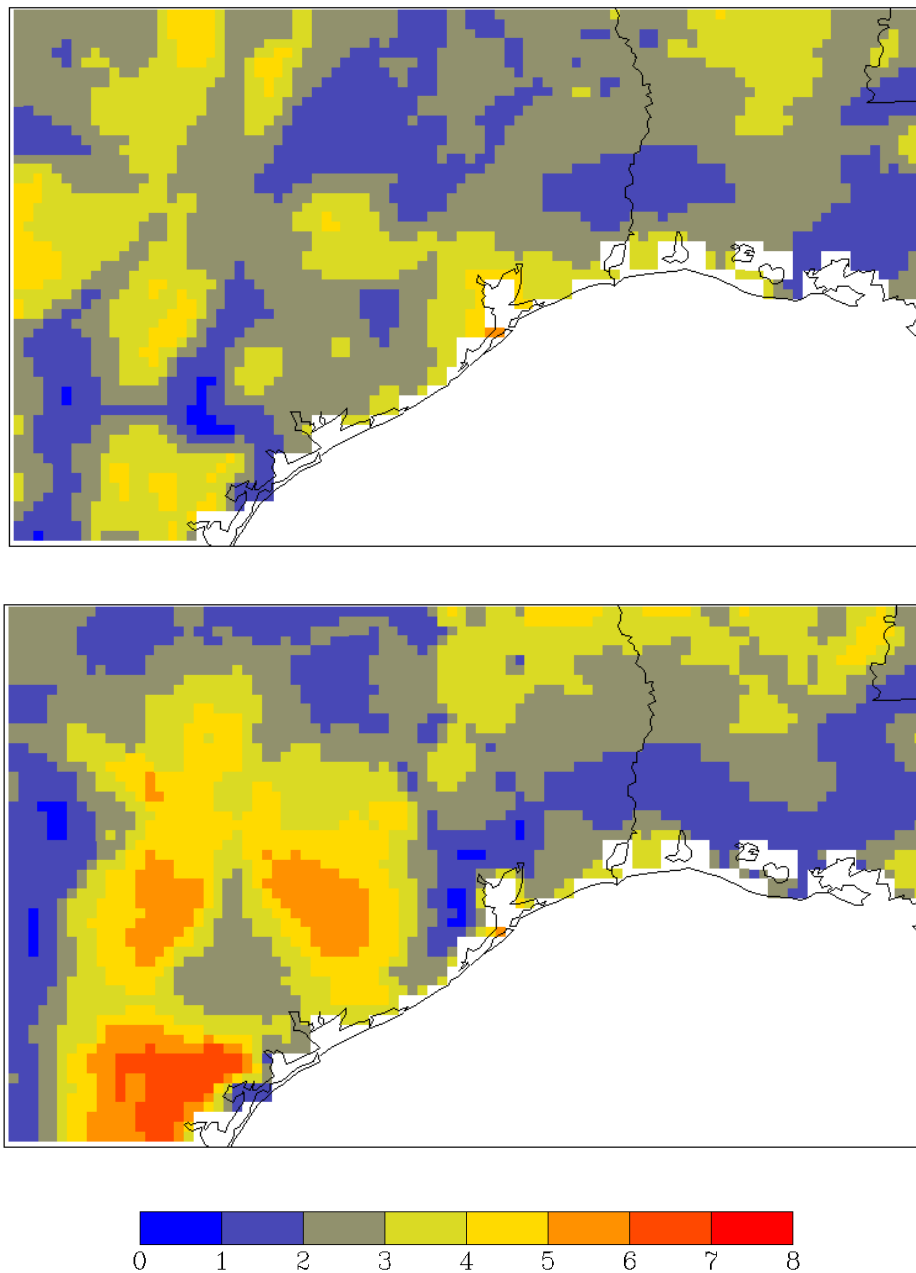


Figure 7.31 Root mean square error (RAMS model minus analyzed observations) in units of °F for temperatures at 2-m for the 12.15 km horizontal resolution grid for the control simulation (top) and the adjusted soil moisture simulation (bottom). Simulation period was for 12 h starting at 1200 UTC 13 September 2006. Instantaneous hourly model data and hourly observations were used.

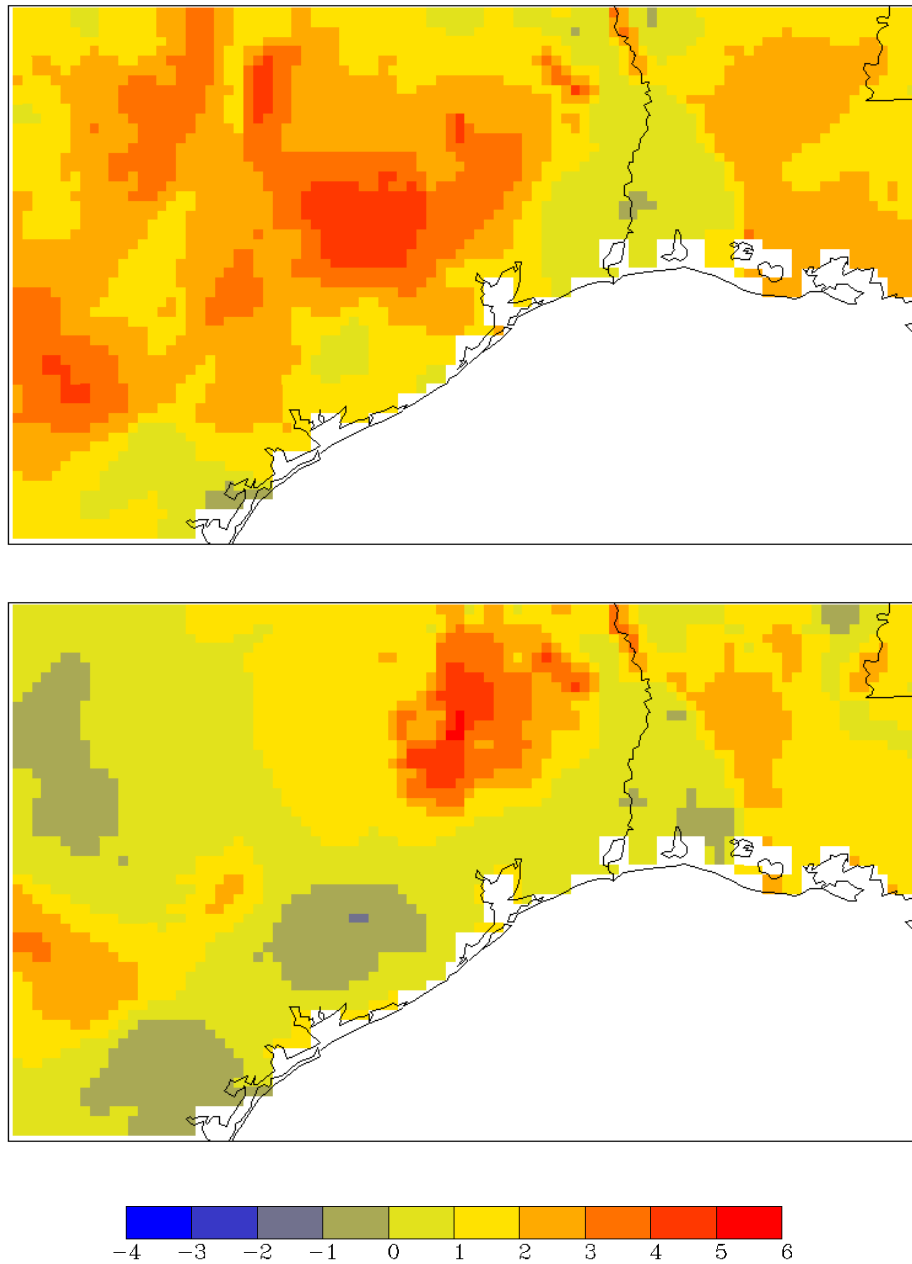


Figure 7.32 Average bias (RAMS model minus analyzed observations) in units of g kg^{-1} for water vapor mixing ratio at 2-m for the 12.15 km horizontal resolution grid for the control simulation (top) and the adjusted soil moisture simulation (bottom). Simulation period was for 12 h starting at 1200 UTC 13 September 2006. Instantaneous hourly model data and hourly observations were used.

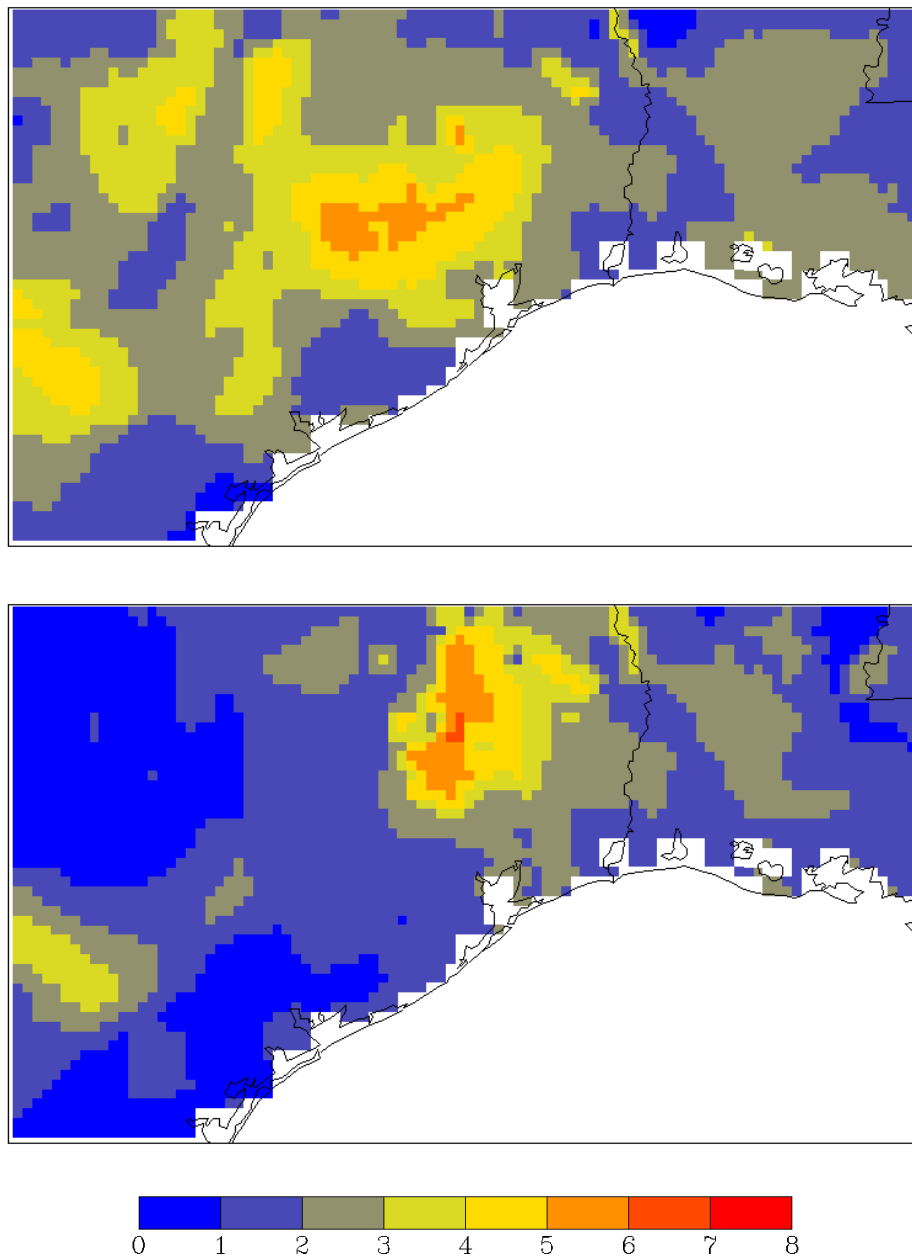


Figure 7.33 Root mean square error (RAMS model minus analyzed observations) in units of g kg^{-1} for water vapor mixing ratio at 2-m for the 12.15 km horizontal resolution grid for the control simulation (top) and the adjusted soil moisture simulation (bottom). Simulation period was for 12 h starting at 1200 UTC 13 September 2006. Instantaneous hourly model data and hourly observations were used.

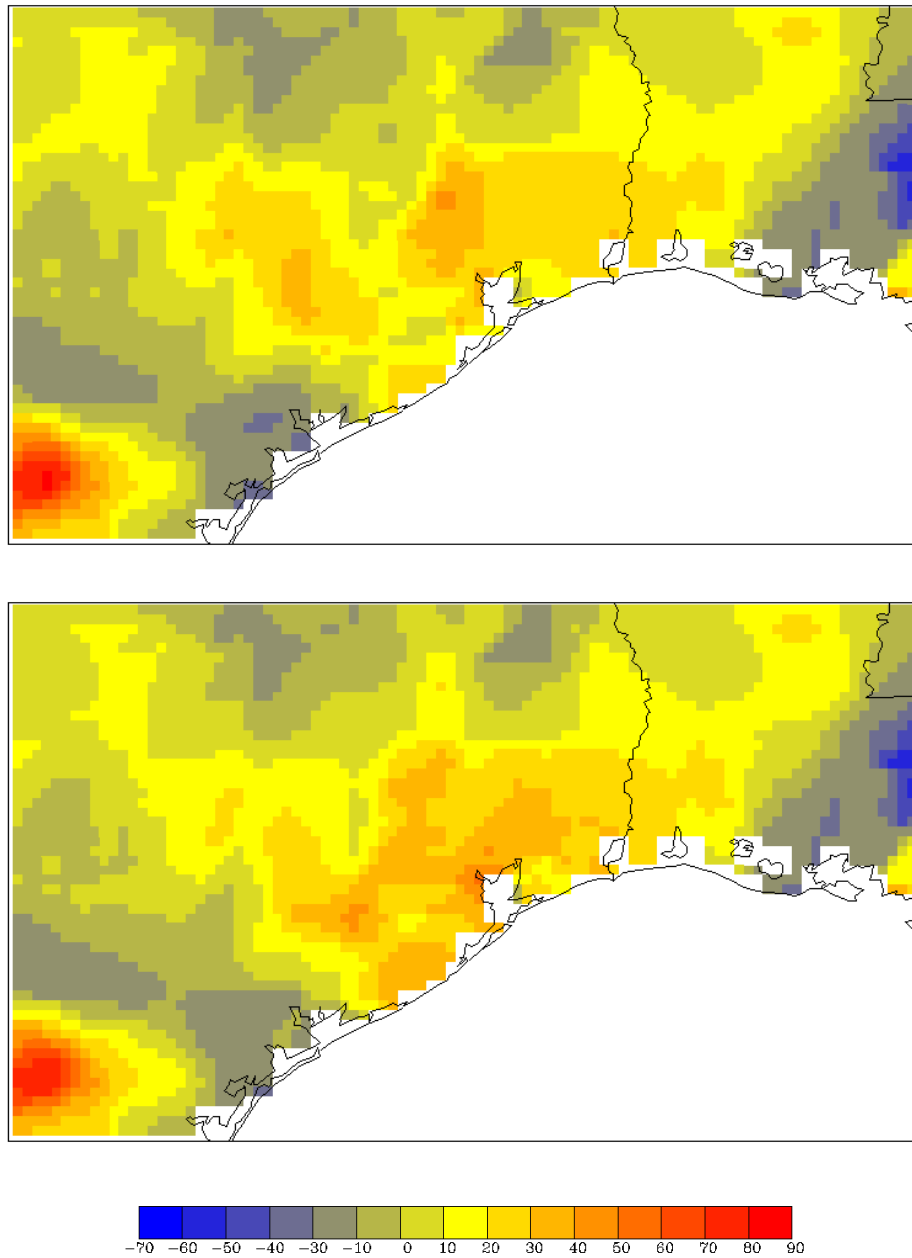


Figure 7.34 Average bias (RAMS model minus analyzed observations) in units of degrees for wind direction at 10-m for the 12.15 km horizontal resolution grid for the control simulation (top) and the adjusted soil moisture simulation (bottom). Simulation period was for 12 h starting at 1200 UTC 13 September 2006. Instantaneous hourly model data and hourly observations were used. Positive (negative) values indicate an angle in a clockwise (counterclockwise) fashion which model winds would have to be rotated to match the analyzed observations.

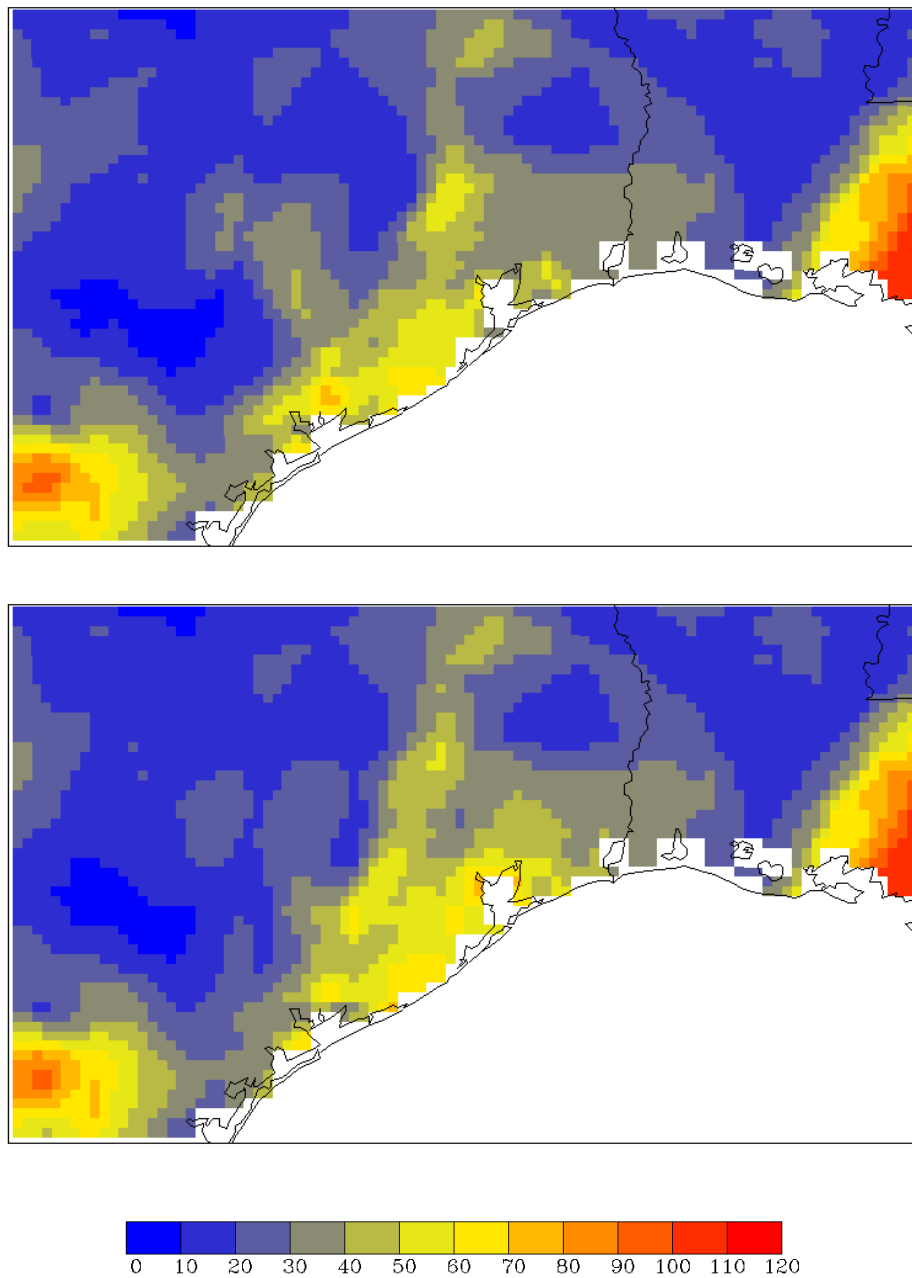


Figure 7.35 Root mean square error (RAMS model minus analyzed observations) in units of degrees for wind direction at 10-m for the 12.15 km horizontal resolution grid for the control simulation (top) and the adjusted soil moisture simulation (bottom). Simulation period was for 12 h starting at 1200 UTC 13 September 2006. Instantaneous hourly model data and hourly observations were used.

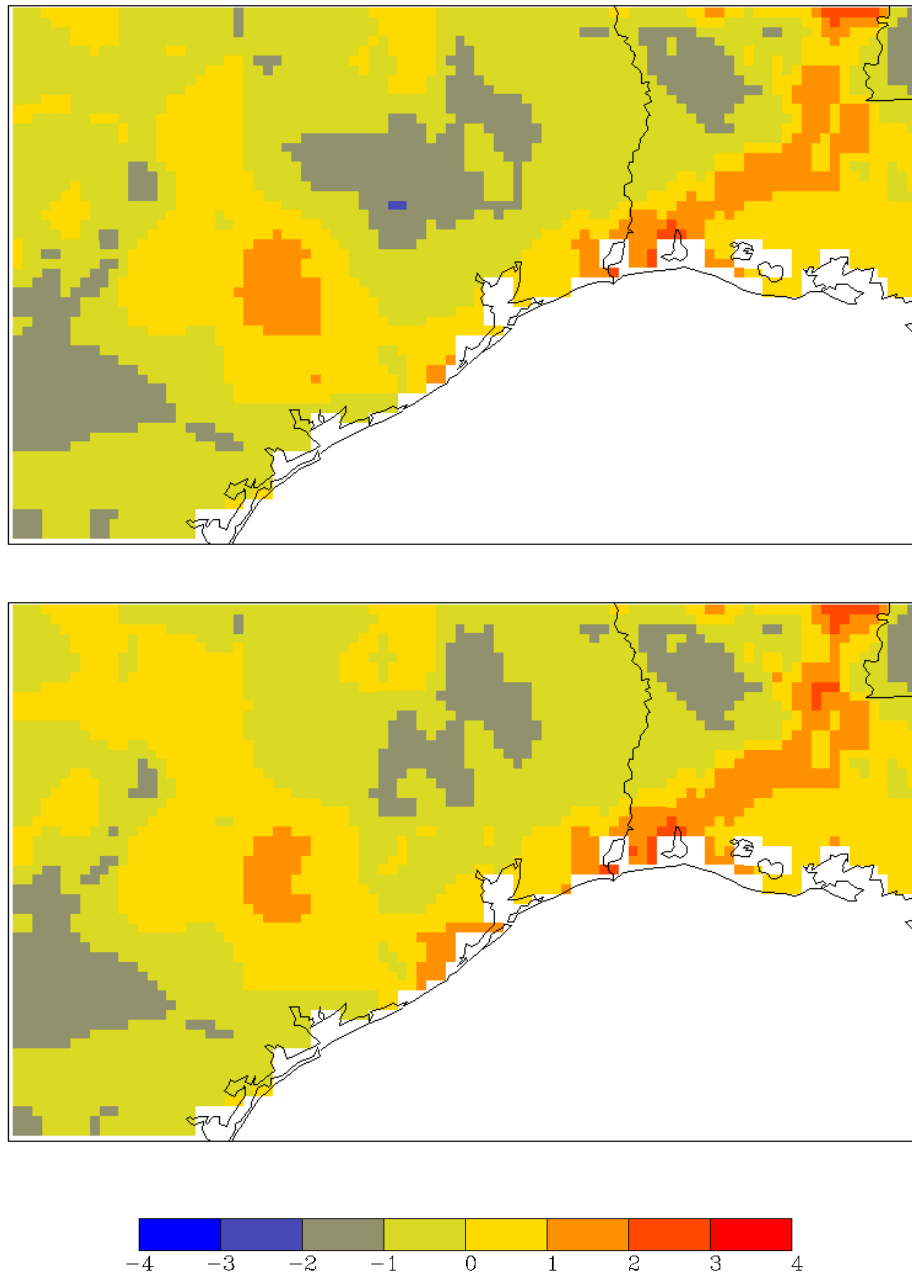


Figure 7.36 Average bias (RAMS model minus analyzed observations) in units of m s^{-1} for wind speed at 10-m for the 12.15 km horizontal resolution grid for the control simulation (top) and the adjusted soil moisture simulation (bottom). Simulation period was for 12 h starting at 1200 UTC 13 September 2006.

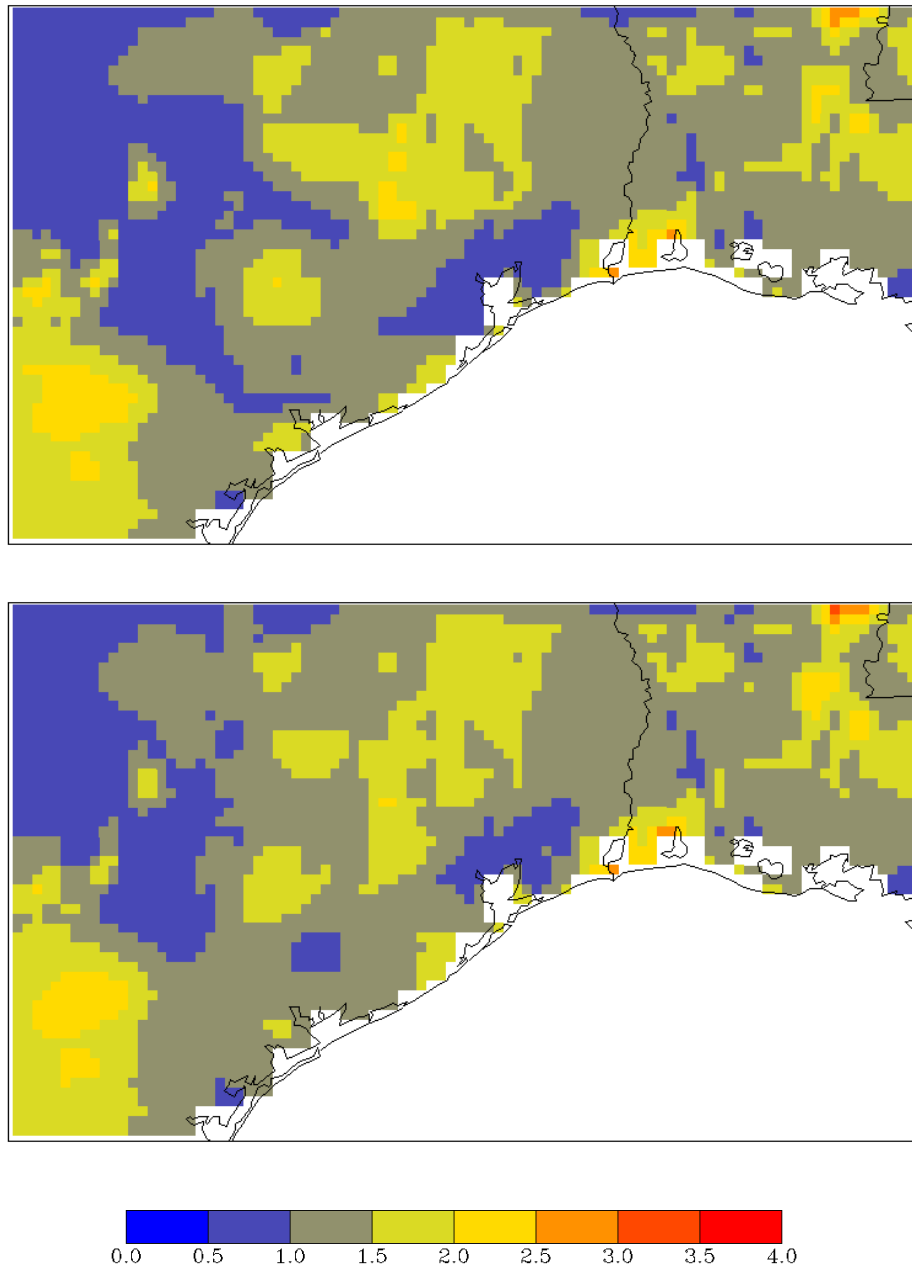


Figure 7.37 Root mean square error (RAMS model minus analyzed observations) in units of m s^{-1} for wind speed at 10-m for the 12.15 km horizontal resolution grid for the control simulation (top) and the adjusted soil moisture simulation (bottom). Simulation period was for 12 h starting at 1200 UTC 13 September 2006.

7.8 Comparison of Model and Observed Wind Profiles

7.8.1 *Wind data processing techniques*

In order to have common variables at the same height, both the model and observed wind profile data had to be transformed using a sequence of steps. The horizontal RAMS model wind components are cartesian components with respect to the polar stereographic map projection. The first step was a time averaging procedure. Model winds which were output every five minutes were averaged in time to correspond to the time averaging period for a given profile (usually a period of 1-h, please see Table 7-4). The second step took this field of time averaged winds and bi-linearly interpolated it to the profiler location in question. This profile of model time-averaged and horizontally interpolated winds will be denoted by $U_{MOD}(k)$ and $V_{MOD}(k)$, where (k) refers to the model σ_H level in question. The third step involved rotating these model cartesian components to earth-relative (with respect to direction) components as in Eqs. (13) and (14), where a_{ij} are constants determined from the map projection parameters, $U_{MOD,E}(k)$ is the true west-east model wind component at level k , and $V_{MOD,E}(k)$ is the true north-south model wind component at level k . These earth-relative model components can then be used to calculate a model wind direction using Eq. (15), where $\beta_{MOD}(k)$ is the model wind direction in degrees at model σ_H level k , δ_U is zero for easterly $U_{MOD,E}(k)$ components, and one for westerly $U_{MOD,E}(k)$ components. Rotation of the model cartesian components does not affect the speed, so the model wind speed S_{MOD} can be calculated as the square root of the sum of the squares of the individual components from either set. At this point we have the model wind direction and wind speed defined at the model σ_H levels.

$$(13) \quad u_{MOD,E}(k) = a_{11}u_{MOD}(k) + a_{12}v_{MOD}(k)$$

$$(14) \quad v_{MOD,E}(k) = a_{21}u_{MOD}(k) + a_{22}v_{MOD}(k)$$

$$(15) \quad \beta_{MOD}(k) = \delta_u 180 + 90 - \tan^{-1} \left(\frac{v_{MOD,E}(k)}{u_{MOD,E}(k)} \right)$$

Considering the observed wind data, the fourth step involved obtaining the observed earth-relative components by using Eqs. (16) and (17), where U_{OBS} is the observed west-east earth-relative component, V_{OBS} is the observed north-south earth-relative component, S_{OBS} is the observed wind speed, and β_{OBS} is the observed wind direction.

$$(16) \quad u_{OBS} = -S_{OBS} \sin(\beta_{OBS})$$

$$(17) \quad v_{OBS} = -S_{OBS} \cos(\beta_{OBS})$$

The fifth step involves integrating the observed earth-relative components with respect to height to obtain vertically averaged components at the model σ_H layers using Eqs. (18) and (19), where $\bar{U}_{OBS}(k)$ is the vertically averaged observed west-east component over the model σ_H layer k , $\bar{V}_{OBS}(k)$ is the vertically averaged observed north-south component over the model σ_H layer k , ΔZ_M is the thickness of the model σ_H layer, and dz_{OBS} is the

$$(18) \quad \bar{u}_{OBS}(k) = \frac{1}{\Delta Z_M} \int u_{OBS} dz_{OBS}$$

$$(19) \quad \bar{v}_{OBS}(k) = \frac{1}{\Delta Z_M} \int v_{OBS} dz_{OBS}$$

$$(20) \quad \bar{\beta}_{OBS}(k) = \delta_u 180 + 90 - \tan^{-1} \left(\frac{\bar{v}_{OBS}(k)}{\bar{u}_{OBS}(k)} \right)$$

$$(21) \quad BIAS = \frac{\sum (A_{MOD} - A_{OBS}) \Delta Z_M}{\sum \Delta Z_M}$$

$$(22) \quad RMSE = \left[\frac{\sum (A_{MOD} - A_{OBS})^2 \Delta Z_M}{\sum \Delta Z_M} \right]^{\frac{1}{2}}$$

thickness of the observed wind data layer. A corresponding observed wind direction over the model σ_H layer k , $\beta_{OBS}(k)$, is then obtained using Eq. (20). The bias and root mean square error (RMSE) of either the wind direction or wind speed is then given by Eqs. (21) and (22), respectively. The differences in Eqs. (21) and (22) are weighted by the model layer thickness since the model σ_H layers are not uniform in size. For a given profiler location, Eqs. (21) and (22) were applied for all observed data and all times to create one statistic apiece for bias and RMSE. These are the statistics which are displayed in Table 7-8 and Table 7-9. When the magnitude of the wind direction difference $\beta_{MOD}(k) - \beta_{OBS}(k)$ is greater than 180° , the difference is converted to an angle with a magnitude which is less than 180° but which retains the sign of the original difference. Further details on the meaning the wind direction error and how it will be displayed in the plots is described in Figure 7.38.

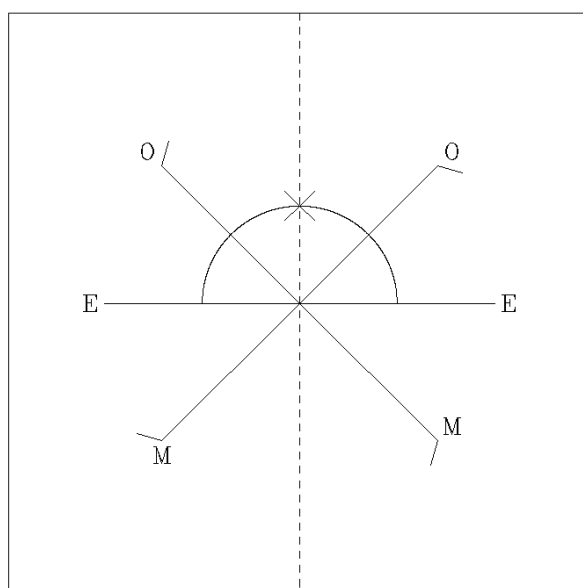


Figure 7.38 Explanation of model wind error plots. First consider the right-hand side of the plot where a model wind vector having a direction of 135° and an observed wind direction of 45° are plotted. The model minus the observed wind direction ($135-45 = +90$) is plotted as a “wind vector” at 90° with the meaning that the model wind vector would have to be rotated counter-clockwise by 90° to match the observed wind direction (denoted by the circular arc in the counter-clockwise direction with the terminating arrowhead). Now consider the left-hand side of the plot where a model wind vector having a direction of 225° and an observed wind direction of 315° are plotted. The model minus the observed wind direction ($225-315 = -90$) is plotted as a “wind vector” at 270° with the meaning that the model wind vector would have to be rotated clockwise by 90° to match the observed wind direction (denoted by the circular arc in the clockwise direction with the terminating arrowhead).

7.8.2 Statistical summary of model/observed wind profile comparisons

Table 7-8 and Table 7-9 show the bias and RMSE statistics (calculated as discussed in section 7.8.1) for the control (CNTRL) and soil moisture adjustment (SOILM) simulations, respectively. The tables have been sorted by ascending values of the wind direction root mean square error (WDIR-RMSE). The statistics were very similar between the two runs and furthermore with respect to the sorted tables there were no differences in the rank of the site locations with respect to WDIR-RMSE. The remaining discussion will refer to the CNTRL results from Table 7-8. Values for the WDIR-RMSE ranged from approximately from 9° at Moody to 45° at Arcola. The values for the wind direction bias, WDIR-BIAS, ranged approximately from 3° at Ledbetter to 31° at Arcola. The values for the wind speed root mean square error (WSPD-RMSE) ranged from near 1 m s^{-1} at Moody to about 4 m s^{-1} at Brenham. The values for the wind speed bias (WSPD-BIAS) ranged from near $+1 \text{ m s}^{-1}$ at Ledbetter to about -3 m s^{-1} at Brenham. Six locations had negative wind speed biases and four had small positive wind speed biases. So in general the model winds were slower than the observed winds and had directions which were more northeasterly to southeasterly compared to the predominant northerly observed flow.

Table 7-8 Summary wind error statistics for the control simulation. Wind direction bias (model minus observed) (WDIR-BIAS), wind direction root mean square error (WDIR-RMSE), wind speed bias (model minus observed) (WSPD-BIAS), wind speed root mean square error (WSPD-RMSE), and model domain resolution used for the comparison (DXG) for the profiler locations indicated. Wind direction is in units of degrees while wind speed is in units of m s^{-1} . Table has been sorted by ascending values of WDIR-RMSE. DXG is the horizontal resolution of the model data used.

LOCATION	WDIR BIAS	WDIR RMSE	WSPD BIAS	WSPD RMSE	DXG
Moody	2.65	8.55	-0.05	1.01	12.15 km
Huntsville	5.32	10.09	-2.23	2.74	12.15 km
Ledbetter	3.10	14.22	0.67	1.76	4.05 km
New Braunfels	13.32	19.27	0.18	1.06	12.15 km
Brenham	18.13	24.84	-2.59	3.69	12.15 km
Jefferson County	28.82	35.78	0.19	1.53	4.05 km
Laporte	25.61	38.15	-1.08	2.70	150 m
Beeville	6.52	43.02	-0.78	1.51	12.15 km
Brazos	10.39	44.96	0.54	1.59	12.15 km
Arcola	31.27	45.31	-2.34	3.53	1.35 km

Table 7-9 Summary wind error statistics for the soil moisture adjustment simulation. Wind direction bias (model minus observed) (WDIR-BIAS), wind direction root mean square error (WDIR-RMSE), wind speed bias (model minus observed) (WSPD-BIAS), wind speed root mean square error (WSPD-RMSE), and model domain resolution used for the comparison (DXG) for the profiler locations indicated. Wind direction is in units of degrees while wind speed is in units of m s^{-1} . Table has been sorted by ascending values of WDIR-RMSE. DXG is the horizontal resolution of the model data used.

LOCATION	WDIR BIAS	WDIR RMSE	WSPD BIAS	WSPD RMSE	DXG
Moody	2.49	8.52	-0.06	1.01	12.15 km
Huntsville	5.52	11.61	-2.11	2.66	12.15 km
Ledbetter	3.47	14.73	0.65	1.76	4.05 km
New Braunfels	13.55	19.46	0.19	1.06	12.15 km
Brenham	17.43	25.60	-2.65	3.70	12.15 km
Jefferson County	28.80	35.78	0.21	1.53	4.05 km
Laporte	26.82	39.92	-0.86	2.75	150 m
Beeville	6.78	43.14	-0.79	1.51	12.15 km
Brazos	10.89	45.12	0.53	1.58	12.15 km
Arcola	32.26	46.67	-2.26	3.37	1.35 km

7.8.3 Spatial plots of the wind error summary statistics

Figure 7.39 is a spatial analysis of the wind direction bias and RMSE results from Table 7-8 from the control run using a Barnes analysis. There were no profilers in the northeastern quadrant of the 12.15-km domain so the patterns there are uncertain. The bias and RMSE plots taken together indicate degradation in the model wind direction performance from northwest to southeast. The wind speed analysis in Figure 7.40 shows a different pattern, with the worst model performance centered from Houston north through the forest area, and then with improving performance outward from the latter area.

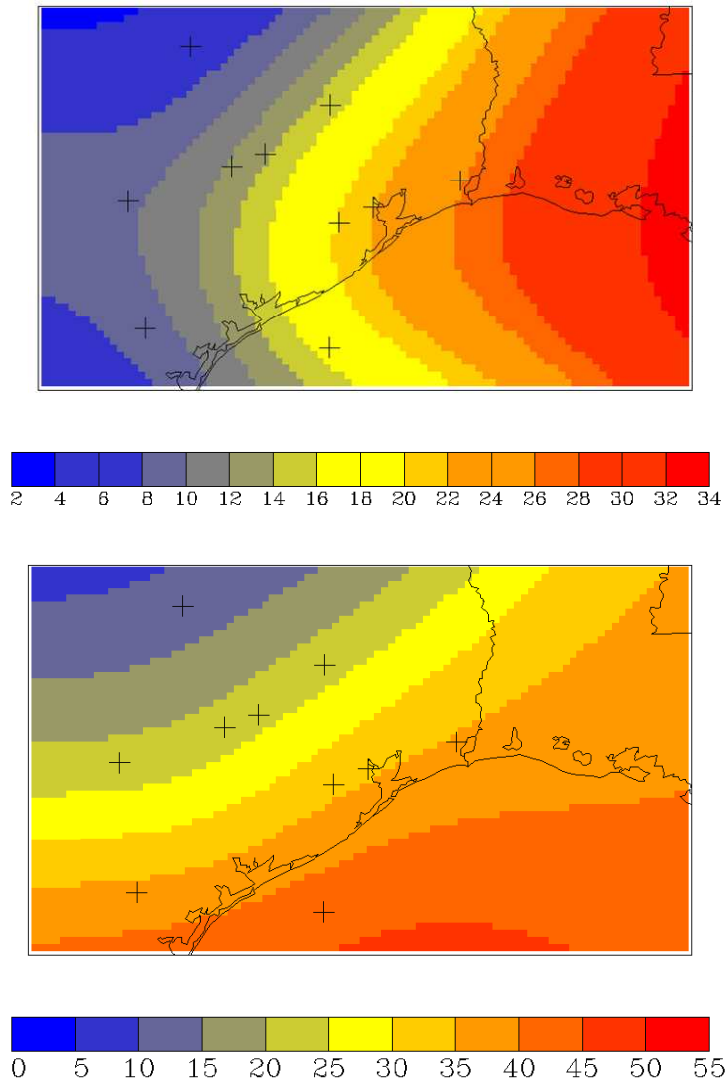


Figure 7.39 (Top) Analyzed model control run wind direction bias (model minus observation) in degrees relative to profiler data. (Bottom) Analyzed model control run wind direction root mean square error (model minus observation) in degrees relative to profiler data. Data are taken from Table 7-8. The profiler data locations plotted as “+” symbols. See the text for additional details.

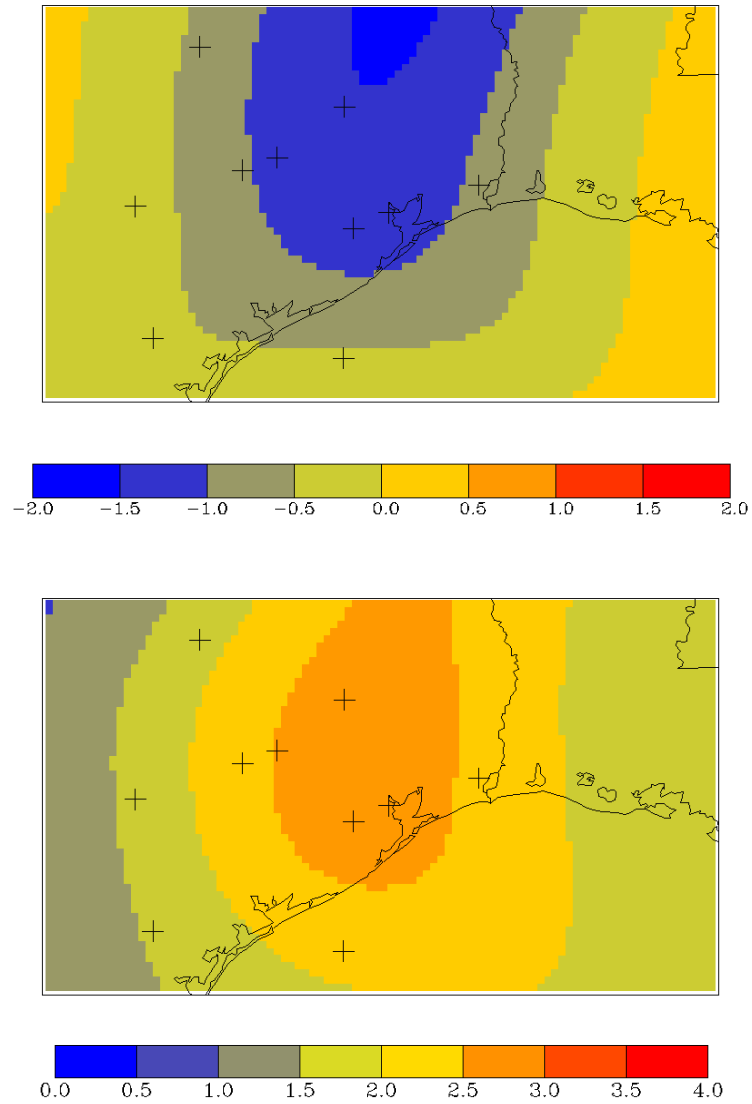


Figure 7.40 (Top) Analyzed model control run wind speed bias (model minus observation) in m s^{-1} relative to profiler data. (Bottom) Analyzed model control run wind speed root mean square error (model minus observation) in m s^{-1} relative to profiler data. Data are taken from Table 7-8. The profiler data locations plotted as “+” symbols. See the text for additional details.

7.8.4 Time-height wind speed and direction bias errors

Figure 7.41 and Figure 7.42 show time-height sections of the wind speed and wind direction errors (defined as model minus observed) for the profilers which were within the RAMS nested grid system and which had data for the period in question. These plots used the control run simulation. Wind speed errors less (greater) than zero indicate model wind speeds less (greater) than those observed. Wind direction errors are plotted according to the description given in Figure 7.38. With a few exceptions all the locations seem to have been initialized well given the small wind speed and direction errors at the starting time of 1200 UTC. Several patterns were observed when all the sites are examined. One noticeable pattern which lasted for most of the 12-h simulation was a layer at heights from 1-4 km with wind speed errors of -4 to -8 m s^{-1} at the sites Arcola, Brenham, Huntsville, and Laporte. These same layers also had sizable wind direction errors having magnitudes of 30-90°. Another noticeable pattern which occurred mainly in the morning to early afternoon hours was a layer at heights from 0-1 km with wind speed errors of +4 to +8 m s^{-1} at the sites Arcola, Brenham, Jefferson County, and Laporte. These same layers sometimes had sizable wind direction errors with magnitudes up to 45°. The relatively good performance at the Huntsville and Moody locations which was displayed in the data in Table 7-8 is also evident in the time-height sections of those profilers. This was likely due at least in part to the fact that both the Moody and Huntsville sites were within the 12.15 km where the nudging towards the observed analyses would have a major impact.

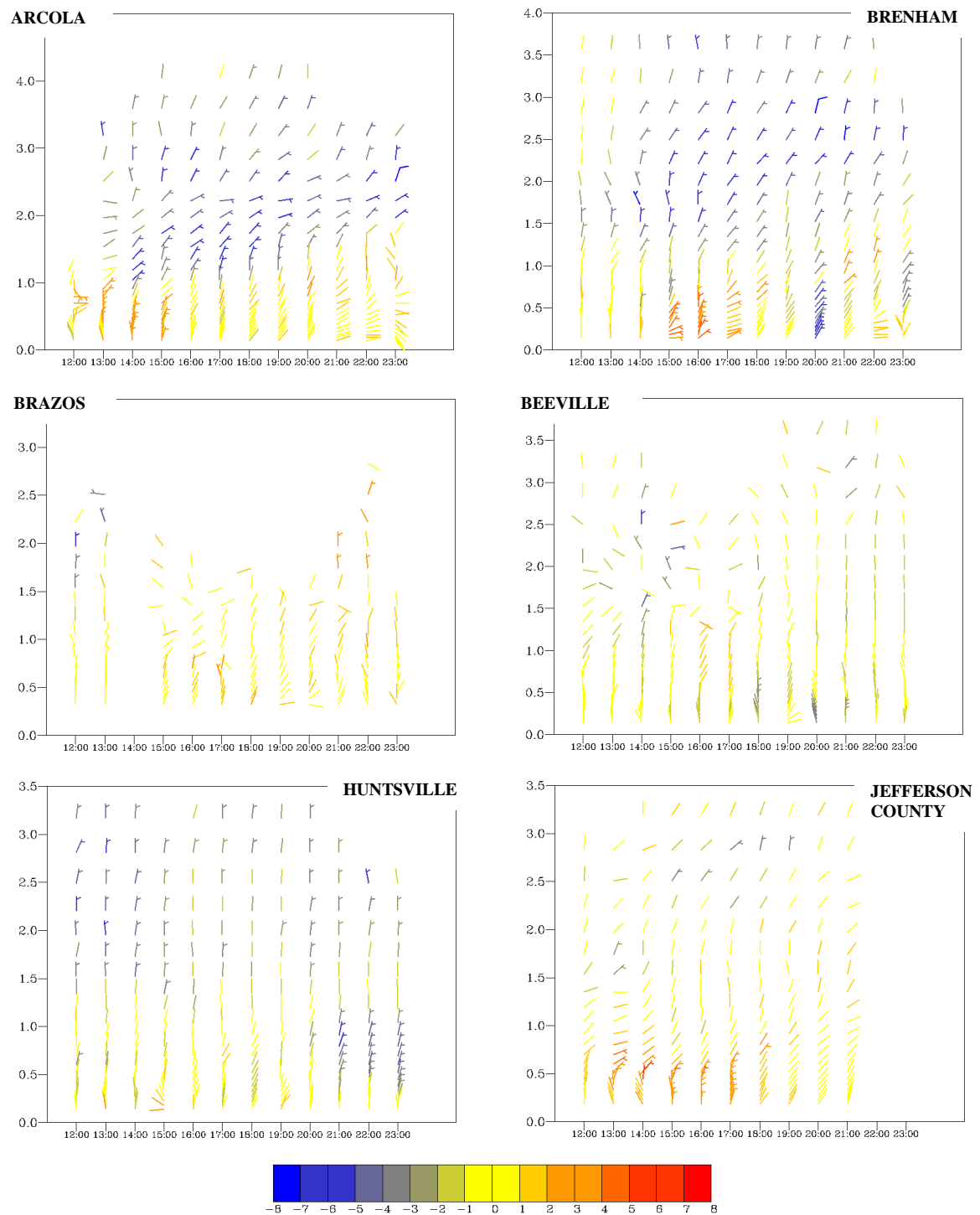


Figure 7.41 Time height sections of the control model run minus observed profiler error for various profiler locations which are indicated at the top of each plot. The magnitude of the wind speed errors are plotted as full barbs for 10 m s^{-1} and half barbs represent 5 m s^{-1} . Wind speeds errors are also plotted in m s^{-1} according to the color bar at the bottom. See Figure 7.38 for an explanation of the wind direction error plotting pattern. The z-axis is the height in km above the local terrain. The x-axis is the UTC time.

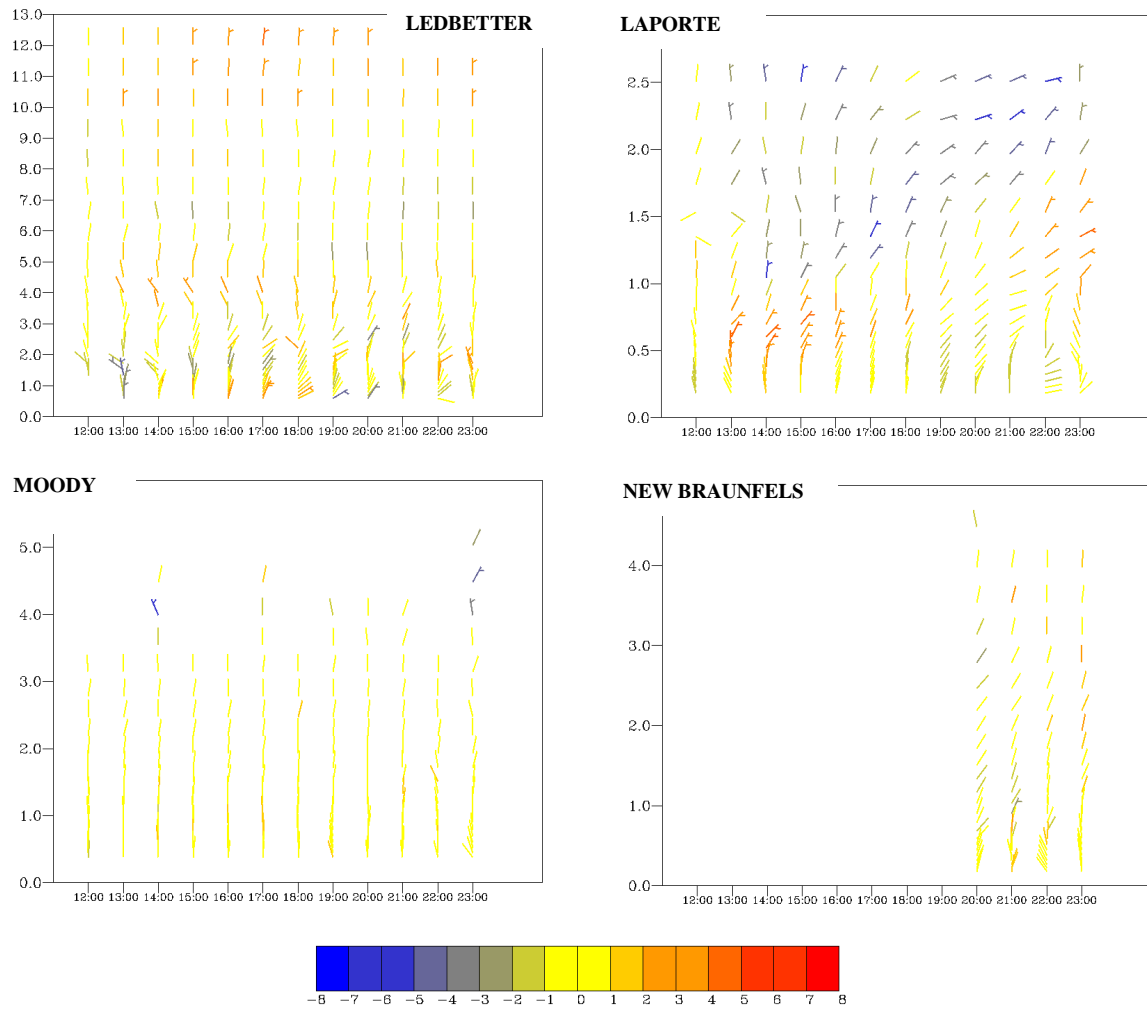


Figure 7.42 Time height sections of the control model run minus observed profiler error for various profiler locations which are indicated at the top of each plot. The magnitude of the wind speed errors are plotted as full barbs for 10 m s^{-1} and half barbs represent 5 m s^{-1} . Wind speeds errors are also plotted in m s^{-1} according to the color bar at the bottom. See Figure 7.38 for an explanation of the wind direction error plotting pattern. The z-axis is the height in km above the local terrain. The x-axis is the UTC time.

7.8.5 Model and observed profiles at the Laporte location

Figure 7.43 - Figure 7.45 focus on the model performance at the Laporte profiler which was the only profiler within the LES 150-m grid. Figure 7.43 shows the time-height sections of the model wind vectors for both the control and soil moisture adjustment simulations. Figure 7.44 shows the observed values, while Figure 7.45 shows the wind error plots for both simulations. The observed winds in Figure 7.44 for the lowest 500-m show northerly flow of 4-6 m s^{-1} for the first 8 h until a transition to northeasterly flow begins at 2000 UTC and by 2300 UTC the flow is northeasterly at around 1 m s^{-1} . The observed winds above 1-km were from the northwest most of the day with maximum speeds of around 10 m s^{-1} . Comparison of the two model wind simulations shows they were similar until about 2100 UTC and later. The soil moisture adjustment run had winds which were more southeasterly than the control run and with wind speeds of 6-7 m s^{-1} whereas the control run maintained weaker flow of 1-2 m s^{-1} . The error plots in Figure 7.45 show three evident patterns for both runs. Both had wind direction errors of flow which were too easterly from 2000 UTC onwards. Both had significant positive wind speed errors in the layer from 0.5-1.0 km above the surface for the 4 h in the morning starting at 1300 UTC. Finally, both had wind speeds slower than observed above 1-km for much of the day with wind direction errors which were once again with the model winds having too much of an easterly component.

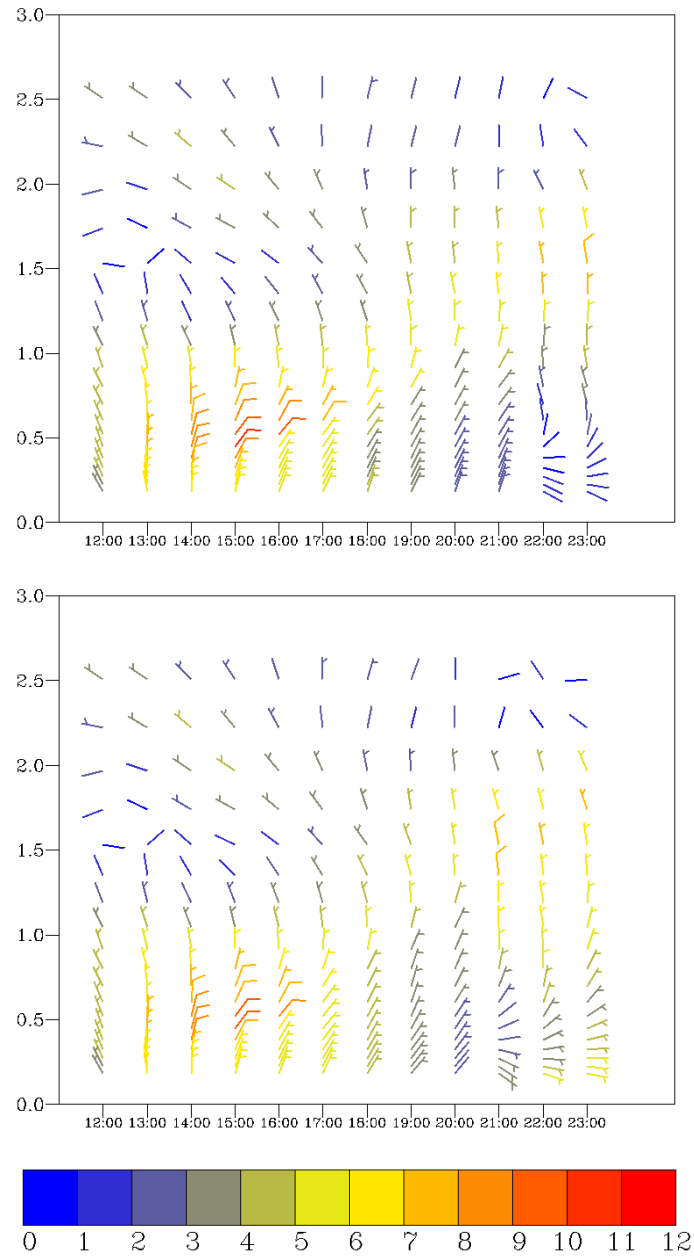


Figure 7.43 Time height sections for Laporte profiler location for the 150-m model control simulation (top) and soil moisture adjustment simulation (bottom). Full barbs represent 10 m s^{-1} and half barbs represent 5 m s^{-1} . Wind speeds in m s^{-1} for each wind vector are color coded as in the color bar at the bottom. The z-axis is the height in km above the local terrain. The x-axis is the UTC time.

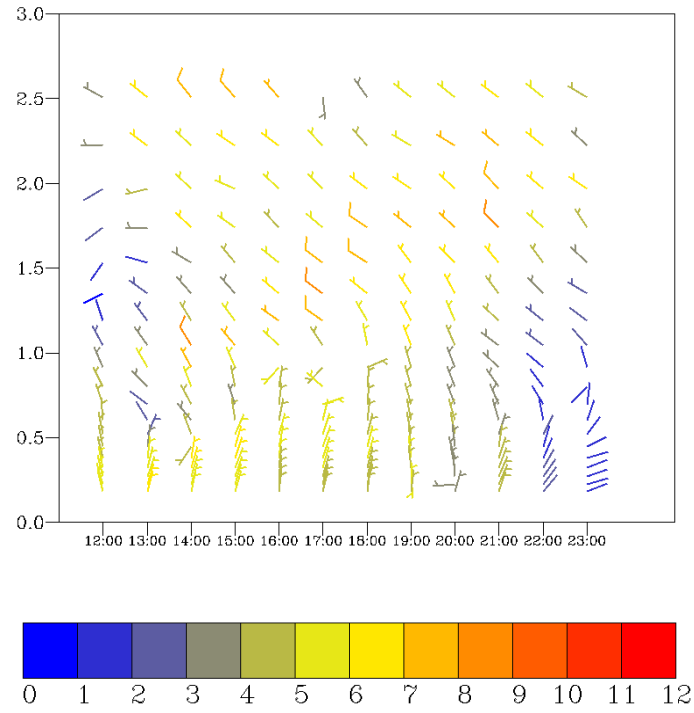


Figure 7.44 Time height sections for observed winds for the Laporte profiler location. Full barbs represent 10 m s^{-1} and half barbs represent 5 m s^{-1} . Wind speeds in m s^{-1} for each wind vector are color coded as in the color bar at the bottom. The z-axis is the height in km above the local terrain. The x-axis is the UTC time.

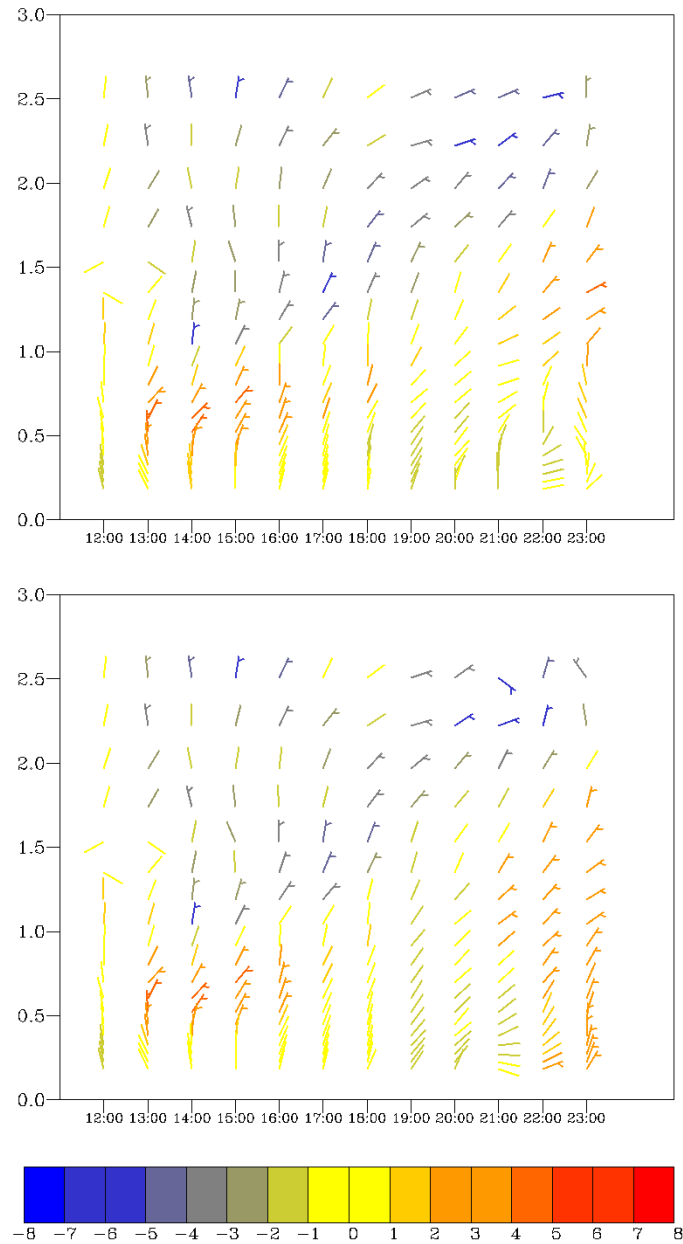


Figure 7.45 Time height sections for model errors at the Laporte profiler location for the 150-m grid model control simulation (top) and soil moisture adjustment simulation (bottom). Full barbs represent 10 m s^{-1} and half barbs represent 5 m s^{-1} . Wind speed errors in m s^{-1} for each wind error vector are color coded as in the color bar at the bottom. The z-axis is the height in km above the local terrain. The x-axis is the UTC time. Wind speed errors are defined as model minus observed. Wind direction errors are plotted as the rotation in degrees required for the model winds to be equal to the observed winds. See the text for additional information.

7.8.6 Discussion of model wind errors

One of the wind error patterns just discussed was the model wind speeds being slower than the observed values at heights from 1-4 km principally at the sites Arcola, Brenham, Huntsville, and Laporte. Since this layer is above most of the model or observed mixing heights (mixing heights to be discussed in section 7.9), it suggests problems with the geostrophic component of the wind and therefore errors in the lower-level thermal fields. The top panel in Figure 7.46 shows the horizontal wind speed at model level 22 ($\sigma_H = 1.534$ km) from the control simulation on the 12.15 grid at 1800 UTC 13 September 2006. It shows a northwest to southeast oriented band of wind speeds of $6-8 \text{ m s}^{-1}$ just north of the HSC which rapidly decreases to a rather large area west of the HSC with much weaker wind speeds of $0-4 \text{ m s}^{-1}$. The four sites mentioned above are in or near this light wind region. The bottom panel of Figure 7.46 shows the geostrophic wind speed at the same time and level, and superimposed on it are the main warm bias regions at 2-m (model minus observed) of the control run as shown in Figure 7.30. There is somewhat of a discrepancy between the two fields, as the wind fields are instantaneous values at 1800 UTC whereas the temperature bias field is a mean bias over the 12-h simulation. However, for the purposes here, it is still a valuable tool. Between the western warm bias region (marked as “1” in Figure 7.46) and the northern warm bias region (marked as “2” in Figure 7.46) there was a corridor of weak geostrophic winds that extends from the HSC area and then to the northwest. This weakness in the geostrophic wind was likely the result of the error in the low-level temperature fields. Thus, it appears that the temperature bias issues in these regions is creating most if not all of the slow model wind speeds in the 1-4 km layer for several sites.

If these temperature bias issues were substantially reduced, there would remain wind speed and direction issues. These would likely be the result of roughness lengths for one or more landuse types that need to be modified. One unresolved issue of implementing the NLCD data on the 150-m and 450-m grids was the knowledge of how to specify the needed geophysical parameters for one or more of the specialized types. For example, there was little guidance to our knowledge on how the roughness length and surface albedo should be specified for the light, moderate, and heavy developed urban categories which were displayed in Figure 7.13.

The remaining evident source of wind errors are the apparent areas of convection along the Gulf coast southwest of Houston and over southeastern Louisiana and to perhaps a lesser extent over the extreme southern portions of the grid (again over the Gulf of Mexico). Since our runs had clouds and precipitation inactivated these circulations could not be simulated. Even with the proper options utilized it would be difficult to simulate these areas realistically.

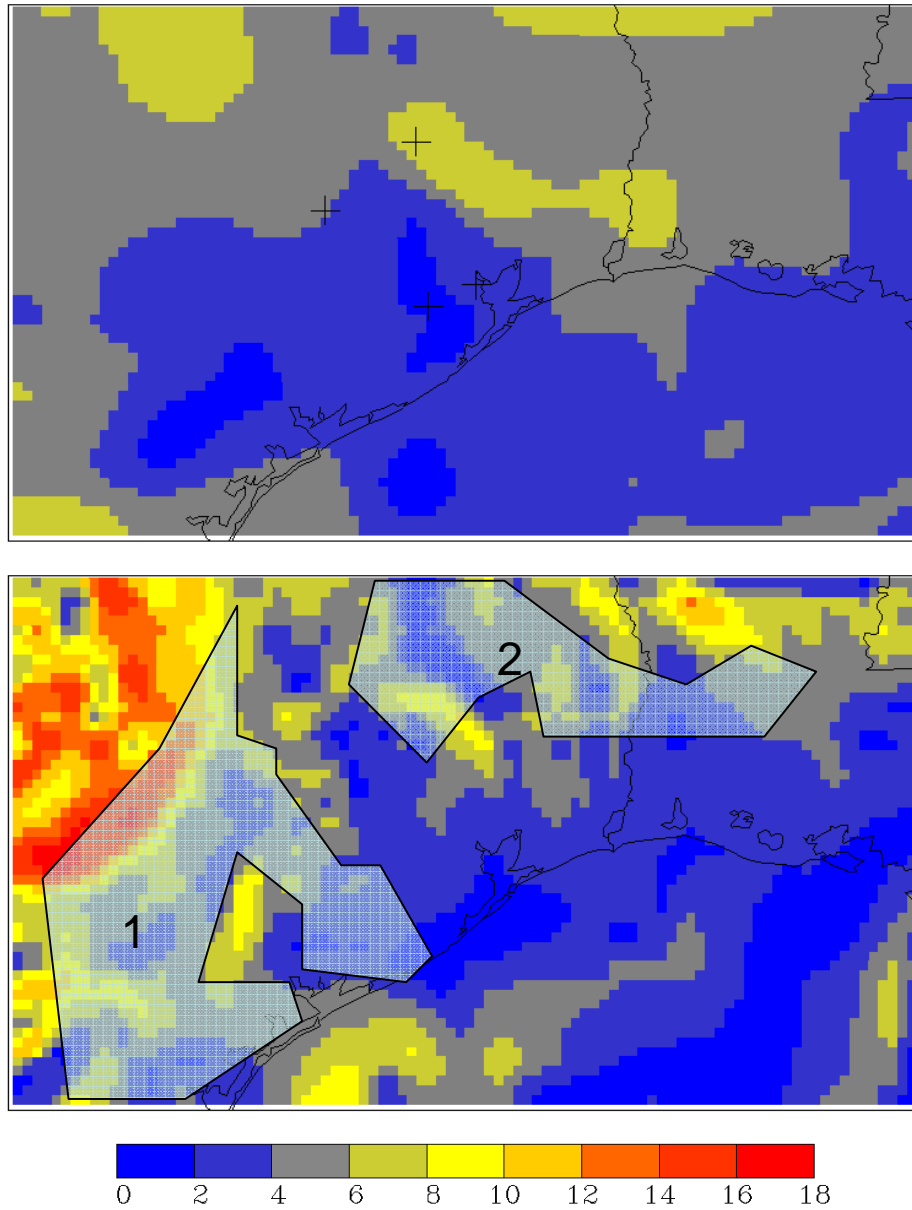


Figure 7.46 (Top) Horizontal wind speed at model level 22 ($\sigma_H = 1.534$ km) from the control simulation on the 12.15 grid at 1800 UTC 13 September 2006. Wind speeds in m s^{-1} as shown on the color bar. The locations of the profiler sites Arcola, Brenham, Huntsville, and Laporte are indicated by “+” signs. (Bottom) (Background) Geostrophic wind speed at model level 22 ($\sigma_H = 1.534$ km) from the control simulation on the 12.15 grid at 1800 UTC 13 September 2006. Wind speeds in m s^{-1} as shown on the color bar. (Foreground) The light blue semi-transparent areas (marked as regions 1 and 2) approximately encompass the warm bias regions from the control run as shown in Figure 7.29. See the text for additional details.

7.9 Comparison of Model and Observed Mixing Heights

7.9.1 *Statistical summary*

Mixing heights are not a prognostic variable within RAMS so they must be diagnosed from other available variables. There are several methods but we have chosen to use the first model level above the surface where the turbulent kinetic energy (TKE) falls below the threshold value of $10^{-3} \text{ m}^2 \text{ s}^{-2}$. The observed mixing heights from the profilers were typically an approximate hourly average, so model-derived mixing height fields from the TKE criteria data were calculated every 5 minutes and then averaged over an hour. Bilinear interpolation from the surrounding four grid points provided an estimate of the model mixing height at the observed location. Table 7-10 shows the bias and root mean square error (RMSE) for the control (CNTRL) and soil moisture adjustment (SOILM) runs with respect to all the locations for the 12.15-km grid, and the Laporte location with respect to the 150-m grid. For the CNTRL run the individual bias values ranged from -29 m at Huntsville to -442 m at Moody, and the CNTRL RMSE values ranged from 203 m at Beeville to 538 m at Moody. For all soundings with respect to the CNTRL 12.15-km grid the bias was -179 m and the RMSE was 319 m. Similar values were noted for the SOILM run, where, for all soundings with respect to the 12.15-km grid, the bias was -116 m and the RMSE was 303 m. The statistics for the Laporte location on the 150-m grid showed a negative bias of 13 m for the CNTRL run and a positive bias of 135 m for the SOILM run. The main conclusion is that model mixing heights were less than observed and RMSE values were on the order of 200-300 m.

Table 7-10 Summary statistics for mixing height for the bias (BIAS) (model minus observed) and rmse (RMSE) for the control (CNTRL) and soil moisture adjustment (SOILM) simulations for the 12.15-km grid (first 7 rows) for the 12-h simulation from 1200 UTC 13 September 2006 to 0000 UTC 14 September 2006. Last row gives the statistics for the Laporte location for the 150-m grid. Model data every 5 minutes was averaged and then compared with the observed values. All values are in units of m. Rows sorted in ascending order based on CNTRL RMSE.

Location	CNTRL BIAS	CNTRL RMSE	SOILM BIAS	SOILM RMSE
Beeville	-138	203	-61	146
Huntsville	-29	232	-104	269
Jefferson County	-124	269	-132	282
Laporte	-125	317	120	306
Brenham	-288	344	-85	154
Moody	-442	538	-363	458
All Soundings (12.15-km) grid	-179	337	-116	303
Laporte (150-m grid)	-123	319	135	388

7.9.2 *Analysis of time series of model and observed mixing heights*

Figure 7.48 and Figure 7.49 show the time series of the model and observed mixing heights for all locations with respect to the 12.15-km grid and the Laporte site with respect to the 150-m grid. For several of the sites the observed values were only available for a few hours so a complete comparison is difficult. With respect to the 12.15-km grid, almost all sites for all times and both model runs had model hourly values which were less than the observed values. The only exception was at Laporte where the soil moisture adjustment run had values which exceeded the observed for part of the afternoon.

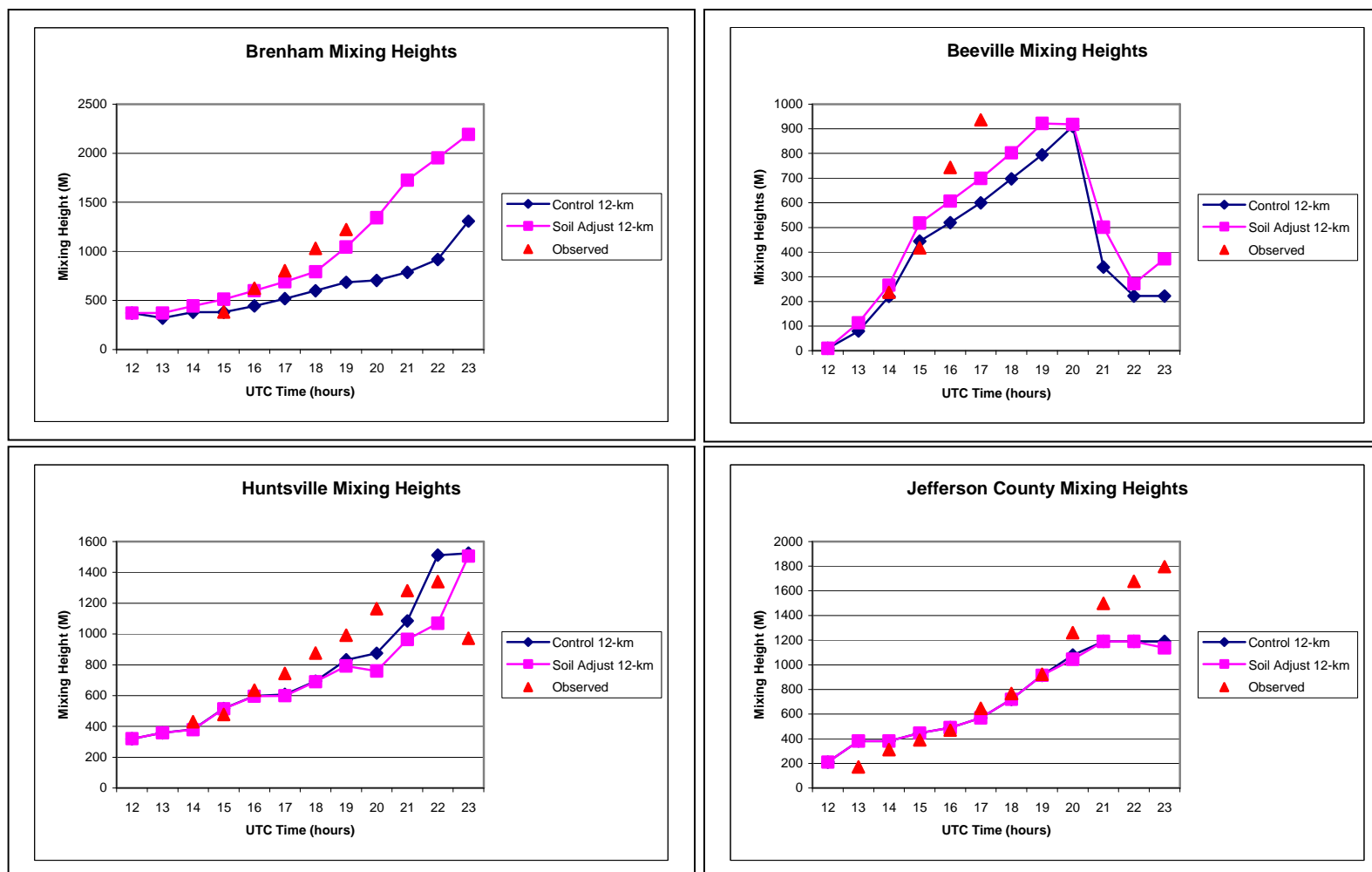


Figure 7.47 Time series of model and observed mixing heights for the locations identified at the top of each plot. The control run values are plotted with blue diamonds, while the soil moisture adjustment values are plotted with pink squares. Observed values are plotted with red triangles. The x-axis is the UTC time in hours and the y-axis is mixing height in m. All model data are from the 12.15-km grid.

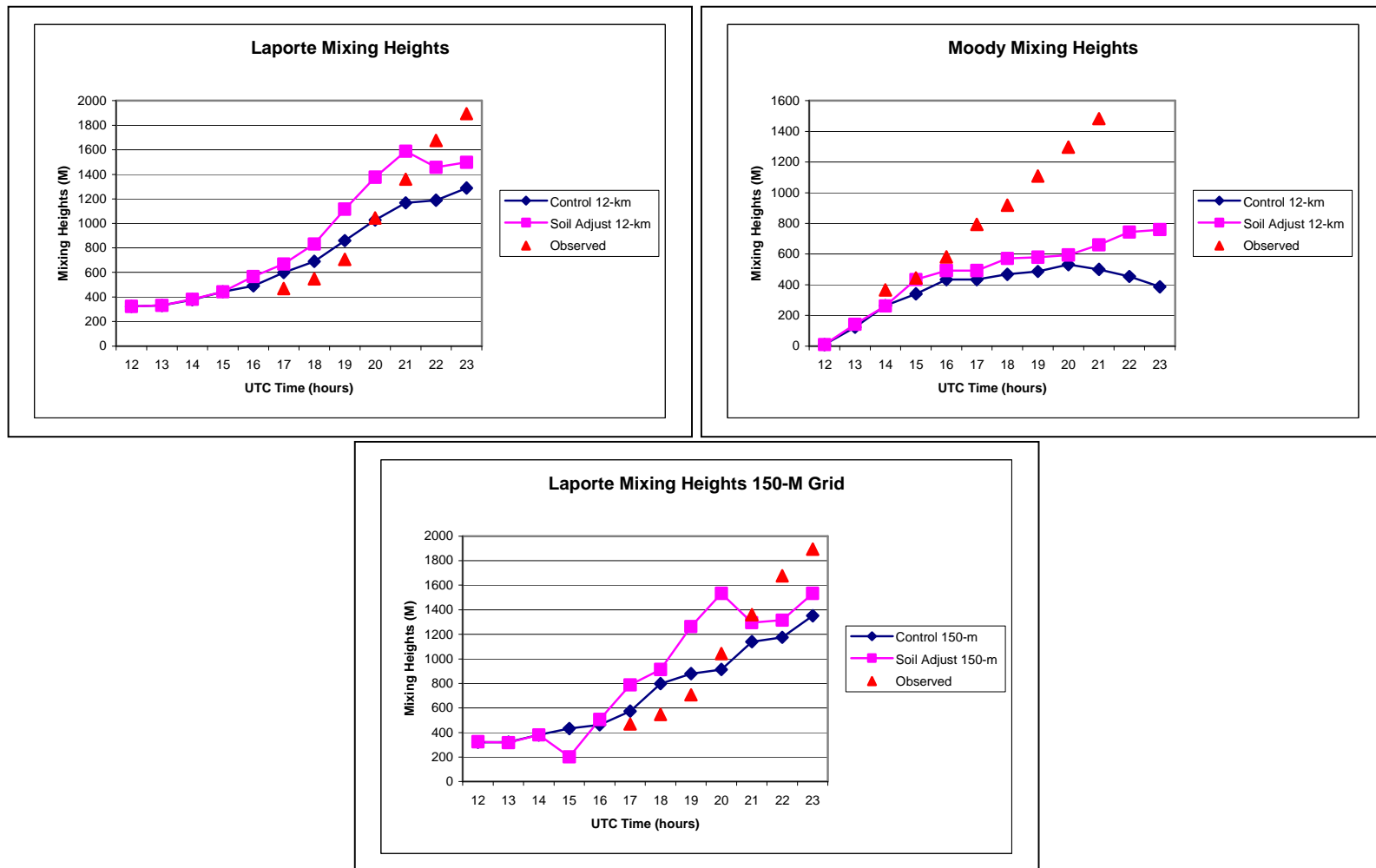


Figure 7.48 Time series of model and observed mixing heights for the locations identified at the top of each plot. The control run values are plotted with blue diamonds, while the soil moisture adjustment values are plotted with pink squares. Observed values are plotted with red triangles. The x-axis is the UTC time in hours and the y-axis is mixing height in m. The plots for the top panels use model data from the 12.15-km grid and the bottom panel uses model data from the 150-m grid.

7.9.3 Spatial distribution of mixing heights on the 150-m grid

Figure 7.49 gives an example of the model mixing height field for the hourly average from 20-21 UTC 13 September 2006 for the 150-m grid for the control simulation. Even though there is likely considerable error in the model field it shows the mesoscale variability of the mixing heights across this small domain with a range on the order of 800 m. With only one observed location available it is difficult to assess model performance.

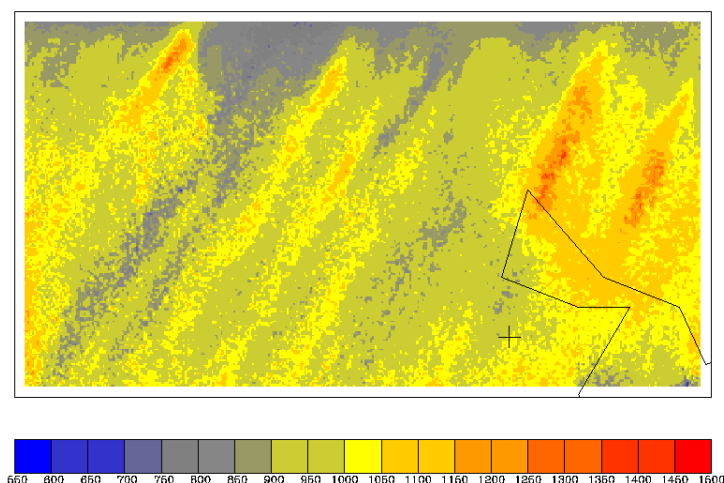


Figure 7.49 Time-averaged mixing heights for the period 20-21 UTC 13 September 2006 for the 150-m grid for the control simulation. Units are in m according to the color bar. Location of Laporte profiler is indicated by the “+” symbol in the southeastern portion of the domain.

7.10 Summary

Based on the model and observed data presented, six issues will be mentioned and briefly summarized. These seven are: 1) warm bias in forest region, 2) warm bias in the western region, 3) impact of warm bias areas on model wind performance, 4) specification of needed parameters for NLCD urban classes, 5) limitations of observed data on 150-m grid, and 6) experiment design constraints on model wind error.

Most of the time spent on trying to improve the model simulation was related in one way or another to the large forested area north of Houston on the 12.15-km grid. This area was important because, for northerly flow regimes such as on 13 September 2006, this is a source region for air traveling over the HSC. Given the tendency for forested areas to be cooler than surrounding non-forested areas and the precipitation which fell over parts of the forest area on 12 September 2006, it probably was a logical choice to enhance the soil moisture in that area to reduce the warm temperature bias. However, it is by no means the only part of the dynamics which needs consideration. Although not mentioned in the report, efforts were made to increase the vegetation bulk heat capacities for the forest regions as another way to decrease the diurnal temperature increase. This attempt was not pursued further because of numerical instability

issues which arose when the increased heat capacities were utilized. Analyzing model performance in this area is also made difficult by the lack of routine hourly NWS surface observations in this region.

A large area in the western part of the 12.15-km grid had a warm and wet bias in both simulations. The wet bias in this area was reduced by decreasing the initial soil moisture but at the expense of increasing the warm temperature bias. This indicates that one or more other parameters need modification in order to correct this bias. Two possible candidates are the surface albedo and the Normalized Differential Vegetative Index (NDVI). Increasing the albedo will decrease the amount of insolation available to heat the surface and therefore will lead to cooler near-surface temperatures. Some effort was spent on this approach with minimal improvement. NDVI fields are used in the RAMS land surface scheme to specify many of the physical parameters related to vegetation such as roughness length, albedo, and leaf area index. As with the soil moisture adjustment procedure described in section 7.7.1, a similar approach was attempted by making a run with the NDVI set to a relatively high constant value of 0.75 (where the maximum value is 1.0). In the same way as with the soil moisture adjustment, similar gradients of the temperature and mixing ratio error with respect to change in NDVI were calculated. A new run was then made with the default NDVI fields adjusted to minimize the near-surface errors. Again, at least within the limited time available in this project, this approach was tested, but the runs with the adjusted NDVI displayed minimal improvement. However, it can be said with confidence that it is related to some aspect of the surface energy balance that is not being specified correctly for that area. Given that parts of this region are agricultural and given the time of year, it is possible that some aspect of harvest has changed the surface characteristics in a way that is not being captured by the climatological fields used to determine the surface characteristics.

The warm bias regions just discussed have their own specific importance, but because temperature biases change the hydrostatic pressure field they also affect the geostrophic component of the wind. As discussed in the report, the two warm bias regions and the resultant weak geostrophic winds are likely the cause for the model winds to be slower than the observed RWP winds at the altitude range of 1-4 km.

The NLCD provided additional detail for the landuse specification, especially for urban areas, for the 150-m and 450-m grids. What was not easily available to our knowledge was how to specify the many required parameters such as roughness length for these different urban categories. While time did not allow us to do sensitivity studies to determine the impact of making such changes, it undoubtedly would impact many important aspects of the boundary layer simulation including mixing heights.

Assessing the model performance on the 150-m model grid was made difficult given the limited observed data available. While a valuable resource, the mixing heights from the Laporte profiler are not enough to measure the model performance over the rest of the 150-m domain, given the large variability of the landuse characteristics over this area.

Since the ultimate goal was to use the model output from RAMS to drive a chemistry model, it is instructive to determine the degree of wind error which is acceptable given the need

to track specific point emission sources. Equation (23) is the simple form from calculus relating the circular arc S to a radius R and an angle Θ measured in radians. For our purposes, S will be set to an integer multiple of the 150-m mesh size of the LES grid as in $N\Delta x$, the radius will be set to half the north-south distance of the 150-m grid as in $(n_y-1)\Delta x/2$, where n_y is equal to 164, and finally the angle will be converted to units of degrees (Θ_D). With these changes, Eq. (23) is recast in the form of Eq. (24), which can be solved for Θ_D given selections for the arc distance $N\Delta x$. Some examples of this simple calculation are given in Table 7-11. For example, an

$$(23) \quad S = R \theta$$

$$(24) \quad N\Delta x = \left(\frac{(N_Y - 1)\Delta x}{2} \right) \left(\frac{\pi}{180} \theta_D \right)$$

Table 7-11 Relationship between $S=N\Delta x$ and the corresponding angle in degrees.

N	N Δx (meters)	Corresponding Angle (deg)
1	150.000	0.7
10	1500.000	7.0
20	3000.000	14.1
30	4500.000	21.1
40	6000.000	28.1

arc of size 1500 m corresponds to an angle of about 7° . Applied to the model winds this implies that the RMSE of the wind direction would have to be of similar magnitude. The best model RMSE in this report was the Moody location which had a RMSE of about 9° . And this assumes that one can accept incorrect parcel locations after the travel distance chosen of about 10 grid cells. So the requirements from the emissions perspective are quite daunting.

7.11 Conclusions

For those not familiar with the data requirements required for assimilating observations, it is appropriate to review those requirements to begin this discussion. As mentioned in section 7.2.2, nudging towards the observed analyses was only done for the 12.15-km grid. It could be argued why not nudge towards the radar wind profilers (either as an analysis or at a point) on all grids? The largest turbulent features in the planetary boundary layer (PBL) have a diameter on the order of the height of PBL itself. Taking this length to be 1000 m (a typical maximum PBL height for 13 September 2006) and using a velocity scale of 5 m s^{-1} gives a time scale on the order of 10-15 minutes. To sample such a feature adequately one would need at least 10 observations within this time window which gives a minimum observational frequency of 60 s. So to nudge towards observed winds on the 150-m and 450-m grids would require observations of this temporal frequency or better. If one were to nudge towards the available hourly profiler observations, one would decrease the wind errors for hourly-averaged model data but at the expense of eliminating most of the turbulent scales of motion those grids were designed to develop in the first place. Nudging could have been attempted on the 4.05-km grid perhaps, but probably not on the 1.35-km grid. Because of the time spent on trying to resolve the temperature and water vapor bias issues there was not time to experiment with the many nudging possibilities on the larger scale grids.

As discussed in section 7.8.6 the model wind errors in the 1-4 km altitude range could likely be made smaller by reducing the low-level warm temperature bias issues in the areas west and north of the Houston area. However, even if this could be accomplished, there would remain substantial wind errors in the PBL itself. Many modeling studies have shown this and we will only cite a few of the most recent ones. Zhong and Fast (2003) compared three mesoscale models (one of which was RAMS) using a nested structure with the fine mesh having an horizontal resolution of just under 1-km to simulate the complex meteorology in the Salt Lake Valley in Utah. This location is an urban area surrounded by mountains and the Great Salt Lake to the northwest. Regardless of the episode selected, the RMSE from the RAMS simulation for the 10-m winds was on the order of 60° . The other models had errors which were similar or larger. Rife et al. (2004) examined the 10-m wind errors for four models: the Eta model, the Rapid Update Cycle version 2 (RUC-2), the Global Forecast System (GFS) model, and MM5. The first three models are operational models run by NCEP while MM5 is a research model (similar to RAMS). The respective model horizontal resolutions were: Eta, 40-km; RUC-2, 40-km; GFS, ~110-km; and MM5, 1.33-km. The evaluation again took place over the Salt Lake Valley. They showed that regardless of the model, or the horizontal resolution of the model, the mean absolute wind direction errors were close to 60° for 12-h simulations which were done over a period of 3 months and compared against 28 observation locations. Rife et al. (2004) gave two reasons why there was a seeming lack of improvement of wind forecasting skill for the finer resolution 1.33-km MM5 grid. The first reason was that small-scale subdiurnal components of the flow not related to terrain features had a large impact on many observation sites. These features are either not captured in the initial states or boundary conditions for the models and/or the physics is not capable of producing them. The second reason was that even though the finer meshes do resolve terrain features with smaller horizontal scales, the circulations they create are also small and even small model errors in phase create substantial errors in the wind fields. The final model comparison to be mentioned is Fast and Darby (2004), who compared RAMS simulated winds in the Salt Lake valley on a grid with a horizontal resolution of 560 m (similar to our next to the finest grid which had a mesh size of 450 m) against radar wind profiler data. The table with their error statistics is reproduced below in Figure 7.50. It shows RMSE in the wind direction approaching 50° at an altitude of 1500 m. The magnitude of these errors is very similar to the ones in this study. Fast and Darby (2004) also mention a similar study by Fast and Shaw (2002), where model winds were compared with radar wind profiler data in the urban area of Philadelphia, Pennsylvania and the RMSE errors were similar to those in the Salt Lake region. So apparently the magnitudes of the wind direction RMSE which were observed in the Salt Lake valley are not limited to areas with complex valley and canyon flows.

NOAA					PNNL				
Height (m AGL)	Speed		Direction		Height (m AGL)	Speed		Direction	
	Bias (m s ⁻¹)	Rms (m s ⁻¹)	Bias (°)	Rms (°)		Bias (m s ⁻¹)	Rms (m s ⁻¹)	Bias (°)	Rms (°)
124	-0.17	2.66	-2.45	36.20	110	-0.63	1.89	-0.49	34.07
234	0.20	2.73	0.32	39.00	220	0.04	1.78	0.36	32.72
344	0.05	2.70	-4.79	40.06	330	-0.14	1.94	-9.66	33.79
454	-0.01	2.92	-3.13	47.11	440	-0.72	1.99	-4.56	36.72
564	-0.56	3.23	-1.77	44.81	550	-0.43	1.91	-1.48	44.49
673	-0.09	3.03	-3.53	46.88	660	-0.03	1.73	-3.04	38.99
783	0.12	3.11	-14.06	50.80	770	-0.28	2.00	-4.86	38.22
838	0.50	3.38	-2.86	52.74	880	-0.78	2.26	4.60	41.93
948	0.73	3.27	2.35	54.15	990	-0.79	1.98	-6.46	49.57
1058	0.43	3.29	11.64	50.47	1100	-0.70	2.14	7.54	35.69
1168	0.63	2.90	15.47	50.90	1210	-0.41	2.37	10.53	38.73
1278	0.14	3.30	19.71	51.39	1320	-0.74	2.73	21.13	43.09
1388	0.71	3.09	11.92	47.45	1430	-1.24	2.75	22.18	51.26
1498	0.18	3.02	3.05	53.43	1540	-0.44	2.48	25.60	45.16

Figure 7.50 Bias (simulated-observed) and rms of the predicted wind speed and direction at the NOAA and PNNL radar wind profiler sites for eight IOPs (after Fast and Darby 2004). See the text for additional details.

Another issue just starting to be discussed in the literature is the appropriateness of using the standard mesoscale turbulence parameterizations on horizontal scales below about 3 km. After comparing 1-km and 10-km mesoscale simulations, Belair et al. (1998) recommended that horizontal resolutions between 200 m and a few km be avoided to remove the conflict between both the grid-scale and the turbulent parameterization trying to resolve the same features. When mesoscale model horizontal resolutions approach the size of the largest PBL eddies, then they are partially resolved by the grid and by the turbulent parameterization at the same time when by design, the turbulent parameterization was intended to simulate the entire spectrum of the turbulence. On this topic again referring to Zhong and Fast (2003) who said “Nevertheless, applying conventional turbulence parameterization at small horizontal scales is a research topic that needs to be addressed by the mesoscale modeling community.” However, to nest down from typical mesoscale data analyses used on the coarse grid for boundary conditions (in the 20-40 km resolution range), to the LES grid domain, one is forced to traverse this “no-man’s land” in the turbulence parameterization spectrum. The implication is that even if the physics on the LES-scale was perfect (which it is not), the boundary conditions being supplied by the nested grids upscale would introduce substantial errors into the LES domain.

For these reasons we conclude that with the present status of models the capability may not exist, even on the LES scale, to produce wind simulations with the necessary accuracy to accomplish the goals of a project like this, where emissions were to be related in space and time to observations downwind which had very fine horizontal resolutions.

7.12 Suggestions

Based on the experience from this study if LES modeling is attempted in the future over the HSC area we would recommend the following five items to be considered. 1) For northeasterly flow cases, as for 13 September 2006, there are little to no surface or upper-air observations to assess model performance in the area basically east of the north-south line between Palestine and Huntsville. Being a significant forested area, air in northeasterly flow travels through this region before arriving in the HSC. Even if this is in a coarse grid model deficiencies over this area are advected towards the finer grids in this type of flow regime. 2) Moderate Resolution Imaging Spectroradiometer (MODIS) 1-km skin temperature data could have been utilized to assess model skin temperatures but that product is typically only available twice a day. We lacked the time to use this observational dataset. 3) Additional profilers in the HSC area would have enabled a better assessment of the mixing height field given the large range of values in that area. 4) A way has to be found to fully utilize the information in the NLCD. We lacked adequate knowledge on how to specify parameters like roughness length and albedo as a function of the urban class. 5) RAMS has an experimental urban canopy option available which requires the specification of drag coefficients on the building to block scale. It is likely that to increase the realism of the flows on LES grids this approach is necessary. We did not attempt to experiment with this type of parameterization.

8 CONCLUSION

This project could not be completed as planned. Its scope had been under-estimated, and we ran out of time while still trying to achieve the objectives of modeling the dynamics of the atmosphere accurately at the LES scale. For near-field chemistry of the HSC emissions, the fine scale LES dynamics of the LES domain are critical, and for LES dynamics, the larger scale dynamics are critical, in addition to establishing appropriate linkages between the multiple scales involved in this project. The region is complex and there were unanticipated problems in a pioneering study such as this. We made various attempts to bring the dynamical simulation into agreement with observations but problems persisted. In some cases, as with the forest region north of Houston, there is lack of observed information which creates problems under northerly flow when the forest region is a source region. More effort is necessary to incorporate the high-resolution satellite-observed landuse information more accurately in RAMS at the various spatial resolutions of the nested grids. The requirement of simulating the atmospheric dynamics precisely enough to match them with observations, particularly of the wind field, at fine scale commensurate with the continuous chemical measurements (SOF, Aztec, P-3), was not possible in such a multiscale simulation in a complex area. Perhaps with more time to explore the many possible causes of the discrepancies, we may have had better luck.

It is our conclusion that in an area such as the HSC, which is very complex in terms of terrain, meteorology and chemistry, the application of LESchem to match the observed details of dynamics (*especially* dynamics) and chemistry is perhaps premature. Yet, the effects of turbulent chemistry are quite possibly important enough to cause significant errors in TDEV. Perhaps a better answer is to apply LES with proper land surface, *observed* larger scale meteorological BC under simple flow conditions, and cyclic BC for finer-scale turbulence first to a simpler region and source such as the Sweeny industrial facility (with no nested meteorological simulations), to obtain realistic dynamics, and then to apply the LESchem results to develop parameterizations of the turbulent chemistry (segregation coefficient in terms of mean concentrations and some mean measure of atmospheric turbulence). Such a parameterization can then be built into LRPM to incorporate the role of turbulent chemistry. The LRPM may then be applied with *observed* boundary layer and plume dynamics as normally done in LRPM applications, to generate estimates of the role of turbulent dynamics in near-field chemistry of petrochemical emissions. Such an LRPM with parameterization of turbulent chemistry can then be applied to the complex HSC scenario, in much the same way as was done in diagnostic mode with the data of TexAQS I (e.g., Figure 2.3), to perform TDEV studies of HSC with the role of turbulent chemistry included.

For now, we plan to salvage at least the application of LRPM to the 13 September 2006 scenario in diagnostic mode, without the role of turbulent chemistry, as part of HARC Project H91, in which we plan to perform diagnostic LRPM TDEV of four other days of TexAQS II also.

Acknowledgements

We wish to thank Jim MacKay of TCEQ for providing us with the emissions data and help in understanding it, and Doug Boyer of TCEQ for his assistance with the mixing height data. We also thank Johan Mellqvist for providing us with the SOF data, Sergio Alvarez for providing the Aztec data, and NOAA-AL for permission to use the P-3 data. We also thank Daewon Byun and his assistants for providing us with the MM5 and CMAQ results. Finally, we would like to thank Jay Olaguere of HARC and Dick Karp of TCEQ for their direction of this effort, and being understanding with the many problems we faced in its execution.

9 REFERENCES

- Alvarez S. et al. (2007). H-63 Aircraft Measurements in Support of TexAQS II, Baylor University Final Report of Project H-63 to Houston Advanced Research Center, June 2007.
- Avissar R. et al. (1998). An Evaluation of the Large-Eddy Simulation Option of the Regional Atmospheric Modeling System in Simulating a Convective Boundary Layer: A FIFE Case Study. *J. Atmos. Sci.*, 55(7):1109-1130
- Bélair, S., P. Lacarrère, J. Noilhan, V. Masson and J. Stein (1998): High-resolution simulation of surface and turbulent fluxes during HAPEX-MOBILHY. *Mon. Wea. Rev.* **126**, 2234–2253.
- Bretheron C.S. et al. (1999). An intercomparison of radiatively driven entrainment and turbulence in a smoke cloud, as simulated by different numerical models. *Q.J.R. Met. Soc.* **125**, 391-423.
- Byun, D., and K. L. Schere (2006): Review of the governing equations, computational algorithms, and other components of the Models-3 Community Multscale Air Quality (CMAQ) modeling system. *Appl. Mech. Rev.*, **59**, 51–77.
- Carter W. P. L. (1996): Condensed atmospheric chemistry mechanisms for isoprene. *Atmos. Environ.* **24**, 4275-4290.
- Chen, F. and W. R. Cotton (1983): A one-dimensional simulation of the stratocumulus-capped mixed layer. *Bound.-Layer Meteor.*, **25**, 289-321.
- Deardorff J.W.(1980). Stratocumulus-capped mixed layers derived from a three-dimensional model. *Boundary Layer Met.* **18**, 495-527.
- EPA (1999) : Science Algorithms of the EPA Models-3 CMAQ Modeling System, EPA-600/R-99/030, Mar 1999.

- Fast, J. D. and W. J. Shaw (2002): Observed and simulated turbulence kinetic energy and dissipation profiles in an urban valley during VTMX 2000. Preprints, *15th Symp. on Boundary Layers and Turbulence*, Wageningen, Netherlands, Amer. Meteor. Soc., 638-641.
- Fast, J. D. and L. S. Darby (2004): An evaluation of mesoscale model predictions of down-valley and canyon flows and their consequences using doppler lidar measurements during VTMX 2000. *J. Appl. Meteor.*, **43**, 420-436.
- Gillani, N. V. (1986): Ozone formation in pollutant plumes: Development and application of a reactive plume model with arbitrary crosswind resolution, EPA/600/S3-86-051.
- Gillani, N.V. et al. (1998): The plume-in-grid treatment of major elevated point-source emissions in Models-3, Preprint Vol., AMS-AWMA Conf Air Poll. Met, Phoenix AZ, Jan. 1998.
- Gillani N.V. and J. Godowich (1999): Plume-in-grid Treatment of Major Point Source Emissions”, Ch. 9 in Science Algorithms of the EPA Models-3 Community Multi-scale Air Quality (CMAQ) Modeling System , EPA-600/R-99/030
- Gillani N.V. and Y. Wu (2003a): Top-down Emissions Verification for the Houston-Galveston Industrial Point Sources Based on Texas AQS Data, Final Report of the U. of Alabama in Huntsville to Houston Advanced Research Center, Contract No. H62002B, June 2003.
- Gillani N.V. and Y. Wu (2003b): Lagrangian modeling of industrial point-source plumes in the Houston-Galveston area, Final Report of the U. of Alabama in Huntsville to Texas Commission for Environmental Quality Contract No. 582-2-48649-01, March 2003.
- Gillani N.V. and Y. Wu (2003c): Exploration of Uncertainty in the Simulation of Power Plant Plume Chemistry, Final Report of the U. of Alabama in Huntsville to the U. S. Environmental Protection Agency STAR Grant No.GR826239-010, April 2003.
- Gillani N.V. and Y. Wu (2004): Sensitivity in Simulated Chemistry in Houston-Galveston Industrial Point Source Plumes to Wind Speed, Precursor Emission Rates and Chemical Mechanism, Final Report of the U. of Alabama in Huntsville to Houston Advanced Research Center, Contract No. H6B-01, June 2004.
- Gopalakrishnan, S. G. and R. Avissar (2000): An LES study of the impacts of land surface heterogeneity on dispersion in the convective boundary layer. *J. Atmos. Sci.*, **57**, 352–371.
- Hadfield, M.G. (1989). The response of the atmospheric convective boundary layer to surface inhomogeneities. Ph.D. thesis, Colorado State Univ., 401pp.
- Hadfield M.G. et al. (1991a). Large-eddy simulations of thermally forced circulations in the convective boundary layer. Part I: A small-scale circulation with zero wind. *Boundary Layer Met.* **57**, 79-114.

- Hadfield, M. G., W. R. Cotton, and R.A. Pielke (1991b). Large-eddy simulations of thermally forced circulations in the convective boundary layer. Part II: The effect of changes in wavelength and wind speed. *Bound. Layer Meteor.*, **58**, 307-327.
- Herwehe, J.A. (2000): A numerical study of the effects of large eddies on trace gas measurements and photochemistry in the CBL, Ph.D. dissertation, Dept. of Atmos. Sci, U. of Alabama in Huntsville.
- Herwehe, J.A. et al. (2002): Initial application of a coupled LES-Photochemical model to examine near-source ozone production from industrial emissions. Paper presented at the 15th AMS Symp. on BL and Turb., Wageningen, Netherlands, July, 2002.
- Homer, C., C. Huang, L. Yang, B. Wylie and M. Coan, 2004: Development of a 2001 national land-cover database for the United States. *Photo. Eng. Rem. Sensing*, **70**, 829.
- Knoderer, C. A. and C. P. MacDonald (2007): TEXAQS-II radar wind profiler, radio acoustic sounding system, sodar, and lidar data quality control and mixing height derivation. Final report prepared for Texas A&M University, STI-907100-3215-FR, 22 pp.
- Koch, S. E., M. desJardins, and P. J. Kocin (1983): An interactive Barnes objective map analysis scheme for use with satellite and conventional data. *J. Appl. Meteor.*, **22**, 1487–1503.
- Luvall, J. C. and H. R. Holbo (1989): Measurements of short-term thermal responses of coniferous forest canopies using thermal scanner data. *Remote Sens. Environ.*, **27**, 1-10.
- Mellor, G. L. and T. Yamada (1982): Development of a turbulence closure model for geophysical fluid problems. *Rev. Geophys. Space Phys.*, **20**, 851-875.
- Moeng, C.-H. (1984). A large-eddy-simulation model for the study of the planetary boundary layer. *J. Atmos. Sci.*, **41**, 980-1006.
- Moeng, C.-H. and J.C. Wyngaard (1986). An analysis of closures for pressure-scalar covariances in the convective boundary layer., *J. Atmos. Sci.*, **43**, 2499-2513.
- Moeng, C.-H., 1986. Large-eddy simulation of a stratus-topped boundary layer. Part I: Structure and Budgets. *J. Atmos. Sci.*, **43**, 2886-2900.
- Moeng, C.-H. and J.C. Wyngaard. 1988, Spectral analysis of Large-eddy simulations of the convective boundary layer. *J. Atmos. Sci.*, **45**, 3573-3587.
- Moeng, C.-H. and J.C. Wyngaard, 1989. Evaluation of turbulent transport and dissipation closures in second-order modeling. *J. Atmos. Sci.*, **46**, 2311-2329.
- Meong, C.H. and R. Rotunno, 1990. Vertical velocity skewness in the buoyancy-driven boundary layer. *J. Atmos. Sci.*, **47**, 1149-1162.

- Moeng, C.-H. et al., 1996. Simulation of a stratocumulus-topped PBL: Intercomparison among different numerical codes. *Bull. Am. Meteor. Soc.*, **77**, 261-278.
- Pielke, R. A., and Coauthors (1992): A comprehensive meteorological modeling system – RAMS. *Meteor. Atmos. Phys.*, **49**, 69-91.
- Ryerson, T. et al. (2003): Effect of petrochemical industrial emissions of reactive alkenes and NO_x on tropospheric ozone formation in Houston, Texas, *J. Geophys. Res.* **108 (D8)**, 4249, doi:10.1029/2002 ID003070.
- Sykes R.I. et al. (1992). Large-eddy simulation of a turbulent reacting plume. *Atmos. Environ.* **26A**, 2565-2574.
- Trainer, M., et al. (1987). Models and observations of the impact of natural hydrocarbons on rural ozone, *Nature*, **329**, 705-707.
- Trainer M., et al. (1991). Observations and modeling of the reactive nitrogen photochemistry at a rural site. *J. Geophys Res.* **96 (D2)** , 3045-3063.
- Trainer, M. (2001): Are the observations made on the NCAR-Electra consistent with chemical processing ? Paper presented at the Texas 2000 Air Quality Study Data Review Meeting, Austin TX, June 2001.
- Walko R.L. et al. (1992). Large-eddy simulations of the effects of hilly terrain on the convective boundary layer. *Boundary Layer Met.* **58**, 133-150.
- Zhong, S. and J. D. Fast (2003): An evaluation of the MM5, RAMS, and Meso-Eta models at subkilometer resolution using VTMX field campaign data in the Salt Lake Valley. *Mon. Wea. Rev.*, **131**, 1301–1322.